

**Multi-Dimensional Radiation
Hydrodynamic Simulations
of the
Non-Magnetic Solar Atmosphere**

Dissertation
zur Erlangung des Doktorgrades
der Mathematisch-Naturwissenschaftlichen Fakultät
der Christian-Albrechts-Universität
zu Kiel

vorgelegt von
Sven Wedemeyer

Kiel
2003

Referent/in : Prof. Dr. H. Holweger

Korreferent/in : Prof. Dr. R. Wimmer-Schweingruber

Tag der mündlichen Prüfung : 09.07.2003

Zum Druck genehmigt : Kiel,

Der Dekan

Contents

Zusammenfassung	1
Abstract	3
1 Introduction	5
2 The Quiet Sun in a Nutshell	9
2.1 Full-Disk Observations	11
2.2 The Solar Structure: From Core to Corona	11
2.2.1 Magnetic Network and Internetwork Regions	13
2.2.2 Magnetic Canopy	14
2.2.3 Typical Scales	14
2.3 Oscillations	14
2.4 Calcium Bright Grains	17
2.5 Bright Cell Points at 1600 Å	19
2.6 Carbon Monoxide	19
2.6.1 Thermal Bifurcation	21
2.7 Energy Flux	21
2.7.1 Radiative Flux	21
2.7.2 Acoustic Flux	21
3 Models of the Outer Solar Atmosphere	25
3.1 Classical Semi-Empirical Models	25
3.2 Models with Prescribed Heating	27
3.3 COmosphere	27
3.4 Multi-Component Models	28
3.5 One-Dimensional Dynamical Models	29
3.6 Multi-Dimensional Models	31
4 Theory	33
4.1 Hydrostatics	33
4.2 Hydrodynamics	33
4.2.1 Hydrodynamic Equations	33
4.2.2 Convection	35
4.2.3 Acoustic Waves	36
4.2.4 Shock Waves	37
4.3 Equation of State	38
4.4 The Radiation Field	39
4.4.1 Intensity	39

4.4.2	Emission and Absorption	39
4.4.3	Source Function	40
4.4.4	Optical Depth	40
4.4.5	Equation of Radiative Transfer	40
4.4.6	Thermodynamic Equilibrium	41
4.4.7	Local Thermodynamic Equilibrium	41
4.4.8	Radiative Flux	41
4.4.9	Mean Absorption Coefficients	42
4.5	Energy Flux	43
4.6	The Autocorrelation Function	43
5	The Radiation Hydrodynamics Code CO⁵BOLD	45
5.1	General Procedure	46
5.2	Hydrodynamics	47
5.2.1	Hydrodynamic Equations	47
5.2.2	Numerical Grid	48
5.2.3	One-Dimensional Hydrodynamics Step	48
5.2.4	Equation of State	49
5.3	Tensor Viscosity	49
5.4	Radiative Transfer	50
5.4.1	Opacity Tables	51
5.5	Boundary Conditions	53
5.5.1	Lateral Boundaries	54
5.5.2	Lower Boundary	54
5.5.3	Upper Boundary	54
5.6	Output Data	54
6	Hydrodynamic Models	57
6.1	The Numerical Grid	57
6.2	Three-Dimensional Models	57
6.3	Two-Dimensional Models	60
7	Results for the Three-Dimensional Reference Model	61
7.1	Structure of the Model Atmosphere	61
7.1.1	Average Stratification	61
7.1.2	Vertical Structure	64
7.1.3	Horizontal Structure	64
7.1.4	Granulation	69
7.1.5	Chromospheric “Background” Pattern	70
7.1.6	Bright Points	72
7.1.7	Cool Regions	72
7.1.8	Pattern Evolution Time Scales	76
7.1.9	Upshot	78
7.2	Waves and Shocks	78
7.2.1	Excitation, Propagation, and Shock Formation	79
7.2.2	Three-Dimensional Structure	82
7.2.3	Velocity Distribution	84
7.2.4	Dependence on Numerical Modelling	86
7.3	Oscillations	86

7.3.1	Velocity Signal, Frequency and Wavenumber Range	86
7.3.2	Power of Plane-Parallel Oscillation Modes	88
7.3.3	Variation of Power with Height	88
7.4	Temperature Distribution	91
7.4.1	Thermal Bifurcation	91
7.4.2	Temperature Stratification	91
7.4.3	Chromospheric Temperature Components	95
7.4.4	Temperature Fluctuations	96
7.5	Radiative and Mechanical Energy Flux	97
7.5.1	Total Flux	97
7.5.2	Flux Divergence	99
7.5.3	Time Dependence of Flux Divergence	101
7.5.4	Chromospheric Emission and Basal Flux	102
7.5.5	Uncertainties and Remaining Problems	105
7.6	Carbon Monoxide	105
7.6.1	Formation, Dissociation, and Concentration	105
7.6.2	Static Atmosphere	106
7.6.3	Dynamic Atmosphere	107
7.6.4	Discussion	109
8	Dependence on Model Assumptions	111
8.1	Model Sample	111
8.2	Temperature Stratifications	112
8.3	Temperature Fluctuations	116
8.4	Velocity Fluctuations and Acoustic Flux Generation	117
8.5	Power Distribution	119
8.6	Radiative Flux	121
8.7	Summary	123
9	Conclusions	125
	Bibliography	133
	Acknowledgements	135

List of Figures

Chapter 1: Introduction

1.1 The solar chromosphere	6
--------------------------------------	---

Chapter 2: The Quiet Sun in a Nutshell

2.1 Full-disk images of the Sun	10
2.2 Schematic structure of the Sun	12
2.3 Granulation pattern	13
2.4 High-resolution Ca II <i>H</i> image	16
2.5 Profile of the Ca II <i>K</i> spectral line	17

Chapter 3: Models of the Outer Solar Atmosphere

3.1 Stratifications of semi-empirical models	26
3.2 Multi-component models	28
3.3 Temperature stratification by Carlsson & Stein (1994)	30

Chapter 4: Theory

4.1 Shock formation	37
4.2 Definition of specific intensity	39

Chapter 5: The Radiation Hydrodynamics Code CO⁵BOLD

5.1 Schematic procedure	47
5.2 Opacity tables	51
5.3 Entropy	53

Chapter 6: Hydrodynamic Models

6.1 Numerical grid	58
------------------------------	----

Chapter 7: Results for the Three-Dimensional Reference Model

7.1 Average stratifications	62
7.2 Vertical slices	63
7.3 Temperature in horizontal slices at different heights	66
7.4 Log. density in horizontal slices at different heights	67
7.5 Velocity in horizontal slices at different heights	68
7.6 Granulation: Numerical model and observation	69
7.7 Time sequence of horizontal temperature slices	70
7.8 Chromospheric “background” pattern	71
7.9 Continuum intensity at 1600 Å	71
7.10 Cool regions	72
7.11 Cool area fraction	73

7.12	Variation of temperature with time	74
7.13	Duration of cool episodes	75
7.14	Pattern evolution: Autocorrelation functions and heigh-dependent time scales . .	77
7.15	Formation and propagation of shock fronts	80
7.16	Vertical wave profiles	81
7.17	Exemplary three-dimensional shock wave	83
7.18	Velocity distribution	85
7.19	Time variation of horizontally averaged velocity	87
7.20	Plane-parallel oscillation modes: Power spectra	89
7.21	Variation of oscillation modes with geometrical height	90
7.22	Height-dependent temperature histogram	92
7.23	Average temperature stratifications	93
7.24	Hot and cool chromospheric temperature components	95
7.25	Temperature fluctuations	97
7.26	Height variation of average energy fluxes	98
7.27	Flux divergence	100
7.28	Time variation of mechanical and radiative flux divergence	102
7.29	Time scales and concentrations of carbon monoxide	108
Chapter 8: Dependence on Model Assumptions		
8.1	Temperature stratifications	114
8.2	Temperature fluctuations	115
8.3	Velocity fluctuations for the basic set of models	117
8.4	Velocity fluctuations for different viscosity parameters	118
8.5	Power spectra and oscillation bands	120
8.6	Maxima of radiative flux divergence	122

List of Tables

Chapter 2: The Quiet Sun in a Nutshell

2.1 Global properties of the Sun	9
--	---

Chapter 6: Hydrodynamic Models

6.1 Hydrodynamic models	59
-----------------------------------	----

Chapter 7: Results for the Three-Dimensional Reference Model

7.1 Composition of the chromospheric emission	103
7.2 Chromospheric emission: Ca II and Mg II line fluxes	104

Chapter 8: Dependence on Model Assumptions

8.1 Model sample	112
8.2 Selected values of the temperature distribution	113
8.3 Velocity fluctuations	117
8.4 Convective velocities and generation of acoustic flux	118
8.5 Power distribution	121
8.6 Radiative flux	122

Zusammenfassung

Selbst nach vielen Jahrzehnten intensiver Forschung bleiben viele Details der Chromosphäre der Sonne ungeklärt. Ursache sind Beobachtungen verschiedener Bereiche des Sonnenspektrums, die zu unterschiedlichen, sich widersprechenden Modellen führten. So legen Beobachtungen im UV (z.B. Ca II $H+K$) die Existenz eines Temperaturminimums am Boden der (nicht-magnetischen) Chromosphäre und einen starken Temperaturanstieg in den Schichten darüber nahe. Dies aber steht in scheinbarem Widerspruch zu der deutlichen Präsenz von Kohlenmonoxid in der Sonnenatmosphäre und den dafür nötigen geringen Temperaturen. Bislang war es nicht möglich, die verschiedenen Diagnostiken mit nur einem einzigen Modell wiederzugeben, obwohl viele Teilaspekte bereits erfolgreich modelliert werden konnten. Darüberhinaus ergibt sich die Frage, wie die hohen Temperaturen entstehen, die von vielen Beobachtungen – wenn auch nicht von allen – gefordert werden. Neben magnetischen Effekten, die bedeutend für die höheren Schichten sind, besteht für die nicht-magnetischen Regionen der unteren Atmosphärenschichten die Möglichkeit der Heizung durch akustische Wellen. Dabei wird allgemein angenommen, dass solche Wellen von starken Strömungen am oberen Rand der Konvektionszone erzeugt werden. In der vorliegenden Arbeit werden die oben angedeuteten Fragen mittels dreidimensionaler Strahlungs-Hydrodynamik-Simulationen untersucht, die alle Schichten umfassen, die für die Erzeugung, Ausbreitung und Dissipation akustischer bzw. Stoßwellen relevant sind. Dazu wird das Computerprogramm CO⁵BOLD verwendet, welches von B. Freytag und M. Steffen entwickelt wurde. Zunächst werden keine Magnetfelder berücksichtigt, so dass sich diese Arbeit ausschließlich auf die Modellierung sogenannter Internetwork Regions beschränkt, d.h., auf Bereiche mit vernachlässigbar schwachen Magnetfeldern.

Mit CO⁵BOLD ist es möglich, die Strahlungstransport- und Hydrodynamikgleichungen zeitabhängig für ein kompressibles Gas auf einem kartesischen Gitter in zwei oder drei räumlichen Dimensionen zu lösen. Umfangreiche Rechnungen ergaben schließlich ein dreidimensionales hydrodynamisches Referenzmodell, sowie weitere zwei- und dreidimensionale Vergleichsmodelle mit unterschiedlichen Modellannahmen.

Das bemerkenswerteste Ergebnis ist die Struktur der Modellchromosphäre, die räumlich und zeitlich sehr variabel ist. Dies wird bereits in horizontalen Schnitten durch das Referenzmodell deutlich, in denen netzwerkähnliche Strukturen aus heißem Gas und dazwischenliegende kühlere Regionen mit Temperaturen bis hinunter zu ~ 1800 K zu erkennen sind. Die Modellchromosphäre ist folglich geprägt durch eine thermische Bifurkation, d.h. die Koexistenz von heißen und kühlen Gebieten. Während die räumlichen Skalen in etwa denjenigen der am Boden der Photosphäre zu erkennenden Granulation entsprechen, so sind die Zeitskalen in der Chromosphäre deutlich kürzer, etwa in der Größenordnung von ~ 20 Sekunden.

Das Aussehen der Chromosphäre ist eine direkte Folge der Wechselwirkung von sich ausbreitenden Stoßwellen. In dem Modell ist deutlich zu erkennen, dass kontinuierlich Wellen nahe dem oberen Rand der Konvektionszone erzeugt werden, die dann nach oben in die dünneren Atmosphärenschichten laufen. In der Regel steilen sich die Wellen in der unteren Chromosphäre

zu Schocks auf, die hohe Temperatur- und Geschwindigkeitsamplituden mit sich bringen. Das Modell zeigt aber nicht nur Dynamik in Form von sich ausbreitenden Wellen, sondern auch stehende (plan-parallele) Schwingungen, die somit die Schichtung als ganzes betreffen. Höhenabhängige Fourier-Spektren, die aus der gemittelten Vertikalgeschwindigkeit gewonnen wurden, zeigen deutlich eine dominierende Oszillationsmode mit einer Periode nahe fünf Minuten. In den höheren Schichten sinkt der Beitrag des 5-min-Bandes allerdings so weit ab, dass die Leistung im 3 min-Band in der mittleren Chromosphäre dominiert. Diese kurzperiodischen Schwingungen sind dagegen in den unteren Schichten unbedeutend. Die gefundenen Moden und deren Höhenverlauf passen qualitativ sehr gut zu Beobachtungsergebnissen, was bedeutet, dass die Dynamik der Sonnenatmosphäre bereits gut wiedergegeben wird.

Angesichts der hohen zeitlichen und räumlichen Variabilität und den damit verbundenen großen Geschwindigkeits- und Temperaturschwankungen wird deutlich, dass die häufig verwendeten eindimensionalen, statischen Modelle die Natur der äußeren Sonnenschichten nicht angemessen wiedergeben können. Dies gilt insbesondere für die Temperaturschichtung, die in "klassischen" semi-empirischen Modellen ein Temperaturminimum und einen Anstieg darüber aufweist. Die mittlere Gastemperatur des dreidimensionalen Referenzmodells weist jedoch nur ein schwach ausgeprägtes, kaum merkliches Minimum und ein annähernd konstantes Niveau darüber auf. Dies wurde bereits in eindimensionalen dynamischen Simulationen von Carlsson & Stein gefunden, die zudem zeigen konnten, dass der Temperaturanstieg der semi-empirischen Modelle auf die nicht-lineare Temperaturabhängigkeit der Planck-Funktion im Ultraviolett zurückzuführen ist. Gemittelte Intensitäten werden daher im UV von hohen Temperaturen, wie etwa in Schockfronten, dominiert, so dass die abgeleiteten Temperaturschichtungen daher irreführend sein können. Dieses Ergebnis wurde anhand einer mittleren Emissivitätstemperatur für das hier vorgestellte Referenzmodell bestätigt, was zeigt, dass die Berücksichtigung der räumlichen und zeitlichen Inhomogenitäten essentiell wichtig ist.

Angeregt durch die gefundenen sehr kühlen Temperaturen wurden erste zeitabhängige Berechnungen zur Bildung von Kohlenmonoxidmolekülen (CO) durchgeführt. Trotz der starken Vereinfachungen zeigen die Rechnungen, dass CO durchaus in der mittleren Photosphäre bis unteren Chromosphäre in signifikanter Konzentration vorhanden sein könnte, wohingegen dies in den Schichten darüber effizient durch das Auftreten von Schockfronten und den damit hohen Temperaturschwankungen unterbunden wird. Entsprechende zeitunabhängige Rechnungen liefern wesentlich größere Konzentrationen, was zeigt, dass Rechnungen zur Bildung von Kohlenmonoxid zeitabhängig sein sollten.

Ein letzter wichtiger Punkt ist die Frage nach der akustischen Heizung der nicht-magnetischen Chromosphäre. Die Konservativität von CO⁵BOLD erlaubt die genauere Analyse der Energieflüsse und deren Divergenz in den oberen Atmosphärenschichten. Für das 3D-Referenzmodell ergab sich, dass genügend akustischer Fluss vorhanden ist, um die beobachtete chromosphärische Emission zu decken – gänzlich ohne zusätzliche Beiträge magnetischer Natur.

Einige Ergebnisse sind abhängig von speziellen Modellannahmen, wie z.B. der Betrag der akustischen Heizung und die Temperaturamplituden in den oberen Modellschichten, während der untere Teil des dreidimensionalen Modells weitgehend unbeeinflusst bleibt. Insbesondere die räumlichen und zeitlichen Skalen und die simulierte Dynamik sind sehr robust gegenüber Änderungen numerischer Details. Somit können in der vorliegenden Arbeit fundierte Aussagen bezüglich der räumlichen und zeitlichen Inhomogenität der Chromosphäre gemacht werden, die offensichtlich sehr wichtig für die Interpretation von Beobachtungsdaten und damit für die Konstruktion eines umfassenden Modells der äußeren, nicht-magnetischen Schichten der Sonne ist.

Abstract

After decades of intense research, still many details of the non-magnetic chromosphere of the Sun remain open. Observations of different spectral features lead to apparently contradicting models. On the one hand, observations in the UV (e.g., Ca II $H+K$) imply the existence of a thermal minimum at the bottom of the chromosphere and a strong temperature increase in the layers above but on the other, the existence of carbon monoxide requires low temperatures at the same heights. Hence, it has been impossible to reproduce all diagnostics with a single comprehensive model so far – although many aspects can be modelled successfully if taken alone. Furthermore, the question arises how the high temperatures are generated which are demanded by various observations – though not by all of them. Next to magnetic effects, which are important for the higher layers, the non-magnetic regions of the lower atmospheric strata might be heated by acoustic waves. It is commonly assumed that such waves are excited by strong flows at the upper boundary of the convection zone.

In this thesis, the above indicated questions are addressed with three-dimensional radiation hydrodynamic simulations which comprise all strata which are relevant for the generation, propagation, and dissipation of acoustic waves and shocks, respectively. The computer code CO⁵BOLD is used, which was recently developed by B. Freytag and M. Steffen. Magnetic fields are not taken into account, restricting the modelling in this thesis to so-called internetwork regions, i.e., areas with negligibly weak magnetic fields.

CO⁵BOLD allows the time-dependent solution of the equations of radiative transfer and hydrodynamics for a fully compressible gas on a grid of Cartesian geometry in two or three spatial dimensions. Extensive computations finally produced a three-dimensional hydrodynamic reference model and additional two- and three-dimensional models with different parameters which were analysed with respect to the posed questions.

The most remarkable result is the structure of the model chromosphere which is highly variable in space and time. This already becomes clear from horizontal cuts through the reference model, which reveal network-like structures of hot gas with enclosed cool regions with temperatures down to ~ 1800 K. The model chromosphere is thus characterised by a thermal bifurcation, i.e., the co-existence of hot and cool regions. While the spatial scales correspond to those of the granulation at the bottom of the photosphere, the time scales are much shorter in the chromosphere than in the layers below, roughly only of the order of ~ 20 seconds.

The appearance of the chromosphere is a direct consequence of the interactions of propagating shock waves. The model shows clearly the continuous generation of waves near the upper boundary of the convection zone and the propagation of the waves into the thin upper atmospheric layers. Typically, the waves steepen into shocks in the low chromosphere, exhibiting large temperature and velocity amplitudes.

Dynamics are not only present in the form of propagating waves, but also as standing (plane-parallel) oscillations, which affect the stratification as a whole. Height-dependent Fourier spectra, derived on the basis of averaged vertical velocities, clearly show a dominating oscillation

mode with a period near five minutes. The contribution of the 5 min band to the total power decreases significantly in the higher layers, so that the power of the 3 min band dominates in the middle chromosphere. The corresponding oscillations of short period are rather unimportant in the lower layers. The modes and their variation with height is qualitatively in line with results inferred from observations. Thus, the dynamics of the solar atmosphere can be reproduced reasonably well.

In view of the high temporal and spatial variability and the connected large velocity and temperature variations it becomes clear that commonly used one-dimensional static models cannot provide a proper description of the outer atmosphere of the Sun. This is in particular true for the temperature stratification, which – in “classical” semi-empirical models features a temperature minimum and a rise in the layers above. The mean gas temperature of the three-dimensional reference model, however, exhibits only a weak, hardly notable minimum and an almost constant level above. This has already been found in one-dimensional dynamic simulations by Carlsson & Stein who also showed that the temperature rise in semi-empirical models is caused by the non-linear temperature dependence of the UV Planck function. Thus, mean UV intensities are governed by high temperatures, as present in shocks, so that inferred temperature stratifications might be misleading, in the sense that they do not represent the average gas temperature. This finding is confirmed by the mean emissivity temperature for the 3-D reference model presented here, indicating the essential importance of taking into account the spatial and temporal inhomogeneities.

Inspired by the very low temperatures, first time-dependent calculations for the formation of carbon monoxide molecules (CO) were performed. Despite strong simplifications the calculations show that CO can build up a significant concentration in the photosphere and low chromosphere, whereas it is effectively suppressed in the layers above – due to the presence of shock waves and the connected large temperature variations. Corresponding static calculations produce significantly higher concentrations, implying the need for a time-dependent approach.

Last but not least, the acoustic heating of the non-magnetic chromosphere is addressed. The conservation properties of CO⁵BOLD allow a quantitative analysis of the energy fluxes and their divergence in the upper atmospheric layers. The 3-D reference model provides sufficient acoustic flux to account for the observed chromospheric emission – without need of additional contributions related to magnetic fields.

Some results depend on particular model assumptions to some extent, such as the amount of acoustic heating and the temperature amplitudes in the upper layers. In contrast, the lower part of the three-dimensional model remains mostly unaffected. In particular the spatial and temporal scales and the simulated dynamics are very robust with respect to changes of numerical details. Hence, in this thesis well-founded statements on the spatial and temporal inhomogeneities of the chromosphere can be made, which are obviously of great importance for the interpretation of observations and thus for the construction of a comprehensive model of the outer non-magnetic layers of the Sun.

Chapter 1

Introduction

The chromosphere is a thin layer of the solar atmosphere, embedded between the photosphere below and the corona above. It is only a few thousand kilometres thick and thus makes up only a tiny fraction of the large radius of the Sun. Moreover, it is largely outshone by the underlying photosphere, which is – as the name implies – the place where most of the visual light is emitted. Under natural circumstances the chromosphere is thus only observable during a total eclipse when the photosphere is totally blacked out by the moon for only a short time (see Fig. 1.1). The colourful appearance gave the chromosphere its name¹. Total eclipses are rather rare events which are only visible from a very limited region on Earth. Hence, laborious expeditions were necessary in the early days of the exploration of the solar chromosphere in the 19th century. Today, the chromosphere is observed with advanced techniques from the ground and from spacecraft. But despite essential progress in the understanding of the outer solar layers, details of the non-magnetic chromosphere remain still open, mainly due to apparently contradicting observations. On the one hand, observations of chromospheric spectral lines in the ultraviolet (UV) such as lines of singly ionised calcium (e.g. Cram & Dame 1983; Carlsson et al. 1997; Krijger et al. 2001) show bright emissions of grainy nature on the entire solar disk (see Sect. 2.4). On the other hand, spectral features of molecules like carbon monoxide are clearly present (see Sect. 2.6 and references therein) and originate from the same heights as the UV emission. While the formation and existence of molecules requires relatively cool temperatures, $T \lesssim 4000$ K, much larger temperatures are indicated by the UV observations. Furthermore, extremely high temperatures of $\gtrsim 10^6$ K are observed at higher altitudes in the low-density corona, while the solar "surface", i.e., the bottom of the photosphere, is characterised by a temperature of only ~ 6000 K. Consequently, the temperature has to rise at some point in order to reach the high coronal values.

A hot chromosphere demands for an efficient heating mechanism which provides the required energy capable of sustaining the observed radiative losses. Apart from magnetic fields the heating is likely to be accomplished by dissipation of acoustic waves. The basic idea of acoustic heating of the outer solar layers goes back on Biermann (1946, 1948) and Schwarzschild (1948) (Schwarzschild originally referred to the corona.) The source of the waves, so to say the "acoustic motor", is believed to be located near the top of the convection zone, which lies below the photosphere and reaches as far as 2×10^5 km inside the solar interior. The solar photosphere is continually perturbed by convective motions and oscillations. The large density gradient of many scale heights (roughly 14 from the photosphere to the base of the transition region) provides the proper conditions for the amplification of initially small perturbations, since any upward propagating disturbance will grow in amplitude to conserve energy – unless it is strongly

¹The name chromosphere is derived from the Greek word for colour.

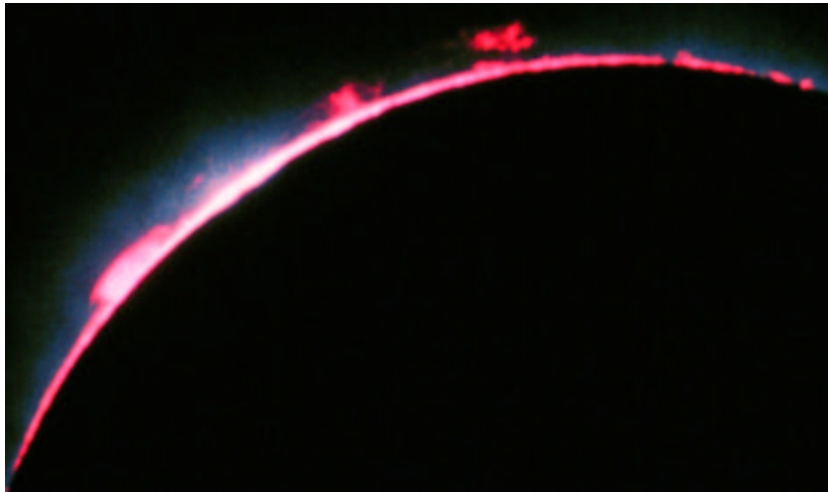


Figure 1.1: The solar chromosphere in profile at the limb of the disk during the total eclipse in August 1999. The bright photosphere is shadowed by the moon. (*Copyright: T. Credner, AlltheSky.com, 1999*)

dissipated. Further up in the atmosphere, the acoustic waves finally steepen into shock waves – like water waves which break on a sloping beach. In this picture, the waves would dissipate in the chromosphere, effectively depositing mechanical energy which has been transported upwards from the convection zone. However, today it is generally assumed that acoustic heating is only significant in the lower chromosphere of the non-magnetic regions while the heating of the upper chromosphere and the corona is due to magnetic effects (see, e.g., Priest 1982).

The picture of propagating sound waves in the solar atmosphere did not solve the puzzle arising from the apparently contradictory observations but it posed the question if the solar chromosphere is a static or a rather dynamic region. The latter is not to be dismissed in view of observations which reveal dynamic events as the widely discussed Ca II K -bright points. A controversy about the nature of the chromosphere of the non-magnetic quiet Sun is going on for many years now (see e.g. Kalkofen 2001; Ayres 2002), dealing basically with the following questions:

- Is the chromosphere of the average quiet Sun a time-dependent phenomenon with a mostly cool background and large temperature fluctuations due to upward propagating shock waves?
- Or is it persistent and always hot with only small temperature fluctuations?
- In short: Is the non-magnetic solar chromosphere hot or cool?
- Is the amount of energy provided by acoustic waves sufficient to explain the heating derived from observations?
- Or are additional contributions related to magnetic fields necessary?

Many attempts have been made to construct models which describe the stratification of the outer layers of the Sun. While the density commonly decreases monotonically with height (above the solar "surface"), the variation of the temperature with height depends largely on the employed observations. Very prominent examples are the semi-empirical models of the non-magnetic chromosphere of the average quiet Sun by (e.g., Vernazza et al. 1981; Fontenla

et al. 1993, see Sect. 3.1) which are mainly based on UV and microwave observations. A common feature of these "classical models" is a temperature minimum of $T_{\min} \approx 4200 - 4400$ K at a height of $z \approx 500$ km above optical depth unity and an outwardly increasing temperature above (see Fig. 3.1). The implied heating of the upper layers is generally assumed to be provided by acoustic waves, generated by the turbulent flows at the top of the convection zone (see, e.g., Musielak et al. 1994; Ulmschneider et al. 1996, and references therein for a quantitative estimate of acoustic fluxes for a wide range of stellar types according to the Lighthill-Stein theory). The energy deposition in the solar chromosphere has been determined by Anderson & Athay (1989b) by means of theoretical models incorporating a prescribed heating. The heating rates were adjusted to generate a temperature structure which reproduces selected observational features, i.e., time- and space-averaged continuum and line intensities in the UV and microwave range. However, the physical conditions for the formation of chromospheric emission lines differ from those appropriate for the formation and existence of molecules like carbon monoxide. Consequently, the CO vibration-rotation line intensities cannot be reproduced with this class of models. On the other hand, models based on CO line fits show a steady temperature decrease in the chromosphere (Wiedemann et al. 1994) which fails to reproduce the UV diagnostics.

Thus, as discussed before, it becomes clear that the temperatures in the chromosphere must be high enough to account for the UV emission and – at the same time – low enough to allow for the formation of CO molecules. The required conditions cannot be simply described with one of the models stated above, neither by a general temperature rise, nor by an always cool stratification. This dilemma led to the idea of a thermally bifurcated chromosphere (e.g. Ayres 1981; Wiedemann et al. 1994; Ayres & Rabin 1996; Ayres 2002) and consequently to multi-component models with contributions from cool and hot gas in different proportions (e.g. Ayres et al. 1986; Avrett 1995; Ayres & Rabin 1996; Ayres 2002). This class of models is able to reproduce observations much more satisfactorily than one-component models, but not all observational constraints could be satisfied, probably because of simplifications still inherent in these models. After all, these models show that the apparent contradiction can be solved if a thermal bifurcation is assumed.

All models mentioned above are hydrostatic and thus cannot account for the dynamic behaviour of the chromosphere but can only describe time-averaged properties. Since the observations show that the chromosphere of the quiet Sun is very dynamic (e.g. Carlsson et al. 1997; Muglach & Schmidt 2001; Krijger et al. 2001; Wunnenberg et al. 2002), a time-dependent modelling is required.

The pioneering work on 1-D time-dependent models of chromospheric heating by acoustic and MHD waves is due to Ulmschneider and collaborators. In a long series of papers starting in the 1970s (e.g., Ulmschneider et al. 1978, 1987; Ulmschneider 1989), they studied the hydrodynamics of the chromospheric layers under the influence of short-period monochromatic waves prescribed at the bottom of their models according to the Lighthill-Stein theory (see above), not only for the Sun but also for different main-sequence stars and giants. Based on these models, they conclude that the "basal heating" of the chromospheres of late-type stars is fully attributable to the dissipation of acoustic wave energy (Buchholz et al. 1998).

A further improvement for the Sun was achieved with the detailed time-dependent 1-D radiation hydrodynamics simulations by Carlsson & Stein (1994, hereafter CS) (see also Carlsson & Stein 1992, 1995, 1997). They successfully modelled CaII H_2V bright points as a result of propagating shock waves which are excited by a piston at the bottom of their model. Unlike Ulmschneider and collaborators, the piston in their model is driven by a velocity pattern derived from observations. Instead of a temperature minimum and a monotonically increasing temperature above, as it is the case for the models by Vernazza et al. and Fontenla et al., CS

find a chromosphere with a mostly cool background and large temperature fluctuations due to upward propagating shocks. Even more remarkable is the fact that they are able to reproduce the rise of the radiation temperature without an increase of the mean gas temperature. Basic reasons are the non-linear temperature dependence of the Planck function in the UV (see, e.g., Ayres & Linsky 1976; Ayres 1991) and the extreme temperature peaks of the shock waves. This lead CS to the conclusion that the chromosphere of the quiet Sun is not persistent but a spatially and temporally intermittent phenomenon which – if averaged temporally – is mostly cool and not hot.

Carlsson & Stein have been criticised (see Kalkofen et al. 1999; Kalkofen 2001), reasoning that their finding is in contrast to observations which indicate a permanent temperature rise. One major point of the criticism concerns the lack of acoustic waves with short periods in the CS model which should not change the properties of the bright points but could be an additional source of energy for chromospheric heating.

A perhaps more important point is that the model by CS is only one-dimensional and therefore, by nature, cannot account for horizontal inhomogeneities. The controversy can only be clarified by more advanced models which can account for spatial and temporal inhomogeneities, i.e., dynamic self-consistent multi-dimensional models. An example for such a model is the work by Skartlien et al. (2000, see also Skartlien 2000) who added coherent isotropic scattering to the Nordlund-Stein code (see, e.g., Stein & Nordlund 1998) to account for deviations from the local thermodynamic equilibrium (LTE), which are expected to occur in the chromosphere.

In this thesis new time-dependent 2-D and 3-D models are presented which were calculated with CO⁵BOLD – a radiation hydrodynamics code recently developed by B. Freytag and M. Steffen (Freytag et al. 2002). As the full name “*CO*nserVative *CO*de for the *CO*mputation of *CO*mpressible *CO*nvection in a *BO*x of *L* Dimensions with *l=2,3*” implies, the code provides desirable conservation properties. Furthermore, it is capable of handling hydrodynamic shocks with a minimum of numerical dissipation, which makes it a good choice for modelling the highly dynamic outer layers of the Sun. Models were created which extend from the upper convection zone to the middle chromosphere. Thereby, generation, propagation, and dissipation of acoustic waves are consistently included in the same simulation. With this tool at hand the following fundamental questions are addressed in the course of this thesis:

- *Is there a real temperature increase in the chromosphere or is it just an artefact due to too simple modelling?*
- *How important are spatial and temporal inhomogeneities for a proper description of the outer solar layers?*
- *What is required for a realistic model which is capable of explaining all diagnostics?*
- *Can the observed radiative emission of the quiet solar chromosphere be sustained by heating due to dissipation of acoustic waves?*

Chapter 2

The Quiet Sun in a Nutshell

The Sun – at first glance a “normal” star of spectral type G2V, aged around 4.5 billion years. It is a sphere of plasma consisting mainly of hydrogen ($\sim 90\%$) and helium ($\sim 10\%$), whereas all other chemical elements (called “metals” in astrophysics) comprise only about $\sim 0.1\%$. The solar radius of $R_{\odot} = 696\,000$ km is 108 times the radius of the Earth; the total mass of 2×10^{33} g is 745 times larger than the mass of all planets, thus constituting almost the entire mass of the solar system. Accordingly, the gravity acceleration at the solar surface is $g_{\odot} = 274 \text{ m s}^{-2}$, 28 times as large as on the surface of the Earth. However, these are all properties which are shared by a large number of other stars in the universe. But still there is an essential difference to other stars, namely the relatively short distance. Thus, apart from the Sun’s importance for life on Earth, it is the only star which allows the direct spatially resolved study of structure and mechanisms, and even in situ measurements which are not possible for other stars, making the Sun an important object for the study of stars in general.

A vast amount of literature has been piled up during many years of intense research, addressing many different solar phenomena with various observations and resulting models. Consequently, a complete description of the literature is far beyond the scope of this thesis. In particular the plethora of magnetic phenomena cannot be addressed in this context, since this thesis is on the modelling of the non-magnetic solar atmosphere. But even the non-magnetic phenomena provide a wide field, so that only a rough overview can be given here without the claim of completeness. Instead, the most relevant facts are described which are needed to define the constraints required for a realistic numerical model of the non-magnetic regions of the outer solar atmosphere.

Table 2.1: Global properties of the Sun.

spectral type		G2V
effective temperature	$T_{\text{eff},\odot}$	= 5780 K
age	\bar{t}_{\odot}	= 4.5×10^9 years
mean distance to Earth	d	= 1 AU = 149.6×10^6 km $\Rightarrow 1'' = 725$ km at solar surface
radius	R_{\odot}	= 6.96×10^5 km
mass	M_{\odot}	= 1.99×10^{33} g
mean density	$\bar{\rho}_{\odot}$	= 1.4 g cm^{-3}
gravity acceleration at surface	g_{\odot}	= 274 m s^{-2} , ($\log g_{\odot} = 4.4$)
escape velocity at surface	$v_{\text{esc},\odot}$	= 618 km s^{-1}

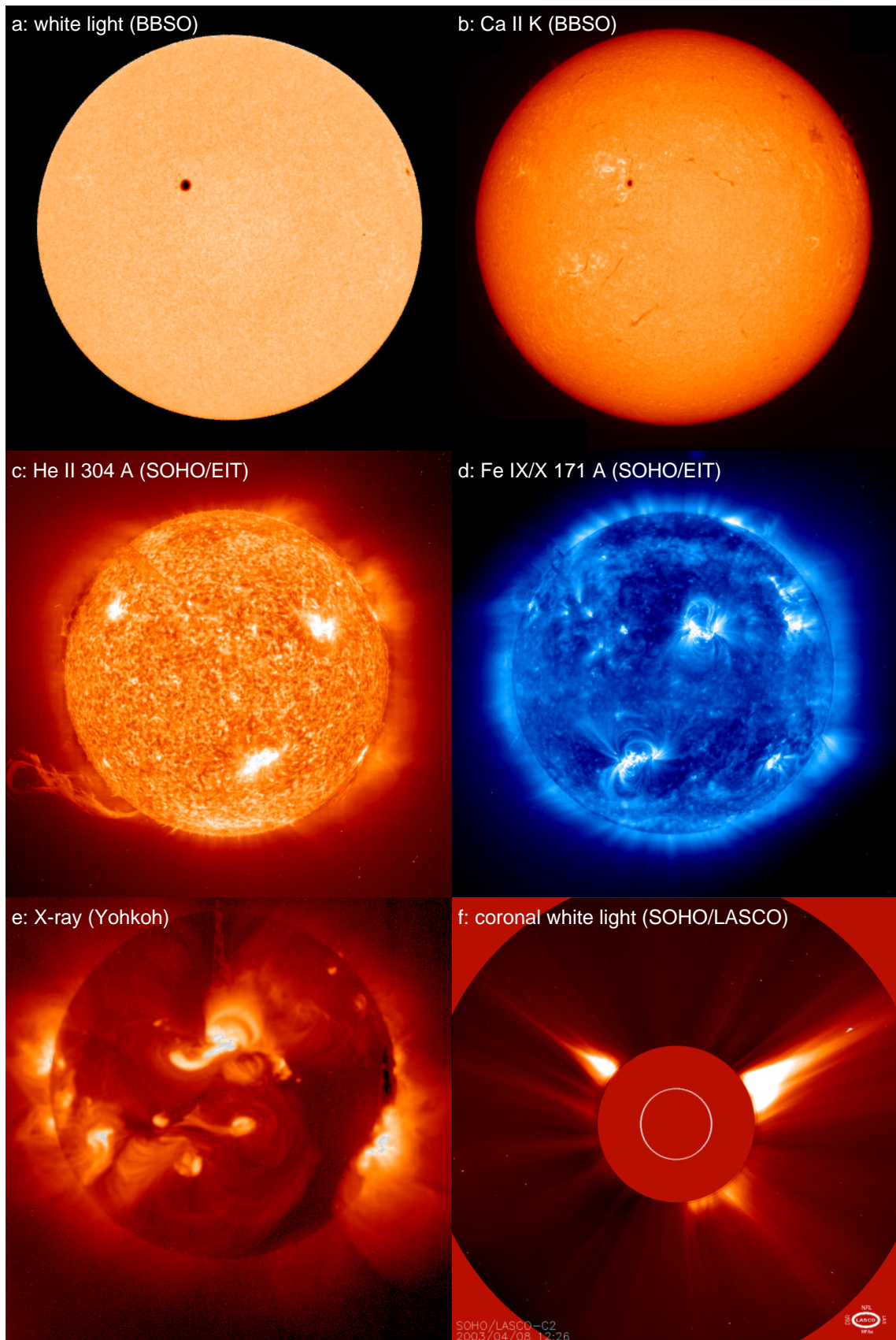


Figure 2.1: Full-disk images of the Sun at different wavelength ranges, (Courtesy of BBSO, SOHO, ESA & NASA, and Yohkoh.)

2.1 Full-Disk Observations

The Sun is continuously emitting a large amount of radiation, distributed over a wide wavelength range. The spectrum of the Sun comprises a continuum with many absorption and also emission lines, extending from the X-ray range, ultraviolet (UV), over the visible spectrum, and infrared (IR) to the radio range. Since different physical conditions are required for the formation of the various spectral features, different height ranges of the solar atmosphere are characterised by different emission. Hence, different diagnostics render different strata of the solar atmosphere and thus – if compared to each other – give an impression of the variation of the Sun’s appearance with height. In Fig. 2.1 full disk images are shown for six different diagnostics. The first panel shows a “simple” white light image as taken at the *Big Bear Solar Observatory* (BBSO). The image renders the *photosphere* from where the bulk of the visible light originates – giving the photosphere its name. The second image was also observed at the BBSO but in the light of the *Fraunhofer* line Ca II *K* ($\lambda = 3933.7 \text{ \AA}$) which is formed in the *chromosphere* (see Sect. 2.4). While the photosphere looks very homogeneous – except for the prominent dark sunspot and the granulation on a much smaller spatial scale –, the chromosphere is more structured, exhibiting dark and bright structures at various spatial scales – plages and filaments, to name just a few of the observed phenomena. There is also a distinct pattern related to magnetic fields which will be discussed in Sect. 2.2.1. Next to these large-scale pattern structures on smaller scales are present which are of particular interest for this thesis and thus will be addressed separately (see Sect. 2.4). The remaining pictures were taken by instruments aboard spacecrafts, e.g., by the *Extreme ultraviolet Imaging Telescope* (EIT) on SOHO (*Solar and Heliospheric Observatory*) for He II 304 \AA (third panel) and Fe IX/X 171 \AA (fourth panel). The first displays the uppermost chromosphere and the lower *transition region*, revealing large-scale structures like the huge prominence in the lower left corner. The Fe IX/X 171 \AA line exposes the nature of the pattern of the *corona* just above: Arches of enhanced emission clearly imply that the corresponding hot gas is confined to magnetic loops which emerge from the solar surface. Magnetic fields govern the appearance of the outermost layers of the Sun, as can be seen from the X-ray picture taken with the spacecraft *Yohkoh* and the coronal white light image recorded with LASCO aboard SOHO (Fig. 2.1.e and f, respectively). In the latter, the bright solar disk (marked by the white circle) was masked so that the fainter structure of the corona is visible. Clearly, the emission protrudes many stellar radii into the interplanetary space, on spatial scales which are very different from the fine-structured lower atmosphere.

2.2 The Solar Structure: From Core to Corona

Before particular observational constraints are defined, a rough overview over the structure of the solar interior and the outer layers is presented here, like it is commonly assumed nowadays (see Fig. 2.2).

Except for the outer layers, the Sun as a whole is characterised by hydrostatic equilibrium, i.e., forces due to gravity and (thermal) pressure are counterbalanced. As a direct consequence, very high temperatures of several million degrees ($T_c \sim 2 \times 10^7 \text{ K}$) and very high densities ($\rho_c \sim 2 \times 10^8 \text{ g cm}^{-3}$) are present in the very centre of the Sun. Under these extreme physical conditions, nuclear hydrogen fusion (“hydrogen burning”) is taking place in the *core*, which releases a large amount of energy. The energy is transported outwards by radiation up to a depth of roughly $2 \times 10^5 \text{ km}$ below the solar surface, where the *convection zone* begins (see also Sect. 4.2.2). From there on, convective motions provide the major mechanism of energy transport, while radiative transport plays only a minor role. The convection zone is characterised by large motion patterns, effectively mixing the plasma.

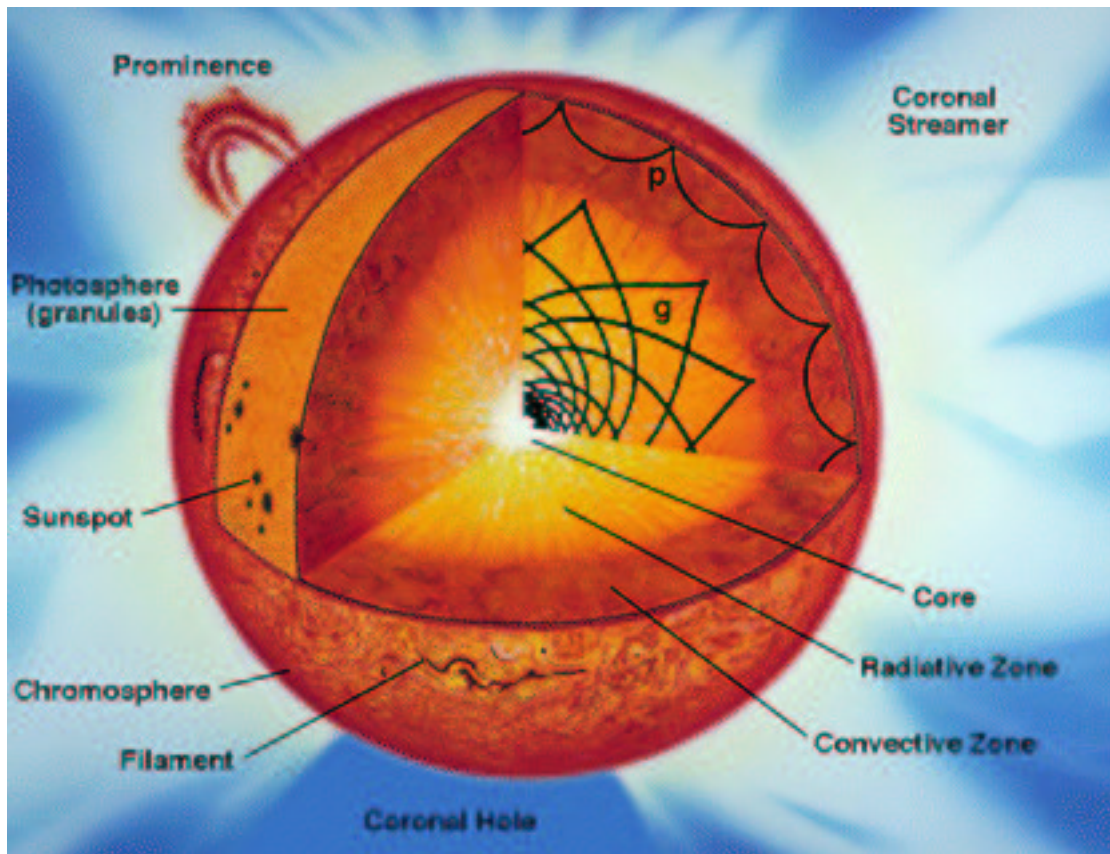


Figure 2.2: Schematic structure of the Sun: From the core, to the radiative and the convective zone, up to the outer layers. (Courtesy of SOHO, ESA & NASA)

Due to the decreasing density and temperature the matter becomes increasingly transparent for radiation, so that finally radiative energy transport becomes effective again and the convective motions cease. In this boundary layer – as the name “*photosphere*” implies – the bulk of radiation is released into the surrounding space. The photosphere is the origin of the radiation continuum and most of the absorption lines. It is only a few hundred kilometres thick, and thus tiny compared to the total size of the Sun.

Owing to the higher opacity, the layers below the photosphere, i.e., the convection zone, are not directly accessible to observations. Hence, only the very top of the convection zone can be seen as grainy pattern at the bottom of the photosphere. The so-called *granulation* (see Fig. 2.3) reveals the tops of convective cells with a typical horizontal extent of the order of 1000 km but with a wide range from very small to large sizes. Individual granules can be observed on average 8 min until they separate or vanish. However, the granular pattern as a whole apparently evolves on time scales of 5 min and less.

The intensity contrast, which renders the granulation in Fig. 2.3, translates into temperature deviations of some 100 K. The higher intensity in the interior of a granule is thus related to the higher temperatures of the gas which rises to the surface following the convective flow. At the “surface”, i.e., the layer where the matter becomes transparent for most of the radiation, the gas is advected laterally away from the cell interior, cools, and finally sinks down into the non-visible convection zone. The cooler gas produces less radiative flux and is thus seen as dark mesh, outlining the granules. The dark structures, commonly referred to as intergranular lanes, are indeed related to down-flowing material.

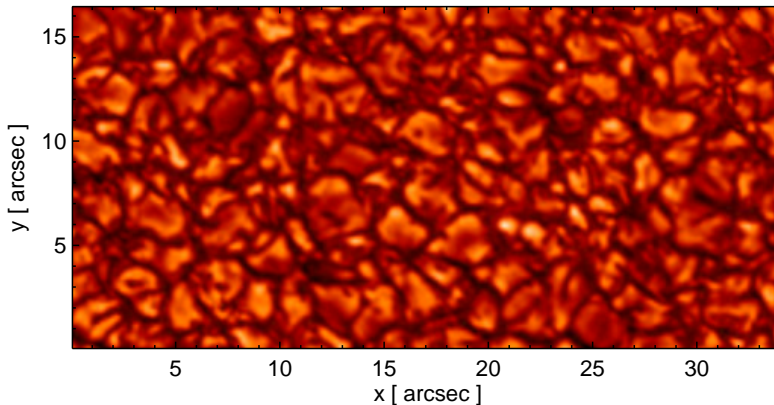


Figure 2.3: Observed granulation pattern. (*Kindly provided by M. Wunnenberg.*)

Overlying the fine granulation, a larger pattern is present, owing to larger and deeper reaching convective flows, namely the *supergranulation*. Its typical cell size is of order 15 000 to 40 000 km, while the lifetime of a supergranular cell is on average roughly ~ 36 hours.

In the photosphere, which can be regarded as the (non-solid) “surface” of the Sun, temperatures of order 6000 to 4000 K are common, pointing out the drastic decrease from core to surface by many magnitudes. The same applies to the density which continues to decrease in the layers above the photosphere. However, the temperature behaves different. In the classical view it reaches a minimum of roughly 4000 K at 500 km above optical depth unity (the “surface”), which defines the boundary between photosphere and overlying *chromosphere*, and continues to rise to coronal values above. However, the thermal structure of the chromosphere is still an open issue and thus subject of the thesis at hand. This is due to the fact that the low-density chromosphere is largely outshone by the bright photosphere, hampering the observations. According to “classical” models, the temperature rises to roughly 20 000 K at the top of the chromosphere, which might be located approximately 2000 km above its lower boundary. In the so-called *transition region* immediately above the temperature finally rises to extreme temperature of a few million Kelvin in the *corona*, although this strata might be only a few 100 km thick. The outermost layer – and thus the interface to the interplanetary medium – is the corona, owing its name (“*crown*”) to the impressive appearance during a solar eclipse. Although the corona extends many solar radii outwards, it comprises only a relatively small fraction of the solar mass due to the continued density decrease. The low density is opposed to the high temperatures which imply a high degree of ionisation and corresponding visible spectral lines, e.g., Fe XIV.

2.2.1 Magnetic Network and Internetwork Regions

In addition to the granulation, the outer solar atmosphere shows a structure on a larger spatial scale, owing to the existence of magnetic fields. Those fields are continuously advected with the hydrodynamic flow towards the boundaries of the supergranulation cells, where consequently an enhanced magnetic field is observed. There, the field is organised mainly in vertical flux tubes. Observations, e.g., $H\alpha$ filtergrams, reveal a network-like pattern which outlines the supergranulation. But this so-called *magnetic network* is not as regular as the correlation to the supergranular flow might suggest. Rather, it consists of crinkled segments which are arranged in an irregular pattern. Between the network elements, sometimes referred to as cell interior, only weak magnetic fields are present (Keller et al. 1994). Thus, magnetic fields are of minor

importance for the dynamics in the so-called *internetwork regions* – except for small isolated patches of magnetic flux within the regions (Livingston & Harvey 1971; Lites et al. 1993, 1999).

2.2.2 Magnetic Canopy

The *magnetic canopy* is a layer of magnetic field parallel to the solar surface, overlying field-free regions in the photosphere. It is formed by field-lines of magnetic flux tubes which spread out horizontally until they merge with the fields of adjacent flux tubes (if of equal polarity), and thus create an extended field, the so-called canopy. The critical height – where the fields above the otherwise non-magnetic atmosphere become important – is commonly stated as roughly around 1000 km (Solanki & Steiner 1990; Schrijver 1995, and references therein). Although the canopy is not expected to affect the wave propagation substantially, a realistic model of the outer solar layers should take into account magnetic fields above the critical height.

2.2.3 Typical Scales

Here, some typical values for the spatial and temporal scales are summarised which give important constraints for a realistic model:

Vertical scales:

- depth of the convection zone: $\sim 2 \times 10^5$ km
- vertical extension of the photosphere (from $\tau_{5000} = 1$ to classical temperature minimum): ~ 500 km
- pressure scale height in the photosphere: ~ 150 km

Horizontal scales:

- horizontal extension of an internetwork region: $\sim 15\,000 - 40\,000$ km (20-55")
- horizontal extension of a granular cell: $\sim 700 - 1500$ km (1-2")

Time scales:

- sidereal rotation period of the Sun (equator): ~ 26 days
- mean lifetime of a supergranule: ~ 36 h
- mean lifetime of a granule: ~ 8 min

2.3 Oscillations

In the previous sections it was demonstrated that the Sun exhibits spatial variations on a wide range of scales. Furthermore, it shows oscillatory temporal variations with short periods of a few minutes. The variations are so subtle that they were not discovered until 1960 by R.B. Leighton. The most prominent oscillation mode is found at a period near 5 min (3.3 mHz) and is consequently referred to as the 5 min oscillation. Once it had been found, a large variety of other oscillation modes was revealed in many different spectral features like in $H\alpha$, the Ca II *H+K* resonance lines, in the UV continuum, and also in spectral features of carbon monoxide – to name just a few. The oscillations show up as Doppler shifts of spectral lines made visible, e.g.,

by so-called Doppler plates which represent the resulting intensity differences between the blue and the red wing of a line.

The 5 min oscillation is not a single mode at a particular frequency but rather comprises modes in a larger frequency range, which is often stated with periods between 3 and 12 minutes, while the maximum amplitude is found slightly below 5 min in the photosphere. Higher up in the solar atmosphere the maximum is shifted towards shorter periods, until the so-called 3 min oscillation(s) becomes dominant in the chromosphere (see, e.g., Kneer & von Uexküll 1993; Krijger et al. 2001; Wilhelm 2002). It is rather a broad band with periods in the range of 2 – 5 min instead of a well-defined single mode.

The variation with height has been investigated in more detail by Cram (1978). Wavelength shifts and intensity fluctuations of different spectral lines such as Ni I 5892.9 Å, Na D₂, Ca II 8542 Å, H α , and at various positions in Ca II *K* were observed. These spectral features correspond to formation heights ranging from the photosphere to the upper chromosphere. Based on these data, a discrete (space-time) Fourier analysis was performed, resulting in $k - \omega$ (diagnostic) diagrams for the different lines. Since the spectral lines originate from different heights in the solar atmosphere, the differences in the $k - \omega$ planes provided insight into the height variation of the power distribution. First of all, it was found that the 5 min oscillations as well as the 3 min oscillations are present at all observed heights. Furthermore, the contribution of the 3 min oscillations with respect to the 5 min oscillation increases strongly with height, making the 3 min oscillation dominant at chromospheric heights. See also Kneer & von Uexküll (1993) for a comparison of simultaneous observations in Mg *b*₂, Ca II *K*, and H α . Other investigations show that the 3 min periods disappear at the formation height of the Lyman continuum, which exhibits only small variations. Thus, these observations imply that the contribution of 3 min oscillations decreases again further up in the atmosphere, likely due to the increasing importance of magnetic fields (magnetic canopy). This is also implied by the fact that 3 min intensity oscillations are seen in spectral lines of doubly-ionised elements but not in the spectra of higher ionised species (Carlsson et al. 1997), which are related to higher temperatures and thus higher formation heights. The increase of the contributions in the 3 min range is also known from theoretical experiments of wave propagation (e.g., Fleck & Schmitz 1991).

The so-called diagnostic diagram, which shows the power distribution as a function of frequency ω and spatial wave length k , reveals different domains and ridges of enhanced power. The excellent match between the observed $k - \omega$ diagram and the theoretical prediction by Ando & Osaki (1975), see also Ulrich (1970), produced a break-through in the understanding of the solar oscillations. They are now interpreted as superpositions of non-radial eigenmodes of the shallow surface layers. The temperature and density stratifications of the Sun provide various effective resonators for standing waves, each giving rise to another mode. The excitation of the modes is likely to occur in quite localised sources at only about 50 – 100 km below the surface (Rutten 1994, and references therein).

The picture of resonators or cavities might hold for the well-stratified interior of the Sun, but is doubted for the inhomogeneous outer layers. In particular, the chromospheric cavity, which was assumed to be responsible for the 3 min oscillations, is very questionable nowadays. The chromospheric oscillations might rather be the result of interference between waves that propagate directly up from a subsurface source and waves that are reflected only once at subsurface layers (Rutten 1994; Kumar 1994, and references therein).

Furthermore, one distinguishes between p-modes and g-modes, for which the restoring forces are pressure and gravity, respectively. The power distribution in the $k - \omega$ plane as well as phase relations can give important clues on the nature of the observed waves, allowing to distinguish between standing, evanescent, or propagating waves. Many interesting aspects arise from the

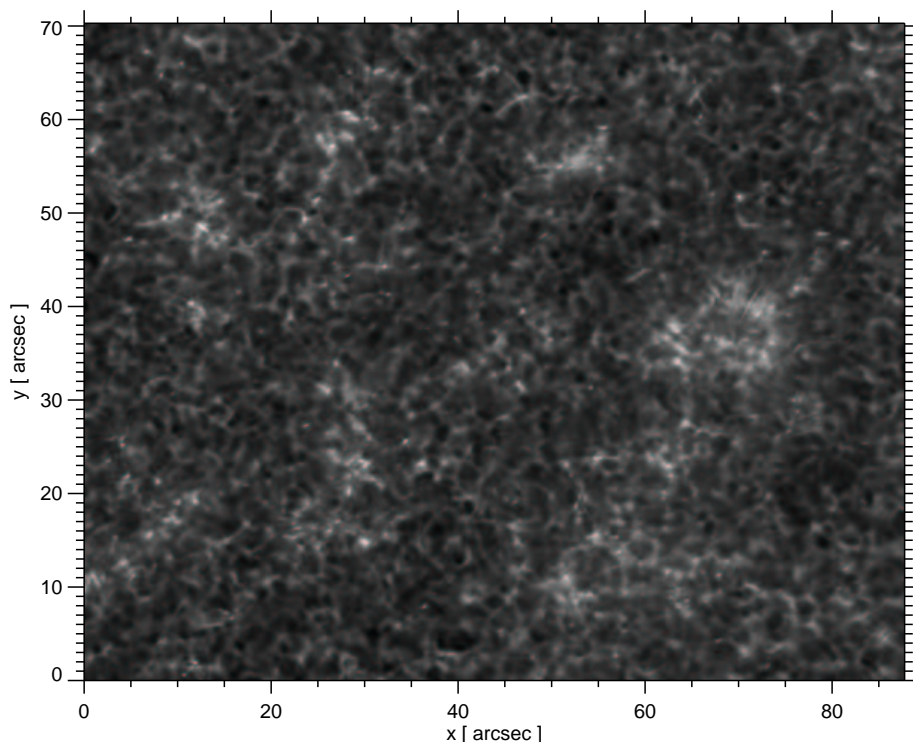


Figure 2.4: High-resolution ($\sim 0.''2$) Ca II H image taken with the *Dutch Open Telescope* at a wavelength of 3968 \AA . One image pixel corresponds approximately to only 50 km on the solar surface. (*Kindly provided by P. Sütterlin.*)

described properties, providing essential insight into the nature of the solar interior and its outer layers. The solar oscillations and their implications are a wide field of their own, which cannot be addressed in more detail in this rough introduction. Moreover, the hydrodynamic model presented in this thesis does not allow a meaningful comparison of $k - \omega$ diagrams and its implication, owing to a too small horizontal extent and thus a too coarse resolution in wave number. Thus, the analysis will be restricted to height-dependent power spectra, without dependence on horizontal wave number (see Sect. 7.3). Particular emphasis is more on the potential connection between oscillations, propagating acoustic waves and the heating of the outer layers. An open issue in this context is the contribution of short-period waves (Wunnenberg et al. 2002) with accordingly high frequencies ($\nu \geq 10 \text{ mHz}$) to the chromospheric heating. While they were supposed to provide a significant contribution (e.g., Kalkofen et al. 1999), no clear evidence for this was found in observations (Krijger et al. 2001).

Finally, it should be remarked that there are essential differences between the internetwork medium and magnetic network elements. The above stated chromospheric oscillations in the 3 min band are mainly an internetwork phenomenon owing to acoustic waves. This is different in the presence of magnetic fields, which are likely to have stabilising influence on the atmosphere. Hence, instead of the internetwork 3 min oscillations, periods in the range of 5 – 20 min are observed. The differences between network and internetwork oscillations have also been subject of intense research (e.g., Kneer & von Uexküll 1993; Lites et al. 1993; Krijger et al. 2001).

The oscillations of the outer solar layers and many related dynamic phenomena (see subsequent sections) are very important ingredients which should be reproduced by any realistic model of the solar atmosphere.

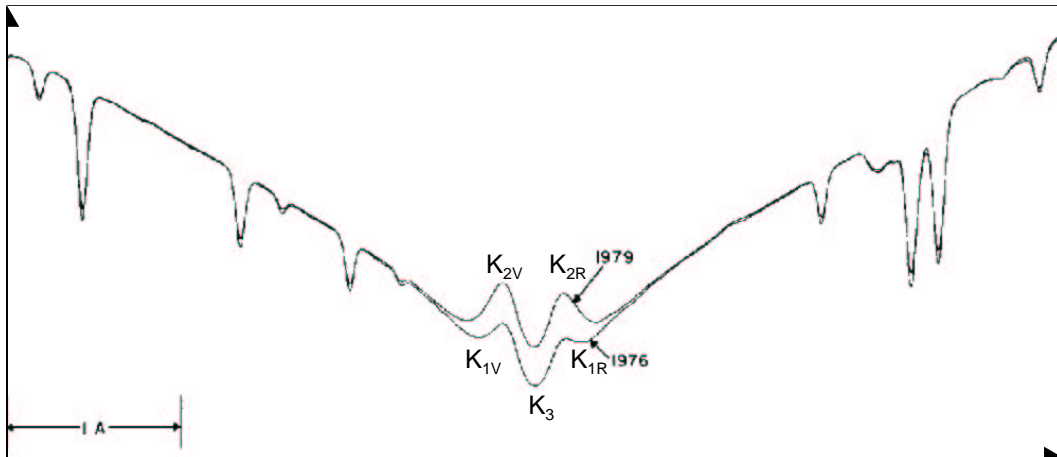


Figure 2.5: Full disk Ca II K line profile at two different stages of the solar cycle. The line components K_{1V} , K_{1R} , K_{2V} , K_{2R} , and the line core K_3 are marked. Based on a figure by White & Livingston (1981).

2.4 Calcium Bright Grains

The solar surface reveals emission of grainy texture when observed in the light of the H and K resonance lines of ionised calcium at wavelengths of 3968.5 \AA and 3933.7 \AA , respectively (see Fig. 2.4). Next to the prominent emission connected to the magnetic network and plages (brighter areas in the figure), the Ca II emission reveals ubiquitous tiny grains of enhanced emission everywhere in the non-magnetic internetwork regions (see Fig. 2.1.b). The bright grains, which are also named bright points, minute bright calcium flocculi, mottles, cell flashes, or cell points, show up as brightenings in a very narrow wavelength range on the violet side of the line centres of the Ca II $H+K$ lines. The emission peaks, which are settled on the broad absorption wings, are labelled as K_{2V} and K_{2R} on the violet (smaller wavelength) and the red side (larger wavelength) of the line core K_3 (see Fig. 2.5). The line components of Ca II H are denoted analogously. As we shall see later, the emission peaks in the K and H lines are taken as evidence for a temperature rise at chromospheric heights; similar implications arise from the Mg II $h+k$ resonance lines (see, e.g., Ayres & Linsky 1976).

The inner parts of the resonance lines show temporal and spatial variations. First of all, they depend on the magnetic activity of the observed regions, providing an excellent proxy for the activity of the Sun and other stars when observed in integrated light and on long time scales. On the other hand, the line profiles show short-term fluctuations depending on time and space. The enhanced emission is confined to small grains, which clearly stand out in the light of Ca II K_{2V} , giving rise to the name “ K_{2V} grains”. These tiny roundish structures have small spatial extents of $\sim 1000 \text{ km}$, are only short-lived ($\sim 1 \text{ minute}$), and often reappear after $2 - 4 \text{ min}$ intervals for mostly $2 - 4$ cycles at about the same location (Cram & Dame 1983; Rutten & Uitenbroek 1991a,b; Lites et al. 1999, and references therein). Furthermore, they are apparently organised in a horizontal pattern of typical scale of $5000 - 10000 \text{ km}$ (Rutten & Uitenbroek 1991a). See also Lites et al. (1999) and Krijger et al. (2001) for exemplary filtergrams.

The broad line wings of the Ca II K resonance lines (see Fig. 2.5), are formed in the photosphere, while the inner parts originate from higher layers, i.e., the chromosphere. Accordingly, the formation heights of the components K_1 , K_2 , and K_3 increase from the top of the photosphere and

the bottom of the chromosphere to its top (see Fig. 1 in Vernazza et al. 1981). This applies to the other resonance lines Ca II H and Mg II $h+k$, too. Observations show a variety of features which have to be properly reproduced by a model. The line profile is often asymmetric to some extent, presumably owing to line shifts of K_3 , and thus indicating velocity gradients across the line-forming layers. Also, K_{2V} appears to be brighter than K_{2R} . But the whole complexity is revealed when the line profiles are tracked in time for single spatial positions. The single line components show strong variations with time which are likely to be connected causally, as following description might imply:

A so-called “bright whisker”, a brightening in the line wing, is seen propagating towards the line core, while at the same time the line core K_3 shows a gradually increasing red-shift. The bright whisker slows as it passes K_1 and finally culminates in an enhanced emission in K_{2V} , which can be seen as bright grain. The bright whisker vanishes, and also the K_{2V} grain does so shortly afterwards, coinciding with a rapid blue-shift of K_3 . At the same time a dark whisker is forming, which precedes the next bright whisker, and the whole cycle starts again. This variation is described in detail in the review article by Rutten & Uitenbroek (1991a). See also Cram & Dame (1983); Rutten & Uitenbroek (1991b); Rutten (1994).

Hence, the chronology of single events implies a dynamic source which moves upwards in the solar atmosphere and thus becomes visible in the different line components at subsequent times. A widely assumed explanation employs the propagation of shock waves which would be able to reproduce the observations (see, e.g., Liu 1974; Rutten & Uitenbroek 1991a, , and many others). Strong evidence is given by the numerical simulations of Carlsson & Stein (see Sect. 3.5 and also by observations (e.g., Krijger et al. 2001; Wunnenberg et al. 2002). Additionally, the red-shift of K_3 , which forms higher up in the chromosphere, implies high downward directed velocities, presumably due to material which falls down after being pushed upwards by shock waves (see, e.g., Rutten & Uitenbroek 1991b).

The repetitive character of the bright grains with periods of mostly 2 – 4 min makes a close connection to 3 min oscillations likely (see Sect. 2.3). Furthermore, the grains are always part of larger areas of coherent oscillations and might be regarded as localised intensity maxima induced by interference of (standing) oscillations in the 3 min band and propagating acoustic waves (see, e.g., Cram & Dame 1983; Rutten & Uitenbroek 1991a; Krijger et al. 2001). The spatial scale of the oscillating areas are much larger than the embedded grains. While Cram & Dame (1983) stated a size of 2000 – 4000 km, larger scales of 8000 km are quoted by Dame & Martić (1987), $\approx 2000 - 6000$ km (3" - 8") by Carlsson et al. (1997). Krijger et al. (2001) describe the pattern as a “background mesh” which is also visible at the shorter wavelengths of their TRACE observations (1550–1700 Å). The mesh can be clearly seen in Fig. 2.4. It is clearly modulated with periods of 2 – 4 min. The bright enhancements travel along the strands of the mesh at often highly supersonic velocities, up to a very extreme value of 100 km s^{-1} (Krijger et al. 2001). Furthermore, Carlsson et al. infer from their SOHO/SUMER observations that the oscillations are exhibited by 50 % of the observed field at any time and are thus extremely common. There might also be a close connection between the 5 min oscillations in the lower layers and the occurrence of chromospheric bright grains, indicating the role of the lower layers for the excitation of the chromospheric phenomenon (Hoekzema et al. 2002).

It is now generally assumed that bright grains are a purely hydrodynamical phenomenon and not related to magnetic fields like, e.g., flux-tubes with enhanced field strength. Observational evidence for this assumption is provided by Lites et al. (1999) who found no direct correlation between H_{2V} brightening and the presence of (weak) internetwork magnetic fields.

Nevertheless, there are reports on isolated patches of magnetic field and correlated long-lived grains but those are rather rare and move only slowly ($\sim 1 \text{ km s}^{-1}$), implying a connection to the

underlying convective flows and thus a different nature than the majority of the bright grains (Nindos & Zirin 1998; Lites et al. 1999). The grains of hydrodynamical origin are by far more common and exhibit much larger velocities.

Note that the facts given above refer to grains in internetwork regions which differ from observed properties of grains in the magnetic network (see Lites et al. 1993).

The shock waves, which are used for the explanation of bright grains, give rise to the idea that they are also responsible for the heating of the quiet internetwork regions. Thus, grains can be regarded as sites of significant dissipation of mechanical energy (see, e.g., Cram & Dame 1983). Finally, one should note the various other observations which also imply a dynamic cause, such as H α grains (Kneer & von Uexküll 1993), features of the Ca II IR triplet (Deubner et al. 1994), “jets” in C I UV lines (Hoekzema 1994), and bright cell points at $\lambda = 1600$ Å (Foing & Bonnet 1984b, see Sect. 2.5). However, further investigations are needed before the nature of all these phenomena and their possible correlation to the calcium bright grains discussed in this section can be clarified satisfactorily.

2.5 Bright Cell Points at 1600 Å

In the UV at 1600 Å structures are observed, which are similar to the bright points in Ca II *H+K* discussed above. They are an ubiquitous phenomenon in the internetwork regions, too. The high spatial and temporal resolution of rocket-based observations enabled Foing & Bonnet (1984b,a) to infer the small spatial scale of the ultraviolet cell grains of order 600 ± 200 km. The points have a typical distance of ~ 1400 km, while the scale of the coherent 3 min oscillations, which are obviously closely connected to this phenomenon, is approximately 8000 km (see also Hoekzema 1994). See Fig. 4 in Foing & Bonnet (1984b) for a nice example of a 1600 Å picture.

The observations at wavelengths around 1600 Å sample the upper photosphere and lower chromosphere (Krijger et al. 2001), so that there is a likely connection to the variation in the Ca II *H+K* lines which originate from the same heights and the layers above. Note also that at wavelengths near 1600 Å so-called C I “jets” are detected, which exhibit Doppler shifts of $> 15 \text{ km s}^{-1}$, twice as common to the blue than to the red, also implying strong upward motions (Hoekzema 1994). However, further investigations are needed to clarify the correlations of the individual phenomena.

2.6 Carbon Monoxide

Observations of features of carbon monoxide in the infrared spectrum of the (quiet) Sun reveal a picture which leads to fundamentally different conclusions for the atmospheric structure than, e.g., derived from the emission reversal in cores of the strong calcium resonance lines (see Sect. 2.4).

Noyes & Hall (1972b) investigated the intensity in the core of the 3-2 R14 CO line in the fundamental vibration-rotation bands ($\Delta V = 1$) near a wavelength of $\lambda = 4.7 \mu\text{m}$ and concluded that the observations suggest the existence of very low temperatures in the (upper) photosphere. Furthermore, Noyes & Hall discovered very prominent intensity oscillations with periods near 5 minutes, which should be formed just in the high photosphere (Noyes & Hall 1972a).

The same spectral CO line was used in a later investigation by Ayres & Testerman (1981), completed with observations of the first-overtone bands ($\Delta V = 2$) at $2.3 \mu\text{m}$ both at the solar limb and at disk centre. The low (brightness) temperatures found by Noyes & Hall (1972b) were confirmed to be as low as $\lesssim 4000$ K and even down to values of only $\lesssim 3700$ K (see Fig. 4-5 in Ayres & Testerman 1981). This result was also verified in a subsequent paper (Ayres et al.

1986). Again, the CO observations did not show a prominent temperature inversion like implied by other diagnostics. Ayres & Testerman explained this "diagnostic dilemma" with the thermal bifurcation of the outer solar layers. Following that idea, the hot plasma would be confined in discrete structures embedded by cool gas which can account for the observed carbon monoxide features. The inhomogeneities would be preferably of small spatial scale and large thermal contrast. Furthermore, Ayres & Testerman state that the CO concentration peaks at an optical depth of $\tau_{5000} \lesssim 10^{-2}$ (for a reference wavelength of 5000 Å).

In the third part of the paper series, Ayres & Brault (1990) reported the identification of oscillations with periods of 5 min (like Noyes & Hall 1972b) and further contributions at 4 min. Related to the oscillations are thermal amplitudes of ≈ 300 K (peak-to-peak) and Doppler shifts of $\approx 1.1 \text{ km s}^{-1}$ (peak-to-peak).

The inferred low CO brightness temperatures, which at first glance contradict other diagnostics, demand for a detailed investigation of the spatial distribution. Constraints on the vertical structure were inferred by Solanki et al. (1994) who observed CO in emission at the solar limb. There, it remains at a constant level up to $0.4''$ (≈ 300 km) above the (continuum) limb before it decreases rapidly in the layers above (see Fig. 2 therein). The authors used the data for the construction of (semi-)empirical models which predict the existence of a cool thermal component ($T \sim 3000$ K) up to a height of roughly 1000 km (see also Ayres & Rabin 1996).

Shortly afterwards, Uitenbroek et al. (1994) carried out similar observations in the 3-2 R14 spectral line, but with an improved technique. They found CO in emission, extending $0.5''$ (≈ 360 km) beyond the continuum limb. Although the finding is qualitatively similar to Solanki et al. (1994), Uitenbroek et al. remark on the difficulties in determining exact radial positions with respect to the limb which are crucial for the interpretation of the results. Furthermore, they report on significant 3 min power in the line-core intensity and mainly 5 min periods exhibited by Doppler shifts. They conclude that the spatial variations are largely of dynamic nature, and that the dynamics thus play an important role in the formation of the dark CO line cores. Finally, Uitenbroek et al. (1994) observed a pattern which is connected to the magnetic network, implying that magnetic fields influence the formation and existence of carbon monoxide notably. However, in the quiet Sun CO is apparently concentrated in bright rings with dark centres, resembling an inverted granular pattern.

Ayres & Rabin (1996) address the question of the vertical extent of the CO emission, too. Their investigation, again based on the $\Delta V = 1$ bands, yields an off-limb extension of $0.6''$ (≈ 440 km) for the strongest lines, indicating the presence of cool gas up to 350 km above the classical temperature minimum, i.e., up to a height of ≈ 870 km above $\tau = 1$.

The horizontal distribution was further examined by Uitenbroek (2000a,b). Recorded spectroheliograms in the cores of strong CO lines clearly showed an inverted granular pattern similar to that already seen earlier by Uitenbroek et al. (1994). Although the spatial scales were close to the observational resolution, dark areas and bright network-like rims were discovered, corresponding to granule centres and intergranular lanes, respectively. Moreover, Uitenbroek reproduced the observed pattern, employing radiative transfer calculations based on a snapshot from a multi-dimensional hydrodynamical model by Stein & Nordlund (1989). The resulting data allowed to investigate the distribution of carbon monoxide in more detail. Accordingly, the highest concentration is found in the middle photosphere, say around 100 – 300 km above optical depth unity, whereby the largest values are located above granule interiors. The concentrations above intergranular lanes (at the same height) are 3 – 4 times smaller. Obviously, the CO distribution is connected to the cooling due to strong adiabatic expansion and cooling above the granule centres. However, the calculations were performed under the assumption of instantaneous chemical equilibrium. Also, neither the radiative cooling action by CO itself nor

advection due to the hydrodynamic flow were taken into account. Nevertheless, this pioneering work showed the importance of solar granulation (and the 5 min oscillations) for CO line formation. Hence, Uitenbroek concludes that carbon monoxide is part of a very dynamic environment, in which there are no (non-magnetic) constantly cool regions. Rather, cool episodes come and go everywhere (Uitenbroek 2000a).

The observations described above clearly show that a realistic model of the outer layers of the Sun must be able to explain the presence of carbon monoxide and the inferred low temperatures (see also Ayres 1991, 2002). Also, the exhibited (spatio-)temporal behaviour provides an important test on the dynamics of a model. Furthermore, the oscillation periods of 5, (4), and also 3 min indicate a height range in the photosphere and low chromosphere, which is thus in line with off-limb observations. Finally, presumably no CO found at heights above approximately 1000 km where the magnetic canopy is assumed to spread out and cover most of the atmosphere above (see Sect. 2.2.2).

2.6.1 Thermal Bifurcation

Carbon monoxide provides another aspect of interest for the outer solar layers, namely thermal bifurcation due efficient radiative cooling of CO molecules. After having been proposed by Ayres (1981) it has been widely discussed in the literature (e.g., Kneer 1983; Muchmore & Ulmschneider 1985; Anderson & Athay 1989b) since it might play an important role for the thermal structure. Since carbon monoxide is an efficient cooling agent, it lowers the temperature of its vicinity. But a lower temperature allows more CO molecules to form, leading to an increase of overall cooling action. This strong self-amplifying surface cooling by CO could cause temperatures of less than 4000 K, even relaxing to values below 3000 K. However, this is only possible if the mechanical heating in the regarded layer stays below $\sim 10^7$ erg cm⁻² s⁻¹. A larger amount of mechanical heating leads to increased dissociation of CO molecules. Less CO molecules imply less radiative cooling and thus higher temperatures, which cause even more dissociation. Consequently, the equilibrium temperature is shifted well above 4000 K up to temperatures of $\gtrsim 6000$ K. At these temperatures other species play an important role, stopping the “CO thermal catastrophe”. Accordingly, the solar atmosphere would stay in low-temperature or high-temperature state, depending on the amount of mechanical heating (see also Anderson 1989; Steffen & Muchmore 1988).

2.7 Energy Flux

2.7.1 Radiative Flux

The total emergent flux at the solar surface has been determined to $F = 6.33 \times 10^{10}$ erg cm⁻² s⁻¹, corresponding to a black body with an effective temperature of 5780 K (see Sect. 4.4.8). This temperature can be interpreted roughly as a surface temperature. The major contributions to the emergent flux originate in the photosphere, while only 10^{-4} and 10^{-5} is emitted in the chromosphere and the corona, respectively. Chromospheric radiation losses are mainly due to the spectral lines of Ca II and Mg II, the Lyman α line, and the H^- continuum. Detailed values, as part of semi-empirical models, are listed in Tab. 7.1.

2.7.2 Acoustic Flux

In contrast to the radiative energy flux, the mechanical counterpart cannot be measured directly. Instead, elaborate theoretical models are used to match the observations. The calculation of

acoustic flux is again a wide field by itself, which is described in more detail in the review articles and course lectures (e.g., Narain & Ulmschneider 1990, 1996; Ulmschneider 2003).

A widely used method of acoustic flux calculation is based on the original theory by Lighthill (1952) and its supplements by Proudman (1952) and Stein (1967). The so-called *Lighthill-Proudman* formula was originally developed for the description of turbulence in a homogeneous isotropic atmosphere without gravitation. It is assumed that generation of acoustic energy occurs in small regions of turbulent flow, which are embedded in a homogeneous medium. Stein generalised the formalism for stratified atmospheres which therefore became applicable to stellar convection zones. The so-called Lighthill-Stein theory as well as the original work by Lighthill both employ a theoretically derived energy distribution of free turbulence, more precisely a *Kolmogorov* spectrum. A range of modifications of the Kolmogorov spectrum is used as well (see, e.g., Musielak et al. 1994; Fawzy et al. 2002a). Furthermore, convection zone models based on the mixing length theory are employed.

An important point, which arises from the theories described above, is the correlation of the (convective) velocity of the turbulent flow and the resulting acoustic power. It was found that quadrupole emission yields the largest contribution to the acoustic flux, owing to destructive interference of monopole and dipole emission, and that the acoustic flux thus is proportional to the eighth power of the convective velocity (Stein 1967; Musielak et al. 1994). Hence, the strong velocity dependence causes the acoustic energy generation to be confined most likely to a thin layer roughly 100 km below the photosphere.

Examples of derived acoustic fluxes for the Sun are of order $5 \times 10^7 \text{ erg cm}^{-2} \text{ s}^{-1}$ (Musiela et al. 1994) and 1.3×10^7 to $1.7 \times 10^8 \text{ erg cm}^{-2} \text{ s}^{-1}$ (Ulmschneider et al. 1996), depending on the applied mixing length parameter. These numbers represent the total available amount of acoustic flux generated by the convection zone – as the result of the stated theoretical calculations.

On the basis of the theoretical calculations predictions can be made for the corresponding emergent radiative fluxes as, e.g., observed in the emission cores of the Ca II and Mg II resonance lines (e.g., Fawzy et al. 2002b). The observed line fluxes, which are available for a wide range of cool stars (Rutten et al. 1991), show a remarkable behaviour: There is obviously a lower limit to the line fluxes which mainly depends on the spectral type of the star. This minimum flux is attributed to acoustic heating only and is also called “basal flux” – a term introduced by Schrijver (1987). Stars with line fluxes in excess of the basal flux obviously require additional flux contributions which are assumed to be of magnetic origin. The good agreement of the basal flux limit by the above described theoretical calculations and the observations (e.g., Ulmschneider 2003) provides substantial evidence for acoustic heating of chromospheres of low-activity stars. In their Section 6.2, Rutten et al. (1991) quote “truly basal fluxes” – i.e., corrected for line-wing contributions which are normally included in spectrophotometry – for F and K stars, while their Figure 5 even allows to interpolate their results for $B - V = 0.67$ as appropriate for G2V stars like the Sun. The resulting basal flux in Mg II $h+k$ is $\log F_{\text{basal}} = 5.5$, while that of Ca II $H+K$ is $\log F_{\text{basal}} = 5.8$ (cgs units). See also the review article by Schrijver (1995).

More values for the mechanical energy flux can be found in the literature but they all point more or less to the same order of magnitude (see, e.g., Steffen et al. 1991, and references therein). The value $F_{\text{mech}} = 2 \times 10^7 \text{ erg cm}^{-2} \text{ s}^{-1}$, as derived by Liu (1974) from a time sequence of Ca II K -line spectrograms for the quiet, i.e., non-magnetic Sun might be too high since it is based on a single acoustic event which might be in excess of the average. Empirical lower bounds for the acoustic flux in the solar atmosphere are given by Deubner (1988): $2 \times 10^7 \text{ erg cm}^{-2} \text{ s}^{-1}$ at 300 km above $\tau = 1$, strongly decreasing to $\sim 1.2 \times 10^6 \text{ erg cm}^{-2} \text{ s}^{-1}$ at $z \approx 800$ km, and $\sim 4.5 \times 10^5 \text{ erg cm}^{-2} \text{ s}^{-1}$ at $z \approx 1500$ km. Note that these heights represent the assumed average formation heights of the different observed spectral lines and – in view of a dynamic and in-

homogeneous chromosphere – should be interpreted with caution. Furthermore, semi-empirical models like those provided by Vernazza et al. (1981) and related theoretical works (Anderson & Athay 1989b) comprise predictions for the acoustic flux and the corresponding line fluxes. For more details see the discussion in Sect. 7.5. Recently, Wunnenberg et al. (2002) derived an empirical value for the contribution of acoustic waves with periods between 50 – 130 s to be $9 \times 10^5 \text{ erg cm}^{-2} \text{ s}^{-1}$.

However, despite the progress in the basic understanding of the heating mechanism by acoustic waves and its importance for the outer layers of the Sun and other stars, many details remain open, owing to the complexity of the phenomenon and its limited observational accessibility. Nevertheless, a detailed realistic model of the solar chromosphere should also be able to reproduce the observed line fluxes, imposing high demands on the numerical modelling.

Chapter 3

Models of the Outer Solar Atmosphere

In this chapter various models of the solar chromosphere are described which will serve as reference for the models presented in this thesis. As mentioned in the previous chapter, different spectral features like Ca II $H+K$ (Sect. 2.4) and carbon monoxide (Sect. 2.6) require different conditions for their formation. Hence, a (semi)-empirical model depends on the underlying set of observations. This results in a contradiction between “classical” chromosphere models with high temperatures, needed to reproduce UV diagnostics, and cool atmospheres, demanded by the existence of carbon monoxide. In addition, models are presented which might point out a way to solve this “diagnostic dilemma”.

3.1 Classical Semi-Empirical Models

This class of models, referred to “semi-empirical classical” models, have in common their static and one-dimensional stratification which was obtained under the assumption of hydrostatic equilibrium. The most remarkable feature, namely the temperature minimum $T_{\min} \gtrsim 4000$ K at the boundary between photosphere and chromosphere ($z \approx 500$ km above optical depth unity) and the rise above, were already exhibited by early models like the *Bilderberg Continuum Atmosphere* (BCA, Gingerich & de Jager 1968) and the *Harvard-Smithsonian Reference Atmosphere* (HSRA, Gingerich et al. 1971).

In the following years advances in observations and theoretical modelling lead to the well-known models by Vernazza, Avrett, & Loeser (1973, 1976, 1981, VAL). In contrast to the BCA, which was exclusively based on continuum observations, a large number of spectral lines were taken into account, while the continuum data in the (Extreme) Ultraviolet and Far-Infrared, and the microwave range remained important ingredients. The Skylab observations were incorporated, which had a spatial resolution of (only) $5'' \times 5''$, effectively averaging the radiation over this area, but also integrated intensities of the whole solar disk. Vernazza, Avrett, & Loeser selected six different components for the (non-magnetic) quiet Sun after their Lyman continuum intensity, as obtained with the Harvard spectroheliometer aboard Skylab. These components range from dark cell point (A) to a very bright network element (F). Model C is of particular interest since it represents the average quiet Sun.

Each component was treated as a plane-parallel atmosphere separately. The sophisticated modelling allowed for departures from the assumption of local thermodynamic equilibrium (LTE) for some elements. Thus, the statistical-equilibrium and radiative-transfer equations were solved for Si I, C I, H, and H^- , while all other atoms and ions were treated in LTE. Molecular lines

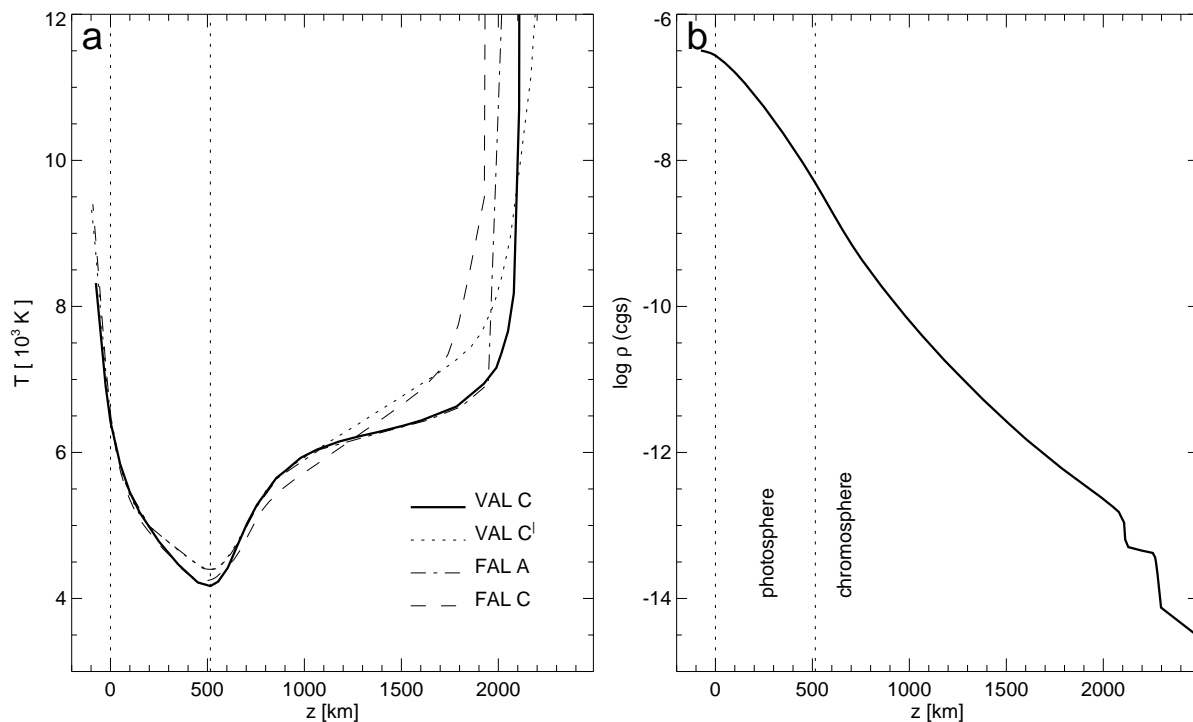


Figure 3.1: Stratifications of semi-empirical models: **a)** Temperature for VAL C, VAL C', FAL A, and FAL C; **b)** Logarithmic density for model VAL C.

were not included. The basic procedure was to calculate theoretical model atmospheres and the resulting emergent spectra. The assumed stratification was altered repeatedly until a satisfactory match between the observed intensities and those computed from the non-LTE calculations was reached.

The resulting temperature and density stratification is plotted for average quiet Sun component (VAL C) in Fig. 3.1. The temperature is decreasing from photospheric values until 4170 K are reached at $z = 515$ km above the height for optical depth unity. The rise in the chromosphere, is strongest in the lower few 100 km, and becomes less steep above. Thus, the temperature of the middle chromosphere is relatively constant compared to the gradients in the photosphere and the transition region. The latter shows a remarkable strong increase which defines the upper boundary of the “classical” chromosphere and continues to coronal values. The density, however, is characterised by a neat nearly exponential decrease.

In addition to the stratifications, which are also available for additional quantities, the extensive work by Vernazza, Avrett, & Loeser (1981) provides other useful outcomes like radiative cooling rates and inferred emergent line fluxes, which will be described in more detail in Sect. 7.5.

Moreover, modified versions of the VAL models were compiled by, e.g., Avrett (1985) and Maltby et al. (1986). The latter present a slight modification of the model by Vernazza et al. (1976) – especially for the lower parts of the photosphere – due to a different normalisation of the infrared intensities for the centre of the solar disk. The modified model is often referred to as VAL C' (see Fig. 3.1.a).

A further development of the VAL models was accomplished by Fontenla, Avrett, & Loeser (1990, 1991, 1993, FAL). Their model components A, C, F, and P correspond to separate stratification for faint, average, and bright regions of the quiet Sun, and a typical plage area.

Differences to VAL occur near the transition region (see Fig. 3.1.a).

Despite the elaborate modelling, basic assumptions – which were necessary at that time – like only one spatial dimension, stationarity and hydrostatic equilibrium were made which by nature cannot provide a comprehensive description of an inhomogeneous, dynamic solar atmosphere – although individual constraints were reproduced reasonably well by this class of models. Cram & Dame (1983) remark that line profiles, e.g., Ca II *K*, predicted by VAL still show a number of differences compared to observations. Moreover, the temperature structure is not capable of explaining the evident observations of carbon monoxide (see Sect. 2.6), demanding for further modifications of the atmosphere models.

Nevertheless, the “classical” models can be regarded as a first major step in the understanding of the (non-magnetic) solar chromosphere. The models, in particular VAL C, are thus well-known and often used as reference, also in this thesis.

3.2 Models with Prescribed Heating

The temperature stratification of the semi-empirical models described in the previous section requires an effective heating mechanism. In the region without significant magnetic fields, the mechanism is thought to be of acoustic nature.

While semi-empirical models are based on the comparison of a set of preselected spectral features with the results from an adjusted atmospheric stratification, Anderson & Athay (1989b) chose a different approach. They solve the ‘classical ab initio model atmosphere problem’ but with prescribed departures from radiative equilibrium. This incorporate solving the equations of statistical equilibrium, radiative transfer, hydrostatics, and energy balance. The resulting model atmosphere depends on the amount of prescribed mechanical heating, and so does the corresponding net radiation loss. The comparison with model VAL C (see Sect. 3.1) finally allows to predict the amount of mechanical energy which is necessary to produce the assumed thermal stratification. See also Sect. 7.5 for more details.

3.3 COmosphere

Wiedemann, Ayres, Jennings, & Saar (1994) observed several late-type stars using the strong vibration-rotation lines of carbon monoxide at $4.6 \mu\text{m}$ ($\Delta\nu = 1$) (see also Sect. 2.6). They determined stellar boundary (CO) temperatures and constructed temperature profiles for the stars α Boo, α Tau, β Gem, and β Dra. The resulting CO-based models show a steady temperature decrease in the chromosphere, at heights where the temperature increases in the semi-empirical models (see Sect. 3.1). Model atmosphere of this kind are sometimes referred to as “COmosphere”.

As the authors state themselves, these models are designed to match the underlying CO observations and thus cannot reproduce UV diagnostics. Furthermore, Wiedemann et al. remark that horizontally homogeneous models like those exclusively based on CO cannot provide an unique description of all chromospheric features and thus point out the importance of thermal bifurcation (Sect. 2.6.1) and therefore required multi-component models which are discussed in the subsequent section.

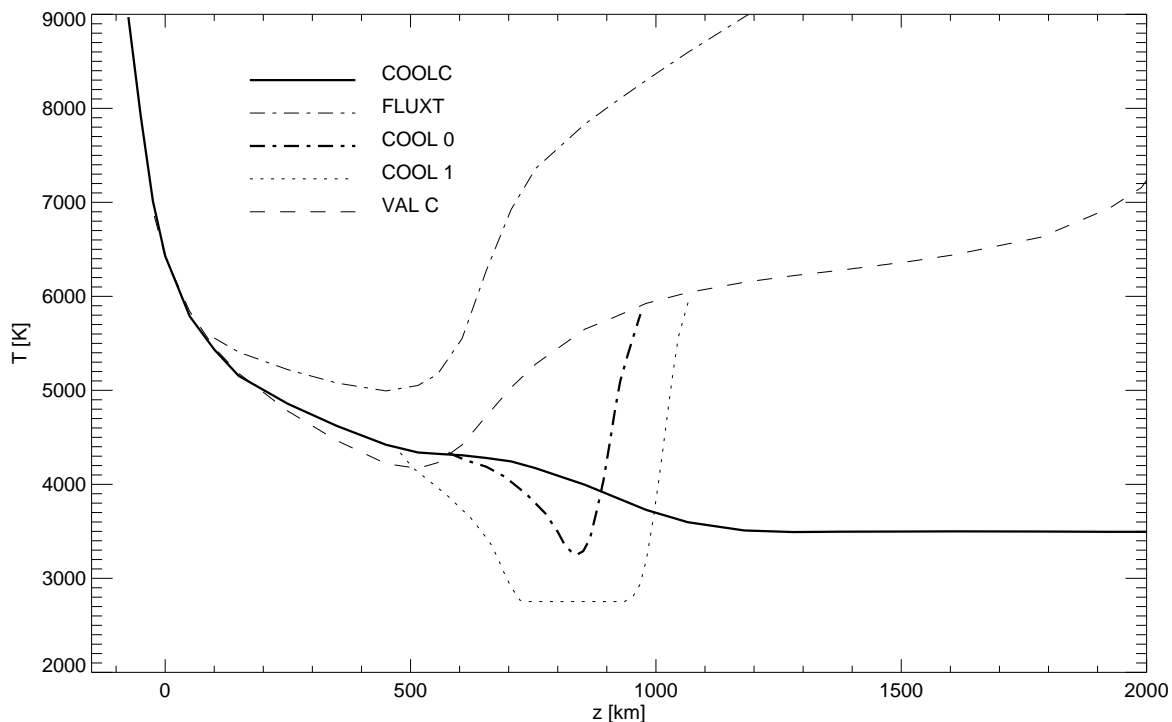


Figure 3.2: Temperature stratifications for COOLC (thick solid) and FLUXT (dot-dashed), COOL0 (thick dot-dashed), COOL1 (dotted), and VAL C (dashed).

3.4 Multi-Component Models

The models presented so far consist of a single component, each one-dimensional and horizontally homogeneous. As mentioned in the previous sections a single component cannot satisfy all diagnostics at the same time, since they require different physical conditions at the same height ranges in the solar atmosphere. This leads to the idea of a thermally bifurcated atmosphere which thus needs to be modelled with separate components.

A prominent example for a multi-component model was proposed by Ayres et al. (1986). They present two different temperature stratifications for a hot flux tube component (FLUXT) and a cool embedding non-magnetic atmosphere (COOLC). Basically, FLUXT is designed to reproduce UV diagnostics, while COOLC can account for carbon monoxide observations.

Hydrostatic and ionisation equilibrium was assumed for the construction of each model atmosphere. All elements/ions were treated under assumption of LTE while departures were allowed for hydrogen. Also, it was assumed that the geometrical cross-sections of the cool and the hot components do not change with height.

The component FLUXT is an exaggerated version of VALP, which was constructed to represent the temperature profile of a plage of moderate strength. The temperature starts to rise at lower heights in VALP compared to VAL C' (Avrett 1985) and also provides much larger values in the photosphere and the layers above (including the temperature minimum). These alterations are necessary to match the changed spectral features related to plage regions. The temperature of the cool component COOLC is identical to VAL C' in the low and middle photosphere, but declines smoothly from the temperature minimum of VAL C' to small values of ~ 3000 K above (see Fig. 3.2).

Finally, the stratifications (and their linear combinations) were adjusted to match line profiles, e.g., Ca II *K*. Based on these adjusted components, spectra were calculated for Ca II *K* and for the vibration-rotation bands of carbon monoxide (see also Ayres & Testerman 1981). A much better fit to observations of CO and Ca II *K* was achieved, but the model still fails to reproduce various UV diagnostics (Ayres & Rabin 1996).

The remaining short-comings demanded for further improvements of the modelling, which led to two-dimensional spectral simulations as done by Ayres & Rabin (1996). They arranged two thermal components in an alternating repetitive pattern. Again, the individual components represent hydrostatic atmospheric stratifications in LTE ionisation equilibrium for the metals, and chemical equilibrium for the most important diatomic molecules. The applied procedure also allowed for a simple treatment of departures from LTE for hydrogen. The LTE radiative transfer was solved along lines of sight for different inclination angles traversing the array of cool and hot components.

Ayres & Rabin (1996) present temperature stratification for two different scenarios: In Scenario Zero (COOL0) the chromosphere is dominated by a cool COmosphere (see Sect. 3.3), which covers 80 % of the area at heights below the magnetic canopy, whereas the classical hot chromosphere is consequently limited to fine structures of small filling factor. This is vice versa in Scenario One (COOL1), in which the cool component is only a minor constituent with a filling factor of 20 %. Although COOL1 is able to reproduce empirical properties of CO, it also implies a high thermal contrast which is not observed. Hence, Ayres & Rabin conclude that the COOL1 is not viable and the cool component should have a larger filling factor than only 20 %.

The temperature stratifications are shown in Fig. 3.2. They exhibit values well below the classical temperature minimum and even low temperature < 3000 K in the case of COOL1 (see also Ayres 2002). Obviously, both scenarios are characterised by a cool low chromosphere and otherwise agree with the “classical” stratification of VAL C’. Hence, the classical chromosphere, i.e., the required high-temperature regime, is shifted upwards beyond heights which are likely to coincide with the magnetic canopy.

The spatial inhomogeneities, which are an important ingredient of the presented multi-component models, tend in principle in the right direction but an even more complex structure might be required for a realistic description of the solar chromosphere. Note also that the filling factor of the cool component implied by the investigations by Ayres and co-workers is in line with findings by Avrett (1995) who proposed a proportion of 60 % for the cool component in his model.

3.5 One-Dimensional Dynamical Models

All models stated above underlie one common assumption, namely stationarity. In view of the observed dynamics of the outer layers, which is vividly demonstrated by the nature of Ca II *K* bright grains (see Sect. 2.4), this assumption by nature produces short-comings in the description of the outer (non-magnetic) layers of the Sun.

Carlsson & Stein (1992, 1994, 1995, 1997, CS) managed to perform detailed time-dependent one-dimensional radiation hydrodynamics simulations. They implicitly solved the equations of mass, momentum, and energy conservation, coupled with a set of atomic rate equations and a non-LTE radiative transfer. The computational grid was adaptive to provide a higher vertical resolution in shock fronts. The upper boundary was transmitting, whereas a piston imposed perturbations at the lower boundary, located 100 km below $\tau_{5000} = 1$ in the convection zone. The velocity pattern, which was a function of time, was derived from a 3750 s long sequence of Doppler shift observations in an Fe I line in the wing of the Ca II *H* line (Lites et al. 1993),

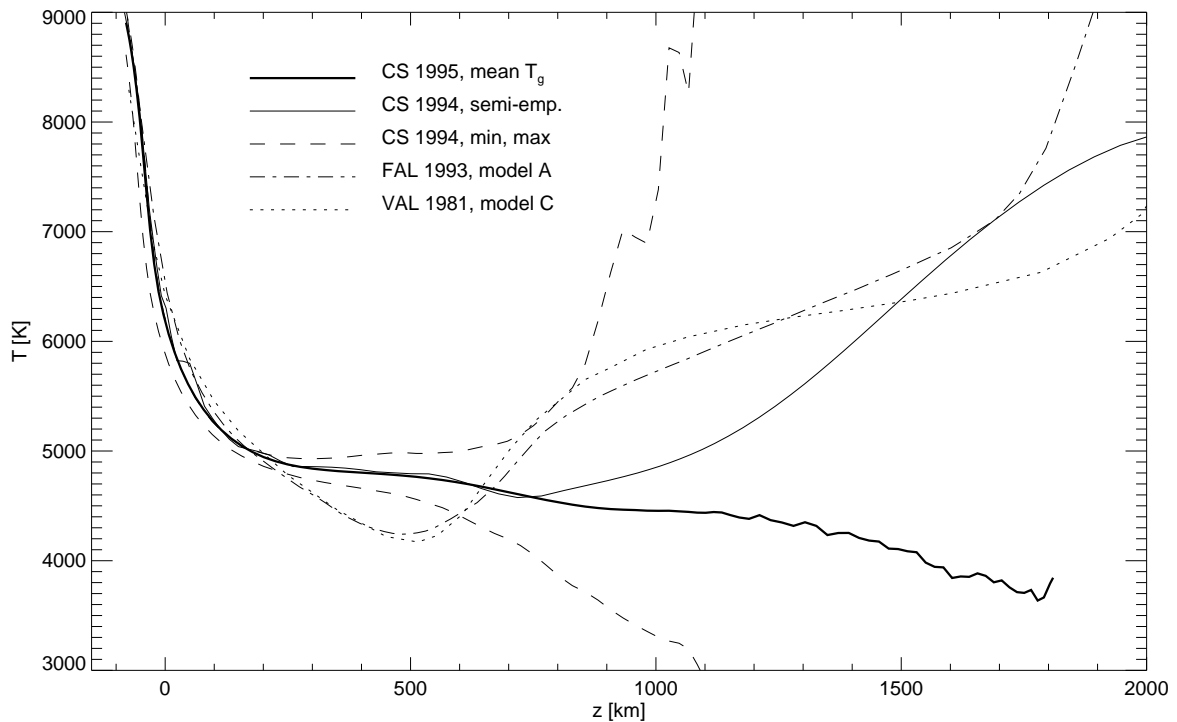


Figure 3.3: Average temperature stratifications of the dynamical 1-D model by Carlsson & Stein (1994): The mean gas (thick solid) and the semi-empirical (thin solid) temperature, and minimum and maximum values (dashed). Additionally, FAL A (dot-dashed) and VAL C (dotted) are plotted as reference.

which is formed at a height of ≈ 260 km above $\tau_{5000} = 1$. The motion pattern of the piston was adjusted to reproduce the Fe I observations. Note that Carlsson & Stein used a sinusoidal piston with different periods from 30 to 300 s in the early work of 1992.

The piston excites upward propagating waves which quickly dominate the appearance of the model atmosphere, which has been initially in radiative equilibrium. The simulated waves steepen into shocks near 600 km, are separated by periods close to 3 min and exhibit velocities of order 10 km s^{-1} at chromospheric heights. Consequently, the dynamical model shows one shock at a time.

Based on this time-dependent model, Carlsson & Stein computed a theoretical Ca II H spectrum and compared it with observations. The excellent match led them to the conclusion that calcium bright points (see Sect. 2.4) are indeed a result of propagating shock waves.

Furthermore, the time-dependent simulations also revealed a drastic difference to semi-empirical models of the solar chromosphere (see Sect. 3.1). Instead of a temperature minimum and a rise above, Carlsson & Stein found a mostly cool background and large temperature fluctuations due to upward propagating shocks, i.e. no chromosphere in the classical sense (see Fig. 3.3).

The difference was identified as caused by the nonlinear temperature dependence of the Planck function in the UV. Consequently, the emission related to the extreme temperature peaks of the shock waves dominates the emergent UV intensities. The intrinsic spatial averaging of the UV intensities, as used for the construction of semi-empirical models like VAL C, can thus be very misleading. This was demonstrated by the semi-empirical temperature stratification which Carlsson & Stein (1994) calculated on the basis of the intensities which resulted from their

dynamical simulations (see thin solid line in Fig. 3.3). The temperature shows a minimum and a rise above and thus is much closer to the semi-empirical models. This led Carlsson & Stein to the conclusion that the chromosphere of the quiet Sun is not persistent but a spatially and temporally intermittent phenomenon which – if averaged temporally – is mostly cool and not hot. A static description can thus be very misleading.

3.6 Multi-Dimensional Models

Last but not least, time-dependent multi-dimensional models provide a powerful approach for the theoretical modelling of the outer layers of the Sun and other stars. Such dynamic and self-consistent models do not suffer from assumptions like stationarity, hydrostatics, or spatial homogeneities nor do they require additional ingredients like a wave-exciting piston at the bottom. But on the other hand the inclusion of more than one spatial dimension means a large increase of required computational power, so that other simplifications and approximations are necessary to make the problem tractable.

In this context, one has to mention the early, pioneering radiation hydrodynamic models by Nordlund & Stein (e.g., Nordlund 1982; Stein & Nordlund 1998) and the many investigations by them and their co-workers over the last two decades. Self-consistent, dynamic models can be used for investigating a wide variety of phenomena of the outer solar layers. For a long time, the major subject was the modelling of convection in the vicinity of the surface layer, its manifestation as granulation, and related dynamic phenomena. For instance, Nordlund & Stein (2001) examined the interaction of convection with resonant oscillatory modes to derive an estimate of the power input into 5 min oscillations (see also Stein & Nordlund 2001).

While the upper boundaries of the models were mostly located in the photosphere, Skartlien, Stein, & Nordlund (2000, see also Skartlien 2000) extended the simulations to chromospheric heights. To account for deviations from the local thermodynamic equilibrium (LTE), which are expected to occur in the chromosphere, Skartlien and co-workers included coherent isotropic scattering to the Nordlund-Stein code. On the basis of this code, they studied the collapse of small granules and their excitation of transient wave emission.

One should also not forget two-dimensional models (e.g., Steffen 2000) which played an important role in the development of sophisticated, state-of-the-art radiation hydrodynamics codes. As we shall in this thesis, two- and three-dimensional simulations allow a variety of different investigations which can be assembled to a consistent picture of the outer layers of the (non-magnetic) Sun.

Chapter 4

Theory

4.1 Hydrostatics

Before we continue with hydrodynamics in the next section, the static case is introduced since it yields some useful relations. First, *hydrostatic equilibrium* is obtained, for instance in a stellar atmosphere, if the height variation of hydrostatic pressure is counterbalanced by gravity:

$$\frac{dP}{dz} = -g\rho, \quad (4.1)$$

where P and ρ denote pressure and density, respectively, g the gravitational acceleration, and z the geometrical height coordinate. This equation is a simple case of the equation of conservation of momentum (Eq. (4.5)), as we shall see in Sect. 4.2. We now define the *pressure scale height*

$$H_p \equiv -\frac{dz}{d \ln P} = -P \frac{dz}{dP}, \quad (4.2)$$

which is a characteristic length for the (local) change of pressure. With the condition of hydrostatic equilibrium Eq. (4.1) the scale height can be written as

$$H_p = \frac{P}{g\rho}. \quad (4.3)$$

Values of $H_p \approx 150$ km are typical for the photosphere of the Sun, whereas the scale height gets larger in the layers below.

4.2 Hydrodynamics

The condition of hydrostatic equilibrium is obviously not fulfilled in presence of the vast motions in the convection zone or in the atmosphere of the Sun. Rather, hydrodynamic phenomena like propagating sound waves demand for a detailed description which accounts for possible spatial and temporal fluctuations.

4.2.1 Hydrodynamic Equations

The three-dimensional hydrodynamic equations consist of the *continuity equation*, the *Eulerian equation of motion*, and the *energy equation*, which are relations for conservation of mass, momentum, and energy, respectively. Here additional terms are included which take into account an external gravity field and the energy change due to a radiative field. The

resulting equations (4.4), (4.5), and (4.6) are thus based on the conservation laws but incorporate non-vanishing source terms. The system of hydrodynamic equations can now be written as:

$$\frac{\partial \rho}{\partial t} = -\nabla \cdot (\rho \vec{v}) \quad (4.4)$$

$$\frac{\partial \rho \vec{v}}{\partial t} = -\rho (\vec{v} \cdot \nabla) \vec{v} - \nabla P - \rho \vec{\nabla} \Phi \quad (4.5)$$

$$\frac{\partial \rho \varepsilon_{\text{ik}}}{\partial t} = -\nabla \cdot [(\rho \varepsilon_{\text{ik}} + P) \vec{v}] - \rho \vec{v} \cdot (\vec{\nabla} \Phi) + Q_{\text{rad}}, \quad (4.6)$$

where Q_{rad} is the energy change due to the radiation field (see Sect. 4.4.8), and ε_{ik} the total energy density. The latter consists of the specific internal energy ε_{i} and a kinetic energy term ε_{k} :

$$\varepsilon_{\text{ik}} = \varepsilon_{\text{i}} + \varepsilon_{\text{k}}. \quad (4.7)$$

The gravitational force is defined as

$$\vec{g} \equiv \vec{\nabla} \Phi = \begin{pmatrix} 0 \\ 0 \\ g \end{pmatrix} \quad (4.8)$$

where the right equals sign is valid for the special case of an exclusively vertically directed force. Note that the energy equation (4.6) can also contain contributions, e.g, due to thermal conduction. Furthermore, viscosity terms can appear in Eqs. (4.4-4.6).

Using the nabla operator in the differential form $\nabla = \frac{\partial}{\partial x} + \frac{\partial}{\partial y} + \frac{\partial}{\partial z}$ and neglecting the radiative contribution Q_{rad} to the energy equation, results in hydrodynamic equations in the alternative forms

$$\frac{\partial \rho}{\partial t} + \frac{\partial \rho v_x}{\partial x} + \frac{\partial \rho v_y}{\partial y} + \frac{\partial \rho v_z}{\partial z} = 0 \quad (4.9)$$

$$\frac{\partial}{\partial t} \rho \begin{pmatrix} v_x \\ v_y \\ v_z \end{pmatrix} + \frac{\partial}{\partial x} \rho \begin{pmatrix} v_x v_x + P \\ v_y v_x \\ v_z v_x \end{pmatrix} + \frac{\partial}{\partial y} \rho \begin{pmatrix} v_x v_y \\ v_y v_y + P \\ v_z v_y \end{pmatrix} + \frac{\partial}{\partial z} \rho \begin{pmatrix} v_x v_z \\ v_y v_z \\ v_z v_z + P \end{pmatrix} = \begin{pmatrix} 0 \\ 0 \\ -\rho g \end{pmatrix} \quad (4.10)$$

$$\frac{\partial \rho \varepsilon_{\text{ik}}}{\partial t} + \frac{\partial (\rho \varepsilon_{\text{ik}} + P) v_x}{\partial x} + \frac{\partial (\rho \varepsilon_{\text{ik}} + P) v_y}{\partial y} + \frac{\partial (\rho \varepsilon_{\text{ik}} + P) v_z}{\partial z} = -\rho g v_z, \quad (4.11)$$

which show more clearly the relations of the three spatial components. Apart from the non-vanishing source terms, the above system of equations can be expressed as ‘‘conservation’’ relations for a basic set of five quantities, namely mass density ρ , mass fluxes ρv_x , ρv_y , and ρv_z for the three spatial directions, and the total energy density $\rho \varepsilon_{\text{ik}}$ (plus proper source terms).

4.2.2 Convection

As we saw in Chap. 2, convection provides an efficient mechanism of energy transport in the outer layers of the solar interior (outer $\sim 20-30\%$ in terms of radius), and thus must be a major ingredient of corresponding numerical models. In this section, we will deduce the *Schwarzschild criterion* for dynamical stability.

Let us consider an element of ideal gas whose temperature is initially in small excess to the surrounding – caused by displacement of fluctuations. A hot element will expand rapidly until pressure equilibrium with the surrounding is restored. Consequently, the specific density within the element becomes smaller than the density of the ambient medium, resulting in a buoyancy force which lifts the bubble upwards. The case is vice versa for elements cooler than the surrounding, which consequently begin to sink. Let us now regard a gas element which is displaced by a height r adiabatically, i.e., without exchanging heat with the surrounding. Pressure equilibrium of the element and the surrounding is assumed, which – if not fulfilled – would be restored on short time scales. The density difference between the element and the surrounding plays now a crucial role for the stability of the stratification. A density gradient of the element which is larger than the one of the surrounding will diminish the density deviation, so that finally the motion of the element is damped out and the element becomes stationary (again). In this case the stratification remains stable. The reverted case, however, causes the displacement of the element to increase exponentially, so that any displacement will lead to instability.

Under the mentioned assumptions, the above described criterion can also be expressed in terms of temperature. Then the element has to stay warmer than its surrounding to maintain the upward motion. Instability is now the case, if the blob remains still warmer than the surrounding after rising some way. This applies vice versa to cool descending elements. Thus, for a continuous convective flow it is necessary that the (adiabatic) temperature T_{ad} of rising elements decreases more slowly with height than the temperature T_{sur} of the surrounding, or in terms of temperature gradients:

$$\left| \frac{dT_{\text{sur}}}{dz} \right| > \left| \frac{dT_{\text{ad}}}{dz} \right|. \quad (4.12)$$

With the definition

$$\nabla \equiv \frac{d \ln T}{d \ln P}, \quad (4.13)$$

Eq. (4.12) can now be expressed (for an ideal gas) in form of the well-known *Schwarzschild criterion*:

$$\nabla > \nabla_{\text{ad}} = 1 - \frac{1}{\gamma}, \quad (4.14)$$

where γ is the ratio of the specific heats. The above equation can be expanded if we also take into account that gas elements do not necessarily behave adiabatically and that the surrounding can be – in the extreme case – in radiative equilibrium:

$$\nabla_{\text{rad}} > \nabla > \nabla_{\text{ele}} \geq \nabla_{\text{ad}} \quad (4.15)$$

This convection condition implies that a strata becomes convectively unstable if (i) the gradient ∇ is large and/or (ii) the gradient ∇_{ad} is small. The first case can be caused by a high opacity κ and a thus small free path length of photons, which decreases the efficiency of the radiative energy transport, whereas in the second case γ is reduced due to (partial) ionisation or dissociation in the regarded layer. The condition is realised in the extended convection region below the photosphere, where hydrogen is partially ionised. This zone is thus sometimes referred to as hydrogen convection zone. However, mostly a combination of energy transport by radiation and convection is realised, rather than exclusive convective transport.

Note that the widely used *mixing length theory* also assumes rising and sinking gas elements, which release their excess energy after a displacement corresponding to a predefined mixing length l . Finally, the role of convection for the energy transport can be expressed in terms of a convective flux, defined as

$$F_{\text{conv}} \propto \frac{l^2}{H_p^3} \rho T (\nabla - \nabla_{\text{ele}}), \quad (4.16)$$

where H_p is the pressure scale height as given by Eq. (4.3). It should be mentioned that convective motions have – in contrast to pure oscillations – an overturning character. Convection is present on various spatial scales like manifested by the solar granulation and supergranulation.

4.2.3 Acoustic Waves

A sound wave (or acoustic wave) represents a deviation from pressure equilibrium of a (non-magnetic) medium, as result of a local rarefaction or compression. The pressure gradient, which is caused by the deviation, is orientated against the propagation direction of the disturbance and tends to restore equilibrium conditions. Note that the resulting (oscillatory) wave is longitudinal, i.e., the perturbation is oriented in direction of propagation.

Let us consider an ambient gas of pressure P_0 and density ρ_0 and small perturbations P_p and ρ_p . After substituting the perturbed quantities $P_0 + P_p$ and $\rho_0 + \rho_p$ into the conservation relations for mass and momentum (Eq. (4.4)-(4.5)), the terms of first order in the perturbations can be separated. Note that using exclusively linear terms is only valid in case of small wave amplitudes. If we now assume an ideal adiabatic fluid, these terms lead to the *wave equation*

$$\frac{\partial^2 \rho_p}{\partial t^2} - c_s^2 \frac{\partial^2 P_p}{\partial x^2} = 0, \quad (4.17)$$

where c_s is the *sound speed*, i.e., the velocity of the propagating perturbation. In the adiabatic case, i.e., the wave does not exchange heat with its surrounding, the (adiabatic) sound speed can be obtained as

$$c_s = \sqrt{\left(\frac{\partial P}{\partial \rho}\right)_s} = \sqrt{\frac{\gamma P_0}{\rho_0}} = \sqrt{\frac{\gamma k_B T_0}{\mu m_H}} = \sqrt{\gamma g H_p} \quad (4.18)$$

and is thus determined by the conditions of the ambient gas. Here k_B is the *Boltzmann* constant, μ the mean molecular weight, and m_H the mass of hydrogen.

However, if heat exchange due to radiation (or conduction) becomes important, then the temperature excess of the wave is reduced. In this non-adiabatic case, the wave is damped and – if the temperature perturbation vanishes – propagates isothermally. A prominent example of a standing acoustic waves is the solar *5 min oscillation*, which is discussed in Sect. 2.3. Note that the sound speed is of order 10 km s^{-1} in the photosphere of the Sun.

Next to acoustic waves, which are also called *p-modes*, owing to the pressure as restoring force, other wave types occur. For instance, so-called (internal) gravity waves (*g-modes*) are due to gravity as restoring force. The both types of modes can be distinguished by means of the $k - \omega$ plane (see Sect. 2.3) which presents the power distribution as function of wavelength k and frequency ω . First, two important limiting frequencies are defined for the isothermal case, namely the so-called *acoustic cutoff frequency*

$$\omega_A = \frac{c_s}{2 H_p}, \quad (4.19)$$

where H_p is the pressure scale height (see Eq. (4.3)), and the *Brunt-Väisälä frequency*

$$\omega_B = \sqrt{g \left(\frac{1}{H_p} - \frac{1}{\Gamma_1 H_p} \right)}. \quad (4.20)$$

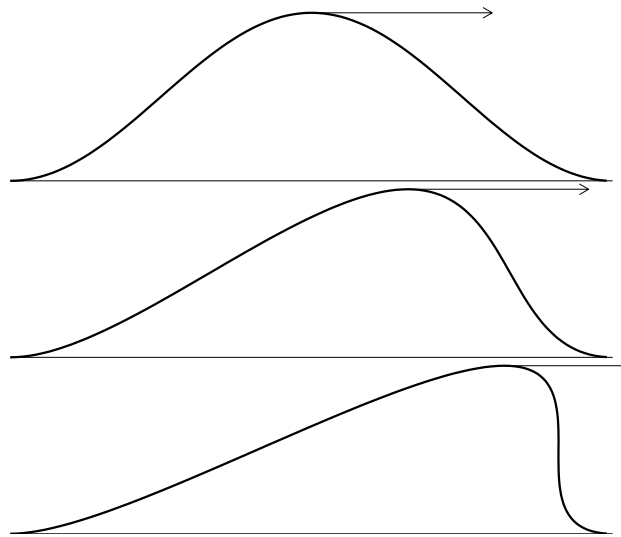


Figure 4.1: Progressive steepening of the wave profile and shock formation.

Propagating waves with a frequency below the acoustic cutoff are suppressed since they move so slow that the surrounding atmosphere has enough time to adjust itself to a new hydrostatic equilibrium and thus removes deviations. Hence, acoustic waves with $\omega < \omega_A$ become evanescent, i.e., their amplitudes decay exponentially. In the *diagnostic diagram*, i.e., $k - \omega$ plane, p-modes are thus restricted to frequencies larger than the cutoff at a wave number $k = 0$ and to the domain above the asymptote $(\omega_B/\omega_A) k c_s$ for large wave number.

Below the domain of evanescence, g-modes are enabled to exist for $k > 0$. For increasing wave number the maximum allowed frequency for gravity waves approaches an asymptote given by the *Brunt-Väisälä* frequency ω_B .

In the outer non-magnetic layers of the Sun, acoustic waves are of particular interest for the energy balance since they transport energy away from their source which then can be deposited elsewhere in the atmosphere, for instance, due to dissipation. As long as the wave amplitude is small, the energy flux associated with a propagating wave is given by

$$F_A = \rho_0 v^2 c_s, \quad (4.21)$$

where v is the velocity amplitude.

So far we regarded only waves of small amplitude, i.e., which represent only small perturbations of the ambient medium. However, if the amplitude grows larger, the deviations become significant and non-linear processes lead to steepening of the wave profile and finally to the formation of hydrodynamic shocks, as we shall see in the next section.

4.2.4 Shock Waves

The amplitudes of the acoustic waves discussed in the preceding section were assumed to be small. In that case all parts of the wave move with the same speed – unless the ambient shows inhomogeneities. The waves thus maintain a fixed shape, consisting of a *crest*, a leading and a trailing *trough*. If we now consider finite wave amplitudes, then the non-linear terms cannot be neglected anymore. As a result the crest of a sound wave has a higher temperature, therefore a higher local sound speed, and thus moves faster than the leading trough. The difference in propagation results in a progressive steepening of the profile and thus in large gradients of

pressure, density, temperature, and velocity (see Fig. 4.1). Moreover, according to Eq. (4.21) we can derive the following relation (see also Kalkofen 2001) if we assume that the acoustic flux transported by the wave is conserved and that the sound speed is constant (which is reasonable for the photosphere and the chromosphere):

$$v \propto \rho_0^{-1/2}. \quad (4.22)$$

Owing to the large density gradient of roughly 14 scale heights from the photosphere to the base of the transition region, the outer solar layers thus provide excellent conditions for the amplification of wave amplitudes. Consequently, any upward propagating disturbance will grow in amplitude to ultimately form a hydrodynamic shock. Now *dissipative processes* are no longer negligible which tend to broaden the wave profile until finally a balance between the steepening and broadening is obtained, resulting in a fixed wave profile. A well-developed shock is finally characterised by a sawtooth profile. Dissipation represents the gradual conversion of wave energy into heat, i.e., random thermal motion. Moreover, the passage of a shock wave compresses and heats the atmospheric gas, which afterwards relaxes to an (initial) equilibrium on a characteristic time scale. Note also that the shock front in a close sense is only a very narrow region with a width of only typically a few mean free path lengths. The extreme jump between the physical conditions of the un-shocked and the post-shock gas (expressed by the *Rankine-Hugoniot* conditions) thus occurs on very small spatial scales which impose high constraints on a realistic numerical modelling.

Dissipation limits the further growth of the wave amplitude which thus has an approximately constant velocity (Ulmschneider 1991). According to Kalkofen (2001) and Eq. (4.21), the acoustic flux F_A and thus also the *dissipation rate* of a shock wave are roughly proportional to the density in this case:

$$F_A \propto \rho, \quad \frac{dF_A}{dz} \propto \rho. \quad (4.23)$$

Hence, the dissipation rate dF_A/dz should decrease with height in the solar atmosphere.

4.3 Equation of State

The *equation of state* characterises the thermodynamic state of matter. It is in principal characterised as relation between three thermodynamic variables like pressure P , density ρ , and temperature T , for instance, in the form $P = P(\rho, T)$. In case of an *ideal gas* the equation of state can be written as

$$P = \frac{\mathcal{R}}{\mu} \rho T, \quad (4.24)$$

where $\mathcal{R} = 8.31 \times 10^7 \text{ erg } K^{-1} g^{-1}$ is the *universal gas constant* and μ the dimensionless *mean molecular weight* which represents the average particle mass in atomic mass units. For convenience, the equation can also be written in the forms

$$P = n k_B T, \quad P V = n \mathcal{R} T, \quad (4.25)$$

where V is the volume and n the number of particles per unit volume.

Note that the equation of state can also be expressed by means of other thermodynamic quantities like, e.g., density ρ and internal energy ε_i as done for the numerical realisation described in Chap. 5. For a proper treatment of the equation of state under stellar conditions, also ionisation of atoms as well as dissociation and recombination of molecules have to be taken into account, additionally requiring the solution of the *Saha* equation and conservation relations for charge and mass.

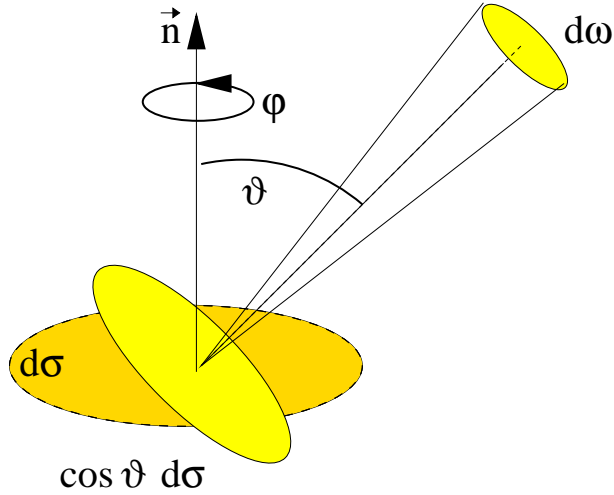


Figure 4.2: Definition of specific intensity

4.4 The Radiation Field

4.4.1 Intensity

The *specific intensity* is an essential physical quantity for the description of the radiation field. Fig. 4.2 shows a surface element of area $d\sigma$ which emits radiation under the angle ϑ relative to the normal \vec{n} . The effective projected area is thus $\cos \vartheta d\sigma$. The amount of energy per time unit dt which is emitted into the solid angle $d\omega$ in the frequency range $[\nu, \nu + d\nu]$ is then given by

$$dE_\nu = I_\nu(\vartheta, \varphi) \cos \vartheta d\sigma d\omega d\nu dt. \quad (4.26)$$

The *mean intensity* J_ν is derived by integrating over all directions, i.e.,

$$J_\nu = \frac{1}{4\pi} \oint I_\nu d\omega = \frac{1}{4\pi} \int_0^{2\pi} \int_{-1}^{+1} I_\nu d\mu d\varphi, \quad (4.27)$$

where $\mu = \cos \vartheta$. Under the assumption that I_ν does not depend on the azimuthal angle φ , what is mostly the case in stellar atmospheres, one obtains

$$J_\nu = \frac{1}{2} \int_{-1}^{+1} I_\nu d\mu. \quad (4.28)$$

4.4.2 Emission and Absorption

Let us consider a beam of radiation which runs through matter, e.g., in a stellar atmosphere. Since photons in the beam are absorbed by the matter, the intensity I_ν is decreased. The intensity variation along a path of length ds can then be expressed by

$$(dI_\nu)_{\text{ab}} = -\kappa(\nu) I_\nu ds \quad (4.29)$$

or in the alternative form

$$\kappa(\nu) = -\frac{1}{I_\nu} \frac{(dI_\nu)_{\text{ab}}}{ds}, \quad (4.30)$$

which defines the *absorption coefficient* $\kappa(\nu)$. Next to true absorption the intensity is also weakened by scattering which can be taken into account in an analogous way, i.e., by the coefficient σ_ν . Consequently, the combined absorption-scattering coefficient is

$$\tilde{\kappa}_\nu = \kappa_\nu + \sigma_\nu. \quad (4.31)$$

Furthermore, the intensity of the radiation beam is also altered by (re-)emission of photons by the matter. Let us now consider a volume element $dV = d\sigma dr$, where $d\sigma$ is the cross-section and dr the height (see Fig. 4.2). For this volume element, which emits the energy dE into the solid angle $d\omega$ for the time dt and frequency range $d\nu$ (compare to Eq. (4.26)), a *emission coefficient* $\eta(\nu)$ can be defined as

$$\eta(\nu) = \frac{dE}{dV d\nu d\omega dt} = \frac{(dI_\nu)_{\text{em}}}{ds}. \quad (4.32)$$

The coefficients depend on frequency and properties of the material like its chemical composition and thermal state.

4.4.3 Source Function

The *source function* S_ν is given by the ratio of emission and absorption coefficient and thus reveals the net contribution of the regarded matter, i.e., if absorption or emission dominates:

$$S_\nu = \frac{\eta_\nu}{\kappa_\nu}. \quad (4.33)$$

4.4.4 Optical Depth

The *optical depth* τ_ν can be defined as

$$\tau_\nu = \int_0^s \kappa_\nu \rho d\tilde{s} \quad \Leftrightarrow \quad d\tau_\nu = \kappa_\nu \rho ds, \quad (4.34)$$

where s is the distance along the line of sight between the observer ($s = 0$) and the observed region; κ_ν is the absorption coefficient which depends on local properties of the matter. Thus, $\tau_\nu(s)$ can be regarded as a measure for the transparency of the regarded medium. Obviously, the more matter is located along the line of sight, the larger the optical depth becomes. In the following, the two cases $\tau_\nu \ll 1$ and $\tau_\nu \gg 1$ are referred to as *optically thin* and *optically thick*, respectively.

4.4.5 Equation of Radiative Transfer

The total change of the intensity is given by the contributions due to absorption (Eq. (4.30)) and emission (Eq. (4.32)) and can thus be written as

$$\frac{dI_\nu}{ds} = -\kappa_\nu I_\nu + \eta_\nu \quad (4.35)$$

or if we use the definition of the source function S_ν in Eq. (4.33):

$$\frac{dI_\nu}{ds} = -\kappa_\nu [I_\nu - S_\nu]. \quad (4.36)$$

This so-called *equation of radiative transfer* can also be expressed as function of optical depth:

$$\mu \frac{dI_\nu}{d\tau} = I_\nu - S_\nu. \quad (4.37)$$

This relation represents the basic formulation of the problem of radiative transfer in stellar atmospheres.

4.4.6 Thermodynamic Equilibrium

In case of *thermodynamic equilibrium* the thermodynamic state of the regarded object can be described with a single temperature. Thus, ionisation and excitation of atoms are described by the equations of *Saha* and *Boltzmann* for the given temperature, and also velocities of the particles are characterised by a *Maxwellian* distribution for this temperature, while the same temperature enters the *Kirchhoff-Planck* function

$$\mathcal{B}_\nu(T) = \frac{2 h \nu^3}{c^2} \frac{1}{e^{h\nu/kT} - 1}, \quad (4.38)$$

which represents the radiation field of an isotropic and homogeneous *black body*. Owing to isotropy the intensity is constant and Eq. (4.37) yields

$$I_\nu = S_\nu = \mathcal{B}_\nu, \quad (4.39)$$

indicating that intensity and source function are identical and simply given by the Kirchhoff-Planck function Eq. (4.38).

4.4.7 Local Thermodynamic Equilibrium

A stellar atmosphere cannot be described properly in terms of a simple thermodynamic equilibrium as defined in the previous section, since it is stratified and thus anisotropic. Nevertheless, the assumption of thermodynamic equilibrium is approximately valid if one regards only a small limited region within the stellar atmosphere. For instance, in dense stellar interiors, where the mean free path of a photon ($l_{\text{phot}} = (\rho \kappa)^{-1}$) is very small, emission and subsequent absorption of a photon occur at places with approximately the same temperature.

A common procedure is to regard a stellar atmosphere as a sequence of layers which, each for themselves – can be described by a *local thermodynamic equilibrium* (LTE). Hence, the source function for each layer is given by the *Kirchhoff-Planck* function Eq. (4.38) for the corresponding local temperature:

$$S_\nu(r) = \mathcal{B}_\nu(T(r)). \quad (4.40)$$

LTE is a common assumption and yields remarkable results if one considers the simplicity of the approach.

4.4.8 Radiative Flux

Based on the definition of the specific intensity in Sect. 4.4.1 (see also Fig. 4.2) we can now define the *radiative flux* by integrating over all solid angles:

$$F_\nu = \oint I_\nu \vec{n} d\omega \quad (4.41)$$

$$= \int_0^{2\pi} \int_{-1}^1 I_\nu \mu d\mu d\varphi \quad (4.42)$$

$$= 2\pi \int_{-1}^1 I_\nu \mu d\mu. \quad (4.43)$$

Hence, the radiative flux represents the net radiative energy flow per time and frequency unit through the surface which is depicted in Fig. 4.2. In this thesis, always the frequency-independent radiative flux F_{rad} is referred, which is derived from Eq. (4.43) by integrating over all frequencies. The radiative flux can be exploited for the definition of *radiative equilibrium*:

$$\nabla \cdot F_{\text{rad}} \equiv 0. \quad (4.44)$$

Moreover, it can also be used to define the effective temperature T_{eff} which represents the temperature which is required by a black body to sustain the given flux:

$$F_{\text{rad}} = \sigma T_{\text{eff}}^4 \quad \Leftrightarrow \quad T_{\text{eff}} = \left(\frac{F_{\text{rad}}}{\sigma} \right)^{1/4}, \quad (4.45)$$

where $\sigma = 5.6705 \times 10^{-5} \text{ erg cm}^{-2} \text{ s}^{-1} \text{ K}^{-4}$ is the *Stefan-Boltzmann constant*. In the case of the Sun, an effective temperature of 5780 K results. Note that this typical temperature is obtained for a Rosseland optical depth $\tau = 2/3$ in a (grey) stellar atmosphere.

Furthermore, the emission of the total stellar surface per time unit – the so-called *luminosity* – can then be derived by

$$L = 4 \pi r^2 F_{\text{rad}}, \quad (4.46)$$

where r is the stellar radius and $4 \pi r^2$ the corresponding spherical surface. The solar radius, which is given in Tab. 2.1, thus leads to luminosity of $L_{\odot} = 3.85 \times 10^{33} \text{ erg s}^{-1}$ for the Sun.

Finally, the *radiative heating rate* Q_{rad} can be inferred from the divergence of the radiative flux:

$$Q_{\text{rad}} = -\nabla \cdot F_{\text{rad}} = -4 \pi \int_0^{\infty} \kappa_{\nu} (J_{\nu} - B_{\nu}) d\nu. \quad (4.47)$$

The quantity Q_{rad} thus represents the change of the internal energy of a gas due to interaction with the radiation field. Hence, Q_{rad} also enters the energy equation Eq. (4.6).

4.4.9 Mean Absorption Coefficients

For some applications it is useful to determine a *mean absorption coefficient*. Depending on the intention, there are various possibilities for the definition of the mean. For instance, demanding for the conservation of the integrated radiative flux (F_{ν}) yields the *Rosseland mean absorption coefficient*

$$\frac{1}{\bar{\kappa}_{\text{R}}} = \frac{\int \frac{1}{\kappa_{\nu}} \frac{dB_{\nu}}{dT} d\nu}{\int \frac{dB_{\nu}}{dT} d\nu}. \quad (4.48)$$

It is obviously a harmonic mean, i.e., the average of a reciprocal quantity, which favours frequencies with the smallest opacities since these frequencies contribute most to the radiative energy flux.

If one instead demands for the correct integrated thermal emission (B_{ν}), a mean of the form

$$\bar{\kappa}_{\text{P}} = \frac{\int \kappa_{\nu} B_{\nu} d\nu}{\int B_{\nu} d\nu} \quad (4.49)$$

is obtained which is commonly referred to as *Planck mean absorption coefficient*. While the *Planck* mean is a good choice in stellar layers close the surface, where the matter becomes optically thin and the condition of radiative equilibrium is nearly fulfilled, the *Rosseland* mean may be preferred in the layers below, as, for instance, realised in the *diffusion approximation* which is valid only in the stellar interior.

4.5 Energy Flux

Outside the core of the Sun, no additional source of energy is provided. Following the conservation laws, the total established energy flux thus remains constant. However, the nature of the energy transport, which is responsible for the transfer from the solar core to the surface layers, depends on the physical conditions of the different strata and can be of very different nature. As we saw in Sect. 2.2, the Sun consists – apart from the core – of a *radiative zone*, a *convection zone*, and an optically thin atmosphere. While unimportant below the convection zone, the mechanical transport plays an important role in the outer parts of the Sun. Radiation, however, is not only responsible for the energy transport in the largest part of the solar interior but also in the solar atmosphere from where finally the energy is emitted into the surrounding interplanetary space – almost exclusively in form of radiation. Transport by thermal conduction is only noticeable in the transition region and the corona above, and is thus neglected for the present considerations.

Under assumption of radiative and mechanical equilibrium, the energy balance can now be written as combination of the radiative flux F_{rad} (Eq. (4.43)) and a mechanical flux F_{mech} :

$$F_{\text{total}} = F_{\text{rad}} + F_{\text{mech}} = \sigma T_{\text{eff}}, \quad (4.50)$$

where the total emergent flux is given by Eq. (4.45). The mechanical flux is, for instance, governed by the convective flux as defined in Eq. (4.16) but can also yield contributions due to acoustic waves (see Eq. (4.21)). Finally, it should be noted that the divergence of a flux reveals its changes, i.e., the fraction of the flux which is converted into another energy form. In this thesis, the conversion of mechanical into radiative flux is of particular interest for investigating the importance of acoustic heating for the non-magnetic chromosphere of the Sun.

4.6 The Autocorrelation Function

The autocorrelation is a correlation coefficient which represents the correlation between two elements of the same variable at different positions. Thus, the autocorrelation can be understood as the cross-correlation of a variable with itself. This is distinct from the more common correlation between two different variables. Given a variable q with N equi-spaced elements (e.g. a time-series), the autocorrelation coefficient \mathcal{A}_q is defined by

$$\mathcal{A}_q(l) = \frac{\sum_{i=0}^{N-l-1} (q_i - \bar{q})(q_{i+l} - \bar{q})}{\sum_{i=0}^{N-1} (q_i - \bar{q})^2} \quad (4.51)$$

where \bar{q} is the average of all elements of the quantity q . The autocorrelation is a function of the (time) lag l . In simple words, the autocorrelation compares the elements q_i and q_{i+l} which are separated by the lag l . The resulting correlation values lie between +1 (if all elements are identical, i.e., perfectly correlate) and –1 in the case of perfect anti-correlation. A value of 0 stands for randomness, i.e., the data do not correlate at all.

The autocorrelation function as defined in Eq. (4.51) may be used for the analysis of time-series with one spatial dimension. For a given function $q = f(x, y, t)$ with two spatial and one temporal dimensions (with N_t time steps), the autocorrelation function can be written in the following

form:

$$\mathcal{A}_{q,2D}(l) = \frac{\sum_{i_t=0}^{N_t-l-1} \langle (q(i_x, i_y, i_t) - \bar{q}) (q(i_x, i_y, i_t + l) - \bar{q}) \rangle_{x,y}}{\sum_{i_t=0}^{N_t-1} \langle (q(i_x, i_y, i_t) - \bar{q})^2 \rangle_{x,y}} \quad (4.52)$$

Again, $\bar{q} = \langle q \rangle_{x,y,t}$ is the average of all elements. The brackets $\langle \rangle_{x,y}$ and $\langle \rangle_{x,y,t}$ stand for the horizontal averaging and for horizontal and temporal averaging, respectively. The main difference to Eq. (4.51) is that now two-dimensional arrays are compared (i.e., multiplied) instead of scalar elements. This is needed for the analysis of image sequences (see Sect. 7.1.8). The sums in Eq. (4.52) have an upper summation index of $N_t - l - 1$ which thus depends on the lag l and the number of time steps N_t . Hence, for large lags l the number of possible indices becomes small, i.e., the number of time step pairs i_t and $i_t + l$, which are compared with each other, decreases with increasing lag. For the maximum lag $l = N_t - 1$, only the index $i_t \equiv 0$ remains. Thus, only the differences between the first time step ($i_t = 0$) and the succeeding steps contribute to the autocorrelation coefficient. On the other hand, a lag $l = 1$ represents the comparison of direct neighbours in the time sequence. A lag $l = 0$ results – by definition – in an autocorrelation value of one, since the compared time steps are identical.

The dependence of the number of possible indices on the time lag l should be kept in mind, when dealing with time sequences which are composed of relatively few time steps. As mentioned above, the number of possible index pairs becomes small if the time lag comes close to the maximum number of time steps, i.e. the statistics become poor for a very large lag.

Chapter 5

The Radiation Hydrodynamics Code CO⁵BOLD

CO⁵BOLD is a radiation hydrodynamics code¹, developed by B. Freytag and M. Steffen, which is used for modelling stellar surface convection. The time-dependent hydrodynamic equations coupled with the radiative transfer equation are solved for a fully compressible, chemically homogeneous plasma in a constant gravitational field in two or three spatial dimensions. The non-local radiation transport can be treated frequency-dependently via the application of a multi-group scheme.

Despite the many advances of the last years, which have been made in numerical techniques as well as hardware performance, still many simplifications and approximations have to be incorporated to render the underlying physical problem feasible:

- **Finite computational box:** The number of grid cells which are necessary to model entire solar-like stars is by far too large for today’s computer facilities. The solution is the restriction on a small fraction of the stellar surface layers which is still large enough to comprise several granules. (*The situation is much better for red giant stars which are structured on larger spatial scales and thus require less resolution. This allows the simulation of entire stars with CO⁵BOLD.*)
- **Fixed Cartesian geometry:** A *Cartesian* grid is used since the deviation from spherical geometry can be neglected for the small computational domain. The grid does not change with time, but can be spatially non-equidistant.
- **No rotation:** The neglect of the Coriolis force is justified since the relevant (hydrodynamical) time scales are short compared to the rotation period of the Sun (see Sect. 2.2.3).
- **Constant gravitational field:** A constant gravitational acceleration is assumed which is legitimate in view of the limited height extent of the computational box and the corresponding small change of the gravitational potential.
- **No magnetic fields:** So far “only” pure (radiation) hydrodynamics are treated. The modelling might thus become increasingly unrealistic in the upper chromosphere and is restricted to regions of negligible magnetic fields, e.g., internetwork regions.

¹CO⁵BOLD is the abbreviation for “COnservative COde for the COmputation of COmpressible COnvection in a BOx of L Dimensions with l=2,3”

- **Homogeneous chemical composition:** Temporal or spatial changes of the chemical composition due to dissociation and recombination or due to processes which cause inhomogeneities of the element abundances (e.g., FIP or gravitational sedimentation) are not taken into account. Instead everywhere in the model the same composition is assumed. (*Changes due to dissociation and recombination can be included.*)
- **Instantaneous ionisation:** For simplicity, ionisation equilibrium is assumed which is reasonable for the solar photosphere and the layers below. In the chromosphere, however, this assumption is not valid to some extent, since there the relaxation time scales are much longer than the hydrodynamical time scales (Carlsson & Stein 2002). (Thus, this will be a point to work on in future.)
- **Local thermodynamic equilibrium (LTE):** The radiative transfer is treated in strict LTE which is a reasonable assumption in the photosphere and in the convection zone. Thus, deviations from LTE, which can occur in the chromosphere, cannot be taken into account since the inclusion of a non-LTE formalism in dynamical multi-dimensional simulations would require immense computational efforts which seem not feasible at present.
- **Limited frequency dependence:** For the same technical reasons as in the point above, the radiative transfer cannot be treated with its full frequency dependence. Instead an elaborate multi-group scheme, or – if still too intricate – a grey, i.e., frequency-independent, scheme has to be used which is legitimate for the photosphere and below.

Nevertheless, the numerical simulations – in particular for the photosphere and the convective layers below – are already quite realistic, as we shall see later for the case of the solar granulation pattern (Sect. 7.1.4). Moreover, the list of simplifications is opposed by a variety of desirable features. For example, the conservation properties of CO⁵BOLD allow to analyse energy fluxes quantitatively, and its modular structure maintains a remarkable flexibility. CO⁵BOLD can be used with different radiation transport modules, for stellar atmosphere cubes or even a whole “Star-in-a-box”. Additional modules are currently under work which will allow the treatment of magnetic fields and dust formation in the near future, although not available during the course of this thesis. Thus, magnetic fields are not included so far, restricting this version of CO⁵BOLD to internetwork regions. Furthermore, the code can be run on a variety of different hardware architectures, from simple desktop computers to multi-processor high-performance machines, on which use of the parallelisation via OpenMP can be made to increase the computational performance.

The code is a state-of-the-art development which takes advantages of the experiences made with other codes. This chapter, however, is designed to give only a rough overview over the most important facts and applied schemes, while further information is available in the CO⁵BOLD online manual and, e.g., in a paper by Freytag, Steffen, & Dorch (2002).

5.1 General Procedure

At the beginning of a simulation, all necessary input data must be provided. This includes the important parameter file which contains all relevant numerical parameters, which define the properties of hydrodynamics, viscosity, and radiative transfer routines including the boundary conditions, and, e.g., the desired time increment for the data output, and the length of the simulation run. It also contains the file names for the opacity table and the equation of state to

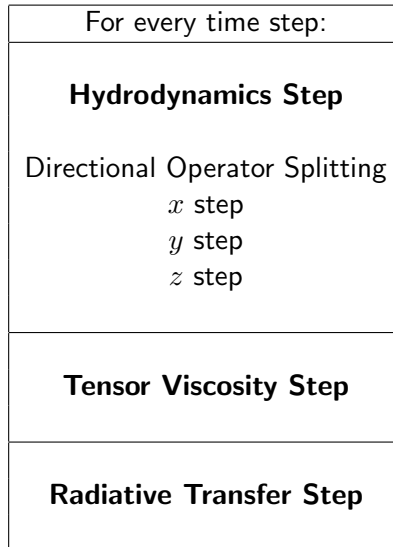


Figure 5.1: Schematic procedure for the computation of a time step in CO⁵BOLD, which is separated into individual steps due to operator splitting.

be used for the current simulation. Next to these files, also a start model – the initial condition – is read, which can be, for example, the final state of a preceding simulation.

An important feature of CO⁵BOLD is the operator splitting which allows to divide the computations into several independent steps, namely one-dimensional Eulerian hydrodynamics, multi-dimensional tensor viscosity, and radiative transfer (see Fig. 5). For each time step the hydrodynamics are treated first, resulting in updates of the basic set of quantities in all grid cells. These quantities are again updated after finishing the radiation transport for this time step. Several conditions control the length of the time step, and initiate a re-computation with a shorter increment whenever necessary. For instance, the hydrodynamics time step is limited by a *Courant* condition.

The subsequent sections provide a more detailed description of the individual computational steps.

5.2 Hydrodynamics

5.2.1 Hydrodynamic Equations

The basic hydrodynamic equations, which have to be solved by CO⁵BOLD, are described in Sect. 4.2. Now a set of independent quantities is chosen which consists of the mass density ρ , the three spatial velocity components v_x , v_y , and v_z , and the internal energy ε_i . The quantities, ρ , ρv_x , ρv_y , ρv_z , and $\rho \varepsilon_{ik}$, which were used originally in Eqs. (4.9), (4.10), and (4.11) are purely algebraic combinations of the new set. As we shall see later, these five quantities are sufficient to describe to thermal and dynamic state of each numerical grid cell.

The hydrodynamics equations Eqs. (4.9)-(4.11) can now be combined to the following system of equations:

$$\begin{aligned}
& \frac{\partial}{\partial t} \begin{pmatrix} \rho \\ \rho v_x \\ \rho v_y \\ \rho v_z \\ \rho \varepsilon_{ik} \end{pmatrix} + \frac{\partial}{\partial x} \begin{pmatrix} \rho v_x \\ \rho v_x v_x + P \\ \rho v_y v_x \\ \rho v_z v_x \\ (\rho \varepsilon_{ik} + P) v_x \end{pmatrix} + \frac{\partial}{\partial y} \begin{pmatrix} \rho v_y \\ \rho v_x v_y \\ \rho v_y v_y + P \\ \rho v_z v_y \\ (\rho \varepsilon_{ik} + P) v_y \end{pmatrix} + \frac{\partial}{\partial z} \begin{pmatrix} \rho v_z \\ \rho v_x v_z \\ \rho v_y v_z \\ \rho v_z v_z + P \\ (\rho \varepsilon_{ik} + P) v_z \end{pmatrix} \\
& = \\
& \begin{pmatrix} 0 \\ \rho g_1 \\ \rho g_2 \\ \rho g_3 \\ \rho (g_1 v_x + g_2 v_y + g_3 v_z) \end{pmatrix}. \tag{5.1}
\end{aligned}$$

Since this system is symmetric for the spatial directions x , y , and z it can be reduced to three independent one-dimensional systems of equations of the form

$$\frac{\partial}{\partial t} \begin{pmatrix} \rho \\ \rho v_x \\ \rho v_y \\ \rho v_z \\ \rho \varepsilon_{ik} \end{pmatrix} + \frac{\partial}{\partial x} \begin{pmatrix} \rho v_x \\ \rho v_x v_x + P \\ \rho v_y v_x \\ \rho v_z v_x \\ (\rho \varepsilon_{ik} + P) v_x \end{pmatrix} = \begin{pmatrix} 0 \\ \rho g_x \\ 0 \\ 0 \\ \rho g_x v_x \end{pmatrix}, \tag{5.2}$$

which is the case for the x -direction. Note that due to the gravity term the right-hand side is non-zero for the z -direction but zero otherwise. This so-called *directional operator splitting* results in the sequential solution of single 1-D sub steps for the different directions. Note that the viscous and radiative terms are treated separately subsequent to the computational hydrodynamics step (Sect. 5.3-5.4).

The individual 1-D steps can now be treated with a fast approximate Riemann solver (Roe 1986) which is modified to account for a realistic equation of state and an external gravity field. A detailed description of the scheme is provided in Sect. 5.2.3.

5.2.2 Numerical Grid

The numerical grid is of *Cartesian* geometry. It can be two- or three-dimensional. The grid is fixed in time but can be spatially non-equidistant which allows to apply a different spatial resolution for different regions.

The basic quantities, which result from the simulation, are stored in output files which use the same grid as used in the course of the hydrodynamical computations. Next to the centres of the grid cells also the boundaries are provided since the cell boundaries are of particular importance for the hydrodynamics (see subsequent section). The cell centres, however, are needed for the treatment of the gravitational field.

5.2.3 One-Dimensional Hydrodynamics Step

The basic relations in Eq. (5.2) can be translated into a discrete form for the numerical grid and thus for one-dimensional columns which are obtained by directional operator splitting. For each

of these columns the hydrodynamic problem is solved by computing the fluxes across the cell boundaries. An approximate 1-D *Riemann solver* (Roe 1986) is used which – in CO⁵BOLD – is modified to account for the non-equidistant grid, a realistic equation of state, and the presence of gravitational source terms. The *partial waves*, which emerge from differences between the grid cells, are advected with upwind-centred fluxes. Note that the corresponding characteristic velocities are also used to check the *Courant condition*, which finally determines the hydrodynamical time step. The profiles of the partial waves within the cells are treated with a *reconstruction scheme*, which uses one of the available slope limiters: *Minmod*, *Van Leer*, *Superbee*, which are all second order upwind schemes, or the more accurate *Piecewise Parabolic Method* (PPM). For the calculations presented in this thesis, the Van Leer scheme (van Leer 1974) was chosen, since it is a good compromise between accuracy and computational speed. Finally, fluxes are obtained which are used to update the basic quantities in the cells of the regarded one-dimensional column.

5.2.4 Equation of State

The equation of state is not computed at run time but has been tabulated in advance to save computational time. Thus, during the simulation the equation can be solved by a bicubic interpolation in the table. For all models presented in this thesis the same EOS table was used. It has been computed for a prescribed chemical composition of hydrogen, helium, and a representative metal with relative abundances $[X, Y, Z] = [0.908, 0.091, 6.4 \times 10^{-4}]$, respectively, and a mean molecular weight of $q_{\text{mol}} = 1.302$. Ionisation of H and He, as well as formation and dissociation of H_2 are taken into account.

During the simulation and also in the course of the “post-simulation” analysis, the density ρ and the internal energy ε_i are used as input parameters. The table thus consists of two-dimensional arrays as functions of density and internal energy which cover a range of 10^{-21} to 0.02 g cm^{-3} in density and -1.48×10^{12} and $3.4 \times 10^{14} \text{ erg g}^{-1}$ in internal energy, respectively. The quantities, which are returned by the EOS routines, are mainly pressure, temperature, sound speed, the adiabatic coefficients Γ_1 and Γ_3 , and further derivatives of the pressure. The procedure can be applied to all grid cells, even for the whole model at once, resulting in the desired thermodynamic quantities for each grid cell.

5.3 Tensor Viscosity

The hydrodynamics scheme is stable enough to handle 1-D and most multi-dimensional problems. However, there are special multi-dimensional cases which make an additional tensor viscosity necessary to ensure stability. An example are strong shocks which are aligned with the computational grid so that they are almost invisible for one-dimensional hydrodynamics (Quirk 1994).

In a separate sub step of CO⁵BOLD viscous energy fluxes are computed which are finally used to update the velocities and the internal energy. The required tensor viscosity is a function of the grid cell lengths and the velocity components of all spatial directions. Furthermore, the parameters $C_{\text{visArtificial}}$ and $C_{\text{visSmagorinsky}}$ enter the computation of the viscosity linearly. They are used to prescribe the amount of artificial (van Neumann type) and turbulent eddy viscosity (Smagorinsky 1963), respectively. In contrast to the one-dimensional hydrodynamics, the tensor viscosity is treated in three (or two) dimensions. Note that the viscosity discussed in this section is not the molecular viscosity but rather a “turbulent”/sub-grid-scale viscosity, which accounts for the (turbulent) flows on scales which remain unresolved by the numerical grid.

5.4 Radiative Transfer

Although the radiation transport is treated under the assumption of strict *Local Thermodynamic Equilibrium* (LTE, see Sect. 4.4.6), one has still in principle to take into account all frequencies for the solution of the equation of radiative transfer (see Sect. 4.4.5). As part of multi-dimensional simulations, an explicit treatment would require by far too much computational power, exceeding today's technical possibilities. Instead, simplifications and efficient algorithms are needed.

First of all, one can neglect the frequency-dependence and perform so-called “grey” radiation transport. In this case the integration of the *equation of radiative transfer* Eq. (4.36) yields

$$\frac{d\tilde{I}}{ds} = \int_0^\infty \frac{dI_\nu}{ds} d\nu = -\kappa \int_0^\infty [I_\nu - S_\nu] d\nu = -\kappa [\tilde{I} - \tilde{S}], \quad (5.3)$$

where \tilde{I} and \tilde{S} represent the integrated quantities and κ the grey mean opacity. Note that the integration comprises the whole frequency range.

An improvement compared to the grey case, which completely ignores the frequency dependence, is to define a number of frequency groups in which the radiative transfer is solved separately. The procedure within a group is similar to the grey case, with the exception that the integral comprises not the whole frequency range but only part of it. Eq. (5.3) can now be expressed for a frequency band i as

$$\frac{d\tilde{I}_i}{ds} = - \int_{\nu_i} \kappa_\nu [I_\nu - S_\nu] d\nu \approx -\bar{\kappa}_i [\tilde{I}_i - \tilde{S}_i] \quad (5.4)$$

where $\bar{\kappa}_i$ is the mean absorption coefficient or opacity for the frequency group. The basic approximation of this so-called *multi-group scheme* (see Ludwig 1992, and references therein) is represented by the right equals sign in Eq. (5.4) and consequently the assumption that $\bar{\kappa}_i$ is constant within a group², although κ depends strongly on frequency. The multi-group scheme is thus influenced by the choice of the group boundaries and the applied average within the groups. Furthermore, the opacity depends on the chemical composition and the thermal state of the plasma/gas. The band-integrated opacities and source functions are hence needed as functions of the thermal state for the solution of the radiative transfer problem if a constant chemical composition is assumed. The required quantities are provided in so-called *opacity tables* which are described in more detail in Sect. 5.4.1.

The procedure stated above, can numerically be realised with different approaches. For instance, a *long-characteristics method* is used in this thesis. The numerical routines, referred to as “*solar radiation transport module*” in CO⁵BOLD, have been developed by M. Steffen on the basis of the older “*2-D Kiel code*” (see, e.g., Freytag, Ludwig, & Steffen 1996). Note that other radiation transport modules are available for CO⁵BOLD, like the *short-characteristics module*, developed by B. Freytag in particular for the simulation of a whole “*Star-in-a-box*”.

In case of long characteristics, the equation of radiation transfer is solved along a large number of rays which traverse the computational box under various azimuthal and inclination angles. The spatial resolution obtained by the rays can be finer than the one of the hydrodynamics grid, which is for example desirable in the presence of large variations of the radiation field in the vicinity of entangled shock wave configurations. As a first step, all necessary quantities, like temperature and density, which are defined on the hydrodynamics grid are interpolated onto a ray. Along this ray the (one-dimensional) radiative transfer is solved by applying the *Feautrier* method (see, e.g., Mihalas 1978), which has been proven to be very stable. Here, the opacity

²Frequency groups are also referred to as (opacity) bands.

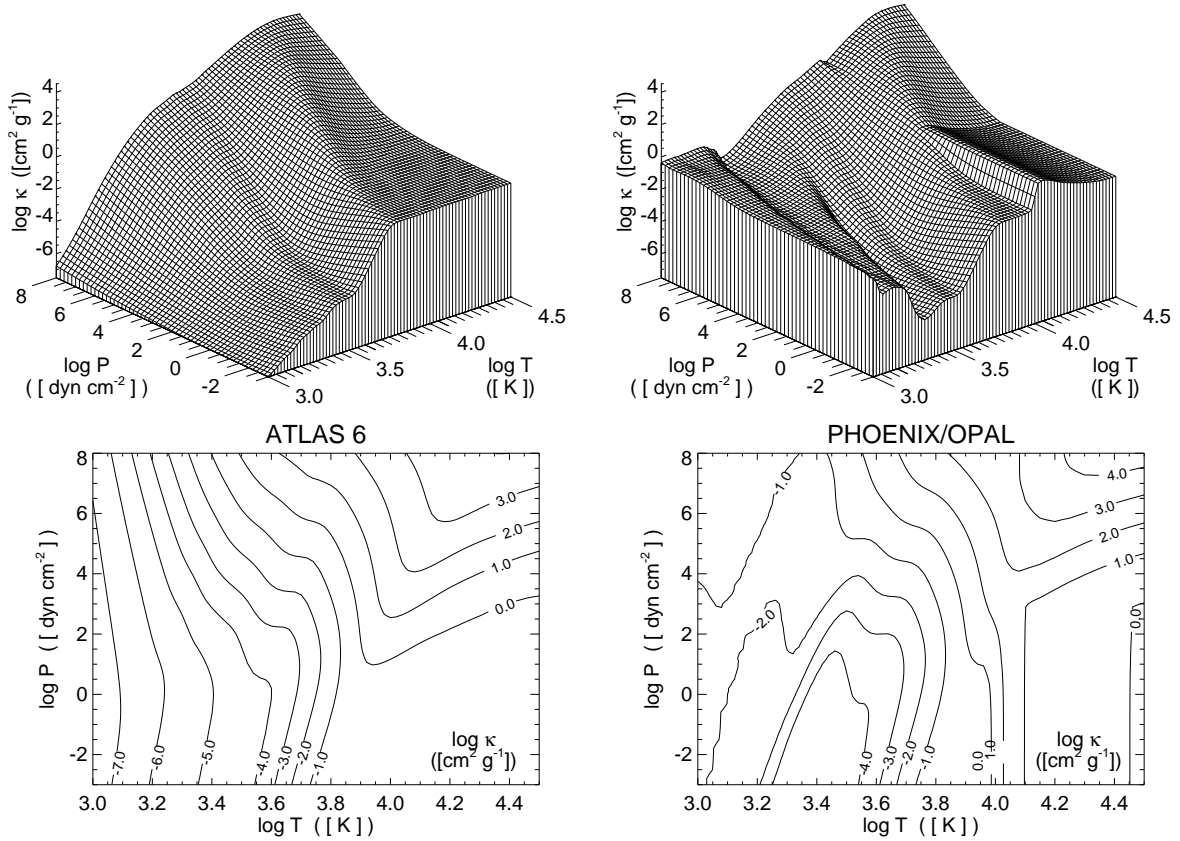


Figure 5.2: Grey opacity as surface and contour plot for the table based on ATLAS 6 (left) and table for PHOENIX/OPAL data (right) for the temperature and pressure range of the ATLAS 6 table. Note that the PHOENIX/OPAL table comprises opacities for a larger pressure and temperature range than shown in this figure.

look-up table also enters the computation. The solution finally results in radiative fluxes and heating rates Q_{rad} (see Eq. (4.47)) which are interpolated back onto the hydrodynamics grid. The rates represent the changes of the internal energy due to radiation transport. Hence, the final step is the update of the internal energy with the radiative heating rates, like it was initially expressed in the equation of conservation of energy Eq. (4.6).

The usage of *periodic boundaries* (see Sect. 5.5) implies that each ray is continued across the boundary and thus re-enters the computational box on the opposite side. This behaviour is critical for large inclination angles, i.e., for rays which are almost horizontal. The extreme case of a horizontal ray would have an infinite length, which is of course unrealistic and thus must be avoided.

5.4.1 Opacity Tables

For the solution of the radiative transfer, opacities and source functions are needed as integral over all frequencies or as integrals for all frequency groups in the non-grey case, as can be seen in Eq. (5.3) and Eq. (5.4), respectively. Consequently, these quantities have to be provided for the numerical calculations in the form of predefined look-up tables. For a given chemical composition, the opacity still depends on the thermal state of the matter, which is here defined

by its temperature and pressure. The source functions depends on the temperature only. Hence, the required table has to provide arrays for opacity and source function for a grid of temperature (and pressure). These values, which are needed for the solution of the radiative transfer equation, can then be derived by simple interpolation in the table, which is shortly referred to as “*opacity table*” (Ludwig 1992).

The opacity for the grey and the non-grey groups are calculated via *Planck* and/or *Rosseland* means or a hybrid form, which combines both means for different pressure-temperature domains (see Sect. 4.4.9). The opacity groups for the non-grey case are obtained by sorting the mean absorption coefficients at different frequencies as follows: A one-dimensional model atmosphere is assumed, which allows to calculate a monochromatic optical depth scale τ_ν for each frequency separately. The geometrical height, where an optical depth unity ($\tau_\nu = 1$) is reached, thus depends on frequency. Moreover, the optical depth τ_R is computed for the frequency-independent *Rosseland* mean and a set of optical depths τ_{R_i} is defined, dividing the scale into discrete groups. For each frequency $\tau_\nu = 1$ corresponds to a geometrical height in the model atmosphere, which on the other hand is represented by a value τ_R on the *Rosseland* scale. The mean absorption coefficients are now sorted by their corresponding position τ_R ($\tau_\nu = 1$) on the *Rosseland* scale into the appropriate group. Hence, each group or band comprises absorption coefficients of comparable value, whereas the different bands roughly correspond to different domains of the stellar atmosphere, from optically thick to optically thin strata. The bands thus represent different components of the spectrum, for instance, continuum, strong and weak absorption lines. Finally, *Planck* and/or *Rosseland* means can be used to derive mean opacities for every band separately. See the thesis by Ludwig (1992) for a more detailed description of this procedure. Note that this way a large number of atomic lines and even molecular features – if available – are taken into account.

The following opacities tables, which have been compiled and processed by H.-G. Ludwig, are used for the simulations in this thesis:

- **PHOENIX/OPAL**, grey Planck/Rosseland mean
- **ATLAS6**, grey Rosseland mean
- **ATLAS6** frequency-dependent **multi-group** scheme with five bands, grey Rosseland mean, Planck/Rosseland means for the individual groups

The two ATLAS6 cases are combined in the same file. For the grey radiation transport only the grey *Rosseland mean opacity* is used, while additional bands with *Planck/Rosseland* means are available for the non-grey modus. The table has been computed from ODFs (*opacity distribution functions*), which are incorporated in the stellar atmosphere program ATLAS6 (Kurucz 1970), for solar abundances which closely match those used for the calculation of the equation of state (see Sect. 5.2.4). The resulting temperature range is $\log T = 3.0$ to 4.5 , whereas the the pressure ranges from $\log P = -3.0$ to 8.0 (in cgs units).

The non-grey groups are separated with respect to optical depth for threshold values of $\log \tau = 0.0, -1.5, -3.0,$ and -4.5 .

For the PHOENIX/OPAL table data from PHOENIX (Hauschildt et al. 1997, and references therein) and the OPAL project (Iglesias et al. 1992) have been combined at a temperature of 12 000 K, where PHOENIX is used for the cool and OPAL for the hot part. The OPAL opacities are in particular compiled for models of stellar interiors, while PHOENIX was designed for atmospheres of cool stars. Hence, the latter includes contributions from molecules. As result of the different purposes, PHOENIX provides *Planck* means while the OPAL opacities are *Rosseland* means. The abundances are the same for OPAL as for the equation of state

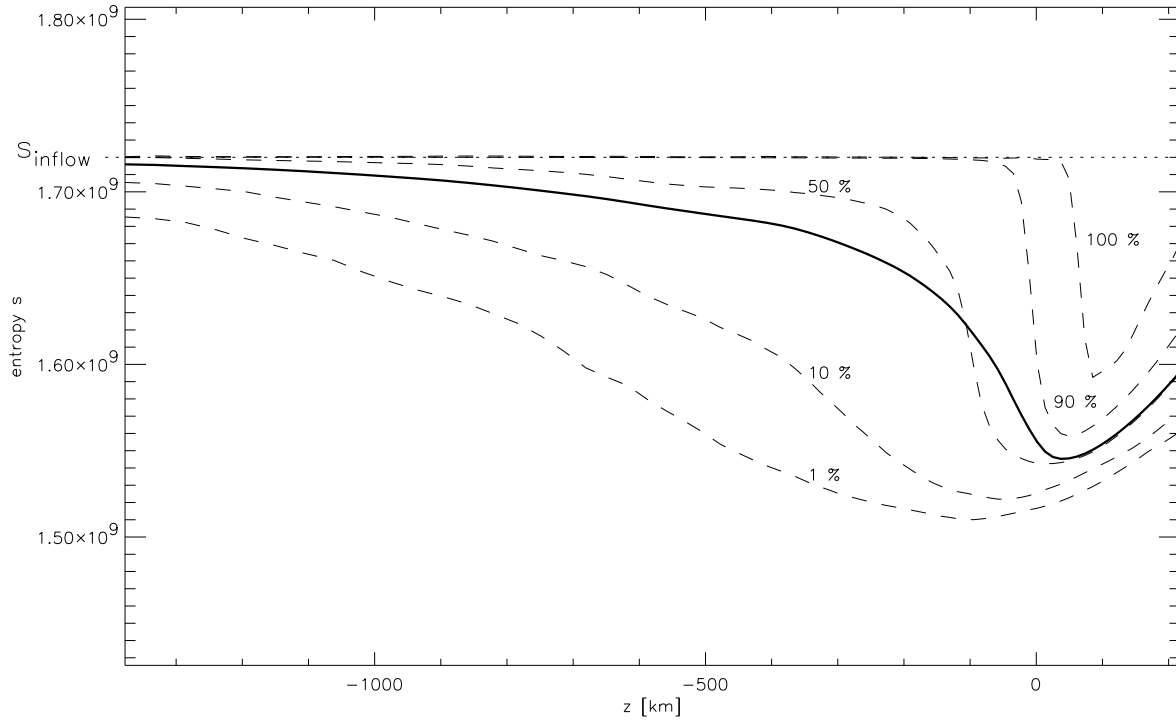


Figure 5.3: Entropy over height for an exemplary three-dimensional model. The dashed lines represent percentiles, i.e., the limits which are superior to, e.g., 90 % of all values at a given height. The 100 % percentile shows a constant plateau below $z \lesssim 0$ km equal to the value of the entropy s_{inflow} , which flowing in at the lower boundary. The solid line marks the height-dependent average entropy.

mentioned in Sect. 5.2.4, and also the PHOENIX abundances are very similar, so that the chemical composition of equation of state and opacities can be regarded consistent. Although the transition between the two data sets is not perfectly smooth at some points in the pressure-temperature regime (see Fig.5.2 at $\log T \sim 4.1$), the combined new table is elaborate in view of the differences between the original data sets. The new table comprises a range of $\log T = 2.7$ to 6.8 in temperature and $\log P = -4.0$ to 15.0 in pressure (all in cgs units). Since the ATLAS6 opacities do not include contributions from molecules, we can study their influence on the results via a comparison with simulations done with the PHOENIX/OPAL table which includes molecular contributions (see Chap. 8). In Fig.5.2 these contributions show up as higher opacity for low pressure and temperature, as they are expected in the outer solar layers.

5.5 Boundary Conditions

Since the computational domain is of finite size, artificial boundaries are required at all sides. In the case of a small piece of the solar atmosphere, the vertical direction has to be treated differently than the lateral ones due to the gravitational force. Furthermore, bottom and top of the computational box are placed in regions of the solar atmosphere which exhibit very different physical conditions and thus require different approaches. For the numerical treatment of the boundary conditions in the course of the hydrodynamics calculations, “ghost cells” are added at

the ends of the one-dimensional grid cell columns, whereby the number of ghost cells depends on the applied reconstruction scheme (see Sect. 5.2.3).

5.5.1 Lateral Boundaries

The lateral boundaries are *periodic*, i.e., the opposing sides are identical. If a gas element is advected across the outer boundary then it will reappear on the opposite side. The same is true for the rays used for the radiative transfer calculations. Thus, in the course of the 1-D hydrodynamics step the quantities in the ghost cells at the one end are equal to those on the other end of the one-dimensional grid column.

The alternative case of closed boundaries may cause reflections of acoustic waves and thus unwanted interferences. The periodic boundaries, however, are reasonable since it can be assumed that the surrounding of the computational box shows in principal the same behaviour as the box interior.

5.5.2 Lower Boundary

The lower boundary, which is located in the convection zone, is assumed to be “*open*”, i.e. material is allowed to flow in and out of the computational box. This requires a more extensive numerical treatment than for lateral boundaries.

First, the material, which is entering the computational box from below, has an entropy as commonly assumed for the deeper convective envelope (Ludwig et al. 1999). Fig. 5.3 shows the entropy as function of height, which clearly exhibits a constant level. The deviations from this are mainly due to downdrafts of cool material which have a lower entropy contrast for larger depth. At the bottom of the presented example, almost all grid cells are characterised by the same entropy. This allows to prescribe a constant entropy for the material which rises through the lower boundary. This entropy is chosen to approach a predefined value s_{inflow} on a characteristic time scale, which can be altered by means of the parameter C_{change} . Furthermore, corrections are applied to density, internal energy, and velocities of the grid cells in the bottom layer in order to reduce deviations of the pressure from the horizontal mean and to provide a vanishing mass flux in the vertical direction, thus conserving the total mass in the model. Note that due to the changes of the quantities performed in the bottom layer the conservation relations are only fulfilled in the layers above. The ghost cells in the hydrodynamics step are finally filled with values which are extrapolated from the bottom layer.

5.5.3 Upper Boundary

The upper *transmitting* boundary turns out to be stable and even allows shock waves to leave the computational box without noticeable reflections. In the opposite direction material can flow into the computational box if the velocity at the boundary is directed downwards. The temperature of the in-flowing material is altered towards a temperature, which is predefined by the parameter c_{surf} in units of the effective temperature T_{eff} , on a characteristic time scale. The latter can be adjusted with the parameter c_{change} . Moreover, the vertical derivative of the velocity components and of the internal energy are zero, while the density decreases exponentially.

5.6 Output Data

Any numerical two- or in particular three-dimensional simulation results in a large amount of data. Thus, a compromise has to be made between accuracy and completeness of the ensemble

of provided quantities on one side and disk space on the other side. In CO⁵BOLD only the basic set of the five quantities density ρ , internal energy ε_i , and velocity components v_x , v_y , and v_z are stored for all grid cells which is sufficient to describe the thermal and dynamic state of the model. These quantities are stored for each grid cell at each desired time step. The computational time step is of order 0.1 to 0.2 s but the full model is only written into a file every 10 or 30 s (or at any arbitrary interval), since this already piles up an immense amount of data. The resulting files have usually the extension “.full”, “.sta”, or “.end” for the “bulk” intermediate, start and end models, respectively.

All other quantities can be calculated afterwards from the stored model snapshots in combination with the tabulated equation of state (see Sect. 5.2.4) and the opacity table (see Sect. 5.4.1).

Moreover, a larger number of useful averaged quantities is stored at run-time in files with the extension “.mean”. These files contain, for example, horizontal averages of energy fluxes (defined on the cell boundaries) and a variety of other quantities as well as the emergent (grey) intensity at the upper boundary of the model.

The time increments for the output into the “.full” and “.mean” can be specified separately in the parameter file. Note that the architecture-independent data format UIO is used, which has been developed by B. Freytag. Please refer to the CO⁵BOLD online manual for a more detailed technical description of the many features of the code.

Chapter 6

Hydrodynamic Models

In this chapter the numerical models are introduced which have been computed in the course of this thesis. See Chap. 5 for details on the radiation hydrodynamics code CO⁵BOLD.

6.1 The Numerical Grid

The numerical grid is the same for all models. It consists of 140×140 horizontal (x, y) and 200 vertical (z) grid points. The horizontal resolution is constantly 40 km, leading to a total horizontal extent of 5600 km (see Fig. 6.1). This corresponds to an angle of $\sim 7''.7$ in ground-based observations. Thus, the model is large enough to comprise several granules and small enough to fit inside a typical internetwork region (see Sect. 2).

The bottom of the original computational box is located at $z \approx -1323$ km in the convection zone and the upper boundary in the middle chromosphere at a height of $z \approx 1789$ km (cell centres at ≈ -1323 km and ≈ 1783 km). Hence, the total vertical extent is 3110 km. In the following, the photosphere can be referred to as the layer between 0 km and 500 km in model coordinates, and the chromosphere as the layer above. The 200 vertical grid points are non-equidistant with a resolution of 46 km at the bottom, decreasing with height down to a constant distance (centre to centre) of 12 km for all layers above $z = -270$ km (see right panel in Fig. 6.1). This way a high resolution is provided for the layers which are of particular interest for this thesis, i.e., the domain where acoustic waves are generated, propagate and dissipate. The lower part (the convection zone) can be modelled with a lower vertical resolution which reduces the number of grid cells and thus saves computational time, memory, and disk space.

Note that the modelling of the uppermost layers might become less realistic with height since there magnetic fields (or more precisely the *magnetic canopy*, see Sect. 2.2.2) play a role which cannot be simulated with the applied version of CO⁵BOLD. This imposes constraints on the choice of the location of the upper boundary: On the one hand, the *upper boundary* should not be placed too high since the uppermost layers might be unrealistic to some extent and thus should not be interpreted too serious anyway, on the other, it should be located far away from the regions of particular interest to minimise possible effects due to the boundary condition. Under these circumstances placing the upper boundary in the middle chromosphere seems to be a good compromise.

6.2 Three-Dimensional Models

The following 3-D models have been calculated (see also Tab. 6.1):

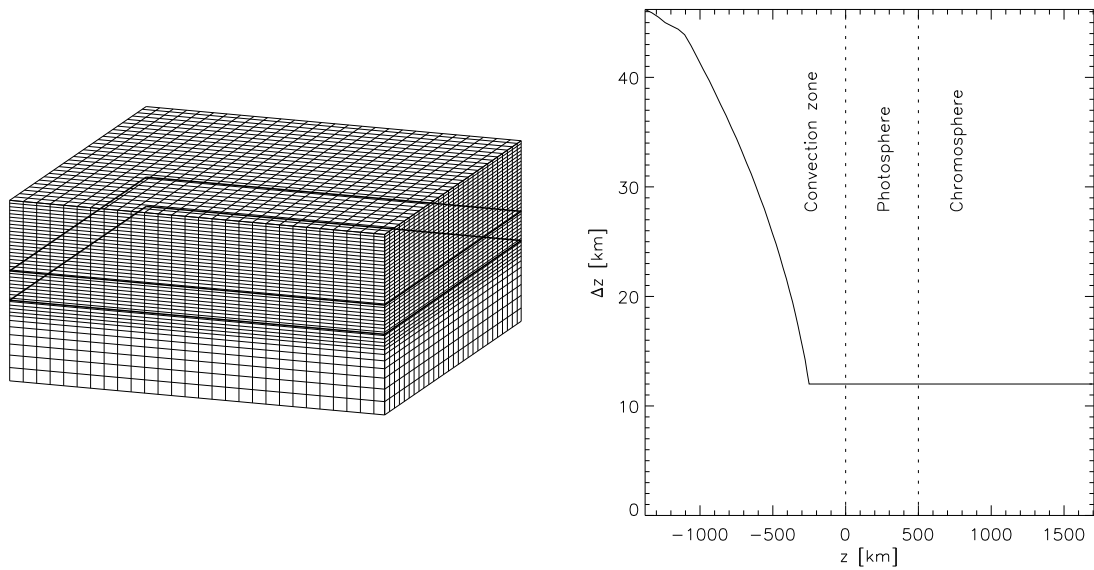


Figure 6.1: Numerical (three-dimensional) grid (left) which is non-equidistant in vertical direction. The decreasing vertical resolution is shown in the right panel. Note that only every fifth boundary is plotted in the grid on the left side.

- **Model 3DgPO with grey radiation transport and PHOENIX/OPAL opacities:**
 Used as *three-dimensional reference model* in this thesis. The first 170 min of the simulation sequence are excluded from the analysis to ensure that the model has sufficiently relaxed, i.e., a (dynamic) equilibrium is reached. The results presented in this thesis are based on another succeeding 151 min simulation time. The output time increment is 30 s for the **full** and 10 s for the **mean** data set. Additionally, a short sequence of 600 s duration is available for which the output time increment is only 10 s for both, the **full** and the **mean** data. The results for this model are discussed in more detail in Chap. 7.
 In case of the 3-D reference model a height offset of $\Delta z = 77.2$ km is applied to make the geometric height scale comparable to other semi-empirical models and observations. This way the origin ($z = 0$ km) corresponds to the temporally and horizontally averaged optical depth unity. The resulting new locations of the boundaries are $z \approx -1400$ km and $z \approx 1710$ km. Note that in Chap. 8 the original numerical grid without offset is used to enable direct comparisons with the other models which are presented in this chapter.
- **Model 3DgA6 with grey radiation transport and ATLAS6 opacities:**
 The only difference to the reference model is the different opacity table (see Sect. 5.4.1). The first hour of the simulation is reserved for relaxation. Only the remaining 168 min are used for the analysis.
- **Model 3DnA6 with non-grey radiation transport and ATLAS6 opacities:**
 This model also employs the ATLAS6 opacity table but for the multi-group scheme. Since five opacity bands are taken into account instead of only one like for the grey models described above, a much larger amount of computational time is needed. However, excluding a relaxation phase of 90 min, still another 62 min are available.
- Modified model 3DgPO with a smaller value for the viscosity parameters (see Tab. 6.1)

The initial model, from which all other models emerge, is based on an already evolved model by M. Steffen which reaches up to the top of the photosphere. On top of this model, more grid cells have been added, resulting in the numerical grid which is described in Sect. 6.1. The temperature and density stratification for these new grid cells were calculated under the assumption of hydrostatic equilibrium. Interestingly, the further *evolution of the model does not depend strongly on the initial condition* because the chromosphere turns out to be highly dynamical on very short time-scales (see Sect. 7.1.8). After only a few minutes of simulation time the initial chromosphere already formed the typical structures which are discussed in Sect. 7.1. Thus, this finding increases the reliability of the inferred results.

The computational time step is typically 0.1 to 0.2 s. Since each time step requires 80 MB disk space, the `full` data set was stored only every 30 s – with exception of the higher sampled partial sequence of 3DgPO with a time increment of only 10 s. The `mean` data need less disk space and are thus sampled with 10 s.

Note that the available lengths of the models are very different. The aim was to provide a relaxation phase of at least one or two hours and an additional sequence of at least two hours duration. In case of 3DgPO and 3DgA6 this goal was attained. The duration of the non-grey simulation 3DnA6 is much shorter since (i) the larger part was excluded for relaxation and (ii) a much larger amount of computational time was required (see above). The need for a long relaxation phase will become clear from the strong influence of the radiative transfer scheme on the results (see Chap. 8). Unfortunately, the simulation of the model 3DgPO with a reduced viscosity parameter of $C_{\text{vis}} = 0.1$, which was set for all models to

$$C_{\text{vis}} = C_{\text{visArtificial}} = C_{\text{visSmagorinsky}}, \quad (6.1)$$

simply ended too early when the *CRAY SV1* computer in the *Rechenzentrum der Universität Kiel* was shut down for good.

Table 6.1: Key properties of the hydrodynamic models computed for this thesis: Radiative transfer scheme, opacity table, viscosity parameter C_{vis} , and available duration of simulation sequence without relaxation phase.

model	rad.	opacity	C_{vis}	time
Three-dimensional:				
3DgPO	grey	PHOENIX/OPAL	0.5	9040
3DgA6	grey	ATLAS6	0.5	10050
3DnA6	multi-group	ATLAS6	0.5	3740
3DgPO	grey	PHOENIX/OPAL	0.1	4320
Two-dimensional:				
2DgPO	grey	PHOENIX/OPAL	0.5	15860
2DgA6	grey	ATLAS6	0.5	10140
2DnA6	multi-group	ATLAS6	0.5	10040
2DgPO	grey	PHOENIX/OPAL	0.1	16460
2DgPO	grey	PHOENIX/OPAL	0.3	7180
2DgPO	grey	PHOENIX/OPAL	1.0	16440

6.3 Two-Dimensional Models

In the course of this thesis, two-dimensional models played an important role for preparing studies in advance of the construction of the first three-dimensional model. Additionally, many test calculations have been performed in 2-D which will be used in Chap. 8 to analyse the difference between two- and three-dimensional simulations.

The first 2-D model was taken as a vertical (x,z) slice from an early 3-D model. Thus, the numerical grid in the x and z -direction is the same as described in Sect. 6.1 (see also Fig. 6.1). The following 2-D models have been calculated:

- **Model 2DgPO with grey radiation transport and PHOENIX/OPAL opacities:**
The same as model 3DgPO but only two-dimensional. It can thus be regarded as 2-D reference model in this thesis.
- **Model 2DgA6 with grey radiation transport and ATLAS6 opacities:**
The same as model 3DgA6 but only two-dimensional.
- **Model 2DnA6 with non-grey radiation transport and ATLAS6 opacities:**
The same as model 3DnA6 but only two-dimensional.
- Modified models 2DgPO with different viscosity (see Tab. 6.1)

The computational time steps are similar to those of the three-dimensional simulations. A 2-D time step, however, needs only 0.57 MB disk space and thus allows for an output increment of 10 s for both the `full` and the `mean` data. The available differences in the durations of the simulation sequences arise from the same reasons as in the three-dimensional case, only that it was attempted to obtain longer sequences in order to counterbalance the lower number of grid cells.

Chapter 7

Results for the Three-Dimensional Reference Model

Here, the three-dimensional reference model 3DgPO, which was introduced in Chap. 6, is described in more detail. First its structure is addressed, in particular the average stratification and the variation of the horizontal pattern with height. Special emphasis is devoted to the model chromosphere and the prominent patterns therein which can be regarded as the major outcome of this thesis. Then, various aspects of the model are investigated, such as the propagation of shock waves, oscillations, the temperature distribution, and even possible implications for the formation and existence of carbon monoxide molecules in the solar atmosphere. Moreover, the energy fluxes are examined, aiming at an estimate for the acoustic flux in the model chromosphere which is required to address one of the underlying questions of this thesis, namely the heating of the solar chromosphere due to acoustic waves.

7.1 Structure of the Model Atmosphere

7.1.1 Average Stratification

Introductory, an overview of the vertical structure of the three-dimensional reference model is given. Horizontally and temporally averaged stratifications are shown for various quantities in Fig. 7.1. The full time sequence of 151 min (see Sect. 6.2) and all horizontal positions have been used for the calculation of these arithmetic averages. The first two panels show the variation with height for the internal energy, and the logarithmic density. These quantities, which are stored during the simulation run, are sufficient to describe the thermodynamic state of the model. The average internal energy decreases from the lower boundary of the model to the bottom of the photosphere ($z = 0$ km), while it stays almost constant in the photosphere and chromosphere. The average density shows a strong decrease over all heights. However, the density gradient is much steeper above the convection zone, provoking important consequences for the propagation of acoustic waves. Furthermore, the density varies by orders of magnitude in the model which thus has to comprise many scale heights at the same time.

The dynamic state of the model is described by the three spatial velocity components v_x , v_y , and v_z . The height-dependent rms-values are plotted for the individual components and for the total velocity ($|v| = (v_x^2 + v_y^2 + v_z^2)^{-1/2}$), too. The horizontal components do not differ significantly (see Fig. 7.1.c). They both show a local maximum of 2.4 km s^{-1} at $\approx +70$ km above the bottom of the photosphere and a strong increase in the chromosphere. The values are in general smaller than for the vertical component, except for the photosphere and the very top of

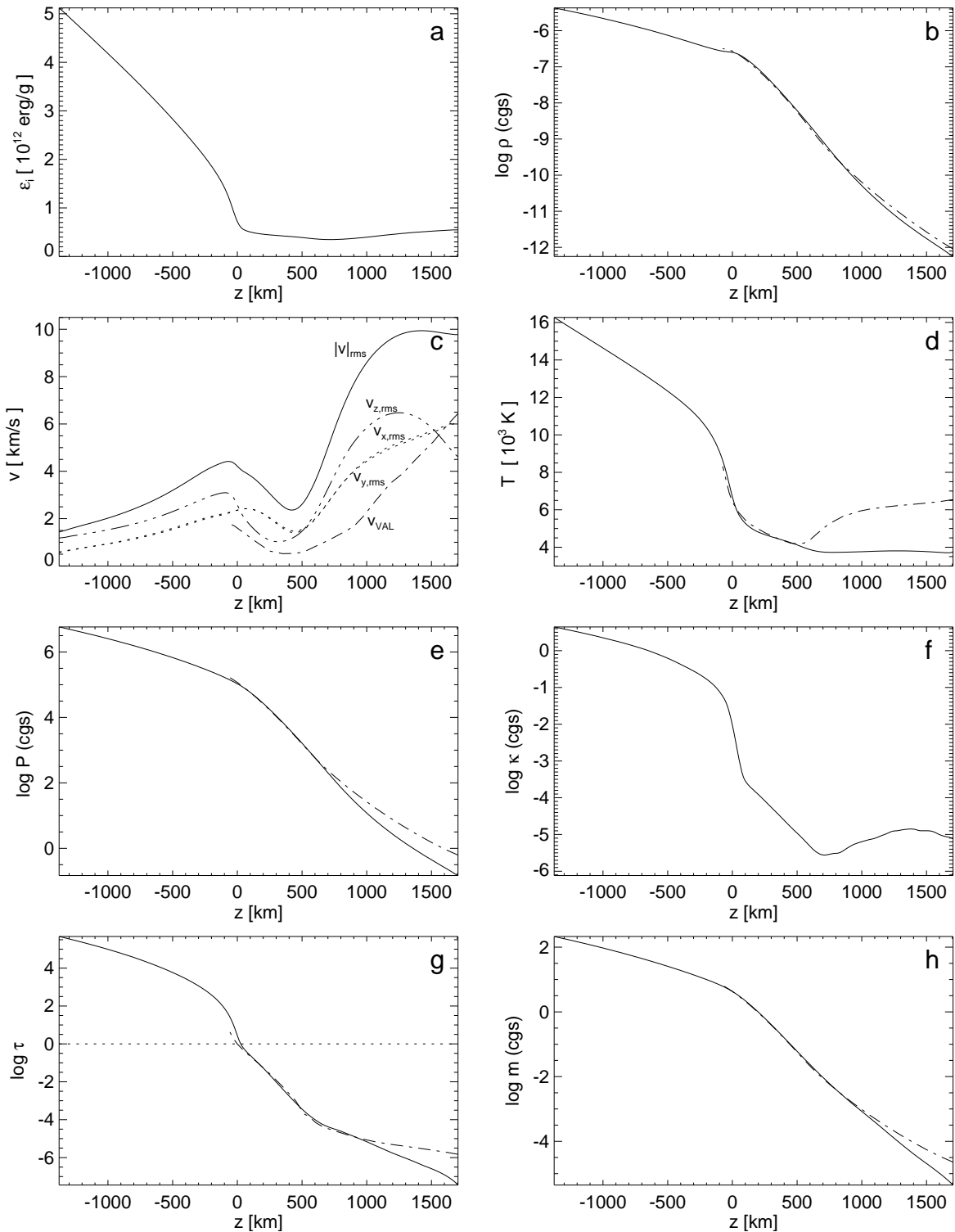


Figure 7.1: Temporally and horizontally averaged stratifications in the 3-D reference model 3DgPO for various quantities: **a)** internal energy, **b)** log. density, **c)** rms-velocities, **d)** temperature, **e)** log. pressure, **f)** log. opacity (grey), **g)** log. optical depth, **h)** log. mass; For some quantities data by Vernazza et al. (1981) (model C) is plotted for comparison (dot-dashed lines) the model. The local maximum of v_z is located at $z \approx -100$ km still below the photosphere and amounts to 3.1 km s^{-1} . Of course, the total velocity shows the same qualitative height variation

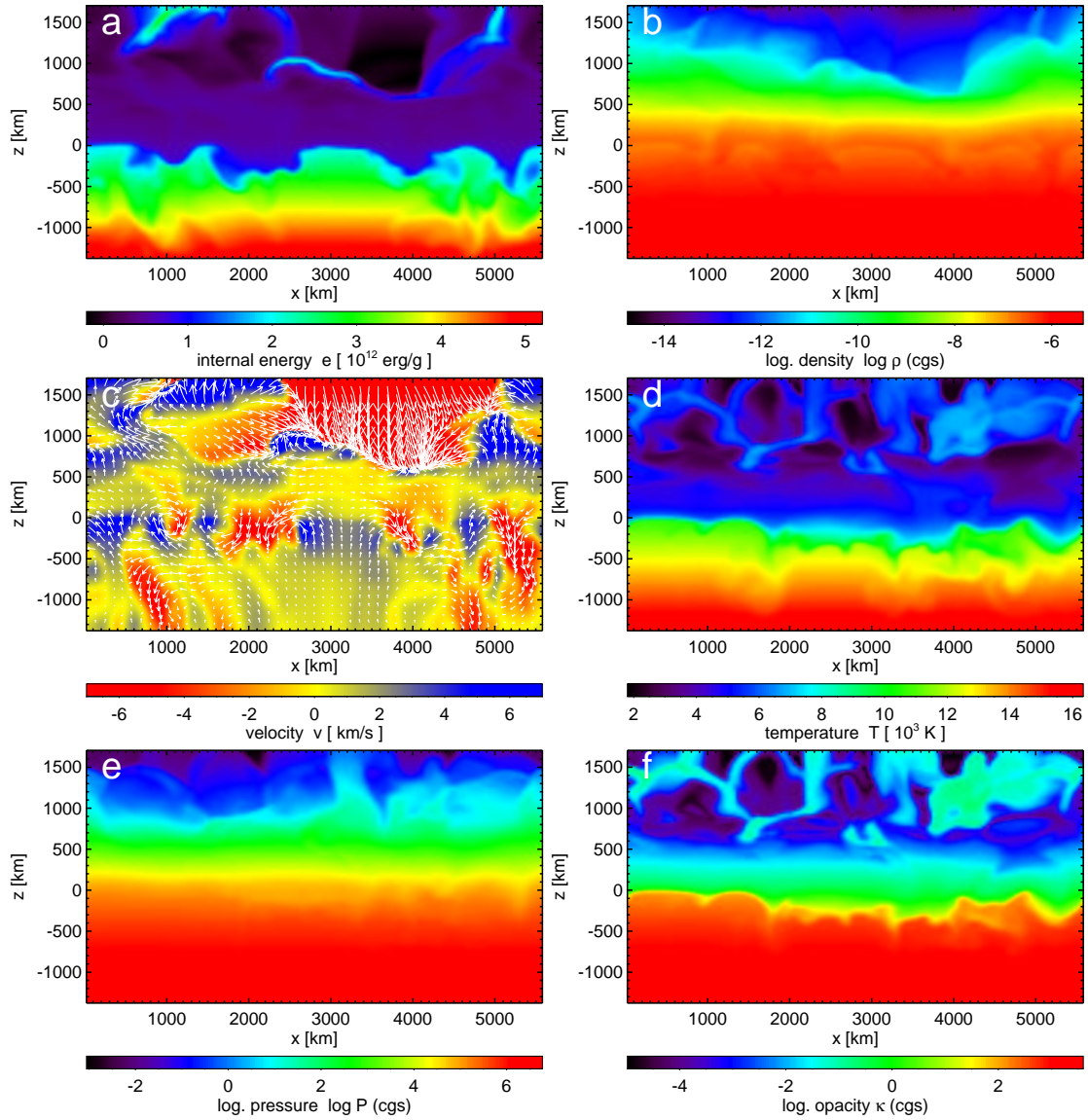


Figure 7.2: Vertical slices taken from the 3-D reference model at an exemplary horizontal position, representing **a)** internal energy, **b)** log. density, **c)** vertical velocity, **d)** temperature, **e)** log. pressure, and **f)** log. grey opacity.

as the individual spatial components, including the existence of a local maximum of 4.4 km s^{-1} at $\approx -70 \text{ km}$ which is related to the vast convective motions. As we shall see later in Sect.7.2, the large chromospheric velocities are caused by fast propagating shock waves.

Another important property of the model atmosphere is expressed by the panels for the grey opacity κ and the optical depth τ . As one approaches from above, the opacity increases by orders of magnitude. The steep gradient at the bottom of the photosphere marks the layers where the matter begins to become opaque ($\tau \gtrsim 1$, see dotted line in Fig. 7.1.g). This steep opacity gradient is caused by the dependence on temperature and pressure (or analogously on the density), as can be seen in Fig. 5.2.

Finally, Fig. 7.1.g shows the average logarithmic mass over height which is needed for comparisons with models which are defined on a mass scale only.

The average stratifications as described above are now compared with model C by Vernazza et al. (1981, see Sect. 3.1 for a detailed description). The variation with height is shown for density, temperature, velocity, pressure, optical depth, and mass as dot-dashed lines in Fig. 7.1. In the case of density (and thus the mass), pressure, and optical depth, the stratifications are in very good agreement for the photosphere and even in the low chromosphere, implying that the basic (average) properties of the lower layers are modelled satisfactorily in the numerical 3-D model. Note that the optical depth is the Rosseland mean τ_{Rossland} (see Sect. 4.4.9) for the three-dimensional numerical model, whereas an optical depth at a reference wavelength of 5000 Å is used by VAL.

However, in the uppermost layers small deviations develop but as already mentioned in Sect. 6.2, these layers are not of particular interest in this thesis. More attention is attracted by the temperature difference in the chromosphere, starting just at the classical temperature minimum. The temperature stratification of the outer solar atmosphere is worthwhile to be addressed separately in Sect. 7.4.2, since it has been the subject of intensive discussions during the last decades.

There is also a difference in the velocities which are of different nature for the compared models. In the semi-empirical model (VAL) a micro-velocity is tabulated whereas the velocities in three-dimensional numerical simulation directly represent the hydrodynamic flow.

7.1.2 Vertical Structure

The outer layers of the solar atmosphere do not only vary strongly with height but also horizontally as can be seen in Fig. 7.2. The figure comprises vertical slices (x, z) for different quantities, taken from a particular time step of the model sequence. The panels a and b show the distribution of the internal energy, and the logarithmic density whereas the vertical velocity component v_z is plotted in panel c. The latter has additional streamlines indicating the velocity field of the vertical plane (v_x and v_y). The remaining panels show the temperature, the logarithmic pressure, and the grey opacity as functions of x and z , respectively. At first glance (in particular in the images for internal energy, temperature and opacity) the model seems to be divided into two major parts:

1. A stratified lower part with small spatial fluctuations and moderate velocities, containing most of the mass.
2. A thin but very dynamic and highly structured upper part, dominated by propagating shock waves.

The boundary between convection zone and photosphere resembles a dividing line which is a consequence of the steep gradients (see also Fig. 7.1). This layer may be interpreted as the solar "surface". It is not plane but shaped by the convective motions, revealing the typical *granulation* pattern, which will be addressed in more detail below. Furthermore, the convective flow can be seen in Fig. 7.2.c, including wider areas of up-flowing material and downflows which are concentrated in narrow channels. There is also a vortex in the lower left corner. As we shall see later, the convection zone is the place where acoustic waves are generated, which finally steepen into shocks in the upper layers of the model atmosphere.

7.1.3 Horizontal Structure

Three-dimensional models even allow to investigate horizontal patterns which change significantly with height. In Fig. 7.3-7.5 horizontal (x, y) slices for the temperature, the logarithmic

density, and the vertical velocity are presented, for heights in the convection zone up to the chromosphere. Additionally, streamlines mark the horizontal velocity field (v_x and v_y) in Fig. 7.5. They trace the hydrodynamic flow for a time interval t_{stream} which is quoted right next to each panel and differs with height due to differences in the velocity amplitudes. The data are all taken from the same time step from the reference model 3DgPO. Thus, the figures show clearly the structural differences of the strata which are described in more detail below:

- The *convection zone* ($z < 0$ km) appears – compared to the upper part of the model – relatively homogeneous, except for narrow regions where the gas is cooler and denser than in the surrounding. The filamentary structures also exhibit large downward directed vertical velocities (see Fig. 7.5.b), indicating concentrated channels of down-flowing cool material. These downdrafts enclose more extended regions of hot up-flowing plasma. Thus, the small narrow channels can be understood as the boundaries of the convection cells.
- At the bottom of the *photosphere* ($0 \text{ km} \leq z \leq 500 \text{ km}$) the convection cells form the granulation pattern, which gives the photosphere its characteristic appearance. As in the convection cells below, hot material is rising in the interior, running into the steep density gradient of convectively stable "surface" layer. There, the matter becomes less opaque so that radiation is able to escape, effectively cooling the gas at the surface. Moreover, the gas expands, resulting in additional cooling and finally lateral flow away from the granule centre. The cool gas begins to sink down again into the convection zone, thus marking the boundary of a granule. Thus, the flow divides into two components: Extended regions of hot rising material, the *granules*, outlined by narrow streets of down-flowing cool gas, the *intergranular lanes* (see in particular Fig. 7.5). The granulation pattern is also shown in Fig. 7.6.
- In the *middle photosphere*, the horizontal velocities are still large compared to the vertical component (see Fig. 7.1.c). Hence, the horizontal pattern changes significantly so that the temperature pattern connected to the granulation is lost only a few hundred kilometres above the bottom of the photosphere. Rather, the pattern of the upper photosphere resembles an *inverted granulation*, i.e., cool gas is located above the granule centres, being hotter at the rims (see Fig. 7.3.d). This known phenomenon is attributed to advection shocks at the granular boundaries. As the gas flows (horizontally) from the granule interior towards the boundaries it encounters the flow from adjacent granules. Consequently, the gas above the intergranular lanes is compressed and heated.
- Further up in the *chromosphere* ($z > 500 \text{ km}$), the pattern even changes more dramatically due to the onset of shock wave formation. As already seen in Fig. 7.2, shock waves are an ubiquitous phenomenon in the model chromosphere. They are present for all time steps, mostly several at the same time. The waves propagate in the vertical as well as in the horizontal directions with large velocity amplitudes (see Fig. 7.1.c and Fig. 7.5.f-h). Consequently, the wave fronts collide with each other, compressing and heating the gas (see Sect. 7.2). The interaction of the waves produces the complicated inhomogeneous and highly dynamical structure of the chromosphere in the three-dimensional model. The structure consists of a *network of hot matter* with small-scale hot spots and enclosed *cool regions*, as shown in the horizontal temperature slices in Fig. 7.3.f-h. The pattern is composed by many propagating shock waves, like the one described in Sect. 7.2.2. The spatial scales are comparable to that of the granulation, as a direct consequence of the correlation between convective motions and the excitation of acoustic waves.

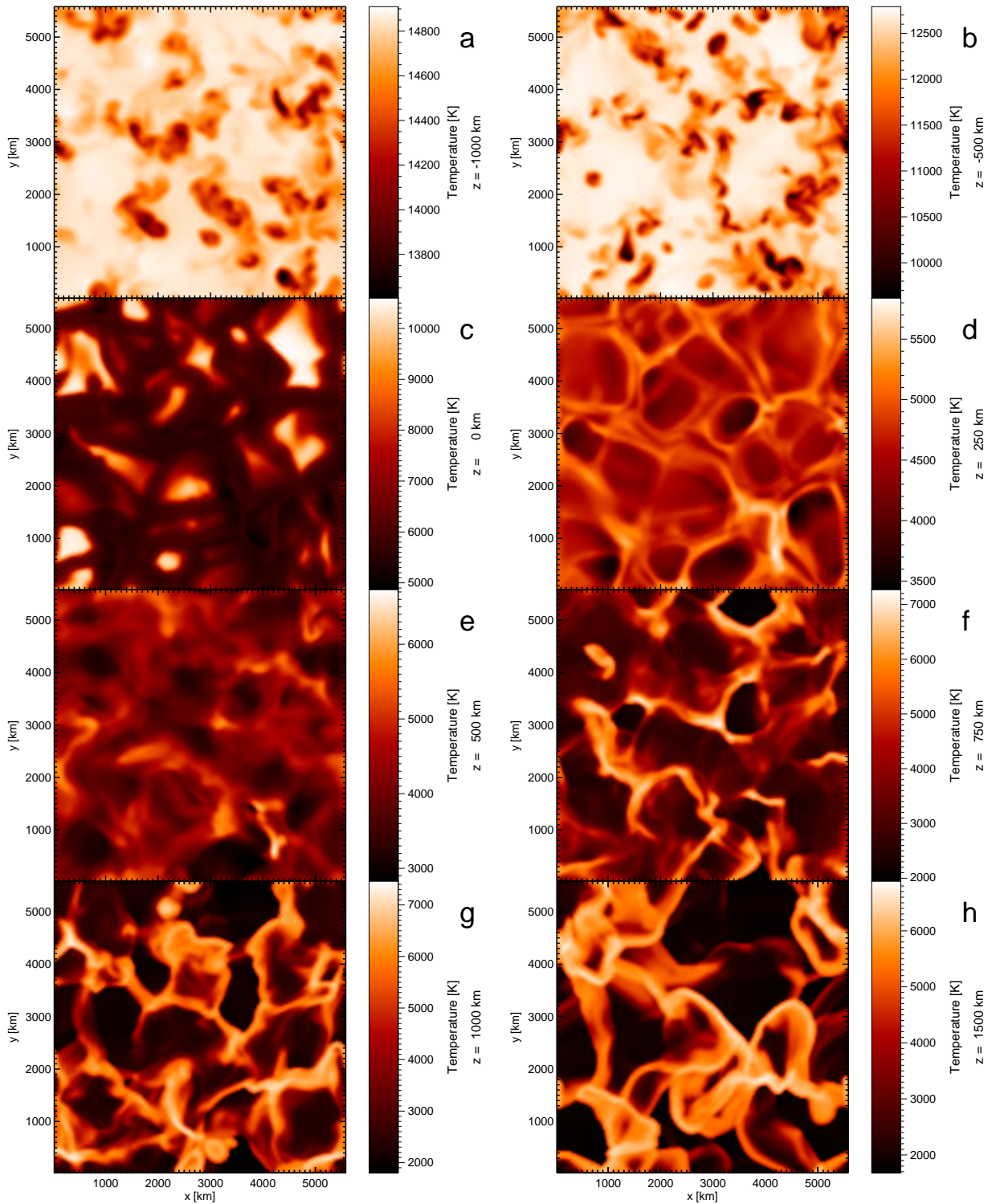


Figure 7.3: Temperature in horizontal slices taken from the 3-D reference model at different heights. **a-b)** convection zone at $z = -1000$ km, and -500 km, **c-e)** photosphere at $z = 0$ km, 250 km, and 500 km, **f-h)** chromosphere at $z = 750$ km, 1000 km, and 1500 km

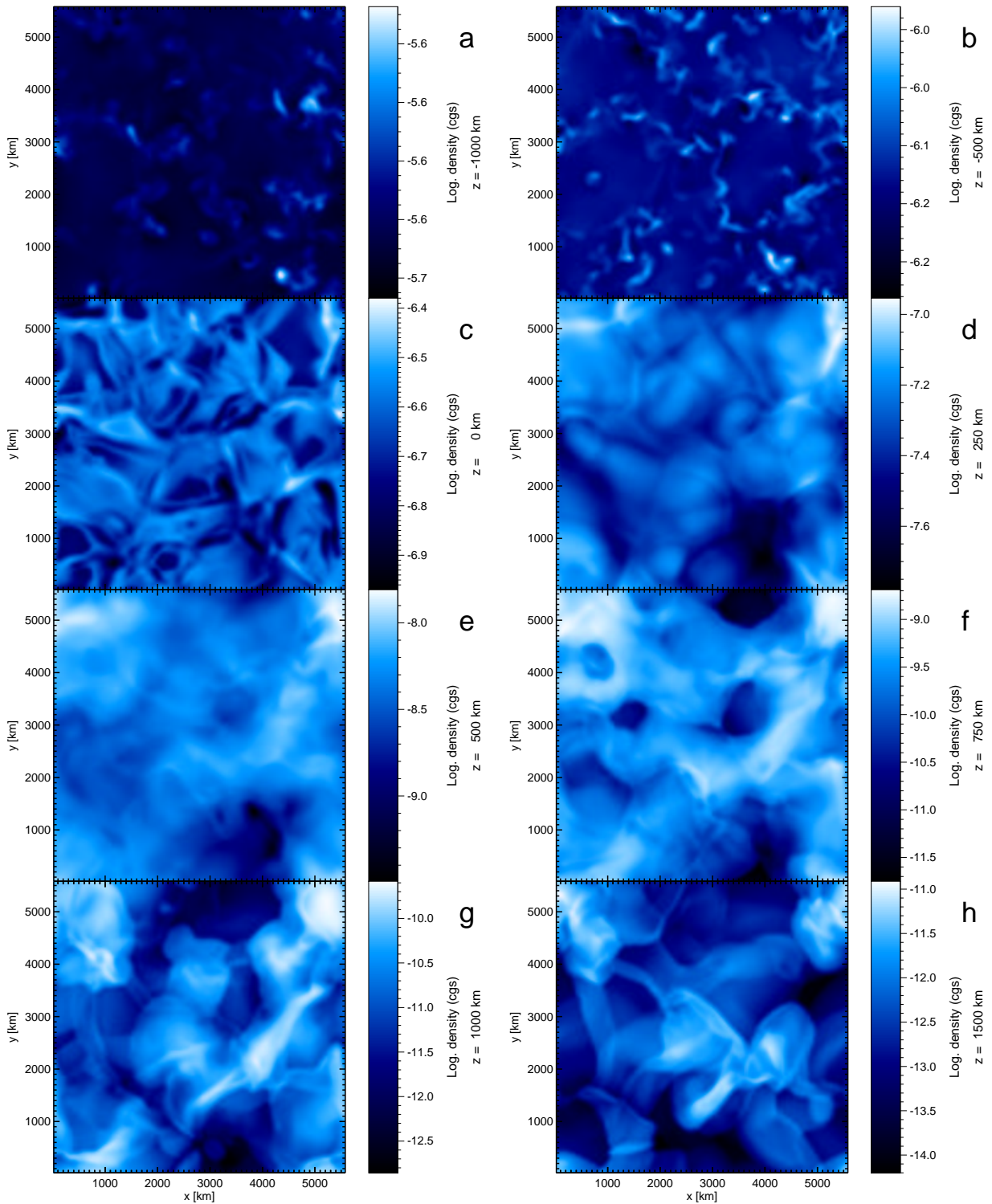


Figure 7.4: Logarithmic density in horizontal slices taken from the 3-D reference model at different heights. **a-b)** convection zone at $z = -1000$ km, and -500 km, **c-e)** photosphere at $z = 0$ km, 250 km, and 500 km, **f-h)** chromosphere at $z = 750$ km, 1000 km, and 1500 km

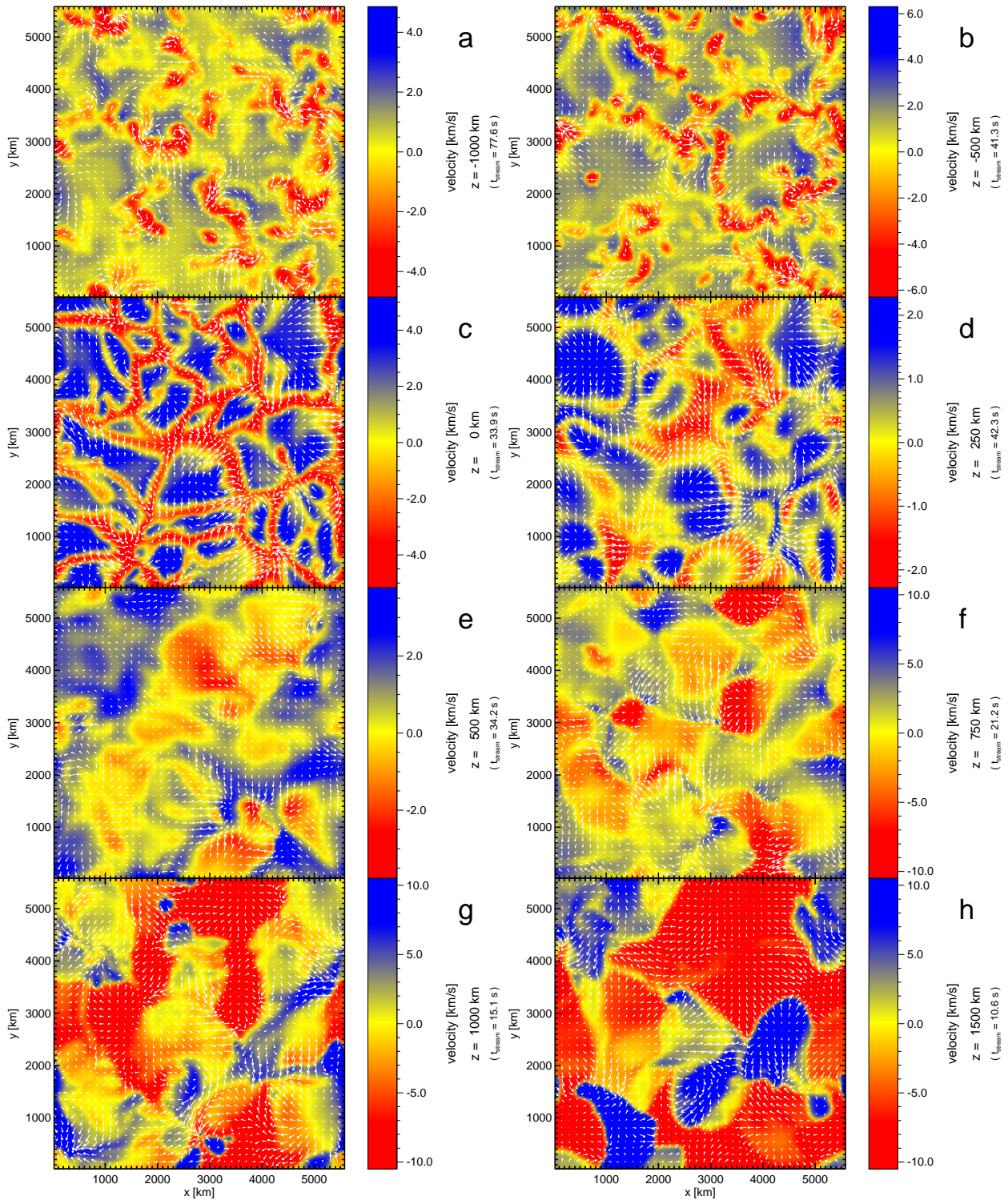


Figure 7.5: Vertical velocity in horizontal slices taken from the 3-D reference model at different heights. **a-b**) convection zone at $z = -1000$ km, and -500 km, **c-e**) photosphere at $z = 0$ km, 250 km, and 500 km, **f-h**) chromosphere at $z = 750$ km, 1000 km, and 1500 km

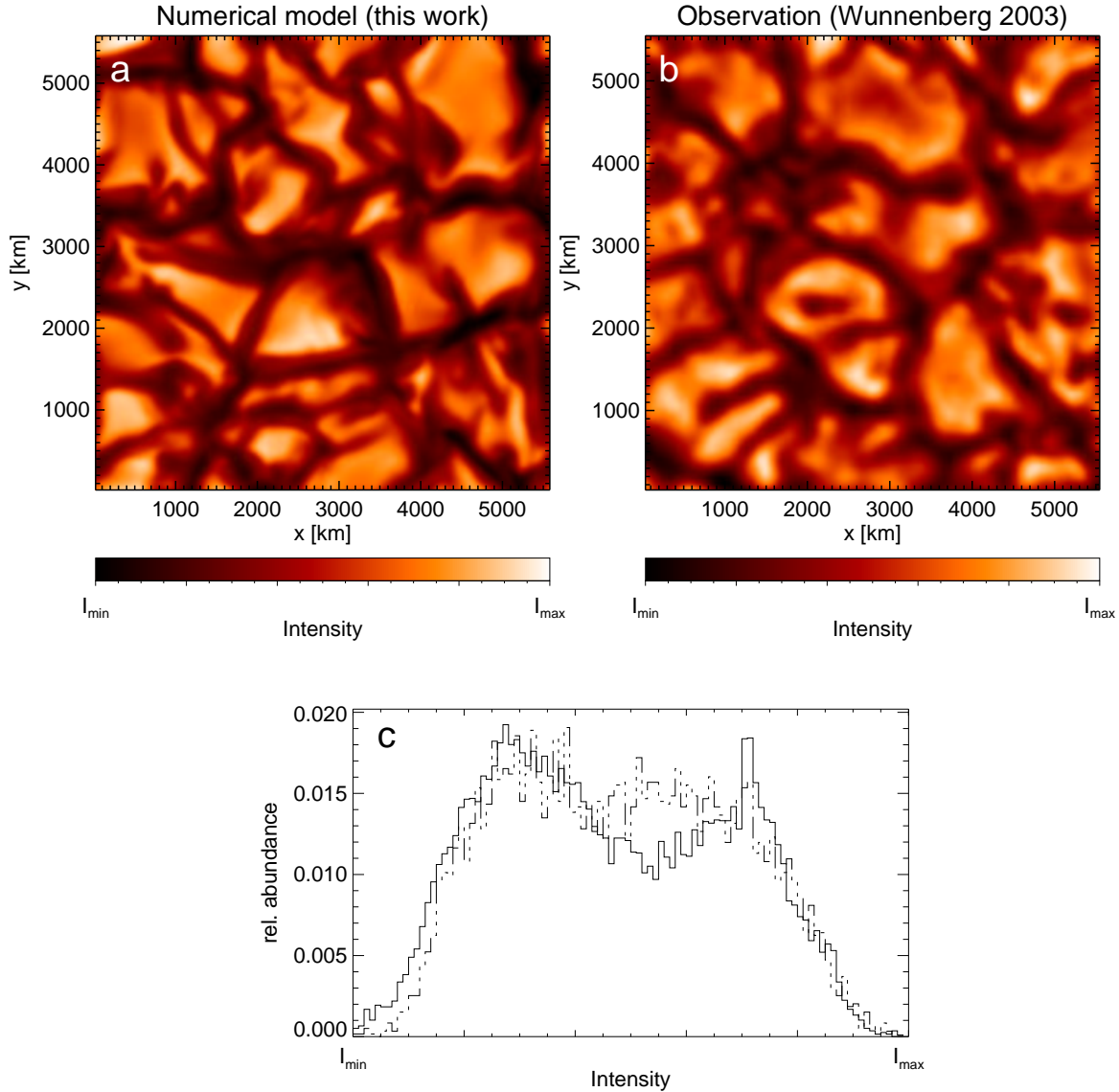


Figure 7.6: Comparison of granulation pattern **a)** Continuum intensity at 5500 \AA from numerical model (3DgPO) **b)** Observed intensity (Wunnenberg 2003) filter centred at 5576 \AA , **c)** Intensity histograms for the numerical model (solid line) and the observation (dashed line). (*The original data were kindly provided by M. Steffen and M. Wunnenberg.*)

7.1.4 Granulation

Based on a snapshot from the 3-D reference model, M. Steffen calculated the continuum intensity at a wavelength of 5500 \AA . In Fig. 7.6 this image is compared with an observed snapshot which was kindly provided by M. Wunnenberg (2003). It was recorded using a filter centred at 5576 \AA . Thus both images show approximately the same spectral range. The observation and the theoretical prediction are remarkably similar with respect to the size of the granules and the intensity contrast (dI_{rms}) which is 21.4% for the numerical model and 20.2% for the observation, respectively. Moreover, the intensity distribution of the numerical model (solid line in Fig. 7.6.c) is very similar to the observed one (dashed line). Thus, this simple comparison illustrates that the modelling of the lower layers is already quite realistic.

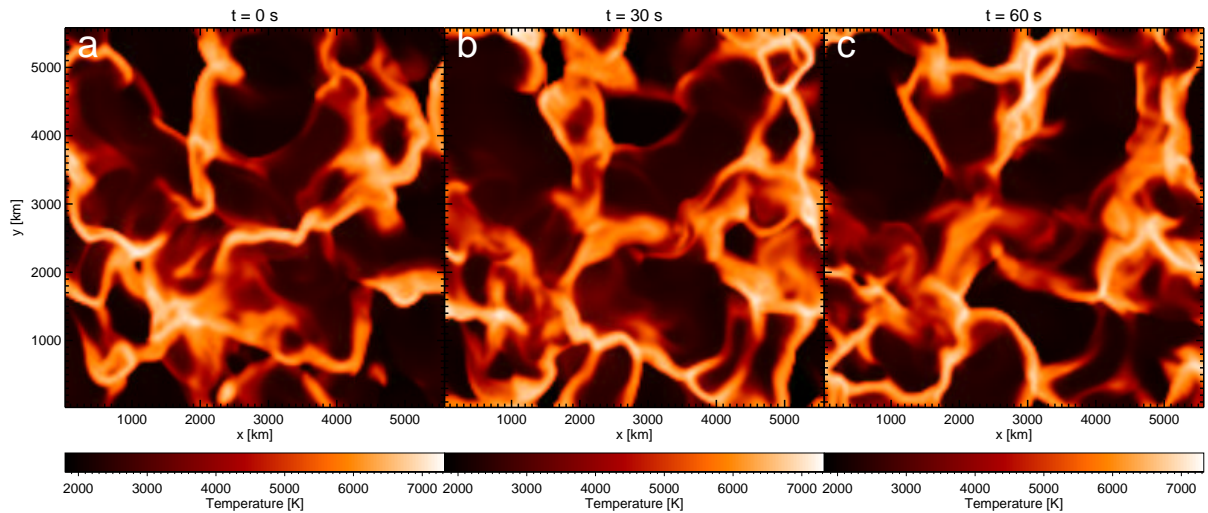


Figure 7.7: A short time sequence of horizontal temperature slices, taken from the 3-D reference model at a geometrical height of $z = 1000$ km with a time increment of $\Delta t = 30$ s.

7.1.5 Chromospheric “Background” Pattern

The chromospheric pattern is not only spatially inhomogeneous but also in time. The short time sequence of horizontal temperature slices in Fig. 7.7 gives an impression of the temporal evolution. *Ring-like structures* (e.g., in the upper right corner of panel b) appear only for a short time before they vanish again. The three images reveal significant differences, though the time step is only 30 s. Due to the large velocities of $\sim 10 \text{ km s}^{-1}$ (see Fig. 7.1.c and Sect. 7.2.3) a wave front passes quickly through a fixed geometrical layer. Hence, one can expect evolution time scales of less than 30 s, which is remarkably short (see Sect. 7.1.8 for a quantitative estimate of the corresponding time scales). However, the general picture remains the same in time, i.e., the chromosphere appears as a *network of hot shocked gas and intermittent cool regions* with temperatures down to ~ 1800 K.

As mentioned in Sect. 2.4, a *chromospheric “background pattern”* is also observed as an ubiquitous phenomenon in internetwork regions. For a qualitative comparison with the three-dimensional hydrodynamical model, a small region was taken from Fig. 2.4 which corresponds to the horizontal extent of the computational box (see Fig. 7.8). The observed pattern consists of *mesh-like structures of enhanced emission and intermittent low-intensity regions* and thus reminds on the chromospheric pattern of the hydrodynamical model which can be seen in Fig. 7.7 and Fig. 7.3. For a quantitative comparison, however, it would be necessary to calculate the intensity which is emitted in the model in the same wavelength range around 3968 \AA and to reduce the spatial resolution until it is comparable to the observations ($\sim 0.2''$). However, already a qualitative comparison just by eye reveals the remarkable similarity with respect to the general topology. In both cases the spatial scales are comparable to the granulation (see Fig. 7.6) but the theoretically predicted temperature distribution exhibits a higher contrast than the observed intensities. This can be explained by the higher horizontal resolution, the fact that the temperature translates in a non-linear way into intensities and the smearing of the observed pattern along the line of sight due to contributions from different heights. Hence, if one smears out the chromospheric temperature pattern presented in Fig. 7.7 horizontally and over a sufficiently large height range, then the observation and the hydrodynamical prediction agree in an excellent way.

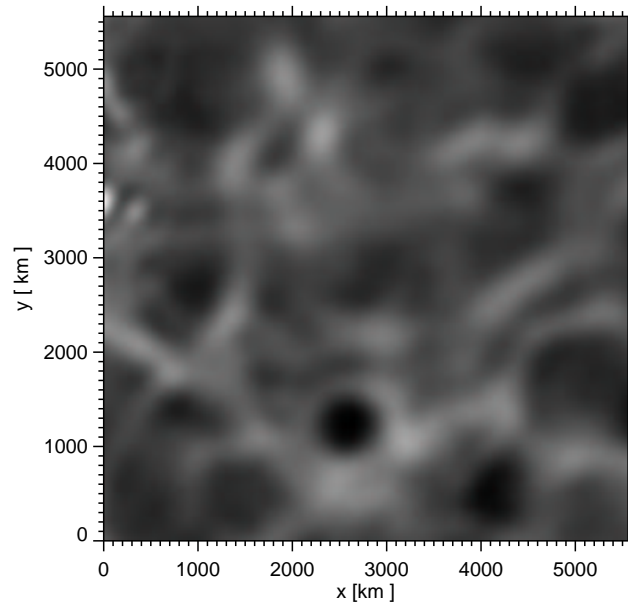


Figure 7.8: “Close-up” of the Ca II H image shown in Fig. 2.4 with the same horizontal extent as the three-dimensional reference model. The chromospheric pattern can be compared with the theoretically predicted temperatures in Fig. 7.7 and 7.3. (*The original data were kindly provided by P. Sütterlin.*)

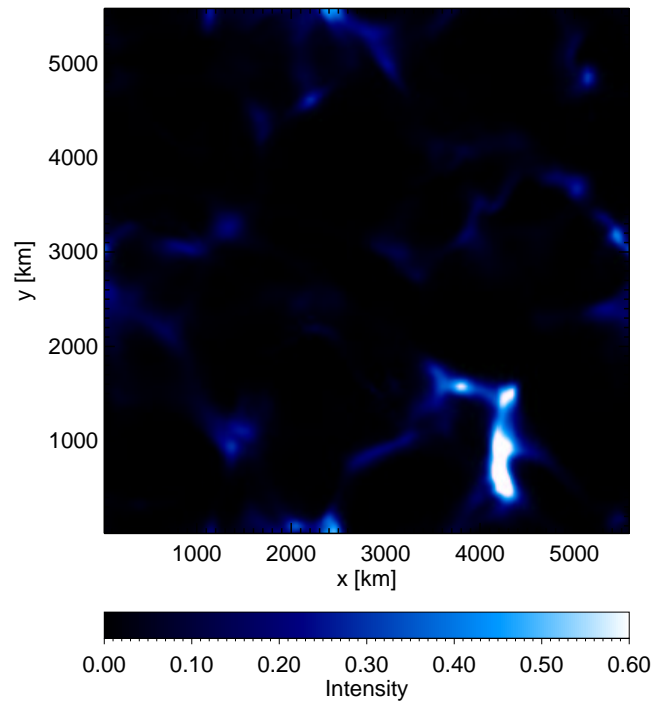


Figure 7.9: Continuum intensity at 1600 \AA calculated based on a snapshot from three-dimensional reference model. Note that all data points with a relative intensity > 0.6 are coloured white. (*The intensity data were kindly provided by M. Steffen.*)

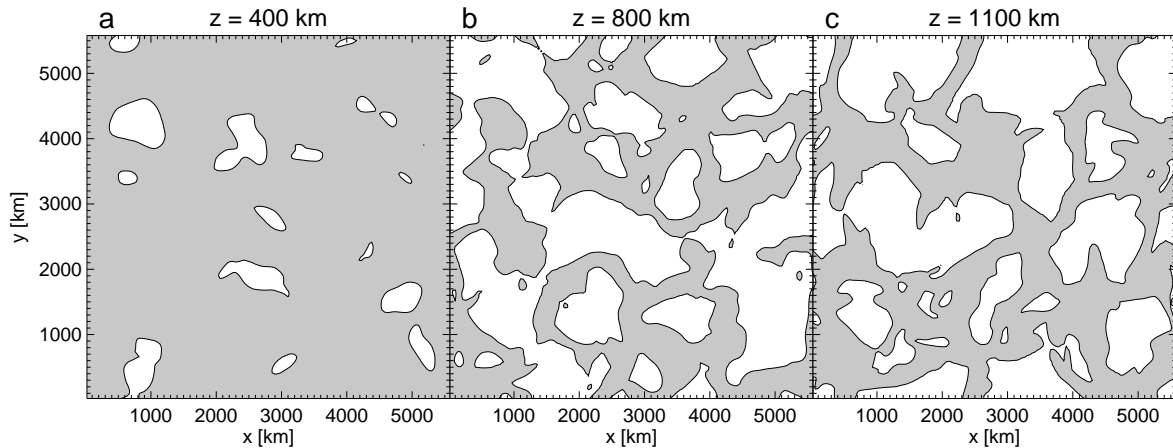


Figure 7.10: Cool regions outlined by temperature contours ($T_{\text{thres}} = 3700 \text{ K}$) in horizontal slices at the geometrical heights $z = 400 \text{ km}$, 800 km , and 1100 km , taken from an exemplary time step of the three-dimensional reference model. The white areas mark the cool regions.

7.1.6 Bright Points

Based on the same snapshot as in Sect. 7.1.4, M. Steffen also calculated the emergent continuum intensity at a wavelength of 1600 \AA in the UV (Fig. 7.9) which looks very different from the intensity at 5500 \AA . The depicted UV intensity originates from higher layers and thus renders the high-temperature structures at chromospheric heights which can be seen in Fig. 7.3. The corresponding source function in the UV depends highly non-linearly on temperature, effectively amplifying the very high temperature/intensity contrast. Consequently, the intensity image is predominated by only a few bright points.

So far only this single intensity image is available so that no further analysis was performed. Thus, it is not clarified yet if the structures seen in Fig. 7.9 can be identified as the bright points which are an ubiquitous phenomenon in observations. Nevertheless, the typical grain size of $\sim 600 \text{ km}$ is in line with the brightening in Fig. 7.9. Also, the distance between adjacent cell points of 1400 km is comparable to the spatial scales of the chromospheric pattern (see Sect. 7.1.3). However, the intensity is clearly connected to the chromospheric structures, which are produced by the interaction of shock waves (see Sect. 7.2). Carlsson & Stein successfully modelled bright points as a cause of propagating shock waves (see Sect. 3.5). Since the dynamics of the three-dimensional model presented in this thesis are similar to the model by CS, one might conclude, that the structures in Fig. 7.9 are indeed the numerical analogue to the observed bright points.

7.1.7 Cool Regions

A striking feature of the three-dimensional model chromosphere is the existence of very cool regions (see, e.g., Fig. 7.3 and Fig. 7.7) with temperatures clearly below the values provided by semi-empirical models like VAL C (see Sect. 3.1). At first glance, the cool areas look like they could be very important for the formation of molecules, e.g., *carbon monoxide*, in the solar chromosphere (see Sect. 7.6). Hence, it is worthwhile to analyse the cool regions in more detail. In this section emphasis is on their temporal and spatial extent.

For the following quantitative analysis, a threshold temperature of $T_{\text{thres}} = 3700 \text{ K}$ is adopted.

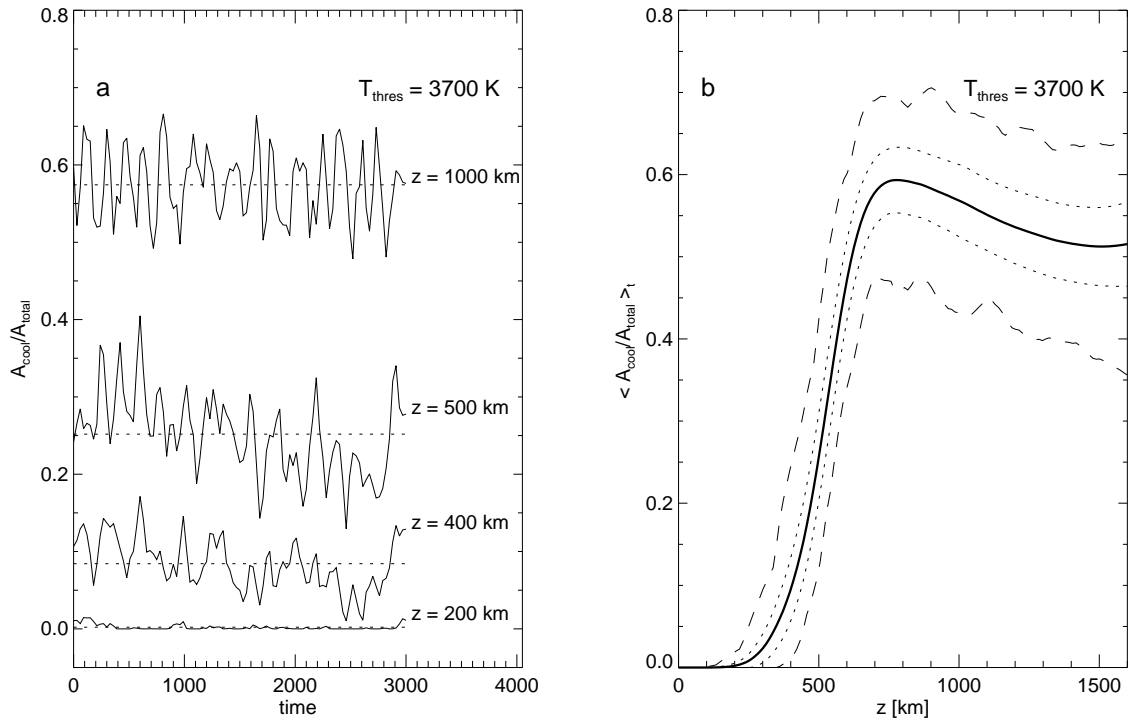


Figure 7.11: Fraction of total cool area with respect to the total horizontal area of the 3-D reference model. The threshold temperature is $T_{\text{thres}} = 3700$ K. **a)** Variation with time at different heights (solid) and time-averages (dotted); **b)** Height-dependent time-average (solid), \pm standard deviation (dotted), and maximum and minimum values (dashed).

Temperatures below this threshold are regarded as "cold". This value has been chosen since (i) it represents a lower limit for the average temperature stratification of the 3-D reference model (see Fig. 7.1.d and also Sect. 7.4.2) and (ii) it has been inferred from observations of the infrared CO fundamental vibration-rotation lines (e.g, Uitenbroek 2000a, see Sect. 2.6).

Following this definition, a cohesive area with a temperature below 3700 K is referred to as a *cool region*. Exemplary cool regions are outlined by contours for the threshold temperature in Fig. 7.10 in horizontal slices at different geometrical heights. Obviously, the number and spatial extent depend on height. While the cool regions are rare and relatively small in the photosphere (Fig. 7.10.a), they totally dominate the appearance of the model chromosphere (Fig. 7.10.b-c). Moreover, instead of well defined regions (like "cool clouds"), open structures are present at chromospheric heights, i.e., the cool regions are connected to adjacent ones. A quantitative determination of the spatial extent and the related area of individual regions is also hampered by structures which continue across the lateral periodic boundaries. In some cases, a cool region connects to itself, resulting in virtually infinite size, which of course allows no meaningful determination of area or diameter. Hence, the spatial extent of individual regions is not easy to express in terms of a simple average diameter. However, except for some rare cases with larger cool areas ($> 2 \times 10^7 \text{ km}^2$), the spatial scales in the chromosphere are roughly comparable to the granulation (see, e.g., Fig. 7.3), i.e., 1000 – 2000 km, associated with an average area of roughly 10^6 km^2 per region.

The fraction of the total cool area is easier to calculate, simply being the number of grid cells in a horizontal plane for a given time step with a temperature below the threshold – with respect

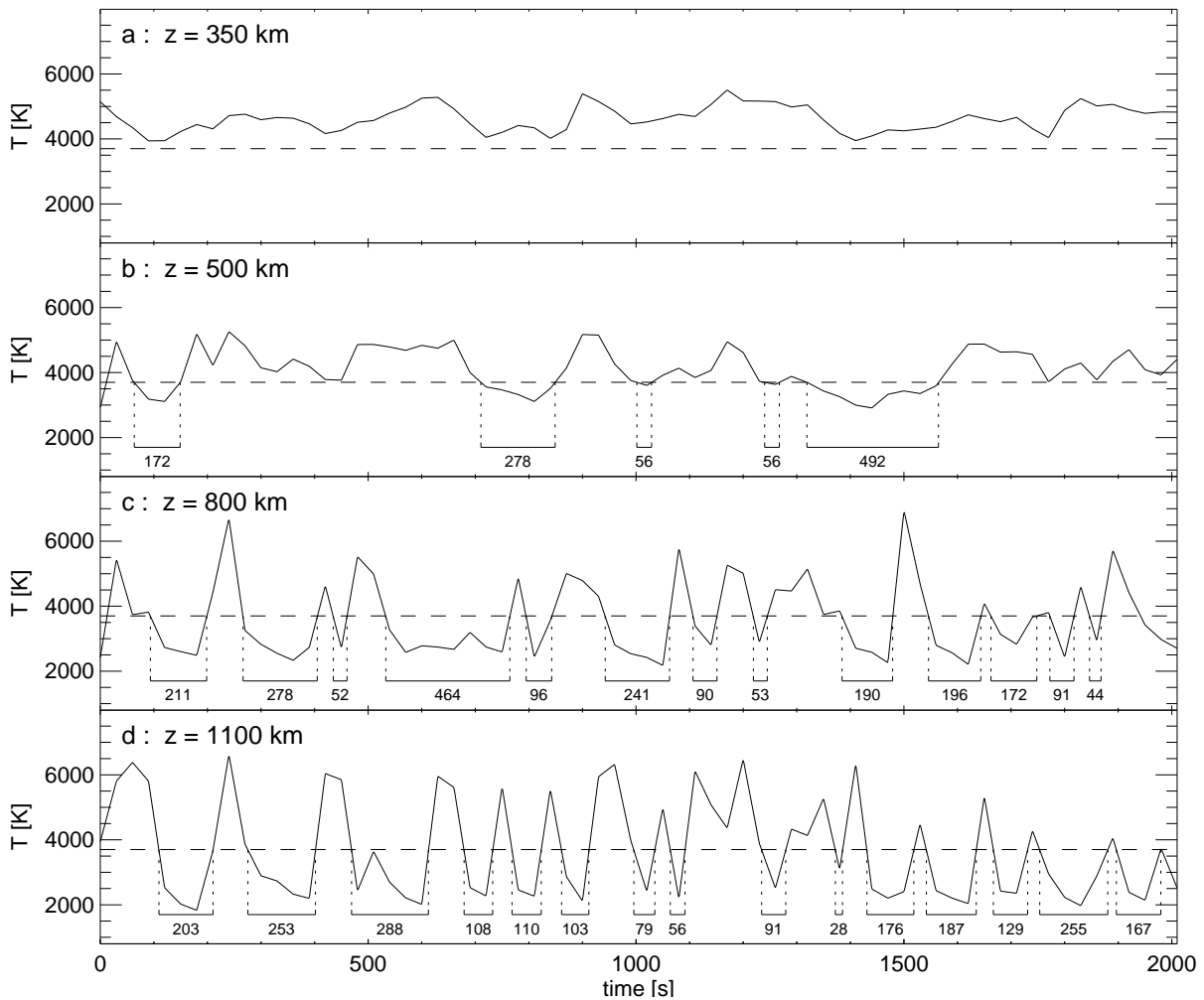


Figure 7.12: Variation of temperature with time for single grid cells at different heights. The cool episodes (time intervals with $T < 3700$ K) are marked with horizontal bars. The duration in seconds is denoted below.

to all grid cells in that slice. The resulting fraction remains relatively constant in time at a particular height (Fig. 7.11.a). Although the pattern changes continuously on short time scales, it obviously shows always the same qualitative picture, e.g., a network of hot matter and enclosed cool regions in the chromosphere. Hence, the cool area fraction depends more on height than on time. The time average, which is shown in Fig. 7.11.b as a function of height, decreases rapidly downwards to the photosphere, owing to the smaller number of cool regions in the lower layers. But in the model chromosphere, on average 50 to 60% of the whole area (at a fixed height) is cool, i.e., the temperature is below 3700 K. This agrees with the findings by Avrett (1995) and Ayres & Rabin (1996) who conclude from their models that the cold component is not only a minor one but could constitute approximately half of the chromosphere or even more. Furthermore, the temperature does not only vary spatially but also in time as shown in Fig. 7.12. Obviously, the model chromosphere exhibits fluctuations of several 1000 K with time (see also Fig. 7.25). Again, this is due to sharp temperature peaks, related to propagating shock waves (see Sect. 7.2), which are present on top of a cool background with temperatures as low as < 2000 K. Now the duration of the cool time intervals with $T < 3700$ K, in the following

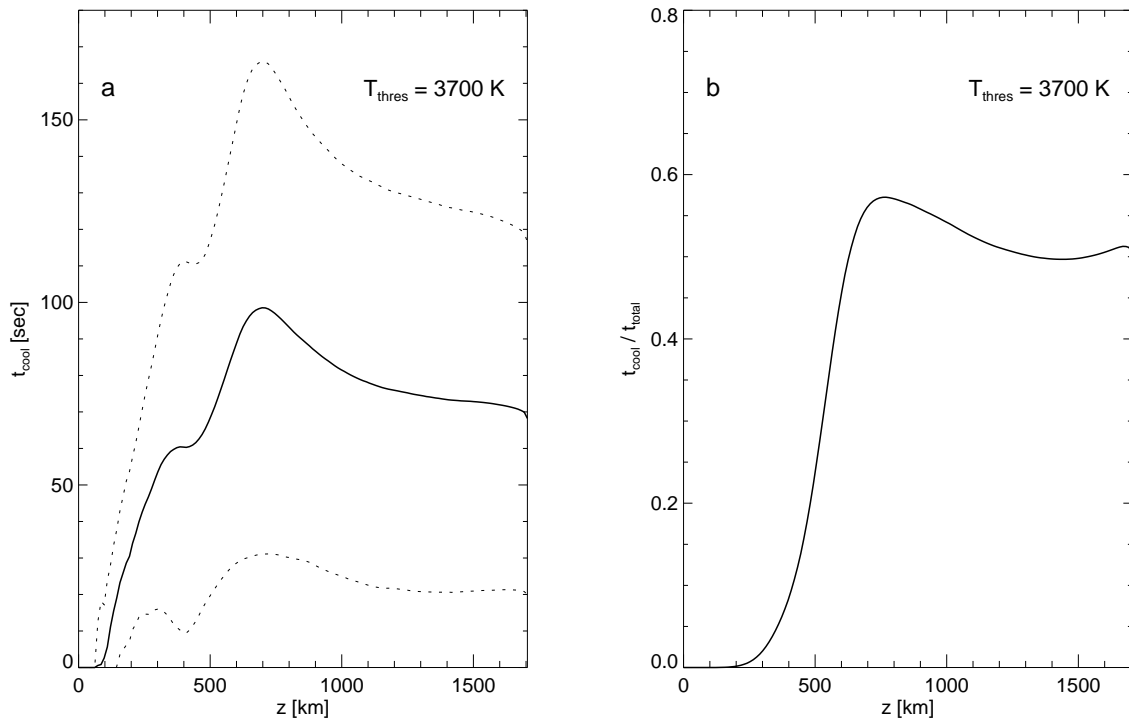


Figure 7.13: Duration of cool episodes in the 3-D reference model for a threshold temperature of $T_{\text{thres}} = 3700$ K. **a)** Absolute values for average (solid) and average plus/minus standard deviation (dotted); **b)** Ratio of cool time to total time.

referred to as *cool episodes*, is investigated. The duration of a cool episode is influenced by the local background temperature and the temperature fluctuations due to the propagating waves. Hence, the height dependence of the temperature distribution (see Sect. 7.1 and also Sect. 7.4) causes the average duration to vary with height. In the chromosphere, the average duration stays more or less constant throughout a wide height range, being 70 – 100 s in the case of the 3-D reference model (Fig. 7.13.a). In some cases the cool episodes are longer than 100 s, even up to extreme values of more than 400 s (see, e.g., Fig. 7.12.b and c). In the photosphere, however, the durations decrease significantly because the average temperature is higher and the fluctuations are smaller than in the layers above. Thus, below $z \sim 100$ km no cool episodes are found.

Not only the duration of single cool episodes but also the sum of all durations is interesting for the chromosphere as a whole. The temperature at a fixed position in the chromosphere of the 3-D model stays half of the time below the threshold of $T_{\text{thres}} = 3700$ K (Fig. 7.13.b), whereas the few cool episodes in the lower photosphere are negligible with regard to the total time. The horizontally and temporally averaged time fraction is identical to the average cool area fraction in Fig. 7.11.d since both represent the height-dependent number of grid cells with temperatures below the threshold value relative to the total number at that height.

In this section it has been demonstrated that *the chromosphere of the three-dimensional reference model is never completely cold and never completely hot*. There are always cool regions next to a hot component, constituting half of the time and the total area. Moreover, the spatial scales are interesting for the interpretation of observations (e.g., carbon monoxide) but on the other hand the time intervals between the passages of hot shock waves are rather short, just 70 – 100 s for

the model chromosphere. Hence, it is not evident how the temporal and spatial scales influence the formation and dissociation of molecules like CO, making detailed calculations necessary (see Sect. 7.6).

Finally, the temporal evolution of the cool regions gives important clues on their nature. Based on the time variation of observed CO intensities (e.g. Uitenbroek et al. 1994), Avrett (1995) concludes that cool regions are not stationary but rather the low-temperature parts of oscillatory waves. This statement is in line with the results of this thesis.

7.1.8 Pattern Evolution Time Scales

In the previous sections it became clear that the chromospheric structures are changing continuously on short time scales (see, e.g., Fig. 7.7). Here, an attempt is presented which aims at a quantitative determination of these time scales. For this, the difference between successive time steps has to be quantified. Mathematically, this can be accomplished by calculating the *autocorrelation function* which is described in more detail in Sect. 4.6. Time series of horizontal temperature slices ($q = T_z(x, y, t)$) like those in Fig. 7.7) are chosen as input. The autocorrelation is then calculated for each geometrical height independently. Exemplary autocorrelation functions are plotted for three geometrical heights over the time lag in Fig. 7.14.a. Starting at a value of one, the profiles decrease since the differences between individual time steps become larger with increasing lag.

The *pattern evolution time scale* is now defined as the time lag for which the autocorrelation $\mathcal{A}_{T,2D}$ has decreased to a value of e^{-1} (for the first time):

$$\mathcal{A}_{T,2D}(t_{\text{pattern}}) = \frac{1}{e} \quad (7.1)$$

The pattern evolution time scale is indicated by arrows for the examples in Fig. 7.14.a. As we will see below, the time scales are much shorter than the duration of the analysed time sequence(s). Hence, the problems related to large time lags (see Sect. 4.6) are of no importance for this investigation. The resulting height-dependent time scale is depicted as thick solid line in Fig. 7.14.b. Since the chromospheric evolution time scale (≈ 20 s) lies below the time resolution of $\Delta t = 30$ s, the procedure has been repeated for the shorter time sequence which is sampled with $\Delta t = 10$ s. This alternative height variation of the pattern evolution time scale (dashed line in Fig. 7.14.b) is very similar to the one for the long model sequence, although the latter comprises a much longer duration. In both cases, the time scale decreases strongly with height from $\approx 100 - 120$ s at the bottom of the photosphere, down to only $\approx 20 - 25$ s in the chromosphere. Since this value is close to the time sampling of the short time sequence (and even below the increment Δt of the long sequence), the chromospheric evolution time scale of ≈ 25 s might only represent an upper limit.

The autocorrelation method has also been applied to the temperature on the optical depth scale, i.e., the temperature on surfaces of equal optical depth ($q = T_\tau(x, y, t)$). Although temperature variations are usually smaller on the optical depth scale compared to the geometrical height scale (see Sect. 7.4.4), the pattern evolution time scales are not much affected above the lower photosphere (see solid dots and dot-dashed line in Fig. 7.14.b). However, at the bottom of the photosphere the time scales differ significantly. There, values of $\gtrsim 200$ s are found for T_τ which are in line with analogous calculations for time sequences of the grey intensity ($q = I(x, y, t)$). The grey intensity at the upper boundary of the model (sampled with $\Delta t = 10$ s) yields to a time scale of 203 s for the long model sequence. Note that the lower photosphere, i.e., the layers near optical depth unity, contributes most to the intensity which thus renders the granulation pattern. There, the temperature distributions on the geometrical height scale and on the optical

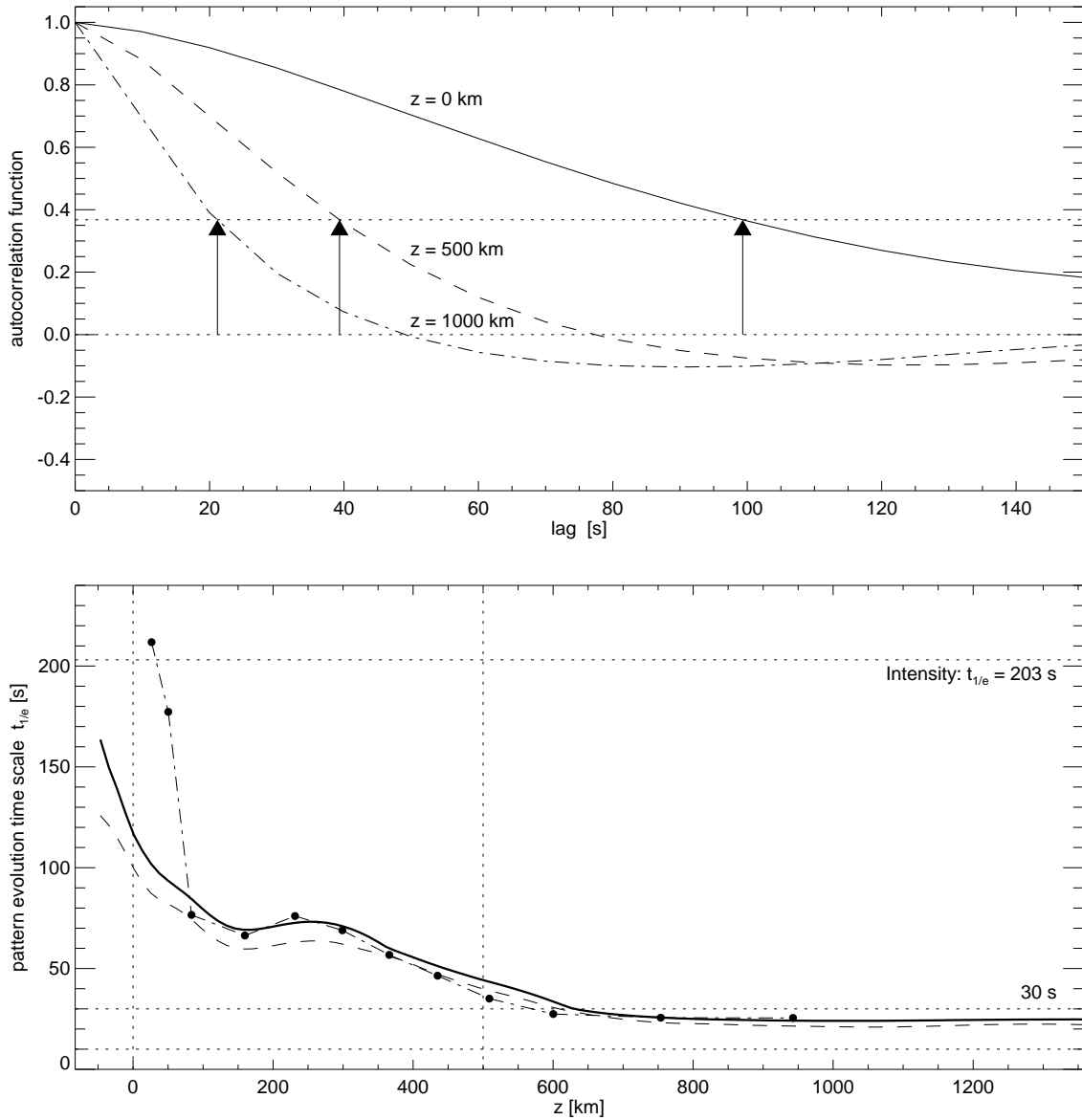


Figure 7.14: Pattern evolution in the 3-D reference model: **a)** Exemplary autocorrelation functions at the geometrical heights $z = 0, 500$, and 1000 km. The arrows mark the time lags for correlation values equal to e^{-1} . **b)** Pattern evolution time scales over height for the time sequence with $\Delta t = 30$ s (thick solid) and the shorter sequence with $\Delta t = 10$ s (dashed). The solid circles (connected with a dot-dashed line) represent the time scales obtained on the optical depth scale, while the upper dotted line marks the time scale derived from an intensity sequence.

depth scale differ significantly, as can be seen from the rms-fluctuations in Fig. 7.25. The temperature on the τ -scale follows surfaces of equal optical depth, which are shaped by the structure of the atmosphere and thus are different from the strictly plane slices $T_z(x, y, t)$. Hence, vertical motions, e.g., due to oscillations, force a structure like a granule to move up and down through the regarded horizontal plane, while the the corresponding τ -plane moves up and down with the matter. Consequently, the reduced fluctuations let a pattern look similar for a longer time, i.e.,

the pattern evolution time scale is prolonged by the smoother appearance on the optical depth scale.

The temperature and intensity distributions are also smoothed due to a coarser spatial resolution. For example, the binning of 4×4 and 6×6 horizontal grid cells of the intensity produces a (granular) time scale of 222 s and 244 s instead of 203 s for the long model sequence, respectively. The resulting horizontal resolution of 160 km and 240 km corresponds to 0.22 and 0.33 arc-seconds for ground-based observations. Clearly, a coarser spatial resolution tends to increase the time scales significantly. Hence, the typical empirical value of $\lesssim 5$ min for the granular pattern evolution can be matched by simply degrading the resolution. This effect should be kept in mind for comparisons with observations. It is also not obvious how the empirical results are influenced by the extended formation heights of spectral lines which cause a smearing along the line of sight. Finally, the finite exposure time of observations and also details like image tracking and data reduction might be points to take care of on the observational side.

Despite the differences in the lower photosphere, general tendencies are revealed. At the very top of the convection zone and also at the bottom of the photosphere time scales around ~ 120 s - ~ 200 s are found, whereas $\lesssim 25$ s are typical for the model chromosphere. This confirms the qualitative impression that the chromospheric structures evolve much faster than the pattern of the layers below, i.e., the granulation. At first, the time scales seem to be too short compared to the empirical estimates but, as described above, the pattern evolution time scale depends of various details, in particular the resolution of the input data. Thus, for a meaningful comparison with observations both data sets, the observational and the numerical, should have comparable properties (resolution etc.) and should be analysed with the same autocorrelation method.

Last but not least it should be mentioned that the pattern evolution time scale in Fig. 7.14.b does not decrease monotonically but exhibits a local maximum in the low photosphere. There is also a local minimum just below, which is present for both time sequences and on the optical depth scale, too. The height of the local minimum roughly coincides with the local maximum of the horizontal rms-velocity components (see Fig. 7.1.c). Hence, the local time scale minimum might be caused by the strong horizontal granular flows in that height range which change the pattern more quickly. The flow becomes weaker above, leading to a (small) increase of the evolution time scale in the middle photosphere, but only until the growing velocity amplitudes due to propagating acoustic waves reduce the time scales to the final chromospheric value.

7.1.9 Upshot

This short overview of the structure of the model atmosphere implies that the widely used one-dimensional, static models cannot provide a proper description of the non-magnetic solar chromosphere. This is in particular true for the dynamics and the spatial fluctuations but also for some average properties like the temperature stratification. The bimodal temperature distribution of the chromosphere, owing to the co-existence of hot and cool regions, has severe consequences, as will be shown in Sect. 7.4, but also provides interesting implications for the interpretation of observations.

7.2 Waves and Shocks

As already quoted in Sect. 7.1, waves are an ubiquitous phenomenon in the upper layers of the three-dimensional reference model, giving it the typical highly structured and dynamic appearance.

7.2.1 Excitation, Propagation, and Shock Formation

The excitation and propagation of acoustic waves in the solar atmosphere is a complex topic by itself and has been subject of many investigations since it became addressable with numerical simulations (e.g. Skartlien et al. 2000; Nordlund & Stein 2001; Stein & Nordlund 2001, and many more). From observations and theoretical models it has been inferred that acoustic waves are excited mostly at the uppermost layers of the solar convective zone. This is also the case for the presented numerical 3-D model, as a simple consideration shows: Following *Lighthill's* theory (see Sect. 2.7.2), the generation of acoustic flux is proportional to a high power of the flow velocity. Hence, the maximum contribution to the acoustic flux is governed by the maximum flow velocity in the convection zone which is found at ≈ -70 km (see Sect. 7.1.1) in the numerical model. This finding is in line with common assumptions (e.g., $z \approx -100$ km quoted by Musielak et al. 1994, see Fig. 3 and 7 therein).

In principle, one has to distinguish between standing and propagation waves. While the interaction of convection with resonant modes leads to the excitation of standing waves, like the most prominent 5 min oscillations (see Sect. 2.3, Sect. 7.3, and also Nordlund & Stein 2001), strong localised pressure perturbations generate propagating acoustic waves.

A localised wave source is, for example, connected to the *merging of downdrafts*, as shown in the left-most column of Fig. 7.15. In the vertical temperature slice in the lower left corner, two downdrafts are outlined by temperature contours. As one goes to the succeeding panels above (following the time axis indicated by the arrow at the left side), the downdrafts move horizontally towards each other until they finally merge. The resulting new downdraft is much larger in the beginning, shrinking to a normal size afterwards (compared to the original downdrafts). After only a short time, the history of the structure is not obvious anymore. Seen from above (in the three-dimensional case), this kind of event corresponds to the collapse of a small granule which shrinks until it disappears in a larger intergranular lane. The latter is the three-dimensional analogue to the downdrafts described above. This mechanism (and also its consequences) has already been investigated in detail in three-dimensional radiation hydrodynamic simulations by Skartlien et al. (2000).

Most interesting, however, is the excitation of acoustic wave trains right above the merging area. As can be seen in Fig. 7.15.a, several pulses of waves are excited which then propagate upwards and form impressive shock fronts at chromospheric heights. On their way up they encounter other waves and inhomogeneities, which are the remnants of earlier wave trains and their interactions. Moreover, smaller temperature enhancements are found just above the downdrafts in the photosphere. These structures are formed by the turn-over of horizontally flowing material into the downdraft, resulting in brightenings at the rim of granules. In Sect. 7.1.3, this pattern was described as inverted granulation.

However, the merging of downdrafts accounts only for a minor contribution to the excitation of acoustic waves. Skartlien et al. (2000) state that these events occur relatively rarely, only one every nine minutes in a computational domain of roughly the same size. More waves are excited as response to the convective motions in general, including localised sources. Such sources are not necessarily connected with downdrafts at the surface. There are also localised pressure perturbations which propagate through the upper convection zone. In some cases the perturbations move nearly horizontally just below the photosphere and thus excite series of waves at different horizontal positions.

Next to different excitation mechanisms, there are differences in the shape of the resulting wave fronts, too. Two extreme cases are shown in Fig. 7.15: A *spherical wave* (middle column) and a *plane wave* (right-most column). The spherical, or arch-like, shock front has been triggered by rather localised pressure waves emerging from the downflow region visible in the deeper layers.

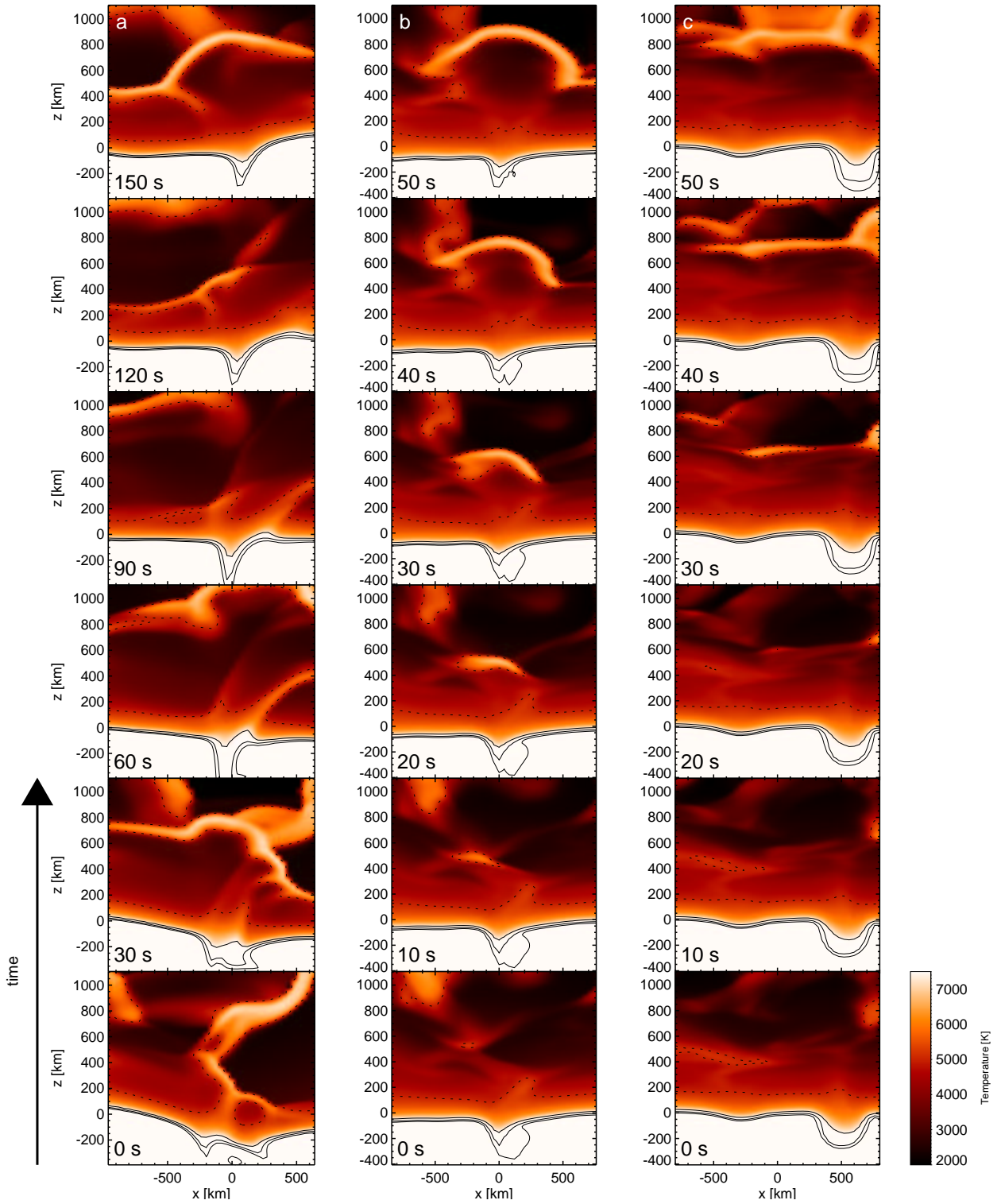


Figure 7.15: Formation and propagation of shock fronts: Each column shows a time sequence of vertical slices (temperature) taken from different positions and times of the 3-D model. **a)** (left column) merging downdrafts, **b)** (middle column) arch-like/spherical wave, **c)** (right column) plane wave. Note the different time steps which are quoted in the lower left corners.

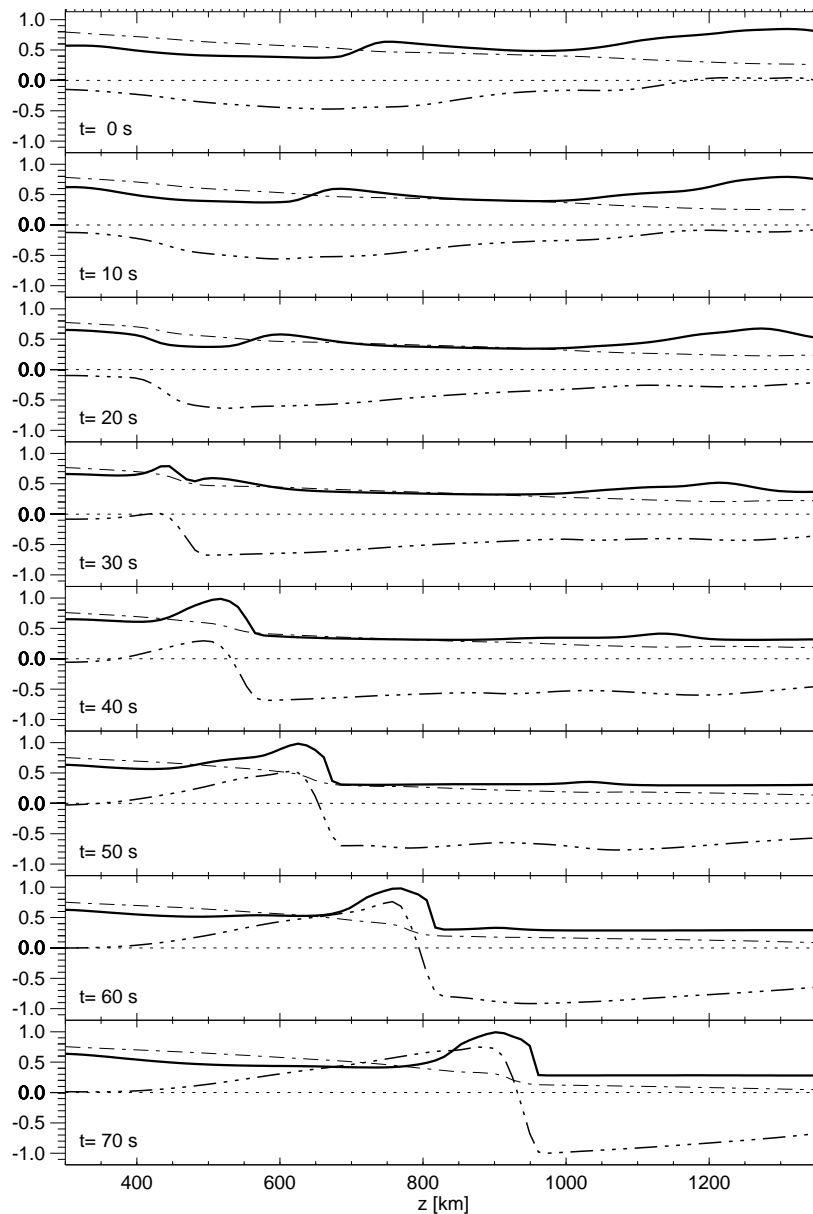


Figure 7.16: Vertical profiles for the propagating wave shown in Fig. 7.15.b at different times near the horizontal centre of the front. The temperature (solid), the vertical velocity component (triple-dot-dashed), and the logarithmic density (dot-dashed) are plotted on a linear scale. The data range 0 to 1 corresponds to 0 K to 7000 K in temperature, -13 to -6 (cgs units) in the logarithmic density, and 0 km s^{-1} to 15 km s^{-1} in the vertical velocity component. The vertical grid is shown at the top of the figure.

Plane waves, like the one in Fig. 7.15.c, can reach large horizontal extents, sometimes over more than the width of the underlying granule(s). Moreover, the wave front seems to preserve the shape of the granular pattern for some time while running upwards. The described effect can be interpreted as a situation where a high amplitude oscillation maintaining a large horizontal coherence (having a large horizontal wavelength) hits the deeper photospheric regions.

Note that the examples shown in Fig. 7.15 have been chosen for their clear and relatively undis-

turbed structure. Usually, interference with neighbouring waves and other inhomogeneities produce a much more complicated picture. Shock waves do not simply pass through each other but show the results of refraction and reflection. In some cases (in the 3-D model) it has been observed that waves change their propagation direction significantly due to strong interactions, including the separation of wave front parts, propagating down again towards the solar surface. Here, the propagation of a acoustic wave is described in more detail for the clear example in Fig. 7.15.b (the spherical wave). A time sequence of one-dimensional height profiles for temperature, vertical velocity, and logarithmic density is shown in Fig. 7.16. The horizontal position of the profiles lies near the centre of the wave front (see Fig. 7.15.b). The initial wave already shows up as a small enhancement of the temperature and the vertical velocity at $t = 30$ s, while the associated density deviation is not noticeable below the chromosphere. As the wave propagates upwards, down the steep density gradient, it accelerates. The amplitudes grow and the initially small perturbation steepens into a shock wave, exhibiting the typical large gradients (see Sect. 4.2.4). Note that the profiles appear smoothed due to the finite vertical resolution of $\Delta z = 12$ km in the upper layers (see Sect. 7.2.4). However, the shock formation takes place in the low chromosphere, like it is the case for most of the waves in the simulation.

Another interesting point can be learned from Fig. 7.16, namely the presence of very high negative vertical velocities (all below the dotted horizontal line). Downward directed velocities can also be seen in the vertical cross-section in Fig. 7.2.c. Apparently, waves often run into low-density material which is flowing down from above at high velocities, exceeding the local sound speed. Hence, the down-flowing material is close to free-fall conditions in those extreme cases. As becomes clear from the analysis of precedent time steps, the material has been pushed upwards by precursory waves and now falls back again. This effect leads to increased velocity gradients as visible in Fig. 7.16. A similar picture has been found in the one-dimensional numerical simulations by Carlsson & Stein (1997, see Fig. 14 therein, and also Sect. 3.5 for a description of their model). Note that there is also observational evidence for downward directed velocities (see Sect. 2.4). It is not obvious how the large gradients influence the shock formation, so that detailed investigations will be necessary in the future.

Finally, the vertical profiles allow a rough estimate of the occurrence of shock waves. Typically, one or two wave fronts are present in a column at a given time in the three-dimensional reference model. This result is in line with the simulation by Carlsson & Stein (1997, see Fig. 14 therein) and thus very reassuring, since the waves in the model by Carlsson & Stein are excited by a piston with a semi-empirical velocity pattern (see Sect.3.5). This implies that the shock frequency in the model presented in this thesis is not unrealistic, although it is a natural outcome without particular assumptions on the velocity distribution.

7.2.2 Three-Dimensional Structure

Among many advantages, three-dimensional models enable the visualisation of structures in all spatial dimensions. Here, the wave, which is shown in Fig. 7.16 in one dimension and in Fig. 7.15.b in two dimensions, is used to illustrate the multi-dimensional structure of propagating shock waves. Note that it is an extraordinary example which exhibits velocity amplitudes above the average (see Sect. 7.2.3). Mostly, individual wave fronts cannot be prepared (and isolated) so clearly like it is case for the more extreme example presented in this section. Nevertheless, it renders possible the investigation of the three-dimensional structure of an individual propagating shock wave in the otherwise entangled model chromosphere.

In Fig. 7.17 horizontal slices for temperature, vertical velocity component, and logarithmic density are shown, next to additional vertical slices and a three-dimensional iso-surface. The temperature on the surface is 6500 K. The vertical slices reveal the spherical character of the

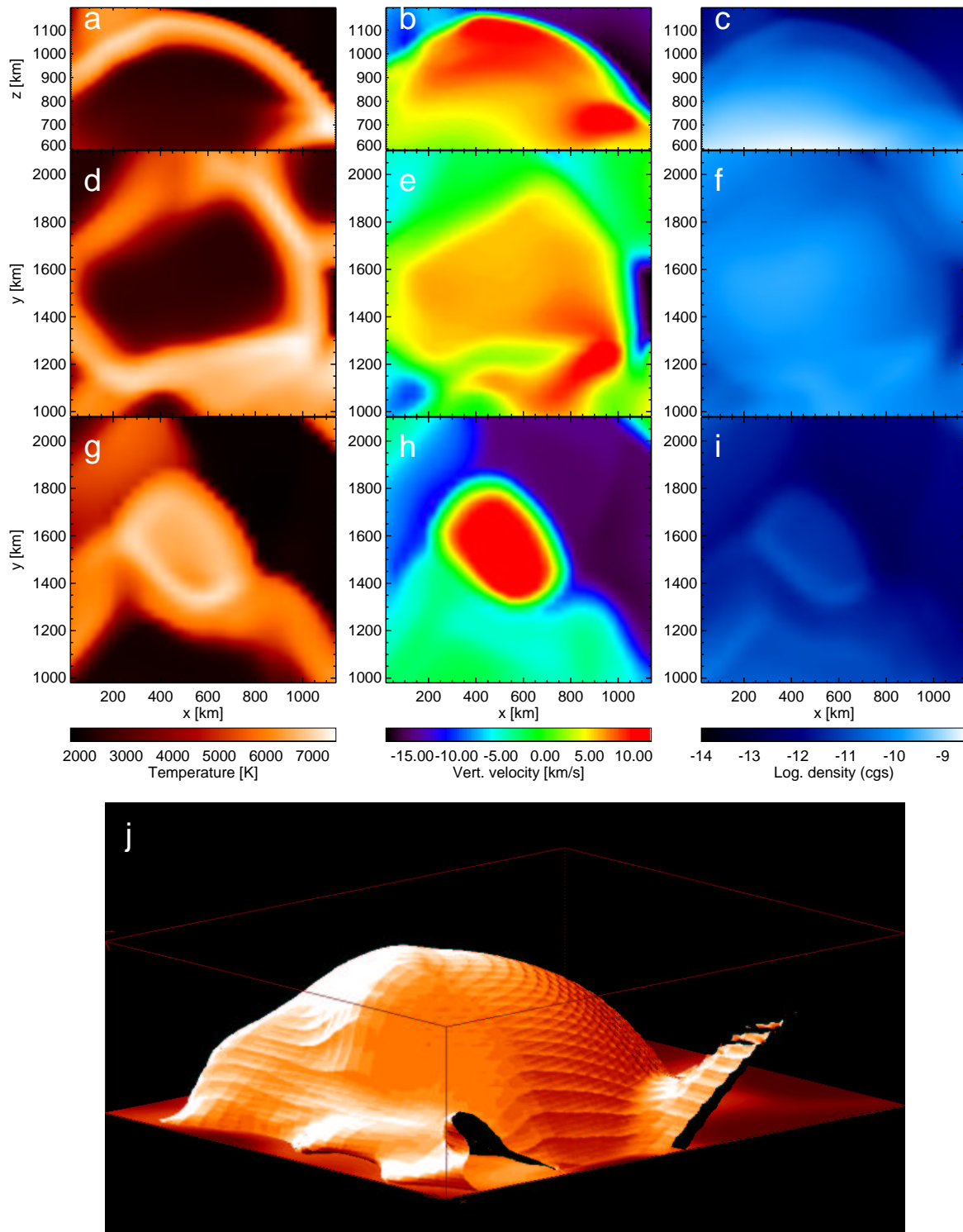


Figure 7.17: Exemplary shock wave: vertical cross-sections for temperature (a), vertical velocity (b), and logarithmic density (c); the same for horizontal cross-sections near the base of the wave (d-f) and near the top (g-i). Panel j) shows a 3-D iso-surface for a temperature of 6500 K.

wave front, as already seen in Fig. 7.15.b. But it is close to spherical geometry in the horizontal plane, too. The slices at different relative heights of the wave show a hot spot at the top which becomes a high-temperature ring of increasing diameter towards the bottom. This pattern gives the chromosphere its typical appearance as a network of hot matter with small hot spots in horizontal slices (Fig. 7.3.f-h, Fig. 7.7).

The high-temperature portion of the wave is concentrated in a thin expanding shell (see also Fig. 7.17.j), whereas high upward directed velocities are found over a larger area, filling the interior of the wave front. The same structure, though more subtle, is present in the density plots.

Material, which is flowing onto the wave front from above, can be seen in the upper right corner of Fig. 7.17.b, black and blue colours). As already stated in Sect. 7.2.1, this material is likely to influence the properties of the shock waves but the details have to be worked further before detailed conclusion can be drawn. Also, the extended region of high upward directed velocities in the interior is very interesting since this rapid flow might be connected to strong adiabatic expansion and thus to an effective dynamic cooling. It is thus likely responsible for the very cool temperatures in the chromosphere of the numerical model.

7.2.3 Velocity Distribution

In the previous sections we took note of the high velocities which are exhibited by the shock wave in the model chromosphere. Here, a quantitative analysis is presented, which focus on the height-dependent distribution of horizontal and vertical velocities.

Histograms have been calculated for each horizontal plane in the three-dimensional reference model for the whole time sequence of 151 min duration. The resulting height-dependent histogram surfaces are plotted in the upper panels of Fig. 7.18 for the horizontal velocity ($v_{\text{hor}} = (v_x^2 + v_y^2)^{1/2}$, left) and the upward directed vertical velocity ($v_{z,\text{up}}$, right). Here, negative vertical velocities are excluded, since the emphasis in this section is on upward propagating shock waves. The vertical axes of the histogram surfaces stand for the relative abundance, i.e., the number of velocities in a bin of $\Delta v = 0.1 \text{ km s}^{-1}$ with respect to all values at that height. Thus, the histograms are normalised to one for each height independently.

The surfaces reveal the interesting height variation of the velocity components. For the deep layers, i.e., in the convection zone, a narrow ridge with high relative abundances is present. It indicates that the velocities are distributed close to a mean value with only small deviations. The distribution differs from this picture around the bottom of the photosphere ($z \approx 0 \text{ km}$), where a protrusion of the histogram surface indicates the existence of a wider range of velocities. This would also be apparent from the height variation of the standard deviation. The distribution at these heights is connected to the changes in the flow pattern at the solar "surface", as already qualitatively described in Sect. 7.1.3. In the upper photosphere, the distribution is again concentrated more closely to a small average value. Both, the horizontal as well as the vertical velocity, exhibit the same qualitative picture. Finally, the dynamics induced by the shock waves change the picture completely at chromospheric heights. There, a very broad spectrum of velocities is present, from very small values to extreme values as high as $\gtrsim 20 \text{ km s}^{-1}$. The height variation is also shown for exemplary geometrical heights in Fig. 7.18.c-d, revealing the nearly *Maxwellian* distribution of the horizontal velocity.

Moreover, percentiles (percentage levels) are presented in the panels e and f. The percentile for a percentage of 50 %, for example, is given by the velocity which is just greater than 50 % of all values. Thus, it marks the upper limit for half of all existing velocities. Percentiles are plotted over height for various percentages from 50 % up to 99 %. At the bottom of the chromosphere ($z = 500 \text{ km}$), 50 % of all horizontal velocities are less than 1.6 km s^{-1} , 95 % stay

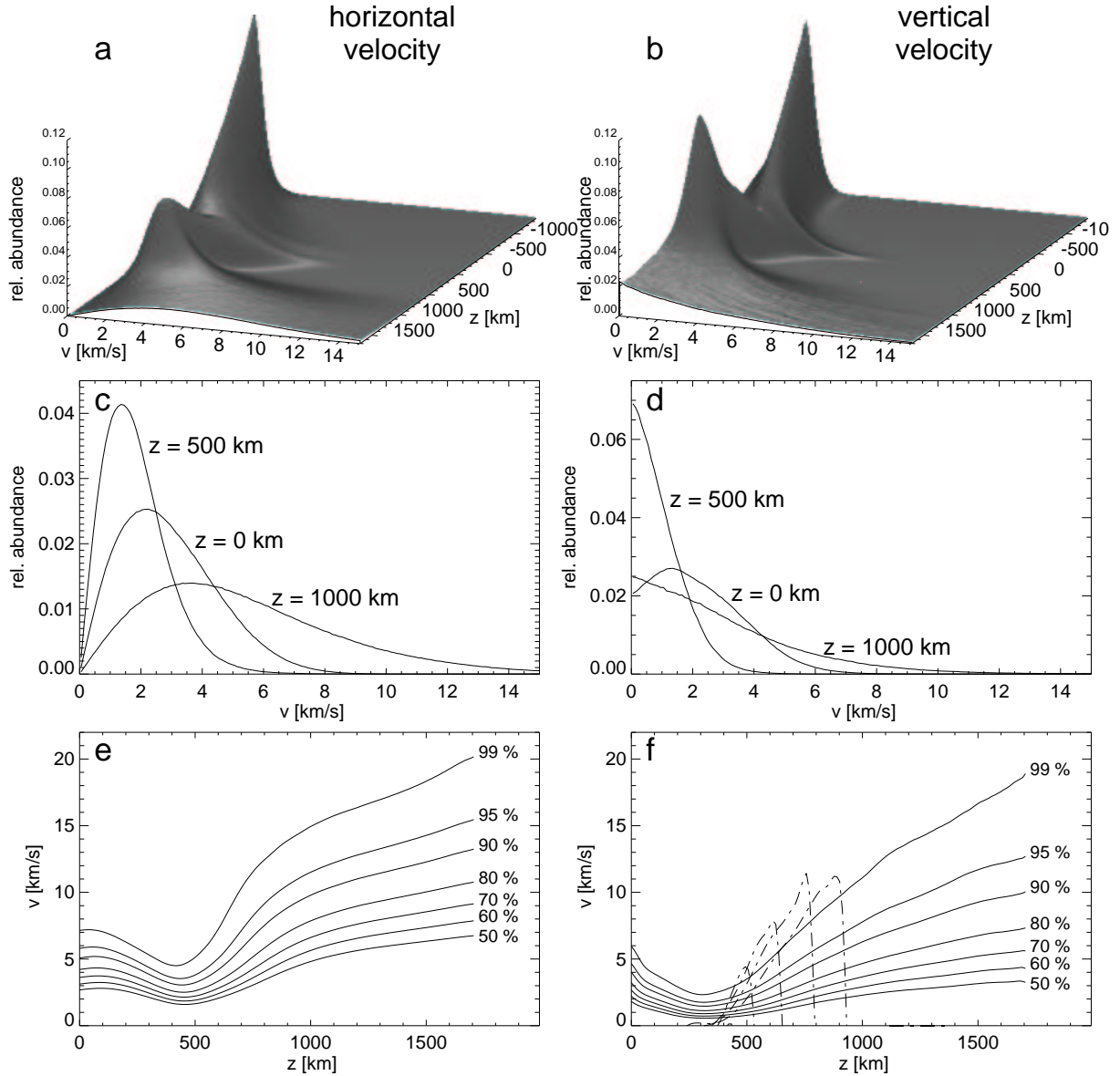


Figure 7.18: Distribution of the horizontal velocity (left column) and the upward directed vertical velocity (right column) in the 3-D reference model. **a-b)** Height-dependent velocity histograms, using bins of $\Delta v = 0.1 \text{ km s}^{-1}$, **c-d)** Histograms at the geometrical heights $z = 0 \text{ km}$, 500 km , and 1000 km , **e-f)** Height-dependent percentiles. The latter mark the limits which include the denoted fraction (e.g., 50 %) of all occurring velocity values. Additionally, the propagating wave from Fig. 7.16 is depicted in the lower right panel (dot-dashed line).

below 3.5 km s^{-1} . Due to the increase with height, the corresponding values are 4.4 km s^{-1} and 10.8 km s^{-1} for 50 % and 95 % at 1000 km , respectively. There, one percent even exceeds a horizontal velocity of 14.1 km s^{-1} . In general, the vertical velocities are slightly smaller; at 500 km 50 % stay below 0.7 km s^{-1} and 95 % below 2.1 km s^{-1} . Higher upward directed velocities, partly related to upward propagating shock waves, are found at a chromospheric height of 1000 km : 2.1 km s^{-1} and 7.0 km s^{-1} mark the upper limits for 50 % and 95 %, respectively.

The most extreme values ($> 99\%$) reach more than 10.0 km s^{-1} . Thus, the chromosphere of the three-dimensional model exhibits velocities of the order of $\sim 10 \text{ km s}^{-1}$, which largely exceeds the (local) sound speed.

Furthermore, the vertical velocity profiles for the exemplary spherical wave are plotted in Fig. 7.18.f (see also Fig. 7.15-7.17 and Sect. 7.2.1-7.2.2). The wave front reaches positive vertical velocities of $v_z \sim 11 \text{ km s}^{-1}$ in the low chromosphere, and thus exceeds even the 99 %-percentile. Hence, the wave is a rather extreme example.

7.2.4 Dependence on Numerical Modelling

The upper boundary is placed at $\sim 1700 \text{ km}$ – far away from the regions which are of particular interest for this work (see Sect. 5.5). As the analysis showed, the transmitting boundary does not influence the propagation of waves (i.e., by reflection) and thus seems not to have important impact on the results of this thesis.

Another point is the limited resolution of the numerical grid (see Sect. 6.1 and Fig. 7.16). It is coarser compared to the model by Carlsson & Stein (see Sect. 3.5), which leads to a larger *spatial smearing* and consequently smoother shock wave profiles. The one-dimensional model by CS exhibits very sharp temperature peaks with large maximum values of $> 8000 \text{ K}$ (see Fig. 2 in Carlsson & Stein 1994), which are larger than the values found in the three-dimensional model ($T_{\text{max,wave}} \sim 7000 \text{ K}$). The peak temperatures are also lowered systematically by other possible shortcomings in the modelling of shocks. For example, the assumption of *instantaneous ionisation*, as adopted in the present simulations, is too simple in the face of the physical conditions in shock waves. There, the time-scales for *radiative ionisation* and *recombination* differ, such that the recombination lags behind in the precursory part of the wave, leading to net radiative heating. This effect produces an amplification of the shock and thus sharper profiles with higher peak temperatures (Carlsson & Stein 1991). Hence, a time-dependent treatment of the ionisation and recombination would un-doubtedly improve the modelling of shock waves.

The spatial smearing also reduces the mechanical heating rate in the wave fronts, since the dissipation is stretched out over a longer time interval – due to the spatially more extended profile. While in comparison to a high resolution case the integral dissipation across the shock front is preserved, this artificial stretching over a longer time interval enables the radiation to smooth the temperature profile more effectively (since the radiation tends to restore equilibrium conditions). The effect might be important for the formation of spectral features, whereas it plays only a minor role for the global energy deposition by shocks, which is of particular interest in this thesis.

7.3 Oscillations

Another observational constraint which should be reproduced by a realistic model of the outer solar layers is the existence of oscillation modes (see Sect. 2.3).

7.3.1 Velocity Signal, Frequency and Wavenumber Range

Since observations show that vertical velocities are by far more important than the horizontal components with respect to the solar oscillation modes (see Sect. 2.3), here only the variations of the vertical velocity component is regarded, i.e., only plane-parallel oscillation modes are investigated.

The results which are discussed in this section are based on the same 151 min long time sequence from the three-dimensional reference model as used in the previous sections. Instead of the

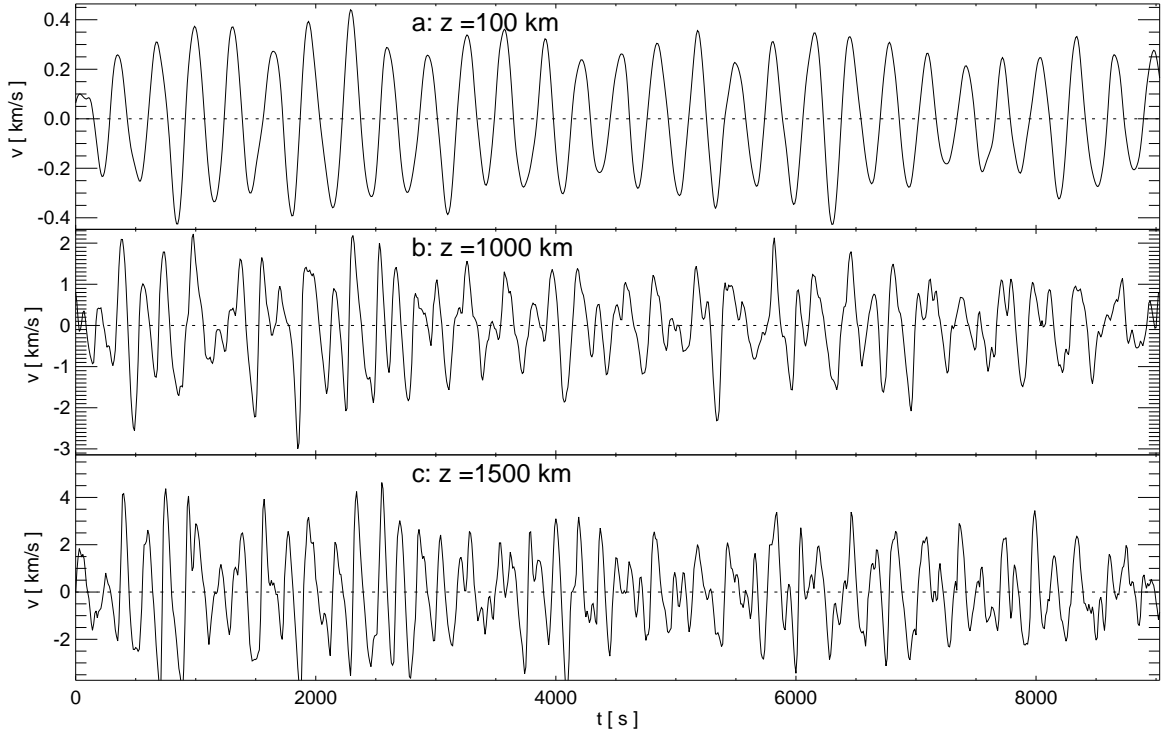


Figure 7.19: Time variation of the horizontally averaged velocity $\tilde{v} = \langle \rho v_z \rangle_{x,y} / \langle \rho \rangle_{x,y}$ in the 3-D reference model at the geometrical heights $z = 100$ km, 1000 km, and 1500 km. Note the different range of the velocity axes.

horizontal average of the vertical velocity component (available in the full data set), the velocity signal was retrieved as

$$\tilde{v} = \frac{\langle \rho v_z \rangle_{x,y}}{\langle \rho \rangle_{x,y}}, \quad (7.2)$$

which is a function of time and geometrical height (see Fig. 7.19). Although the results for both quantities do not differ much, the latter seems preferable for some reasons. First, it assures that only high velocities related to mass motion are taken into account. Hence, grid cells of higher density contribute more to the velocity signal than low-density elements. This is closer to the determination of velocities from observed intensities and related line shifts. Perhaps more important is the fact that the velocity \tilde{v} is derived from the mean data set which has a higher time sampling of 10 s instead of only 30 s as for the velocity in the full data set.

This height- and time-dependent discrete velocity signal, which is shown in Fig. 7.19, will be used as input for a Fourier analysis. The corresponding resolution of the angular frequency $\Delta\omega$ and of the (linear) frequency $\Delta\nu$ is limited by the length \bar{t} of the input signal:

$$\Delta\omega = \frac{2\pi}{\bar{t}} \quad \Leftrightarrow \quad \Delta\nu = \bar{t}^{-1}, \quad (7.3)$$

where $\omega = 2\pi\nu$. Consequently, the frequency resolution for the analysed sequence is $\Delta\nu = 0.11$ mHz. On the other hand, the maximum frequency, known as *Nyquist frequency*, is determined by the time resolution Δt of the input signal:

$$\omega_{\max} = \frac{\pi}{\Delta t} \quad \Leftrightarrow \quad \nu_{\max} = (2\Delta t)^{-1} \quad (7.4)$$

The Nyquist frequency is 50 mHz for the time sampling of $\Delta t = 10$ s, compared to only $16.\bar{6}$ mHz in the case of $\Delta t = 30$ s.

The limited horizontal extent L of the computational domain and the finite spatial resolution Δx impose analogous restrictions on the (horizontal) wave number:

$$\Delta k = \frac{2\pi}{L}, \quad k_{\max} = \frac{\pi}{\Delta x} \quad (7.5)$$

This limits the horizontal wave number to the range $\Delta k_x = 1.12 \text{ Mm}^{-1} \leq k_x \leq 78.6 \text{ Mm}^{-1}$ for the 3-D reference model. Unfortunately the wavenumber resolution is too low for a meaningful comparison with observations. The most interesting part of the $k-\omega$ plane, i.e., the range which yields most of the power, mostly concentrated in the so-called p-mode ridges, is limited roughly by $\omega \lesssim 30$ mHz and $k_{\text{hor}} \lesssim 1.2 \text{ Mm}^{-1}$ (see, e.g., Deubner et al. 1979; Kneer & von Uexküll 1993). Hence, no useful $k-\omega$ digram can be derived on the basis of the present numerical models. Following Eq. (7.5) a much larger horizontal extent of the model would be required. Consequently, only the temporal variations of the velocity are investigated in this thesis.

7.3.2 Power of Plane-Parallel Oscillation Modes

Using a *Fast Fourier Transformation* algorithm (FFT), height-dependent power spectra are calculated. The sum of the relative power at all frequencies is normalised to one at all heights independently. The Fourier zero component is always zero due to the subtraction of the time average of the velocity prior to the FFT. (The absolute velocity amplitudes can be seen in Fig. 8.4.a, for example.) In Fig. 7.20 the resulting power spectra are shown for exemplary geometrical heights in the photosphere ($z = 100$ km) and in the chromosphere ($z = 1000$ km, 1500 km) which correspond to the velocity signals shown in Fig. 7.19. Only frequencies below 15 mHz are plotted because higher frequencies yield no significant power. For all heights the maximum power is found at a frequency of $\nu = 3.10$ mHz (5.38 min). This result closely matches solar observations which show maximum power at a period near 5 minutes in the photosphere. The frequency of $3.\bar{3}$ mHz (5 min) is marked with the left vertical dotted line in Fig. 7.20. In the numerical model, there is also some power at the frequencies right below and in particular above the maximum. Thus, the power of this 5-min oscillation is concentrated in particular in one strong mode at $\nu = 3.10$ mHz with relatively little power at the adjacent frequency bins. This is different for the 3 min oscillation(s) which stretch over a wider frequency range. Within this range, the maximum power is found at a frequency of 6.08 mHz. But next to this mode, there are several frequencies which also contribute significantly to the power in the 3 min range. The frequency $3.\bar{3}$ mHz (3 min) is marked with the right vertical dotted line in Fig. 7.20.

7.3.3 Variation of Power with Height

Observationally the variation of the power spectrum with height can be determined by using spectral lines which originate from different heights of the solar atmosphere. Depending on the particular spectral line, a more or less extended height range contributes to the formation of the line. Consequently, the variation of the power spectra with height remains uncertain to some extent. This is different for numerical models in which each grid layer can be analysed separately.

The variation with height in the 3-D reference model is shown for the strongest mode at $\nu = 3.10$ mHz in Fig. 7.21.a. The power contributed by this mode decreases from $\approx 76\%$ in the convection zone and lower photosphere down to $\approx 14\%$ at the upper boundary of the model at a height of ≈ 1700 km. By that this mode is much stronger than all other individual modes

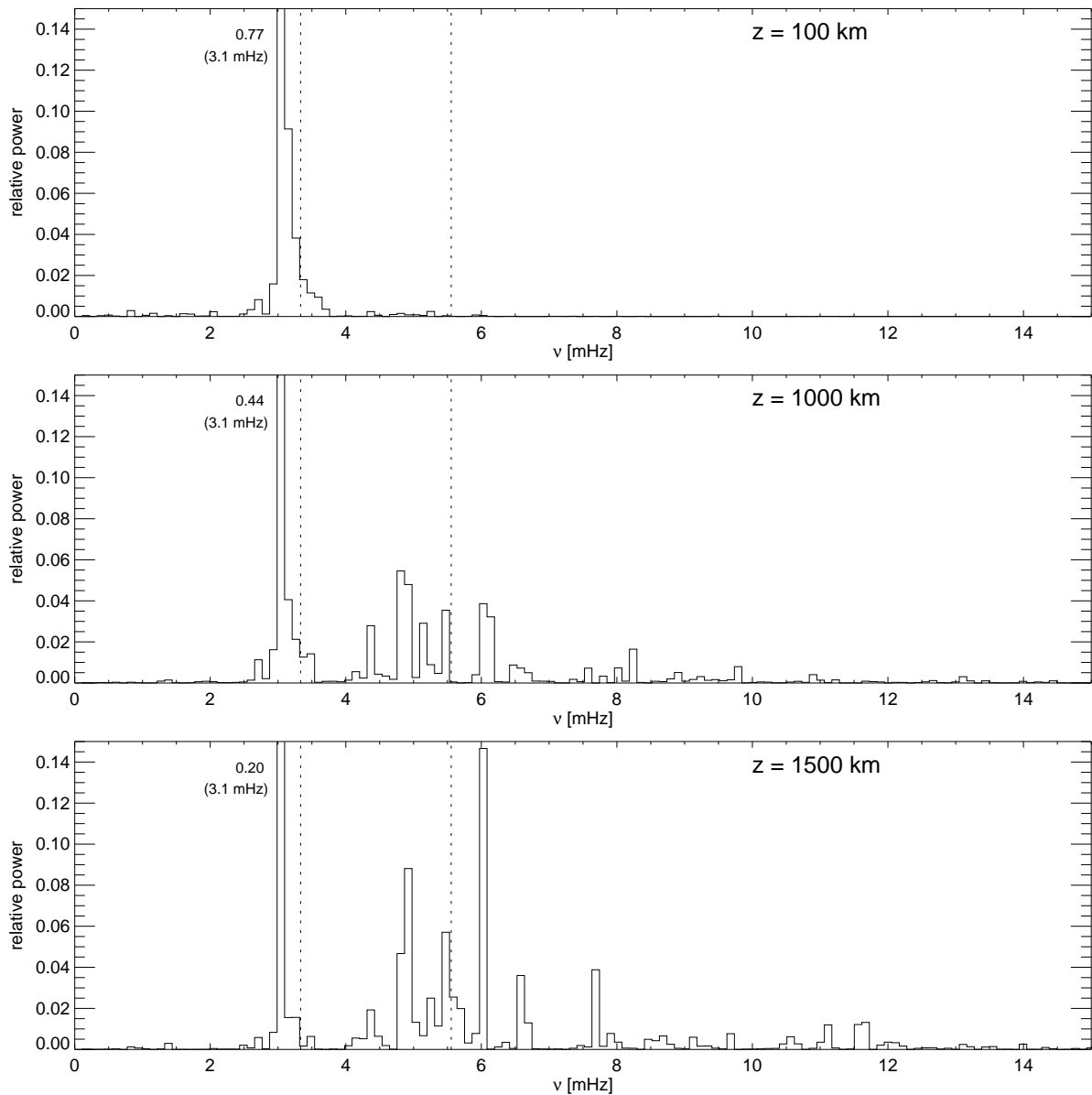


Figure 7.20: Plane-parallel oscillation modes in the 3-D reference model: Power spectra for the geometrical heights 100 km, 1000 km, and 1500 km. The dotted vertical lines mark the frequencies which correspond to oscillation periods of 5 min and 3 min.

which are shown in Fig. 7.21.b. The contributions to the total power are mostly less than 10% for these modes, except for the mode at $\nu = 6.08$ mHz. Like many others in the 3 min range, this mode only yields significant power above the low chromosphere. It reaches a maximum of 15% at $z \approx 1500$ km and is thus the strongest mode in the 3 min range in the middle chromosphere. As already mentioned above, there are several frequencies in the 3 min range at which comparable power is present in the chromosphere. To demonstrate the difference between the oscillations in the 5 min and 3 min range more clearly, the power is summed up in the following frequency bands:

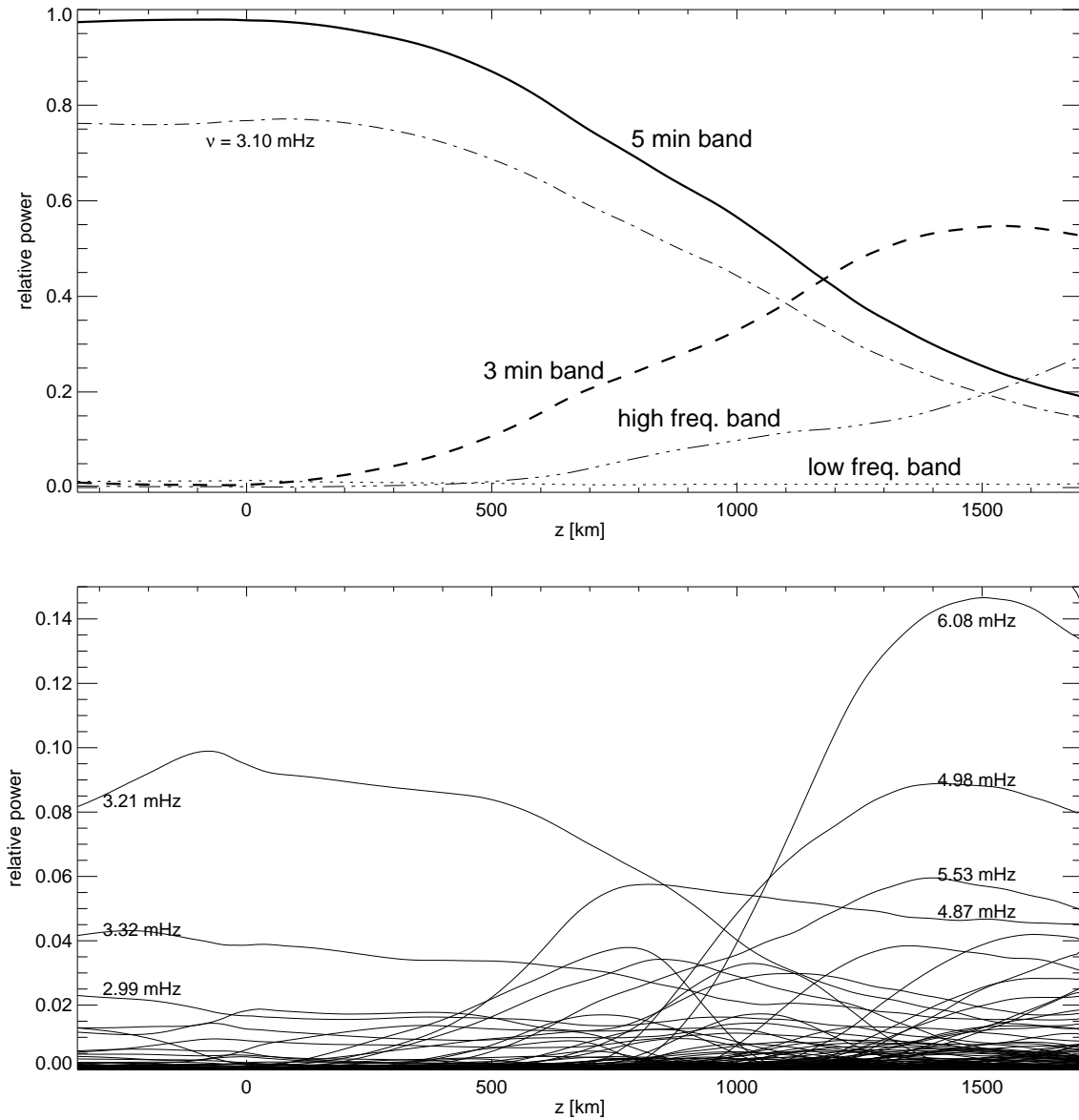


Figure 7.21: Variation of oscillation modes with geometrical height: **a)** frequency bands for 5 min and 3 min oscillations, and higher and lower frequencies, and the strongest mode ($\nu = 3.10$ mHz), **b)** individual oscillation modes;

low frequencies	:	<	2.4 mHz,		\gtrsim	420 s
5 min band	:	2.4 mHz –	4.0 mHz,	≈ 250 s	–	≈ 420 s
3 min band	:	4.0 mHz –	7.2 mHz,	≈ 140 s	–	≈ 250 s
high frequencies	:	>	7.2 mHz,		\lesssim	140 s

The frequency bands have been chosen to comprise the significant oscillations in the 5 min and 3 min range, resulting in different band width. In Fig. 7.21.a the total power in these bands is plotted over height. In the convection zone almost all power ($> 97\%$) is provided by the 5 min oscillations, mainly due to the frequencies $\nu = 3.10 - 3.32$ mHz. In the layers above the fraction decreases strongly until only $\approx 19\%$ are due to the 5 min oscillations at the upper boundary. For

the 3 min band it is vice versa. The modes are unimportant in the low photosphere and below but they provide significant power in the chromosphere. Above $z \approx 1200$ km the 3 min range contributes up to $\approx 55\%$ which is more than for the otherwise predominant 5 min oscillations. At the frequencies below the 5 min band ($\nu < 2.4$ mHz) almost no power is present ($< 1\%$), i.e., oscillations with periods longer than ≈ 7 min play no important role. This is different for the higher frequencies with corresponding periods below ≈ 140 s. Above the photosphere the power in this range increases until $\approx 27\%$ of the total power are reached near the upper boundary. For frequencies which correspond to periods below 100 s this contribution is $\lesssim 16\%$. The high frequencies are presumably due to the existence of shock waves and the corresponding short dynamical time scales in the chromosphere.

Note that the theoretical mode spectra presented here are much more sparse than observed. This is due to the properties of the limited computational box (like the relatively small extent) and consequently fewer possible modes. Thus, compared to the observations, the available power is concentrated in relatively few modes, increasing the power of the individual modes.

Nevertheless, the essential results of the present analysis are the existence of the 5 min and 3 min oscillations and the fact that the 5 min range is predominant in the photosphere, whereas the 3 min oscillations are only found in the chromosphere. These findings are line with observations (see, e.g., Cram 1978, and Sect. 2.3). Hence, one can conclude that the three-dimensional reference model (here in particular the dynamics) already reproduces basic observational constraints for the oscillations.

7.4 Temperature Distribution

7.4.1 Thermal Bifurcation

In Sect. 7.1.3 we took notice of the *co-existence of hot and cool regions* in horizontal planes of the three-dimensional reference model. For a quantitative description of the temperature distribution, a height-dependent temperature histogram was calculated, i.e., temperature histograms were computed for each horizontal slice for all time steps of the 151 min of simulation time. Temperature bins of $\Delta T = 100$ K were used. The relative abundance is normalised with respect to the number of grid cells in each horizontal slice. The result is shown in Fig. 7.22. Clearly, the temperature is distributed close to a mean value with only moderate deviations in the photosphere (see Fig. 7.22.b). This photospheric temperature ridge continues into the chromosphere where a second component shows up at higher temperatures (see Fig. 7.22.c-d). This hot component represents the propagating shock waves in the chromosphere and the resulting high temperatures (Sect. 7.2).

Hence, the co-existence of a cool background and hot shocked material in the chromosphere, as described qualitatively in Sect. 7.1, shows up as a double-peaked distribution with an intermediate range. This phenomenon is referred to as *thermal bifurcation* in this thesis but note that it is not caused by the influence of carbon monoxide as cooling agent like proposed by Ayres (1981, see Sect. 2.6.1). Rather, it is due to the propagating shock waves which on one hand exhibit high temperatures and, on the other hand, induce dynamic cooling of the traversed region (see Sect. 7.2.2).

7.4.2 Temperature Stratification

In this section, the average temperature stratification (see also Fig. 7.1) and the consequences of the thermal bifurcation (see Sect. 7.4.1) are discussed.

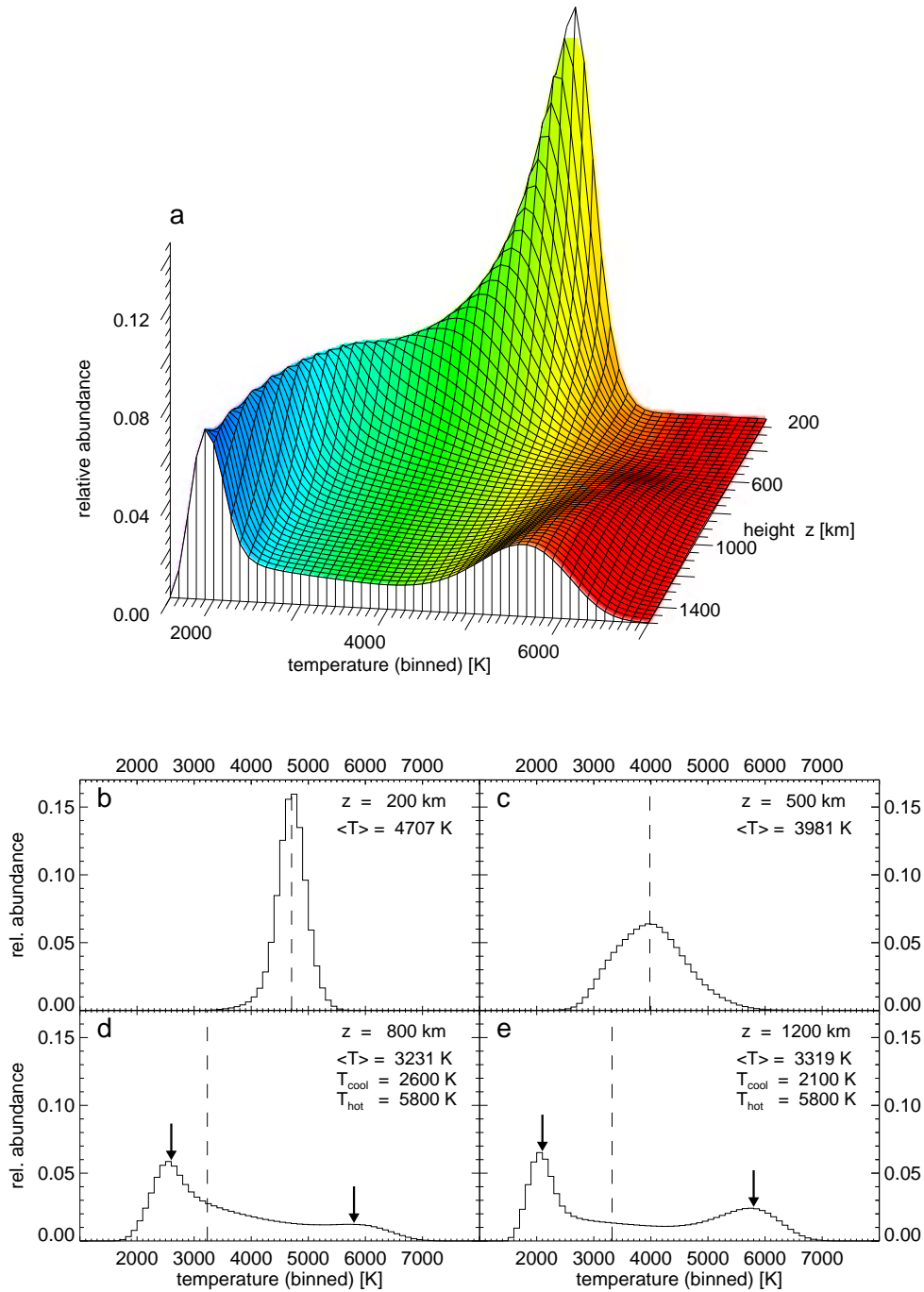


Figure 7.22: Temperature histograms for the 3-D reference model for all heights (a) and for particular heights in the photosphere (b-c) and d-e) in the chromosphere. The relative abundance (vertical axis) is the number of grid cells within a temperature bin with respect to all cells at that height. The dotted lines marks the mean temperature, while the arrows mark the hot and the cool temperature component (chromosphere only).

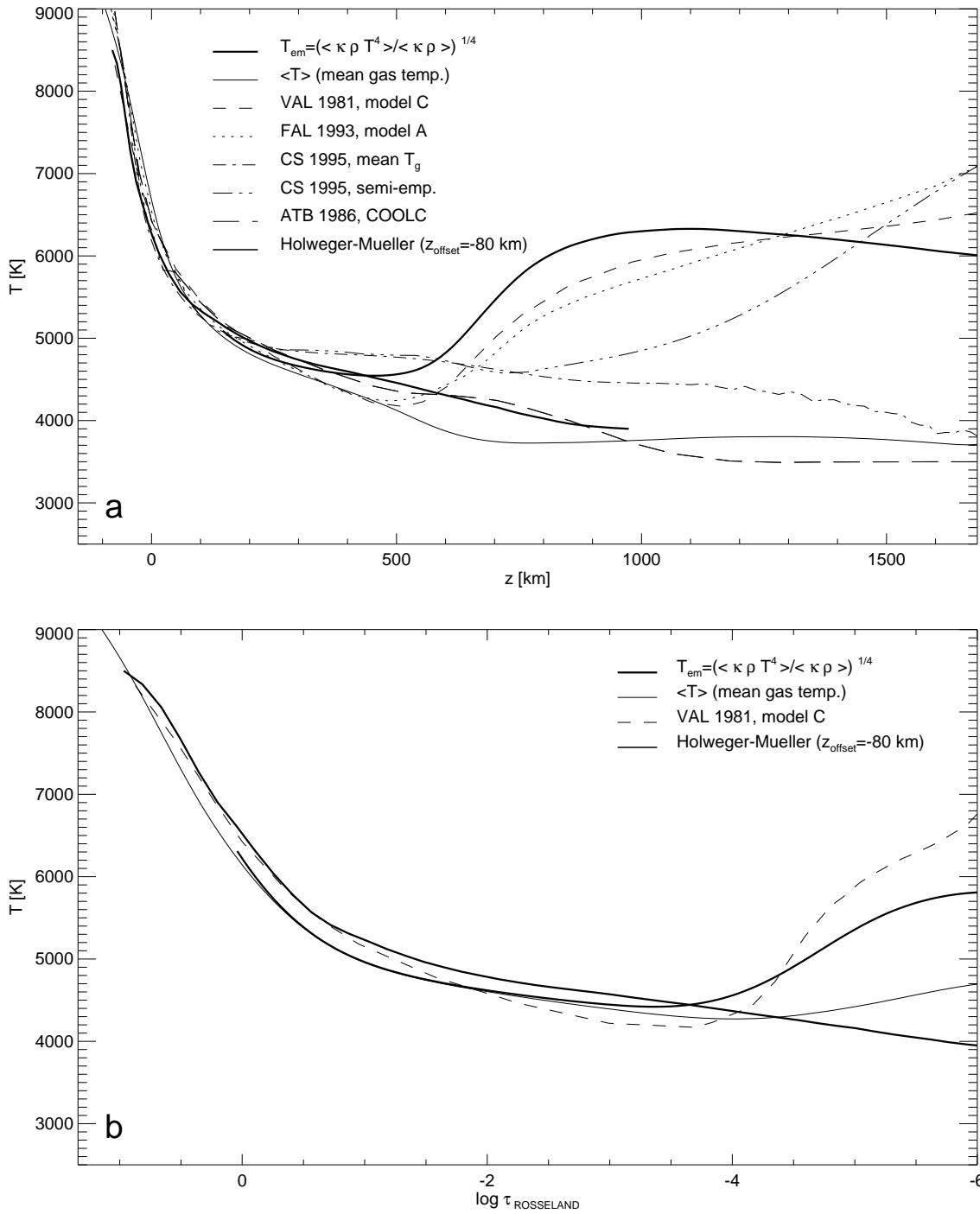


Figure 7.23: Temperature stratifications of different models on a geometric height scale (a) and on an optical depth scale (b): Horizontally and temporally averaged grey emissivity temperature and mean gas temperature for the 3-D reference model, model C by Vernazza et al. (1981), model A by Fontenla et al. (1993), mean gas temperature and semi-empirical stratification of the dynamical model by Carlsson & Stein (1995), and COOLC by Ayres et al. (1986).

The horizontally and temporally averaged gas temperature for the sequence of 151 min simulation time (thin solid line in Fig. 7.23.a) decreases with height until it reaches values between 3800 K and 3700 K above $z = 730$ km, i.e. in the chromosphere. *It does not show a notable temperature minimum nor a significant temperature increase in the chromosphere* like it is the case in the semi-empirical models by VAL and FAL (Fig. 7.23.a, see also Sect. 3.1 for more details on the models). This behaviour is similar to the mean gas temperature in the one-dimensional radiation hydrodynamic simulation by Carlsson & Stein (1995) which does not show a temperature increase, too (Fig. 7.23.a, see also Sect. 3.5). The semi-empirical models, which are derived from spatially and temporally averaged intensities, are static and homogeneous and thus can only describe average properties of the chromosphere. Carlsson & Stein pointed out that the chromospheric temperature rise in these models is only an artefact caused by the averaging of the highly *non-linear Planck function* in the UV (see also, e.g., Ayres & Linsky 1976; Ayres 1991). Furthermore, CS confirmed this by calculating a temperature distribution for their dynamical model in a similar way as VAL. They adjusted a steady-state temperature stratification to reproduce the time-averaged intensity as function of wavelength which is a result of their dynamic simulation. The resulting semi-empirical model by CS is a much better fit to the models by VAL and FAL.

Unfortunately no extensive wavelength-dependent intensities are available for the hydrodynamical simulation presented in this thesis. However, a qualitatively similar quantity can be calculated by averaging the temperature weighted with density ρ and opacity κ where brackets $\langle \rangle_{x,y}$ stand for horizontal averaging:

$$T_{\text{em}}(t, z) = \left(\frac{\langle \kappa \rho T^4 \rangle_{x,y}}{\langle \kappa \rho \rangle_{x,y}} \right)^{1/4}. \quad (7.6)$$

This quantity will be referred to as “*average grey emissivity temperature*”. The resulting temperature distribution, as it was calculated on a geometrical scale, (thick solid line in Fig. 7.23.a) is much more similar to model C by VAL and model A by FAL. It exhibits a *temperature minimum* at approximately the same height, and the temperature values reached in the middle chromosphere are comparable. This qualitative match is better than expected from such a crude approximation. Thus, like done by Carlsson & Stein before, the temperature stratifications of the semi-empirical models can be reproduced without a significant increase in the mean gas temperature.

Moreover, up to a height of $z \sim 500$ km the mean gas temperature in the 3-D reference model matches almost perfectly the semi-empirical models. Above that height the thermal bifurcation becomes increasingly significant, i.e. the temperature fluctuations become large. Therefore, the assumption of spatial and temporal homogeneity is not valid in the chromosphere. The variations in the chromosphere occur on scales – horizontally, vertically, and temporally – which are so small that they can hardly be resolved in observations so far. This might be the reason why they have been neglected for the construction of the semi-empirical models by VAL and FAL. Note also that the mean gas temperature in the 3-D reference model provides lower values than the simulation by Carlsson & Stein. This agrees with the remark by Ayres (2002) who argues that the Carlsson-Stein model is even not cold enough in view of carbon monoxide diagnostics. As discussed in Sect. 3.4, COOLC by Ayres et al. (1986) exhibits very low temperatures, capable of explaining the CO observations (see Fig. 7.23.a). The original column mass scale was converted into a geometrical height scale on the basis of model C by VAL. COOLC was constructed to represent a cool component. It is successful in reproducing the spatially averaged CO properties, but, on the other hand, it cannot explain the UV diagnostics (Ayres & Rabin 1996). The chromospheric temperatures are below the classical minimum temperature and decrease to

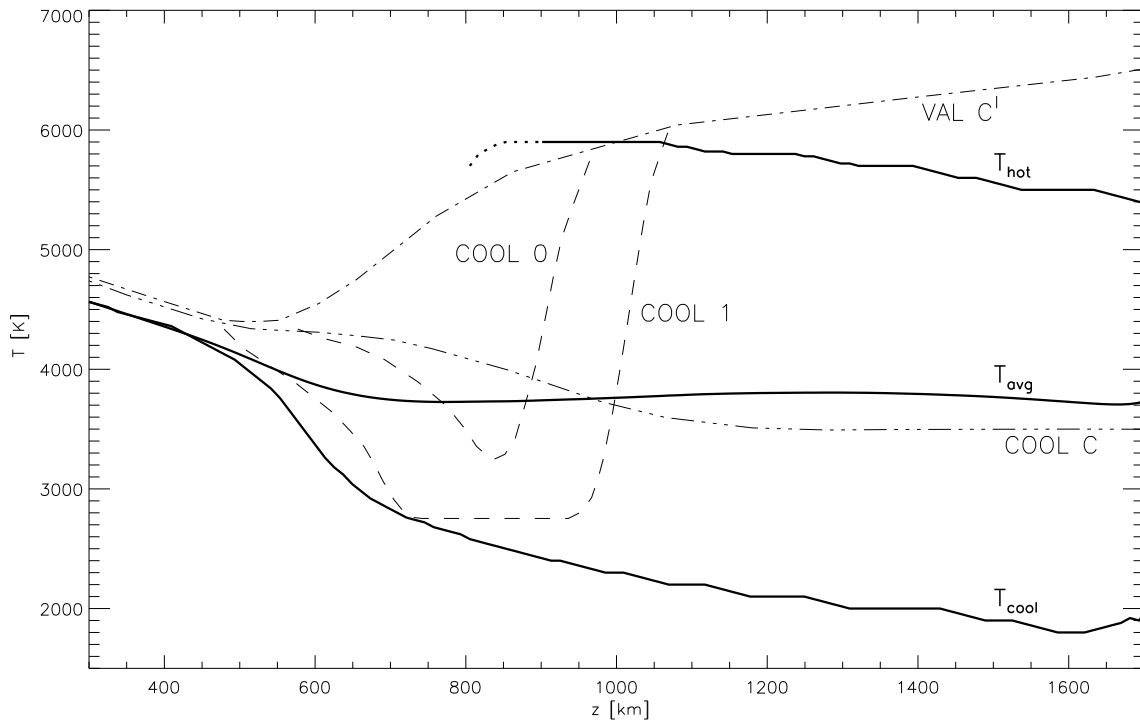


Figure 7.24: Hot and cool temperature components and average temperature stratification of the 3-D reference model, denoted with T_{hot} , T_{cool} , and T_{avg} , respectively. Also the models COOLC, COOL0, COOL1, and VAL C' are shown.

~ 3500 K. Since the mean gas temperature in the hydrodynamical model is even lower than for COOLC up to a height of ~ 970 km, the former model might provide the right conditions to account for the CO observations at lower heights than COOLC. See also Sect. 7.4.3 for a comparison with individual temperature components.

The averages presented so far are calculated on a geometrical height scale. In contrast, the average grey emissivity temperature and the simple arithmetic average in Fig. 7.23.b are calculated on an *optical depth scale*. On the geometrical height scale smaller mean gas temperatures are reached, and the minimum values even differ by more than 500 K. That is caused by the fact that fluctuations appear much smaller on surfaces of equal optical depth (see e.g., Uitenbroek 2000b). In a wave front the optical depth increases significantly. Thus, averaging on an optical depth scale is done on surfaces which are not plane but shaped by the spatial inhomogeneities while averaging on a geometrical height scale is done on strictly plane surfaces which cut through the inhomogeneities. Consequently, the temperature distribution on a surface for a particular optical depth differs from the one for a corresponding geometrical height, leading to different horizontal averages and thus different temperature stratifications.

7.4.3 Chromospheric Temperature Components

In the previous section, the average temperature stratifications are compared to various models, including two-component models. The thermal bifurcation (see Sect. 7.4.1) allows to determine a *hot and cool component* for the three-dimensional reference model, too.

Fig. 7.24 shows the height variation of the resulting *hot component* for heights above $z \approx 800$ km.

Below, the hot temperature ridge flattens out, so that no distinct peak can be determined (see right arrow in Fig. 7.22.d). In the chromosphere, the temperature is about 5900 K and decreases with height to 5400 K in the upper part of the model. Hence, the hot component is comparable to the semi-empirical models C by Vernazza et al. (1981) and C' by Maltby et al. (1986) for the height range 800 – 1000 km and to model A by Fontenla et al. (1993) at $z \approx 900 - 1100$ km, respectively.

The *cool background component* is also plotted in Fig. 7.24. It is identical to the horizontally and temporally averaged temperature stratification in the photosphere and below because there the fluctuations are much smaller due to the absence of shock waves. Thus, the temperature is distributed close to the mean stratification (see also Fig. 7.22). In the chromosphere, the average stratification stays at an almost constant level around 3700 K, while the temperature of the background component drops to values as low as 1800 K in uppermost layers. These values are much lower than found in the models COOLC by Ayres et al. (1986) and COOL0 by Ayres & Rabin (1996). Around $z = 800$ km the standard 3-D model is comparable to COOL1 (Ayres 2002), but COOL1 was constructed under the assumption that the cool component is only a minor constituent.

Note that the results in this section apply only to the 3-D reference model. Some models, e.g. the 3-D model with non-grey radiation transport lead to significant differences in the temperature distribution and thus to other temperature components (see Chap. 8).

7.4.4 Temperature Fluctuations

The rms-temperature fluctuations are defined as

$$\frac{dT_{\text{rms}}}{T_0} = \frac{\sqrt{\langle (T - T_0)^2 \rangle_{x,y,t}}}{T_0}, \quad (7.7)$$

where $T_0 = \langle T \rangle_{x,y,t}$ is the temporally and horizontally averaged temperature stratification. The quantity dT_{rms}/T_0 has been calculated on a geometrical height and analogously on an optical depth scale for the same model sequence as in Sect. 7.4.2 (Fig. 7.25). It is strongly height-dependent as can be seen directly from the horizontal slices in Fig. 7.3 for different heights and the temporal temperature variation in Fig. 7.12. Obviously, the lower layers of the model atmosphere are relatively homogenous with only small temperature fluctuations, in contrast to the inhomogeneous chromosphere.

Like for the temperature stratification (Sect.7.4.2) there is a difference between the geometrical height scale and the optical depth scale. Again the temperature deviations are much smaller on a surface of a particular optical depth than for a corresponding geometrical height. Thus, the temperature fluctuations appear to be smaller on the optical depth scale (see e.g., Uitenbroek 2000b).

In both cases the average lies below $dT_{\text{rms}}/T_0 \sim 0.42$. For particular horizontal positions and time steps, values of ~ 1.0 or even up to ~ 2.5 in corresponding 2-D models can be reached.

A comparable quantity $\delta T/T$ has been used by Kalkofen (2001) to distinguish between the two opposing cases of a hot chromosphere with small temperature fluctuations ($\delta T/T \sim 0.1$) and a cool one with large fluctuations ($\delta T/T \sim 10$). The reference model lies in between these cases. A better spatial resolution of the shock waves (and details like dynamic ionisation) in the simulations would presumably lead to higher temperature peaks and accordingly to larger temperature deviations.

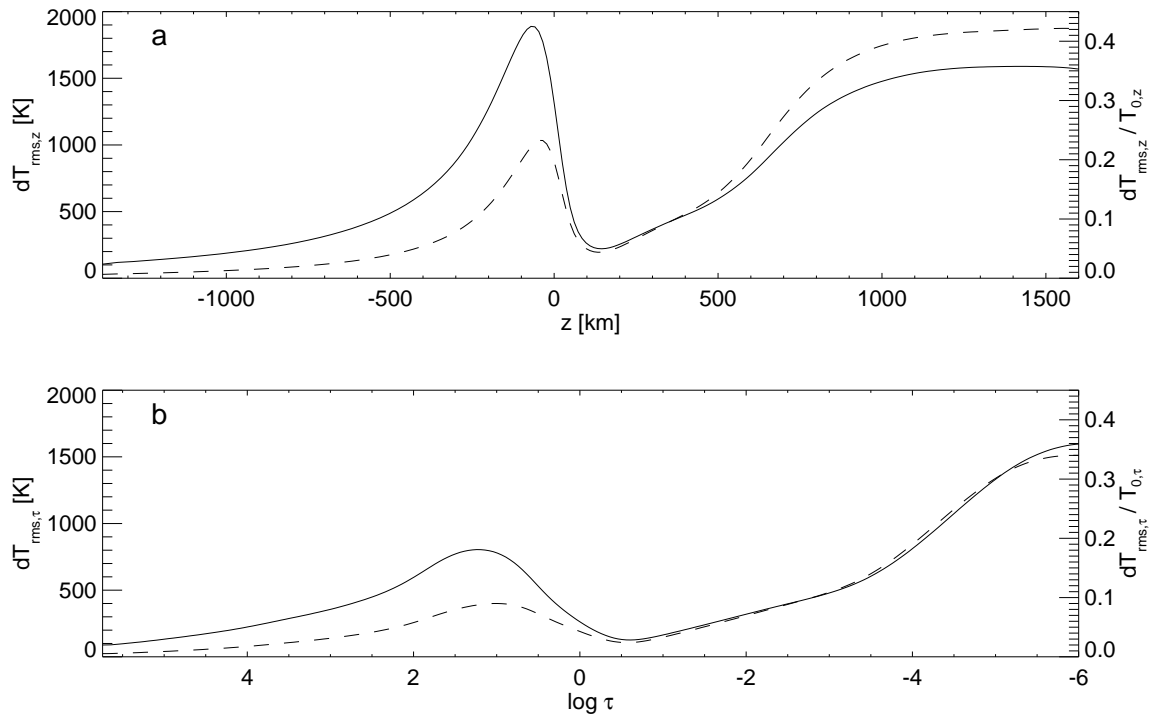


Figure 7.25: Horizontally and temporally averaged temperature fluctuation: Absolute deviations dT_{rms} (solid, left axis) and relative quantity dT_{rms}/T_0 (dashed, right axis) **a)** on the geometrical height scale and **b)** on the optical depth scale.

7.5 Radiative and Mechanical Energy Flux

Acoustic heating implies the deposition of energy due to the dissipation in shock waves which are described in Sect. 7.2. The released mechanical energy is converted into radiative energy which can leave the optically thin layers and is finally accessible to observations. Hence, the behaviour of the energy fluxes in the numerical model might give important clues on the heating by acoustic waves. In this section it is attempted to determine the acoustic flux in the chromosphere directly.

7.5.1 Total Flux

At the upper boundary of the three-dimensional reference model, an average radiative energy flux of $6.42 \times 10^{10} \text{ erg cm}^{-2} \text{ s}^{-1}$ is emitted. This value is only 1.4 % higher than the actual radiative flux of the present Sun, $6.33 \cdot 10^{10} \text{ erg cm}^{-2} \text{ s}^{-1}$, which corresponds to an effective temperature of 5780 K (see Sect. 2.7.1). Thus, the model is representative of a typical G2V star.

As already mentioned in Chap. 5, CO⁵BOLD is a conservative code, i.e., the total energy flux is constant over height when averaged horizontally and over a sufficiently long time interval. This special feature facilitates the quantitative analysis of the fluxes.

As already mentioned in Sect. 4.5, the total flux is composed by a mechanical and a radiative part:

$$F_{\text{total}} = F_{\text{mech}} + F_{\text{rad}} \quad (7.8)$$

This equation simply states the separation of the total flux into the radiative flux and a "rest", comprising all other fluxes. The radiative flux F_{rad} is directly available as horizontal average

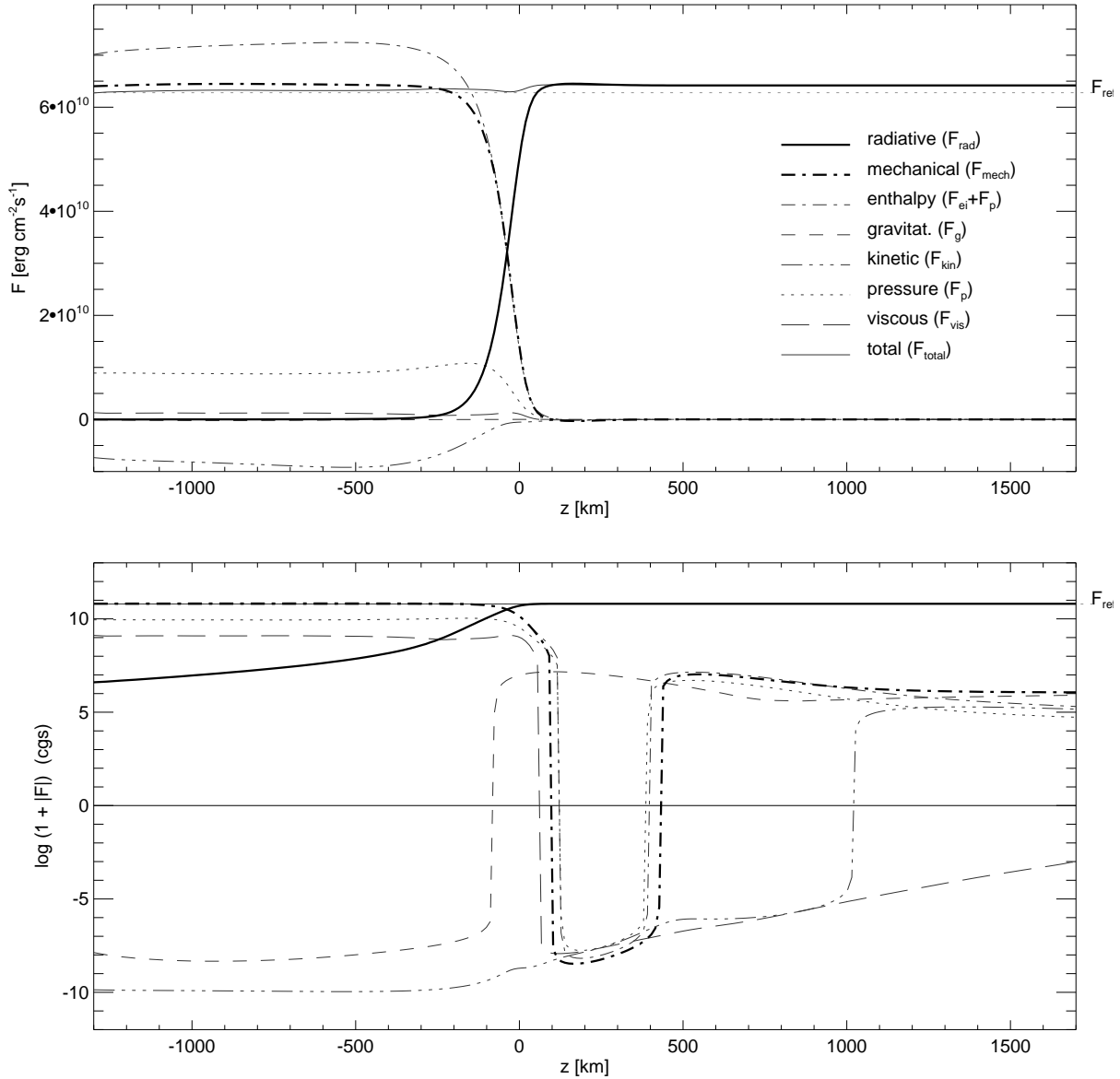


Figure 7.26: Time-averages of the horizontally averaged radiative, mechanical (uncorrected), and total energy flux. Additionally, various partial fluxes and the literature value of the total emergent flux (upper thin dotted line) are shown. The lower panel shows the quantity $\text{sign}(F) \log(1 + |F|)$, which allows to present negative and positive flux values on a logarithmic scale next to each other, making smaller contributions visible.

in the mean output data of CO⁵BOLD (see Sect. 5.6), whereas the mechanical flux has to be calculated from the following (partial) energy fluxes which are also provided by the mean output: The enthalpy flux ($F_{\varepsilon i} + F_p$), the pressure flux F_p , the kinetic F_{kin} , the gravitational F_g , and the viscous energy flux F_{vis} . Note that the fluxes are defined on the cell boundaries instead of the cell centres like most other variables. Based on these data, the mechanical flux can now be derived by

$$\langle F_{\text{mech}} \rangle_{x,y} = \langle F_{\varepsilon i} + F_p \rangle_{x,y} + \langle F_{\text{kin}} \rangle_{x,y} + \langle F_g \rangle_{x,y} + \langle F_{\text{vis}} \rangle_{x,y} \quad . \quad (7.9)$$

Calling it an mechanical flux is justified since contributions to the rest – besides the truly mechanical part – (i.e. convective flux, viscous flux, flux of potential energy) become increasingly unimportant in the chromospheric layers which are of particular interest for this thesis. In the chromosphere the radiative flux is the major contributor to the total flux, as can be seen in Fig. 7.26. It also shows the horizontally and temporally averaged height profiles of the fluxes listed above and the composed mechanical energy flux (thick dot-dashed line). The figure nicely illustrates the change in the energy transport which is of convective nature in the lower layers and almost totally radiative in the upper layers, including the necessary transition which defines the bottom of the photosphere.

However, the above definition of the mechanical flux also includes the advection of potential energy connected to mass motion (e.g., due to the up and down caused by the 5 min oscillations, see Sect. 7.3). Thus, in case of too short time sequences or otherwise poor statistics (e.g., due the relatively small number of vertical columns in 2-D models) the mechanical energy flux should be corrected for the resulting mass flux:

$$(F_{\text{mech}})_{\text{mfc}} = F_{\text{mech}} - (\Delta F_{\varepsilon_{\text{ip}}})_{\text{mfc}} - (\Delta F_{\text{kin}})_{\text{mfc}} - F_{\text{g}} \quad (7.10)$$

The correction consists of the subtraction of the gravitational term and additional terms for the enthalpy

$$(\Delta F_{\varepsilon_{\text{ip}}})_{\text{mfc}} = \langle \rho v_b \rangle_{x,y} \frac{1}{2} \left[\frac{(\langle \rho \varepsilon_i \rangle_{x,y} + \langle p \rangle_{x,y})|_i}{\langle \rho \rangle_{x,y}|_i} + \frac{(\langle \rho \varepsilon_i \rangle_{x,y} + \langle p \rangle_{x,y})|_{i+1}}{\langle \rho \rangle_{x,y}|_{i+1}} \right] \quad (7.11)$$

and analogously for the kinetic energy flux

$$(\Delta F_{\text{kin}})_{\text{mfc}} = \langle \rho v_b \rangle_{x,y} \frac{1}{2} \left[\frac{\langle \rho e_{\text{kin}} \rangle_{x,y}|_i}{\langle \rho \rangle_{x,y}|_i} + \frac{\langle \rho e_{\text{kin}} \rangle_{x,y}|_{i+1}}{\langle \rho \rangle_{x,y}|_{i+1}} \right] \quad (7.12)$$

where ρv_b is the mass flux through the cell boundary (denoted by the subscript b). The other variables in Eqs. (7.11) and (7.12) are: the internal energy per volume unit $\rho \varepsilon_i$, pressure p , density ρ , and kinetic energy (per volume) ρe_{kin} . They are all defined on the cell centres. The corresponding value on the enclosed boundary is calculated by the arithmetic average of the adjacent cells (subscripts i and $i + 1$, see brackets in Eqs. (7.11)-(7.12)).

The final mechanical flux is, e.g., $3.8 \times 10^6 \text{ erg cm}^{-2} \text{ s}^{-1}$ and $2.5 \times 10^5 \text{ erg cm}^{-2} \text{ s}^{-1}$ at 800 km and 1500 km, respectively. This compares to empirically derived estimates, e.g., by Deubner (1988): $\sim 1.2 \times 10^6 \text{ erg cm}^{-2} \text{ s}^{-1}$ and $\sim 4.5 \times 10^5 \text{ erg cm}^{-2} \text{ s}^{-1}$ at that heights. Liu (1974) states a mechanical energy flux of $2 \times 10^7 \text{ erg cm}^{-2} \text{ s}^{-1}$ at a height of 520 km, which is a bit larger than the corresponding value of $\approx 1 \times 10^7 \text{ erg cm}^{-2} \text{ s}^{-1}$ in the reference model. This is still consistent because the estimate by Liu is based on a single acoustic event, while in this thesis average values are derived – which by nature are smaller than those for particular events. Thus, the absolute level of the mechanical flux is in line with observations, considering the difficulties and uncertainties connected to the determination of the acoustic/mechanical flux which cannot be measured directly (see Sect. 2.7).

In view of the underlying question, i.e., if the (model) chromosphere is heated acoustically, the changes of the fluxes in the upper layers are of interest and thus are examined in the following sections.

7.5.2 Flux Divergence

The radiative flux is almost constant in the upper layers (see Fig. 7.26) but there are still minor changes to the flux in the chromosphere which indicate the conversion of mechanical into

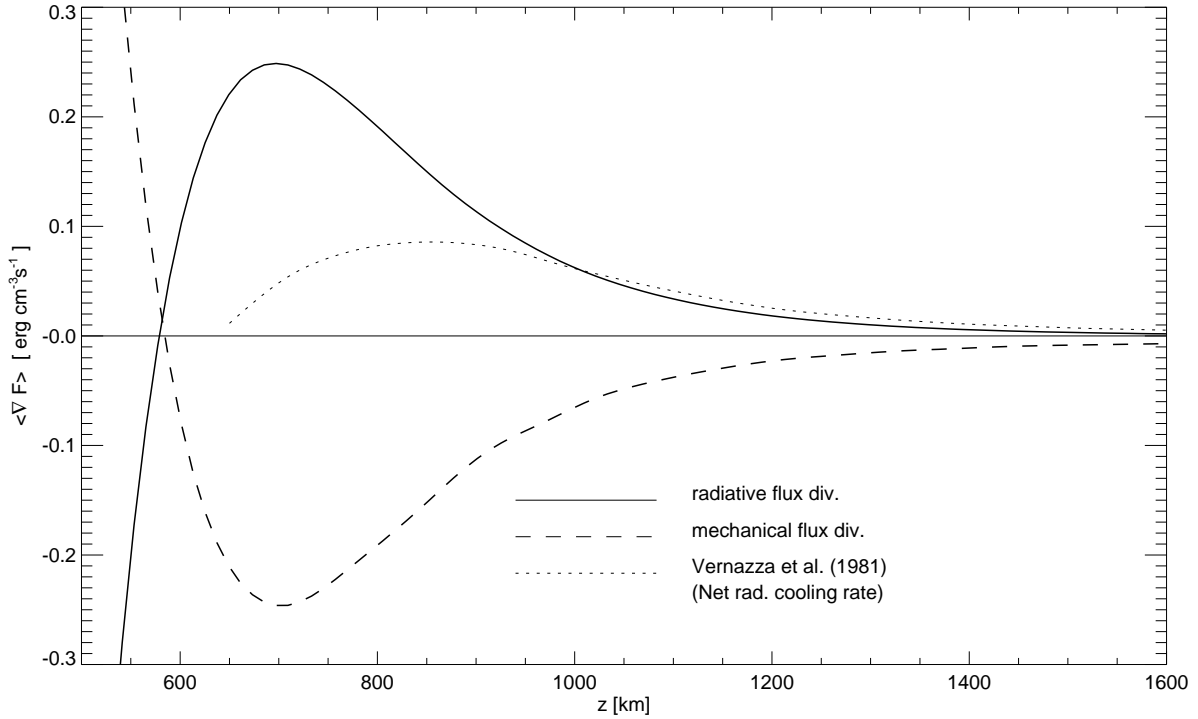


Figure 7.27: Time-average of the divergence of the horizontally averaged radiative and mechanical energy flux. The net radiative cooling rate given by Vernazza et al. (1981) is plotted for comparison.

radiative flux. As mentioned above the chromospheric contribution to the total emergent flux is expected to be only of the order of 10^{-4} , i.e., $F_{\text{rad,chrom}} \approx 6 \times 10^6 \text{ erg cm}^{-2} \text{ s}^{-1}$ (see Sect. 2.7.1). The treatment of such small fractions of rather large numbers imposes high demands on the modelling. The conservation properties of CO⁵BOLD can be considered an asset in this regard, allowing for meaningful investigations of such small deviations.

Mathematically, the deviations can be calculated via the divergence of the flux:

$$\text{div} \vec{F} = \vec{\nabla} \cdot \vec{F} = \frac{\partial F_x}{\partial x} + \frac{\partial F_y}{\partial y} + \frac{\partial F_z}{\partial z} \quad (7.13)$$

The horizontal contributions to the divergence vanish due to the periodic lateral boundaries (see Sect. 5.5) if averaged horizontally:

$$\left\langle \vec{\nabla} \cdot \vec{F}_{\text{rad}} \right\rangle_{x,y} = \left\langle \frac{\partial F_{\text{rad},x}}{\partial x} + \frac{\partial F_{\text{rad},y}}{\partial y} + \frac{\partial F_{\text{rad},z}}{\partial z} \right\rangle_{x,y} = \left\langle \frac{\partial F_{\text{rad},z}}{\partial z} \right\rangle_{x,y} \quad (7.14)$$

Thus, the flux divergence can be determined by simply calculating the height derivative. This is straight-forward since the horizontally averaged fluxes are directly available as functions of height and time in the mean output data set of CO⁵BOLD (see Sect. 5.6). Only the mechanical flux has to be calculated additionally in the way described in Sect. 7.5.1. The resulting height profiles depend strongly on time, as we shall see in Sect. 7.5.3. Hence, it is recommended to average also over a time interval which should be as long as possible. The time averages of the mechanical and the radiative flux divergence are plotted in Fig. 7.27 for chromospheric heights. The radiative divergence becomes positive just above the photosphere at 570 km, reaching a

maximum value of $0.25 \text{ erg cm}^{-3} \text{ s}^{-1}$ near $z = 690 \text{ km}$. Exactly the same values – except for the opposite sign – are found for the minimum of the mechanical flux divergence which is corrected for mass flux. This indicates the conversion of mechanical into radiative energy, giving rise to chromospheric radiation losses. The height of the maximum and minimum, which thus marks the strata with the highest average contribution to the chromospheric emission, agrees with the typical formation height of shock waves (see Sect. 7.2.1).

The divergence of the radiative flux can be compared to the net radiative cooling rate given by Vernazza et al. (1981) which is based on their model C (see dotted line in Fig. 7.27). Both profiles are qualitatively similar, including a decline above the local maximum which is correlated with the decreasing density (see Sect. 4.2.4). The quantitative difference (i.e., the absolute scale) is not surprising in view of the completely different modelling approaches – a one-dimensional static semi-empirical model and three-dimensional hydrodynamic simulations on the other side. Furthermore, Anderson & Athay (1989a) state that the radiative losses in the VAL C model might be too small by a factor of two or more due to the incomplete inclusion of iron lines. In their model, which is related to VAL C, iron accounts for 50 % of the radiative flux in the chromosphere (see Tab. 7.1 and Sect. 3.2). Taking this into account would no doubt improve the match between the two curves. Note that the opacities used for the presented simulations with CO⁵BOLD include the contribution of iron lines, although in the grey approximation. However, it should be kept in mind that VAL C and related models might still bear uncertainties, arising from the misleading construction of the temperature stratifications as discussed in Sect. 7.4.2. The comparison should thus only be regarded as qualitative.

7.5.3 Time Dependence of Flux Divergence

The remarkable clarity of the divergence profiles, which are presented in the previous section, is not self-evident in view of the orders of magnitude which lie between the original fluxes and the small residual divergence. Thus, high statistics are necessary for a meaningful analysis, i.e., a large number of vertical columns and/or long time sequences. This causes the analysis of two-dimensional models (see Sect. 6.3) to be much more difficult and less reliable compared to the presented three-dimensional case.

For the investigation of the time variation, the flux divergence is averaged temporally over time intervals of 1800 s with time increments of 900 s. The intervals thus overlap. The resulting height profiles for the various intervals are shown in Fig. 7.28 for the radiative and the mechanical flux divergence (corrected for mass flux). They differ with respect to the value and location of the maximum/minimum, and the height where the divergence becomes positive/negative, respectively (Fig. 7.28.a). While the values in the uppermost layers seem to be less affected in both cases, the mechanical flux divergence shows much stronger variations with time than the radiative one. This can also be seen from the time variation of the maximum and minimum values in Fig. 7.28.b. Additionally, the chromospheric minima of the uncorrected mechanical flux divergence are plotted. The variations exceed those for the corrected flux by far, leading to a standard deviation of $0.53 \text{ erg cm}^{-3} \text{ s}^{-1}$ instead of only $0.07 \text{ erg cm}^{-3} \text{ s}^{-1}$. Obviously, the mass flux correction, which is described in Sect. 7.5.1, reduces the temporal fluctuations of the mechanical flux divergence significantly. It thus should be applied to increase the quality of the analysis. Nevertheless, the mechanical flux divergence becomes less uncertain if a much longer time sequence is taken into account for the time average than used in the example presented here. The variations of the radiative flux divergence are even smaller. The corresponding standard deviation is only $0.02 \text{ erg cm}^{-3} \text{ s}^{-1}$. Hence, it is recommended to use the radiative flux divergence for quantitative conclusions if the available time sequence is too short for a stable result from the mechanical flux.

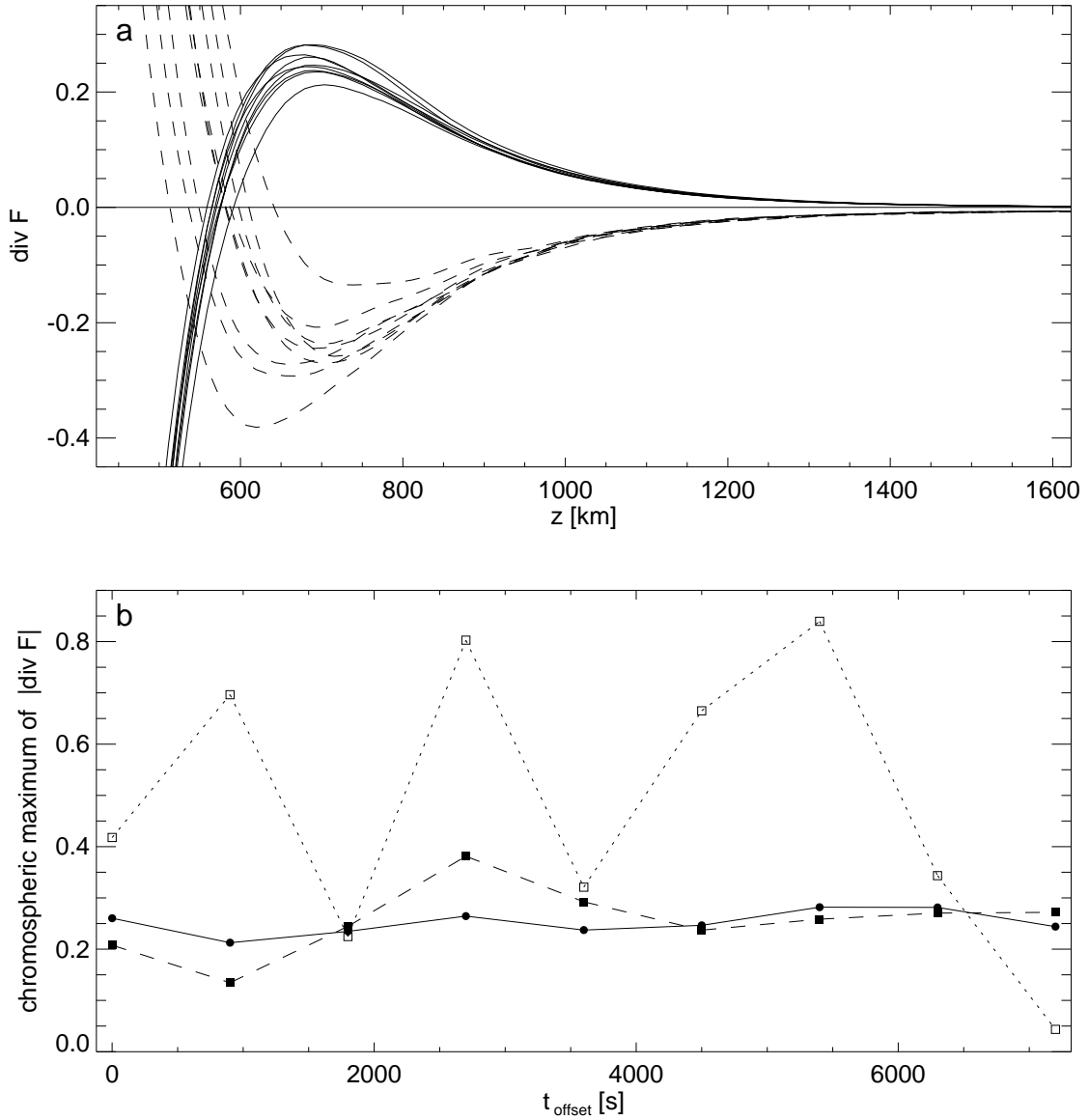


Figure 7.28: Time variation of the mechanical and the radiative flux divergence, averaged over time intervals of 1800 s with an increment of 900s. **a)** Height profiles for the different time intervals (solid: radiative, dashed: mechanical). **b)** Time variation of the chromospheric maximum of the radiative flux divergence (solid line) and the absolute chromospheric minimum of the mechanical flux divergence, corrected for mass flux (dashed) and uncorrected (dotted).

7.5.4 Chromospheric Emission and Basal Flux

Despite remaining uncertainties, the three-dimensional reference model can be used for the determination of the total chromospheric emission. It is derived by integration of the radiative flux divergence over those heights where the divergence is positive, i.e. from 570 km to the top of the model at 1710 km:

$$\Delta F_{\text{rad}} = \int_{570 \text{ km}}^{1710 \text{ km}} \langle \vec{\nabla} \cdot \vec{F}_{\text{rad}} \rangle_{x,y,t} dz = 7.9 \times 10^6 \text{ erg cm}^{-2} \text{ s}^{-1} \quad (7.15)$$

Hence, the chromospheric contribution to the total emergent flux ($6.42 \times 10^{10} \text{ erg cm}^{-2} \text{ s}^{-1}$) is 1.2×10^{-4} , which greatly matches the commonly stated fraction of 10^{-4} .

A comparison of the total radiative flux – not to mention the mechanical flux – is not straightforward, since direct empirical values are not available, neither for the Sun, nor for other solar-like stars. Instead, fluxes in the emission cores of Ca II $H + K$ and Mg II $h + k$ are widely used as proxies for the total chromospheric emission. In order to convert total flux into line fluxes one can take advantage of published theoretical chromospheric models. Although one-dimensional, these models are otherwise elaborate and can help to estimate the relative contribution of the main emission lines to the total flux. In Tab. 7.1 the chromospheric emission is listed for various spectral lines (and continua) as given by the models by Vernazza et al. (1981, VAL81), Avrett (1981), and Anderson & Athay (1989b). The values by VAL81 are only printed for the sake of completeness, since the newer, more accurate compilation is provided by Avrett (1981). The latter is also available in the book by Stix (1989).

According to the Avrett-Stix data, Ca II $H+K$ and Mg II $h+k$ make up 25.1 % and 21.1 % of the total chromospheric emission, respectively (see Tab. 7.1). Anderson & Athay (1989b) include the emission of iron lines in the energy balance more completely. Hence, the fraction of energy emitted by Mg and Ca is smaller. Accordingly, the contribution of Mg II $h+k$ reduces to 11.4 % in the Anderson-Athay model (see Tab. 7.1). Note that here the total radiative flux is quoted as $1.44 \times 10^7 \text{ erg cm}^{-2} \text{ s}^{-1}$ (the exact sum of the individual line fluxes), while in the original work by Anderson & Athay only the rounded value of $1.4 \times 10^7 \text{ erg cm}^{-2} \text{ s}^{-1}$ is given. Furthermore, the emission of Ca is only available as the sum of $H + K$ and the infrared triplet. In the Avrett-Stix

Table 7.1: Chromospheric emission in $10^5 \text{ erg cm}^{-2} \text{ s}^{-1}$. After Vernazza et al. (1981, VAL81), Avrett (1981, see also Stix 1989), and Anderson & Athay (1989b). The values in parentheses represent relative contributions to the total flux.

		VAL81	Avrett (1981)	Anderson & Athay (1989b)
Ca II	K	7 (15 %)	6.4 (14.2 %)	–
	H	5 (11 %)	4.9 (10.9 %)	–
	854.2 Å	7 (15 %)	6.8 (15.1 %)	–
	849.8 Å	6 (13 %)	5.5 (12.2 %)	–
	866.2 Å	5 (11 %)	4.6 (10.2 %)	–
Mg II	k	5 (11 %)	5.2 (11.6 %)	–
	h	4 (9 %)	4.3 (9.6 %)	–
H	Ly α	3 (7 %)	3.4 (7.6 %)	–
H [–]	free-free	2 (4 %)	2.2 (4.9 %)	–
	bound-free	2 (4 %)	1.7 (3.8 %)	–
Ca II	H,K	12 (26 %)	11.3 (25.1 %)	–
Ca II	H,K,IRT	30 (65 %)	28.2 (62.6 %)	38 (26.4 %)
Mg II	h,k	9 (20 %)	9.5 (21.1 %)	16 (11.1 %)
H	total	7 (15 %)	7.3 (16.2 %)	14 (9.7 %)
Fe	total	–	–	72 (50.0 %)
C	total	–	–	4 (2.8 %)
Total		46	45.0	144

data the total Ca II emission amounts to 62.6 % of the total flux (see Tab. 7.1), leading to a ratio of the H and K lines ($F_{\text{Ca II H+K}}/F_{\text{Ca II H+K+IRT}}$) of 0.4 with respect to the total Ca II flux. Adopting this value, a contribution of 10.6 % is inferred for Ca II $H+K$ from the Anderson-Athay model. These figures may serve to illustrate theoretical uncertainties involved in converting total into line fluxes.

Finally, the line fluxes can be predicted for the three-dimensional reference model. For that, the line fluxes in the models mentioned above (see Tab. 7.2) are scaled to the total chromospheric emission of $7.9 \times 10^6 \text{ erg cm}^{-2} \text{ s}^{-1}$. The models by Avrett (1981) and VAL81 have been used, both leading to fluxes of $\sim 2 \times 10^{10} \text{ erg cm}^{-2} \text{ s}^{-1}$ and $1.5 - 1.7 \times 10^{10} \text{ erg cm}^{-2} \text{ s}^{-1}$ for Ca II and Mg II, respectively. VAL81 also provide a net radiative cooling (see Fig. 7.27 and also Fig. 49 in Vernazza et al. 1981) from which the chromospheric emission can be calculated by integration. The 3-D hydrodynamic model ends at a height of $z \approx 1710 \text{ km}$, but there are still contributions to the emergent flux from higher layers in the model by VAL81, mainly by hydrogen. Integration of the net radiative cooling rate up to a height of only $z = 1710 \text{ km}$, like in the model presented here, results in a lower total flux of $3.8 \times 10^{10} \text{ erg cm}^{-2} \text{ s}^{-1}$. Since the individual contributions due to Mg II and Ca II are small above $z = 1710 \text{ km}$, the upper integration limits has no influence on the corresponding emission (see case c in Tab. 7.2). The line fluxes resulting for the 3-D model are slightly higher than for the two cases discussed before, namely $2.5 \times 10^{10} \text{ erg cm}^{-2} \text{ s}^{-1}$ and $1.9 \times 10^{10} \text{ erg cm}^{-2} \text{ s}^{-1}$ for Ca II and Mg II, respectively. However, the Anderson-Athay model appears preferable because it includes iron in more detail. It yields only $0.84 \times 10^6 \text{ erg cm}^{-2} \text{ s}^{-1}$ in Ca II $H+K$ and $0.88 \times 10^6 \text{ erg cm}^{-2} \text{ s}^{-1}$ in Mg II $h+k$.

These predictions may be compared to the observed lower limit of chromospheric emission in solar-type stars, the so-called ‘basal’ flux – a term introduced by Schrijver (1987). It is thought to represent the non-magnetic part of chromospheric emission arising from acoustic heating alone (see Sect. 2.7). The hydrodynamical predictions made above are $\log F \sim 6.3$ and 6.2 , if the data by Avrett and VAL81 is used, and $\log F = 5.92$ and 5.94 otherwise for Ca II $H+K$ and Mg II $h+k$, respectively. This compares with the values of $\log F_{\text{basal}} = 5.5$ and $\log F_{\text{basal}} = 5.8$ (cgs units)

Table 7.2: Chromospheric emission: Total radiative fluxes and line fluxes in units of $10^6 \text{ erg cm}^{-2} \text{ s}^{-1}$ based on different models and thus different contributions to the total flux. Logarithmic values are given in parentheses.

	total flux	Ca II H+K	Mg II h+k
a) VAL81	4.6 (6.66)	1.2 (6.08)	0.9 (5.95)
b) VAL81, $z < 1710 \text{ km}$	3.8 (6.58)	1.2 (6.08)	0.9 (5.95)
c) Avrett (1981)	4.5 (6.65)	1.13 (6.05)	0.95 (5.98)
d) Anderson & Athay (1989b)*	14.4 (7.16)	1.52 (6.18)	1.6 (6.20)
this work, scaled a)	7.9 (6.90)	2.1 (6.32)	1.5 (6.18)
this work, scaled b)	7.9 (6.90)	2.5 (6.40)	1.9 (6.28)
this work, scaled c)	7.9 (6.90)	1.98 (6.30)	1.67 (6.22)
this work, scaled d)*	7.9 (6.90)	0.84 (5.92)	0.88 (5.94)
Rutten et al. (1991): minimum (basal) flux	–	0.6 (5.8)	0.3 (5.5)

* assuming $F_{\text{Ca II H+K}}/F_{\text{Ca II H+K+IRT}} = 0.4$, see text for details

derived from the observations by Rutten et al. (1991) (see Sect. 2.7.2). This suggests that the basal flux in solar-type stars is truly of acoustic origin and can be reproduced reasonably well by hydrodynamic models, like the one presented in this thesis. The result, however, should still be taken with caution since some uncertainties remain, which are discussed in the subsequent section.

7.5.5 Uncertainties and Remaining Problems

The determination of acoustic fluxes is a long existing problem, which has been addressed with various approaches. On the observational side, uncertainties arise due to the spectrophotometric separation of line-wing contributions and weak chromospheric emission cores. There are many problems on the theoretical side, too. First of all, the true acoustic flux is not easy to separate from the total mechanical flux, in particular in the lower layers. Moreover, additional simulations show that the flux values are slightly dependent on model assumptions like the numerical viscosity. Switching off the additional tensor viscosity results in an increase of the chromospheric maximum of the radiative flux divergence by a factor of less than two. The usage of frequency-dependent radiation transport also produces significant differences in the flux divergence. In Chap. 8 the influence of model assumptions on the result is discussed in more detail. Despite the disturbing uncertainties the basic conclusion that non-magnetic 3-D hydrodynamical models are able to explain basal chromospheric fluxes in solar-type stars is likely to remain valid.

For a solid determination of acoustic fluxes further improvements of the modelling are required. One point is the radiation transport in the chromosphere. There, the radiative losses are dominated by strong, optically thick lines of ionised calcium, magnesium, and iron. This cannot be approximated by a grey approximation (nor in the optically thin limit). Instead, it might be necessary to solve the equations of statistical equilibrium – next to the hydrodynamics, and radiative transfer. This would be a straight-forward way to measure emergent line-fluxes from a numerical model but it also requires a huge amount of computational resources. The solution could be the inclusion of crude model atoms with only a small number of the most important energy levels and transitions for the major contributors to the chromospheric radiation losses, such as Ca II and Mg II.

7.6 Carbon Monoxide

As seen in the previous sections, the physical conditions of the model chromosphere are strongly variable in space and in time. It is not obvious how this behaviour affects the formation, dissociation, and spatial distribution of carbon monoxide molecules (CO) in the outer layers of the Sun. Thus, detailed time-dependent calculations are required to examine this interesting question which might provide essential insight into the nature of the solar chromosphere. Here, a first simple approach is presented.

7.6.1 Formation, Dissociation, and Concentration

The following considerations are based on a work by Ayres & Rabin (1996) and an application by M. Steffen (priv. comm., 2002). Like done by Ayres & Rabin (1996), the only formation process of CO molecules is here assumed to be radiative association,



whereas it is destroyed by collisional dissociation,



Furthermore, simplifying assumptions on the relevant chemical reactions are made, neglecting alternative formation channels and linked molecules. The following constraints for the concentrations (represented by brackets) of carbon, oxygen, and carbon monoxide are devised:

$$[\text{C}] = 1 - [\text{CO}] \quad (7.18)$$

$$[\text{O}] \approx 1 \quad (7.19)$$

The CO concentration is defined as the fraction of C atoms bound in CO,

$$[\text{CO}] \equiv \frac{n_{\text{CO}}}{n_{\text{C}}} \equiv \frac{n_{\text{CO}}}{A_{\text{C}} n_{\text{H}}}, \quad (7.20)$$

where n_{CO} , n_{C} , and n_{H} are the number densities of carbon monoxide, carbon, and hydrogen, while A_{C} denotes the abundance of carbon with respect to hydrogen. The temporal evolution of the CO concentration is then governed by the differential equation

$$\frac{d}{dt} [\text{CO}] = k_1 - k_2 [\text{CO}]. \quad (7.21)$$

According to Table 2 by Ayres & Rabin (1996), the constants k_1 and k_2 depend on the number density of neutral hydrogen atoms, n_{H} , and on the temperature T as

$$k_1 = 2.5 \cdot 10^{-5} n_{15} \tilde{T}^{0.6} \quad (7.22)$$

and

$$k_2 = k_1 \left(1 + 40 \tilde{T}^{22.2} \right), \quad (7.23)$$

whereby the notations $n_{15} = n_{\text{H}} / (10^{15} \text{ cm}^{-3})$ and $\tilde{T} = T / (5000 \text{ K})$ are adopted.

7.6.2 Static Atmosphere

First, the simple case of a static atmosphere is analysed, i.e., only the temporally and horizontally averaged stratification of the three-dimensional reference model is regarded (see Sect. 7.1.1). There, the amount of carbon monoxide molecules does not change with time:

$$\frac{d}{dt} [\text{CO}] = 0. \quad (7.24)$$

Consequently, Eq. (7.21) reduces to

$$[\text{CO}]_{\text{eq, stat}} = \frac{k_1}{k_2} = \left(1 + 40 \tilde{T}^{22.2} \right)^{-1}, \quad (7.25)$$

which is the equilibrium CO concentration for the static case. Starting from a non-equilibrium concentration $[\text{CO}]_0$ at time $t = 0$, the equilibrium value is approached in an exponential way,

$$[\text{CO}](t) = [\text{CO}]_{\text{eq, stat}} + \left([\text{CO}]_0 - [\text{CO}]_{\text{eq, stat}} \right) e^{-t/t_{\text{CO}}^{\text{chem}}}, \quad (7.26)$$

where $t_{\text{CO}}^{\text{chem}}$ is the characteristic chemical time scale:

$$t_{\text{CO}}^{\text{chem}} = k_2^{-1} = \frac{4 \cdot 10^4}{n_{15}} \frac{\tilde{T}^{-0.6}}{1 + 40 \tilde{T}^{22.2}} \text{ [s]}. \quad (7.27)$$

This time scale is plotted as a function of height for the mean temperature and density structure of the three-dimensional reference model in Fig. 7.29.a (solid line). It shows a strong variation with height, ranging from only ≈ 0.1 s at $z = 0$ km ($\tau = 1$) to $\gtrsim 10^6$ s at $z = 1000$ km. This variation is mainly due to the height dependence of the density, and only partly due to the temperature dependence. The high power of the temperature in Eq. (7.27) is opposed to – compared to the density – relatively small variations. The found time scales are in line with the findings by Avrett et al. (1996) who quote a range from one minute at a height of 100 km to several hours at $z = 1000$ km, and with the work by Ayres & Rabin (1996) who give time scales of 10 h for conditions near the classical temperature minimum (black dot in Fig. 7.29.a). (See also Ayres 1991.)

The corresponding equilibrium CO concentration $[\text{CO}]_{\text{eq,stat}}$ is computed according to Eq. (7.25) and plotted in Fig. 7.29.b (thin solid line). Like the time-scale it is obviously strongly height-dependent. While only little carbon monoxide is present in the low photosphere, a large concentration of $[\text{CO}] \gtrsim 0.9$ is found in the lower chromosphere and above ($z \gtrsim 600$ km). It even reaches a value of 0.94, implying that almost all carbon in the chromosphere is bound in CO.

7.6.3 Dynamic Atmosphere

So far, only the static case has been regarded. In the following, the dynamics of the atmosphere are taken into account, leading to a fundamentally different result. Based on the considerations Sect. 7.6.1, M. Steffen wrote appropriate numerical routines and also did first calculations for four representative vertical columns, extracted from the 3-D reference model. The four time sequences were only of 2000 s duration (see Fig. 7.12 for an example of the temperature variations). However, the calculations have been repeated for this thesis. The new data consist of sequences at every tenth column, each for the total duration of 151 min. The resulting larger number of columns (14×14) improved the statistics significantly.

The calculations which are described below, are preformed for each selected vertical column separately. Thus, the coefficients k_1 and k_2 , which are calculated from the gas temperature and the density according to Eqs. (7.22) and (7.23), depend not only on height and time but also on the selected column and thus on the horizontal position in the model. Given these coefficients, Eq. (7.21) is solved for each height step, using a standard fourth-order Runge-Kutta method. If necessary, the time-sequence from the numerical model is repeated until a dynamic equilibrium is obtained. The calculations thus result in height- and time-dependent CO concentrations for each column.

The thick solid line in Fig. 7.29.b represents the horizontally and temporally averaged CO concentration as function of height. Obviously, CO is present in the photosphere and in the low chromosphere with a maximum concentration of $\langle [\text{CO}] \rangle_{x,y,t} \sim 0.10$ at $z \sim 340$ km. In the layers above ($z \gtrsim 700$ km) almost no carbon monoxide is found, whereas concentrations up to 0.42 show up during the simulations at particular positions, e.g., in the middle photosphere near $z \approx 300$ km (see dot-dashed line in Fig. 7.29.b). This is consistent with the results from a theoretical investigation by Uitenbroek (2000a), which on average exhibits the highest concentrations in the middle photosphere, and the off-limb observations by Solanki et al. (1994), Uitenbroek et al. (1994), and the earlier work by Ayres & Testerman (1981). For example, Ayres & Testerman state a maximum CO concentration at an optical depth of $\tau \lesssim 10^{-2}$ which corresponds almost exactly to a height of 300 km in the hydrodynamical model presented here (see Sect. 2.6). Furthermore, it is interesting to derive an effective time scale for the adjustment of the dynamic equilibrium concentration. It should lie between the limiting cases of very large and very small

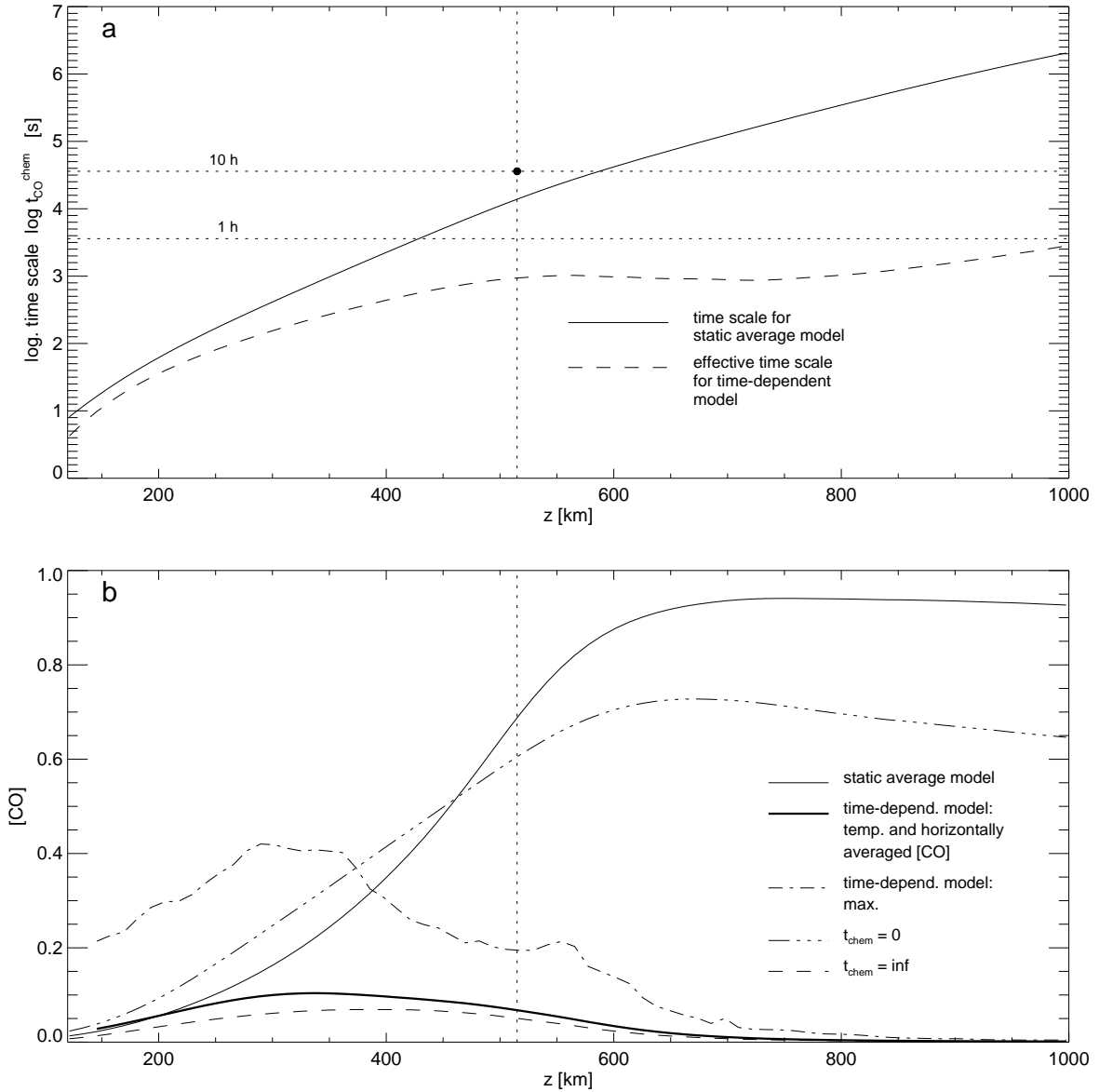


Figure 7.29: Carbon monoxide in the solar atmosphere: **a)** Chemical time scale $t_{\text{CO}}^{\text{chem}}$ for the averaged 3-D stratification (solid) and for the time-dependent calculation $t_{\text{CO}}^{\text{chem,dyn}}$ (dashed). The black dot indicates a time scale of 10 hours at the classical temperature minimum (Ayres & Rabin 1996). **b)** Equilibrium CO concentration for the averaged 3-D stratification (thin solid), and average CO concentration of the time-dependent calculation (thick solid) together with the corresponding maximum and minimum values (dot-dashed), and the limiting cases for a zero and an infinite time scale (triple-dot-dashed and dashed, respectively). $[\text{CO}] = 1$ means that all carbon is bound in CO molecules.

ratios of chemical to hydrodynamical time scales:

$$\frac{\langle k_1 \rangle_t}{\langle k_2 \rangle_t} < [\text{CO}]_{\text{eq,dyn}} < \left\langle \frac{k_1}{k_2} \right\rangle_t. \quad (7.28)$$

The right-hand case ($[\text{CO}]_{\text{eq,dyn}} \approx \langle k_1/k_2 \rangle_t$) represents instantaneous chemical equilibrium, i.e., the time scales are short compared to the hydrodynamical time scales ($t_{\text{CO}}^{\text{chem}} \ll t_{\text{hyd}}$). In the opposing case ($t_{\text{CO}}^{\text{chem}} > t_{\text{hyd}}$), the CO concentration is well approximated by

$$[\text{CO}]_{\text{eq,dyn}} \approx \frac{\langle k_1 \rangle_t}{\langle k_2 \rangle_t}. \quad (7.29)$$

Compared to the static case, the constant coefficients k_1 and k_2 in Eq. (7.25) are here replaced by the corresponding time averages. As seen in Eq. (7.23), k_2 is a highly non-linear function of the temperature. Consequently, the time average is governed by the high temperatures (due to shock waves). It is thus higher than the corresponding coefficient for the temporally averaged stratification:

$$k_2 \left(\langle n_{15} \rangle_t, \langle \tilde{T} \rangle_t \right) \leq \left\langle k_2 \left(n_{15}, \tilde{T} \right) \right\rangle_t \quad (7.30)$$

This results in a much smaller CO concentration than implied by the mean temperature. The limiting cases are plotted in Fig. 7.29.b for a zero and an infinite chemical time scale. The concentration of the dynamic model lies well between the extreme cases in the low photosphere but stays closer to the profile for high time ratios ($t_{\text{CO}}^{\text{chem}} \gg t_{\text{hyd}}$) in the layers above. Recall that there very short hydrodynamical time scales are present (see, e.g., Sect. 7.1.8 and Sect. 7.2). Finally, the characteristic time scale for the dynamical model can be stated as

$$t_{\text{CO}}^{\text{chem,dyn}} = \frac{1}{\langle k_2 \rangle_t}, \quad (7.31)$$

which is also shown in Fig. 7.29.a (dashed line).

7.6.4 Discussion

While the mean static and the (multi-dimensional) dynamic atmosphere result in the same concentration in the low photosphere ($z \lesssim 200$ km), dramatic differences are revealed in the layers above. First of all, the maximum values of the average concentrations diverge by nearly a whole magnitude. Moreover, the height distribution shows an almost constant plateau of high values in the upper layers of the static atmosphere but a restriction to the photosphere and low chromosphere otherwise. The fundamental difference clearly shows the importance of treating the CO problem time-dependently.

The decline of the CO concentration in the upper layers of the dynamic model is again due to higher fluctuations related to propagating waves and thus due to the reaction rates which are highly non-linear functions of temperature. The molecules are efficiently destroyed during the passage of high-temperature regions in shock fronts, where the chemical reaction time scales are short. The time scales are much longer in the subsequent cool episodes (see Sect. 7.1.7), slowing down the formation of molecules. Consequently, only moderate concentrations can be build up before the next shock wave arrives. The low CO concentration in the upper model atmosphere is thus a consequence of the onset of shock formation and the related higher temperature peaks above $z \sim 700$ km (see Sect. 7.2 and 7.4.1).

There is also a large difference in the effective chemical time scales for the static and the dynamic atmosphere (see Fig. 7.29.a), which increases with height. As discussed in the previous section, the time scale is significantly lowered due to the high-temperature portions in the dynamic case, whereas the average temperatures remain moderate and thus result in a higher time-scale. Moreover, the effective time scale is governed by the shortest times which are related to the highest temperature peaks and thus the propagating shock waves. The resulting difference is as large as $\gtrsim 2$ magnitudes in the chromosphere.

However, the time scales are still much larger than the hydrodynamical scales in the upper layers, so that the CO concentration might not be able to follow the quick temperature fluctuations. This is suggested by other works, too (see, e.g., Avrett et al. 1996). Hence, the correlation between CO concentration and temperature is probably poor. From this point of view, there might also be no connection between the existence of carbon monoxide and the cool regions, which are described in Sect. 7.1.7.

Finally, it must be emphasised that the calculations described above are just a beginning and still suffer from severe limitations. They can only serve as a first estimate of the height profile of [CO] under time-dependent conditions. It also becomes clear that improved simulations could contribute largely to the understanding of the presence of carbon monoxide molecules in the outer layers of the Sun. An improved modelling should take into account the following points:

1. time-dependent treatment of the (non-equilibrium) concentration (as done here in principle)
2. alternative formation channels, resulting in a more complete chemical reaction network which also takes into account multi-step reactions (see, e.g., Ayres & Rabin 1996; Uitenbroek 2000a)
3. back reaction of the CO concentration on the radiative cooling rate
4. advection of CO, i.e., the transport of molecules with the hydrodynamic flow

An example of an alternative formation mechanism via the molecule OH is described by Ayres & Rabin (1996) for which they quote time scales of only 20 s. On the other hand, the destruction time scale could be less than one second for a temperature of $T = 6000$ K, a temperature which is easily reached in shock waves in the hydrodynamical simulation. Thus, the formation time scales might be closer to the dynamical time scale in the solar photosphere and chromosphere whereas the destruction time scale implies almost instantaneous dissociation. A more complete list of reactions controlling the high-temperature H_2 - OH - CO chemistry is given in Table 2 by Ayres & Rabin (1996).

So far the existence of CO molecules is only taken into account in the grey opacity table from PHOENIX/OPAL (see Sect. 5.4.1), which of course can only account for a mean representative concentration for a given density and temperature (resp., internal energy). As revealed by this investigation a (quasi-)static approach might be very misleading, so that a fundamentally different picture can be expected from time-dependent simulations which include the back reaction of CO on its environment. Moreover, a full treatment of CO as cooling agent is likely to amplify the thermal bifurcation of the outer solar layers (see e.g., Ayres 1981; Anderson & Athay 1989b; Steffen & Muchmore 1988).

Further on, a model, which properly takes into account the transport of molecules with the atmospheric flow, is likely to result in a larger height extent of the region with significant CO concentration, while leaving the level of maximum [CO] largely unaffected. It is also not obvious how the horizontal distribution based on the hydrodynamical would look like, i.e., if there would be inhomogeneities with regions of higher concentrations or if the distribution would be uniform. At least, vertical columns like assumed by Ayres (2002) seem rather unrealistic in view of the dynamics at chromospheric heights. The investigation by Uitenbroek (2000a) implies that carbon monoxide is mainly concentrated above granules, matching the inverted granulation pattern which is visible in observations of CO lines (see Sect. 2.6). But since the investigation is based on a single snapshot from a hydrodynamical model and also instantaneous chemical equilibrium is assumed (see Sect. 2.6), the need for detailed calculations still remains.

Chapter 8

Dependence on Model Assumptions

A detailed error analysis seems difficult in view of the complexity of the applied radiation hydrodynamics code and the resulting data. Nevertheless, the influence of particular ingredients and parameters can be investigated by means of comparisons between different models. For this purpose, a number of two- and three-dimensional simulations has been performed, which are described in more detail in Chap. 6 (see also Tab. 6.1). Most parameters and ingredients are the same for all models – like the numerical grid and the entropy of the in-flowing material at the lower boundary ($s_{\text{inflow}} = 1.72 \times 10^9 \text{ erg K}^{-1} \text{ g}^{-1}$). On the other hand, pairs of models have been created which differ in only one essential parameter. Hence, the influence of the following numerical details

- **Spatial dimensions**
- **Opacity table**
- **Radiative transfer**
- **Tensor viscosity**

can be analysed for the following set of selected aspects:

- **Temperature stratification**
- **Temperature fluctuations**
- **Velocity fluctuations and generation of acoustic flux**
- **Power spectra for plane-parallel oscillation modes**
- **Emergent radiative flux and chromospheric maximum of the flux divergence**

8.1 Model Sample

The basic set of models, which is used for the comparisons, is listed in Tab. 8.1. It comprises pairs of models which only differ in one of following parameters/ingredients: Spatial dimension, opacity table, or radiative transfer scheme. Additionally, the influence of the amount tensor viscosity has been investigated for some selected aspects.

Two- and three-dimensional simulations with PHOENIX/OPAL and ATLAS6 opacity tables are available. The main difference between the two grey opacity sets is the inclusion of molecular contributions in PHOENIX (see Sect. 5.4.1). Thus, the comparison mainly points out

Table 8.1: Sample of models which is used for investigating the influence of particular model assumptions. See Chap. 6 for more information about the individual models.

- **Spatial dimensions:** 2-D ↔ 3-D:
 - 2DgPO ↔ 3DgPO,
 - 2DgA6 ↔ 3DgA6,
 - 2DnA6 ↔ 3DnA6;

- **Opacity table:** PHOENIX/OPAL ↔ ATLAS6:
 - 2DgPO ↔ 2DgA6,
 - 3DgPO ↔ 3DgA6;

- **Radiative transfer:** grey ↔ non-grey (multi-group):
 - 2DgA6 ↔ 2DnA6,
 - 3DgA6 ↔ 3DnA6;

- **Tensor viscosity**
 - 2DgPO: $C_{\text{vis}} = 0.1 \leftrightarrow 0.3 \leftrightarrow 0.5 \leftrightarrow 1.0$
 - 3DgPO: $C_{\text{vis}} = 0.1 \leftrightarrow 0.5$

the effect of the molecular contributions. Alternatively to the grey radiative transfer, also a multi-group scheme was applied (see Sect. 5.4). However, the frequency-dependent multi-group opacities are only available from ATLAS6. For the investigation of the influence of the amount of tensor viscosity on some selected aspects of this thesis, the numerical parameters $C_{\text{visArtificial}}$ and $C_{\text{visSmagorinsky}}$, which control the contribution of the artificial and the Smagorinsky type viscosity, are always set equal:

$$C_{\text{vis}} = C_{\text{visArtificial}} = C_{\text{visSmagorinsky}}. \quad (8.1)$$

8.2 Temperature Stratifications

As mentioned in Sect. 7.4.2, no significant temperature minimum – as exhibited by “classical” semi-empirical models (see Sect. 3.1) – is found in the average gas temperature of the three-dimensional reference model 3DgPO. As can be seen in Fig. 8.1, this is also true for the other models which are analysed in this chapter. In contrast, a well-defined minimum is present for the average emissivity temperature for all models with grey radiative transfer. The simulations with multi-group scheme, however, result in a slightly decreasing temperature for most of the height range. A qualitatively similar behaviour is also revealed on the optical depth scale, although the grey models show a small increase of the average gas temperature for small optical depths. In Tab. 8.2 the average gas and emissivity temperatures for selected geometrical heights and optical depths are stated. Additionally, the emissivity temperature minima are listed.

Spatial dimensions: In the upper layers, there are differences of up to $\sim 400 - 500$ K in the average gas temperature of the grey 2-D and 3-D models, whereas the non-grey simulations diverge by less than 100 K in the middle chromosphere. However, in the non-grey case large differences are found in the photosphere. The non-grey profiles for the average emissivity temperature also diverge by up to ~ 300 K in the middle chromosphere and neither exhibit a

Table 8.2: Average temperature values and temperature fluctuations are listed for selected geometrical heights and optical depths, as well as the minima of the emissivity temperature on both scales. Note that the non-grey simulations do produce no well-defined temperature minimum. P/O stands for PHOENIX/OPAL opacities, A6 for ATLAS6 opacities, and m-g for multi-group.

Model	Unit	2DgPO	2DgA6	2DnA6	3DgPO	3DgA6	3DnA6
Dimensions		2-D	2-D	2-D	3-D	3-D	3-D
Opacity		P/O	A6	A6	P/O	A6	A6
Rad. transport		grey	grey	m-g	grey	grey	m-g
Average gas temperature at fixed geometric heights:							
$T_{g,z}$ ($z = 500$ km)	[K]	3635	3634	3891	4308	4324	4404
$T_{g,z}$ ($z = 1000$ km)	[K]	3322	3394	3723	3744	3735	3795
Minimum of average emissivity temperature on geometric height scale:							
$T_{em,z,min}$	[K]	4541	4608	—	4545	4647	—
$z(T_{em,z,min})$	[km]	403	379	—	535	511	—
Average emissivity temperature at fixed geometric heights:							
$T_{em,z}$ ($z = 500$ km)	[K]	4680	4850	4536	4551	4647	4517
$T_{em,z}$ ($z = 1000$ km)	[K]	5775	6343	4408	6235	6383	4074
Average gas temperature at fixed optical depths							
$T_{g,\tau}$ ($\log \tau = -2$)	[K]	4346	4485	4488	4603	4702	4677
$T_{g,\tau}$ ($\log \tau = -4$)	[K]	4236	4464	4032	4272	4371	4242
Minimum of average emissivity temperature on optical depth scale:							
$T_{em,\tau,min}$	[K]	4440	4497	—	4420	4510	—
$z(T_{em,\tau,min})$		-2.2	-2.4	—	-3.4	-3.3	—
Average emissivity temperature at fixed optical depths:							
$T_{em,\tau}$ ($\log \tau = -2$)	[K]	4461	4560	4576	4619	4719	4692
$T_{em,\tau}$ ($\log \tau = -4$)	[K]	5746	5457	4471	4557	4671	4284
Temperature fluctuation on geometric height scale:							
dT_{rms}/T_0 at $z = 0$ km		0.25	0.27	0.30	0.22	0.23	0.22
dT_{rms}/T_0 at $z = 200$ km		0.11	0.12	0.14	0.04	0.05	0.04
dT_{rms}/T_0 at $z = 1000$ km		0.41	0.41	0.24	0.38	0.38	0.13
Temperature fluctuation on optical depth scale:							
dT_{rms}/T_0 at $\log \tau = 1.0$		0.09	0.09	0.08	0.09	0.09	0.09
dT_{rms}/T_0 at $\log \tau = -0.5$		0.04	0.04	0.05	0.02	0.02	0.02
dT_{rms}/T_0 at $\log \tau = -5.0$		0.40	0.32	0.24	0.30	0.28	0.10

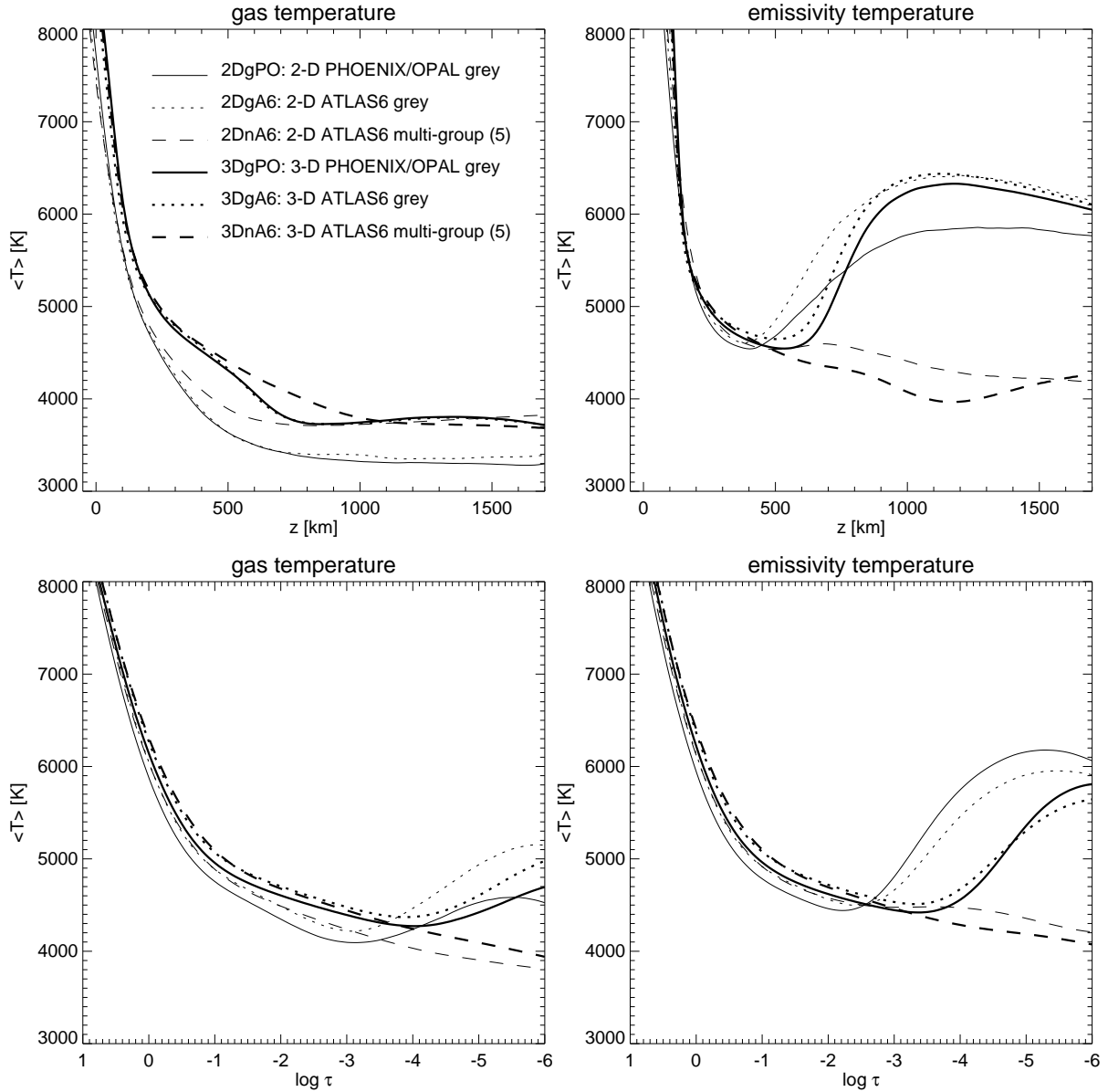


Figure 8.1: Temperature stratifications for the basic set of models on the geometric height scale (upper panels) and on the optical depth scale (lower panels). Average gas temperatures are plotted on the left and average emissivity temperatures on the right, respectively.

well-defined minimum nor a strong increase in the upper layers. In contrast, all grey models feature a temperature minimum of $T_{\text{em},z,\text{min}} = 4540 - 4650$ K. The spatial dimension has only little influence on the minimum value on its height. In two-dimensional models the minimum is found at lower heights and the surrounding “low-temperature basin” is confined to a smaller vertical extent. The same qualitative picture applies to the stratifications on the optical depth scale, although the deviations of the average temperature are in general smaller.

Opacity tables: The choice of the opacity table has only limited influence on the temperature stratifications, i.e., mostly $\Delta T \lesssim 100$ K. This is also true for the emissivity temperature minimum, whereby the difference is larger in 2-D than in 3-D. The optical depth scales, which are

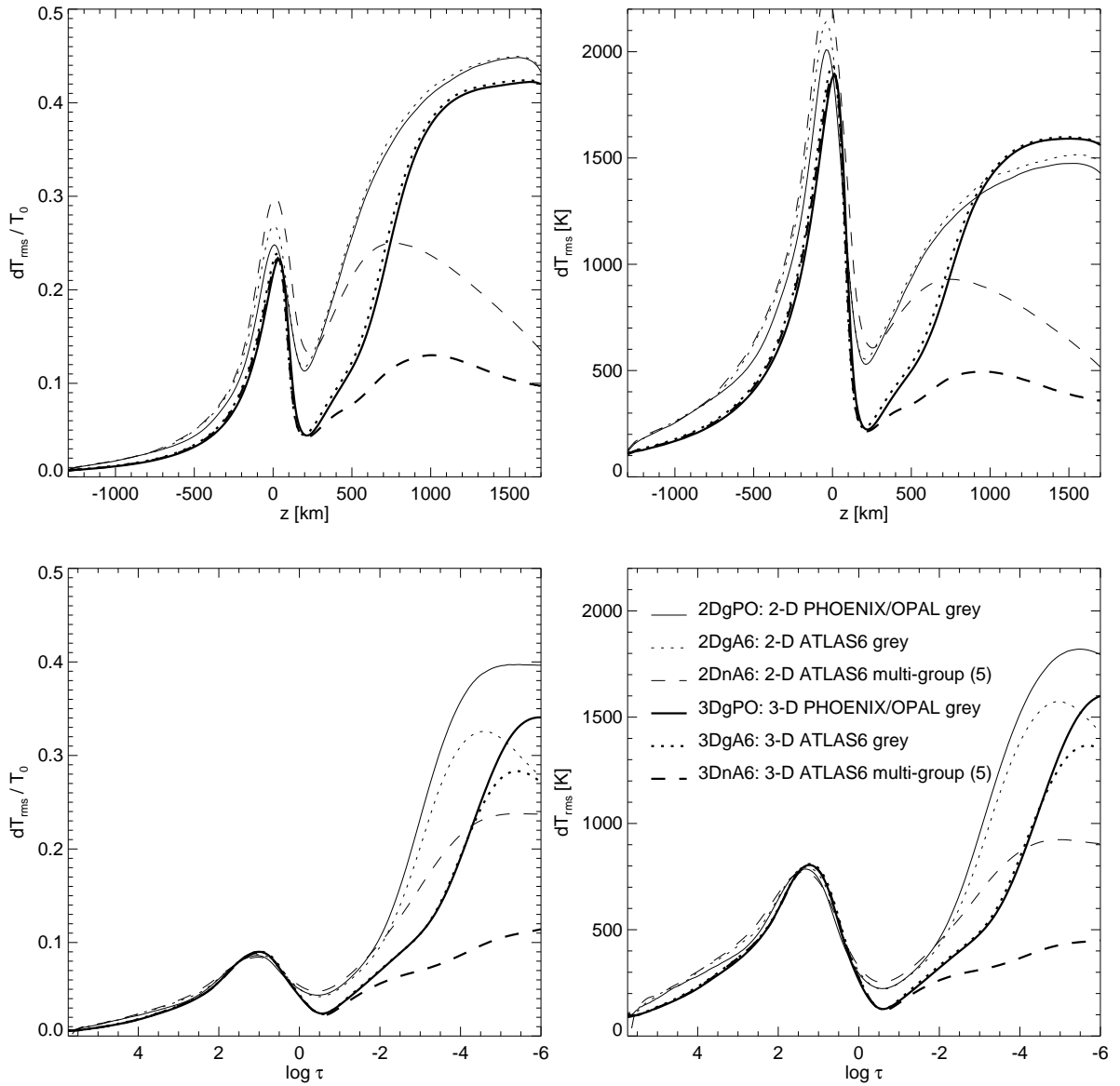


Figure 8.2: Temperature fluctuation for different models on the geometric height scale (upper panels) and on the optical depth scale (lower panels). The fluctuations are plotted as relative quantities dT_{rms}/T_0 on the left and as absolute quantities dT_{rms} on the right.

of essential importance for the averaging procedure, are of course directly affected by differences in the opacities so that the profiles diverge stronger on the τ scale. There, the gas temperatures obtained with the PHOENIX/OPAL table are generally lower than for the ATLAS6 table, whereas the situation is vice versa in case of the emissivity temperature.

Radiative transfer: The simulations with grey and multi-group radiative transfer differ fundamentally with respect to the chromospheric temperature stratifications. The picture is the same for both types of temperature mean and on the geometrical height scale as well as on the optical depth scale, the picture is the same: The profiles are identical to the grey case in the photosphere and below, while the differences become increasingly larger in the higher layers.

The emissivity temperatures even differ by > 2000 K at geometrical heights in the chromosphere, indicating the crucial importance of a proper treatment of the radiative transfer under chromospheric conditions.

8.3 Temperature Fluctuations

Let us first recall the definition of the rms-temperature fluctuation:

$$\frac{dT_{\text{rms}}}{T_0} = \frac{\sqrt{\langle (T - T_0)^2 \rangle_{x,y,t}}}{T_0}. \quad (8.2)$$

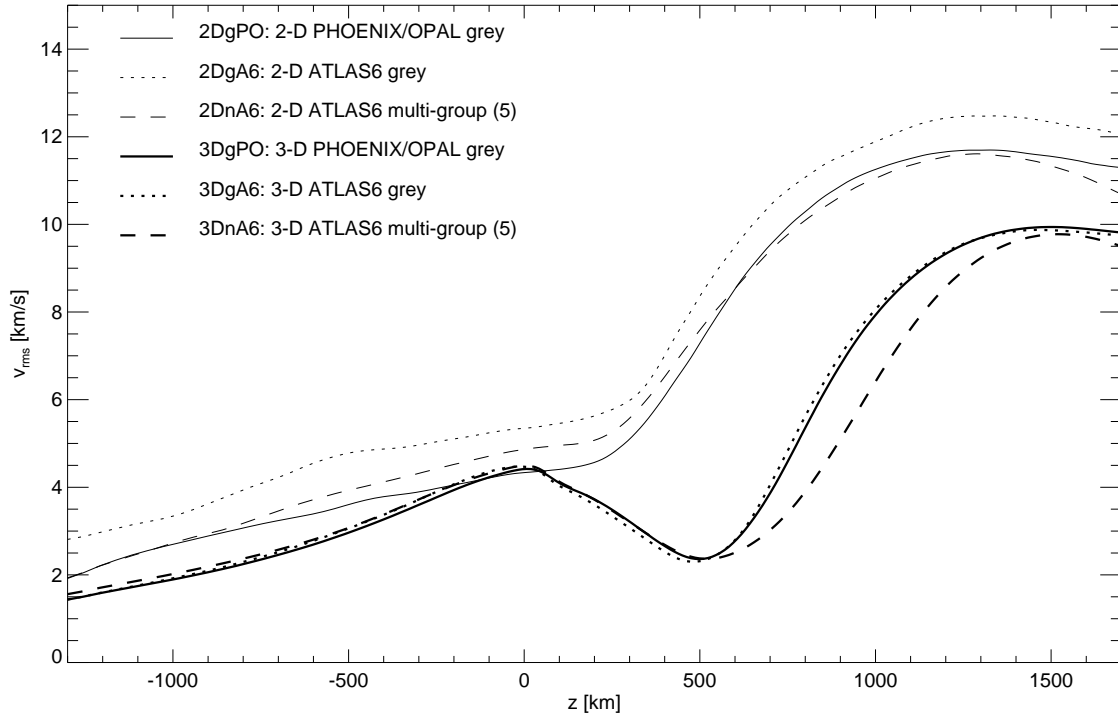
Here, $T_0 = \langle T \rangle_{x,y,t}$ is the temporally and horizontally averaged gas temperature. In Tab. 8.2, values are listed for exemplary geometrical heights and optical depths. Moreover, height-dependent profiles are plotted for the basic set of models in Fig. 8.2 on the geometric height scale and on the optical depth scale. Note that in the latter case, the averages in Eq. (8.2) are calculated on surfaces of equal optical depth τ instead of equal geometrical height z . While the τ -surfaces are shaped by the inhomogeneities in the atmosphere, the rigid z -planes just cut through the structures and thus yield larger fluctuations. The differences between the scales is largest near the maxima at the boundary between photosphere and convection zone ($z \sim 0$ km and $\log \tau \lesssim 0$), owing to the large temperature gradients exhibited by the regarded layer.

Spatial dimensions: The influence of the spatial dimension on the temperature fluctuations is obviously negligible in the convection zone. In the layers above, however, the models with only two dimensions generate larger fluctuations than the three-dimensional models. This can be attributed to the common finding that two-dimensional simulations exhibit more vast motions, while the third spatial dimension has compensative influence.

Opacity tables: The grey opacity tables have obviously only negligible influence on the results, except for the uppermost layers on the optical depth scale. These still moderate differences are due to the different τ -surfaces which result from the different opacities.

Radiative transfer: The situation is very different for the comparison of models with grey and non-grey radiation transport. While there is no difference below the middle photosphere, the height profiles of dT_{rms} diverge dramatically in the chromosphere. This indicates the importance of an appropriate treatment of radiative transfer under chromospheric conditions.

Tensor viscosity: The models with a different amount of tensor viscosity show the same qualitative height variation than the basic set of models. In the two-dimensional case, however, a larger viscosity of $C_{\text{vis}} = 1.0$ produces a height variation of the temperature fluctuation which closely matches the result for the three-dimensional reference model, while a lower viscosity tends in the opposite direction. The parameter C_{vis} affects mostly the profiles above the middle photosphere and has only negligible influence on the lower layers. The analysed 3-D models, however, show no notable difference in terms of dT_{rms} at all. The rms-temperature fluctuations of the three-dimensional reference model are thus robust against a change of the amount of tensor viscosity which is a very reassuring result.

Figure 8.3: Velocity fluctuations v_{rms} for the basic set of models.

8.4 Velocity Fluctuations and Acoustic Flux Generation

The rms-fluctuations of the absolute velocity

$$v = \sqrt{v_x^2 + v_y^2 + v_z^2} \quad (8.3)$$

are defined as

$$v_{\text{rms}} = \sqrt{\langle (v - v_0)^2 \rangle_{x,y,t}}, \quad (8.4)$$

where v_0 is the horizontal and temporal average. The resulting height-dependent v_{rms} profiles for the basic set of models and for the additional models with different amounts of tensor viscosity are presented in Fig. 8.3 and Fig. 8.4.a, respectively. Values for the velocity fluctuations are listed in Tab. 8.4 for exemplary heights, which are chosen to represent the most prominent features of the v_{rms} profiles.

In principle, they look like the rms-temperature fluctuations discussed in Sect. 8.3, i.e., small values in the lower layers, a local maximum near the boundary between convection zone and

Table 8.3: Velocity fluctuations of different models at selected geometrical heights.

Model	Unit	2DgPO	2DgA6	2DnA6	3DgPO	3DgA6	3DnA6
$v_{\text{rms}}(z = 0 \text{ km})$	$[\text{km s}^{-1}]$	4.33	5.35	4.87	4.41	4.47	4.49
$v_{\text{rms}}(z = 500 \text{ km})$	$[\text{km s}^{-1}]$	7.28	8.36	7.59	2.36	2.31	2.38
$v_{\text{rms}}(z = 1500 \text{ km})$	$[\text{km s}^{-1}]$	11.55	12.33	11.34	9.94	9.87	9.77

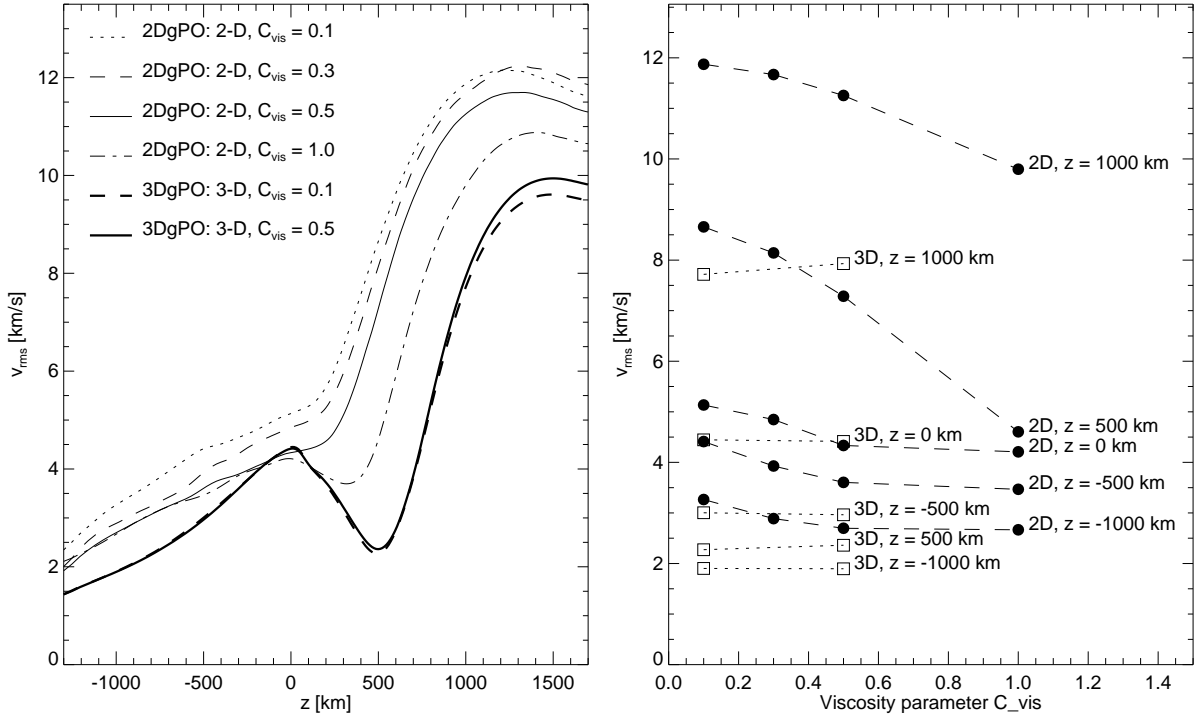


Figure 8.4: Velocity fluctuations v_{rms} for models with different viscosity parameter C_{vis} . **a)** Variation with height; **b)** Variation with viscosity for particular heights.

photosphere, and a strong increase in the chromosphere. The influence of particular model assumptions is also similar. Unfortunately, the v_{rms} profiles for the 2-D model exhibit no well-defined maximum in the convection zone – with exception of 2DgPO ($C_{\text{vis}} = 1.0$). In contrast, all three-dimensional models allow the determination of the local maximum which is regarded as an average convective velocity v_{conv} . The convective velocity is of particular interest since it can be used to estimate the generation of acoustic flux. Following the *Lighthill-Stein* theory, the acoustic flux is proportional to the eighth power of the convective velocity (see Sect.2.7.2). The obtained results are listed in Tab. 8.4. Now, the influence of the model assumptions can be investigated in terms of the rms-velocity fluctuations and the related generation of acoustic flux.

Table 8.4: Convective velocities and generation of acoustic flux for different three-dimensional models.

model	v_{conv} [km s ⁻¹]	v_{conv}^8 [10 ⁵ km s ⁻¹]
3DgPO ($C_{\text{vis}} = 0.5$)	4.432	1.488
3DgPO ($C_{\text{vis}} = 0.1$)	4.450	1.538
3DgA6	4.474	1.604
3DnA6	4.493	1.660

Spatial dimensions: In contrast to the three-dimensional models, which form a close group for most of the height range, the influence of particular parameters and ingredients is more pronounced in the 2-D case. Similar to dT_{rms} , two-dimensional models produce larger fluctuations. Here, profiles for simulations of different spatial dimension diverge already in the convection zone. Moreover, the differences become as large as $\gtrsim 5 \text{ km s}^{-1}$ in the upper layers. Hence, fluctuations in 2-D can be up to a factor ~ 3 larger than in 3-D. This point emphasises the importance of the third spatial dimension for modelling the dynamics.

Opacity tables: In the 2-D case, using ATLAS6 opacities produces an almost constant increase of order 1 km s^{-1} with respect to PHOENIX/OPAL opacities. The three-dimensional models, however, reveal no significant influence of the opacity tables. Hence, the inferred convective velocities are very similar, resulting in only $\approx 7 \%$ more acoustic flux for the ATLAS6 table. This is remarkably similar if one considers that the velocities were raised by a power of eight.

Radiative transfer: In two dimensions the difference which arises from the different radiative transfer schemes is of order $\sim 1 \text{ km s}^{-1}$ for the whole height range, whereas for the three-dimensional models the effect is not present in the lower layers and still small in the chromosphere. Consequently, the derived convective velocities are almost identical and produce only a acoustic flux difference of $< 4 \%$.

Tensor viscosity: As seen for the temperature fluctuations, a larger amount of tensor viscosity in the two-dimensional simulations produces v_{rms} profiles which are closer to the 3-D results (see Fig. 8.4). Hence, only the 2-D model with the largest parameter $C_{\text{vis}} = 1.0$ exhibits a well-defined local maximum at the bottom of the photosphere.

In three dimensions, however, the viscosity has only little influence on the rms-velocity fluctuations. The reference model (3DgPO, $C_{\text{vis}} = 0.5$) has an only slightly smaller convective velocity than the model with decreased viscosity (3DgPO, $C_{\text{vis}} = 0.1$), leading to a difference of only $\sim 3 \%$ for the generation of acoustic flux in the convection zone.

8.5 Power Distribution

Despite differences in the amplitudes of particular oscillation modes, the general picture is the same for all models. Oscillations with periods near 5 min dominate in the photosphere (Fig. 8.5.a), while significant contributions in the 3 min range are present in the chromosphere (Fig. 8.5.b, see also Tab. 8.5). The integrated power within the 5 min and 3 min bands are shown in Fig. 8.5.c and d as functions of height, respectively. Obviously, all models show a transition from a dominating 5 min band to a “chromospheric” 3 min band. However, there are differences with respect to power values and the height where the power in both bands is equal. The latter is marked by squares in Fig. 8.5 and are also listed in Tab. 8.5. The heights can be regarded as dividing line between the regimes of the two different dominating oscillation periods. Please refer to Sect. 7.3.3 for the definition of the adopted frequency bands.

Unfortunately, the compared model sequences are of different duration, which causes unequal frequency resolution of the power spectra. Thus, the comparison should be regarded as qualitative only until all simulations can be continued towards larger and equal durations. In particular the influence of the ATLAS6 grey opacities is unexpectedly large for unknown reasons, although the effected models show the same qualitative power distribution as the others. Hence, only the influence of the spatial dimensions and the radiative transfer modus yields clear conclusions.

Spatial dimensions: Higher spatial dimension causes larger contributions of the 5 min band in the lower layers of up to $\sim 14 \%$. Thus, the heights where the 3 min oscillations take over

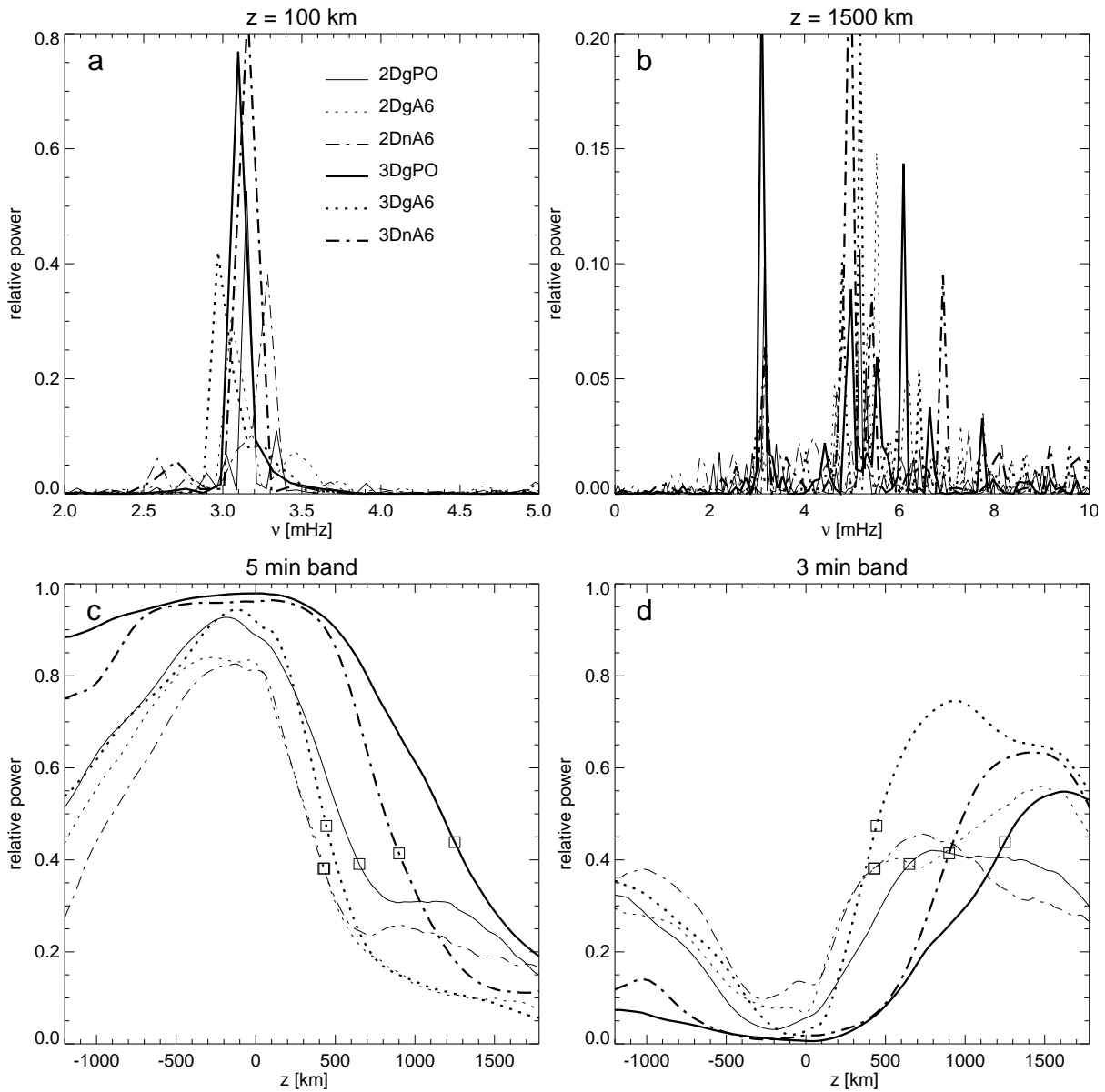


Figure 8.5: Power spectra for plane-parallel oscillations in different models. **a-b)** Power spectra at $z = 100$ km and $z = 1500$ km, respectively. **c)** Integrated power in the 5 min band and **d)** in the 3 min band. Squares mark the heights where the power in the 5 min and 3 min band are equal.

are shifted upwards from the low chromosphere in 2-D to its middle part in 3-D – with the mentioned exception of the grey ATLAS6 case. The situation is not that clear for the 3 min band in the upper layers and should thus not be interpreted quantitatively. However, in 2-D there are significant 3 min contributions in the lower part of the convection zone.

Radiative transfer: Again, differences between grey and non-grey radiative transfer become only significant above the photosphere, where deviations from both schemes occur.

8.6 Radiative Flux

The radiative flux, which is emitted at the upper boundaries of the models, varies by $\sim \pm 10\%$ around a reference value of $F_{\text{ref}} = 6.28 \times 10^{10} \text{ erg cm}^{-2} \text{ s}^{-1}$ which corresponds to the flux of the Sun, or in other words, to an effective temperature of 5780 K (see Sect. 2.7 and 4.4.8). Obviously, the same in-flowing entropy at the lower boundary leads to a different energy output at the top.

Furthermore, there are large differences in the divergence of the radiative energy flux (∇F_{rad}), although the height profiles are qualitatively similar for all models. (Refer to Fig. 7.27 for an example.) However, in particular the chromospheric maximum value of ∇F_{rad} depends strongly on the adopted model assumptions and with it the vertical position of the peak and the height where the flux divergence gets positive. Note that the presented averages depend strongly on the number of grid cells at a particular height and the available duration of the simulation, rendering the results inferred from 3-D simulations more reliable (see Sect. 7.5.3).

Spatial dimensions: All comparisons between simulations of different spatial dimensions point out that in 2-D the emergent flux at the upper boundary is reduced by a factor 0.85 – 0.88 with respect to the 3-D case. On the other hand, the chromospheric maximum radiative flux divergence is ~ 5 to ~ 9 times higher for the two-dimensional models. Hence, using an only two-dimensional approach for the simulation of the chromospheric energy balance is no good idea.

Opacity tables: The influence of the opacity table is not that drastic, although the emergent radiative flux is reduced by $\sim 10\%$ if PHOENIX/OPAL opacities are used instead of ATLAS6. Also, the peak value ($\max(\langle \nabla F_{\text{rad}} \rangle)_{\text{chromo}}$) is reduced by a factor of 0.6 – 0.8 for PHOENIX/OPAL compared to ATLAS6.

Radiative transfer: The two applied methods for the radiative transfer produce results which diverge by only $\lesssim 7\%$ in terms of emergent flux. On the other hand, the radiative flux divergence is strongly affected. Using a grey radiative transfer results in 5 – 7 times higher values for

Table 8.5: Power in the bands for plane-parallel 5 min and 3 min oscillations in different models at fixed heights at the top of the convection zone and in the middle chromosphere. Also, the heights and power values are listed where the power of both bands is equal.

Model	Unit	2DgPO	2DgA6	2DnA6	3DgPO	3DgA6	3DnA6
Power in 5 min band for fixed heights:							
$P_{5\text{min}} (z = -100 \text{ km})$		0.92	0.83	0.82	0.98	0.94	0.96
$P_{5\text{min}} (z = 1500 \text{ km})$		0.24	0.10	0.19	0.29	0.09	0.12
Power in 3 min band for fixed heights:							
$P_{3\text{min}} (z = -100 \text{ km})$		0.04	0.08	0.13	0.01	0.02	0.01
$P_{3\text{min}} (z = 1500 \text{ km})$		0.38	0.56	0.31	0.54	0.65	0.63
Height of equal power in 5 min and 3 min bands:							
P_{eq}		0.40	0.38	0.38	0.44	0.47	0.41
$z (P_{\text{eq}})$	[km]	670	430	427	1258	443	907

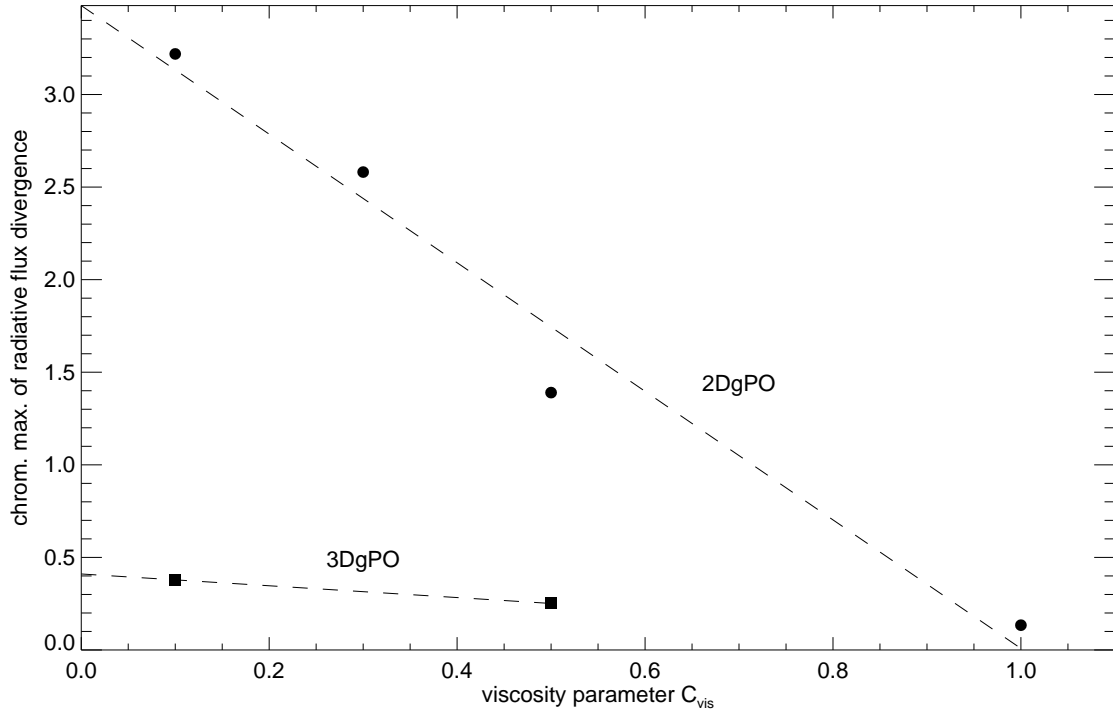


Figure 8.6: Chromospheric maxima of the radiative flux divergence as function of the viscosity parameter C_{vis} . The values for the 2-D models (2DgPO) and the 3-D models (3DgPO) are marked by solid dots and solid squares respectively. Additionally, the dashed lines represent the results from linear regression for both groups separately.

the chromospheric peak with respect to the multi-group scheme.

Tensor viscosity: Finally, the influence of the tensor viscosity on the flux divergence can be analysed. Fig. 8.6 shows the chromospheric peak values as function of the adopted viscosity parameter C_{vis} , revealing the strong dependence on the amount of viscosity. In two and in three dimensions the chromospheric maximum of the radiative flux divergence decreases for larger C_{vis} , although the effect is obviously not that drastic in the 3-D case.

Table 8.6: Radiative flux at the upper boundaries of different model in units of $F_{\text{ref}} = 6.28 \times 10^{10} \text{ erg cm}^{-2} \text{ s}^{-1}$ and chromospheric maxima of the radiative flux divergence.

Model	2DgPO	2DgA6	2DnA6	3DgPO	3DgA6	3DnA6
Radiative flux at model top:						
$\langle F_{\text{rad}} \rangle_{x,y,t} / F_{\text{ref}}$	0.871	0.972	0.912	1.022	1.108	1.076
Divergence of radiative flux:						
$\max(\langle \nabla F_{\text{rad}} \rangle) _{\text{chromo}}$ [erg cm ⁻³ s ⁻¹]	1.39	2.30	0.46	0.25	0.33	0.05
z_{max} [km]	564	540	696	768	732	792

8.7 Summary

Finally, the results which are most relevant for this thesis can be summarised as follows:

- The velocity fluctuations of the three-dimensional models turn out to be very robust with respect to the different opacity tables, radiative transfer schemes, and different amount of tensor viscosity.
- Owing to the similar velocity fluctuations, the generation of acoustic flux in the three-dimensional reference model differs not more than $\sim 10\%$ for the various analysed model assumptions.
- Despite quantitative differences, all analysed models show the same qualitative power distribution for plane-parallel oscillations which are dominant for periods near 5 min in the lower layers and near 3 min in the chromosphere.
- The grey radiative transfer and the multi-group scheme produce fundamental differences in the temperature fluctuations and the average emissivity temperature stratification of the chromospheric layers. However, this does not necessarily mean that the grey radiative transfer is unrealistic. Rather, the opacity bands used in the multi-group scheme are optimised for the photosphere and might thus not be appropriate for the higher layers.
- The chromospheric maximum of the radiative flux divergence depends strongly on the prescribed amount of tensor viscosity, although the effect is much smaller in 3-D than in 2-D.
- Due to the additional spatial dimension, 3-D simulations exhibit less vigorous dynamics as in the 2-D case, leading to large differences for almost all analysed aspects of the model atmosphere. Two-dimensional models tend to be more extreme.
- The influence of the analysed model assumptions mostly tends to be smaller in the lower layers.
- In contrast to the temperature fluctuations, the general topology of the chromospheric pattern and the corresponding spatial scales are not affected by using a different radiative transfer or opacity table.

Note that these conclusions are based on the selected parameters only. Obviously, particular model assumptions cause differences in the fluctuations and average stratifications of the temperature and thus differences in depending properties like the extent of thermal bifurcation, duration and size of cool episodes and cool regions for a fixed threshold of $T_{\text{thres}} = 3700$ K, respectively, and inferred chromospheric temperature components. The divergence of the radiative flux seems to be another point which is worthwhile to be investigated in more detail in future studies. However, many of the mentioned uncertainties at chromospheric heights are connected to the difference between the grey radiative transfer and the applied multi-group scheme. In order to check which is more realistic, the results should be compared to alternative radiative transfer schemes which are more appropriate for chromospheric conditions.

On the other side, the lower layers of the three-dimensional reference model are only affected to a small extent and, moreover, the dynamics in the 3-D models are largely unsusceptible to changes of the analysed parameters. This is very reassuring in view of the various phenomena which require a realistic modelling of the underlying dynamics. Thus, the qualitative picture of a dynamically bifurcated chromosphere remains even if some numerical details are not perfectly adjusted to chromospheric conditions so far.

Chapter 9

Conclusions

The *dynamic thermal bifurcation* and the related inhomogeneous appearance of the non-magnetic three-dimensional model chromosphere can be regarded as the essential result of this thesis. The spatially and temporally intermittent structure is caused by interaction of *propagating hydrodynamic shock waves*, which are generated by processes related to convective motions and oscillations in the lower layers. The structure, which can also be understood as *interference pattern*, consists of *cool regions* with remarkably low temperatures and a mesh of hot shocked material. The co-existence of low and high temperatures thus allows for molecular features *and* chromospheric emission lines in the emergent spectrum. Hence, the presented model is in principle capable of reproducing the different diagnostics in a self-consistent way, solving the controversial debate which arose in the last decades.

Recent observations, for instance performed with the *Dutch Open Telescope* (DOT, see Rutten et al. 2002), provide an excellent spatial resolution (see Sect. 2.4). Observations in the light of Ca II *H* thus reveal a mesh-like pattern which is ubiquitous in internetwork regions. The mesh consists of very narrow bands of enhanced emission on spatial scales which are comparable to the underlying granulation and is commonly interpreted as interference of oscillations and propagating acoustic (shock) waves (e.g., Krijger et al. 2001, see Sect. 2.4). It is remarkably similar to the temperature slices in the model chromosphere which are indeed due to interference of purely hydrodynamic waves. Hence, the presented numerical simulations give not only strong support for the interpretation of the observations, but also enable detailed investigations of the responsible mechanisms. However, the similarity demands further detailed comparisons between observations and theoretical models which are essential to make progress in understanding the nature of the non-magnetic solar chromosphere.

A major advantage of the models presented in this thesis is the fact that they are self-consistent, i.e., no piston is needed at the lower boundary in order to excite propagating and standing acoustic waves. Rather, the wave excitation comes for free as result of the motions in the modelled convective layers. In the lower part of the models oscillations with periods near 5 min dominate, while this role is assigned to modes in the 3 min band in the (middle) chromosphere. Since this is in qualitative agreement with observations, the numerical models provide a – at least qualitatively – correct picture of the underlying oscillation modes.

A comprehensive model must be capable of explaining the large variety of dynamic phenomena exhibited by the outer layers of the Sun like, e.g., the prominent Ca II *H+K bright points*. Thus, correct modelling of the underlying dynamics is of great importance. The three-dimensional reference model meets basic observational constraints, as various aspects of the analysis showed – for instance, the convincing reproduction of the *granulation* pattern. Hence, the modelled dynamics can be regarded as a reliable foundation.

Furthermore, it must be emphasised that the thermal bifurcation is caused by interaction of hydrodynamical waves and *not* due to radiative cooling by *carbon monoxide* molecules. In the present numerical simulations, CO is only taken into account in the grey opacity tables where the influence of the corresponding molecular opacity contributions seems to be of minor importance (see Chap. 8). However, the real influence of carbon monoxide might be underestimated, and a more detailed treatment of CO as cooling agent could even amplify the thermal bifurcation (see Sect. 2.6.1). Moreover, the CO distribution in the solar atmosphere needs further clarification since it provides – next to UV diagnostics – important observational constraints. The calculations described in Sect. 7.6 demonstrate that there is a non-negligible amount of carbon monoxide present in the lower chromosphere, as implied by observations.

Many aspects can already be modelled very realistically, and do depend on particular model assumptions only to small extent. The lower layers of the model, i.e., the photosphere and below, have been adopted from earlier well-established 3-D simulations and, moreover, are unsusceptible for changes of the analysed numerical details (see Chap. 8). The lower part of the three-dimensional reference model can thus be regarded as reliable. Consequently, the topology of the chromospheric pattern, which arises from the dynamics of the lower layers, and its spatial and temporal scales are very similar for different model assumptions even if compared to the non-grey case. In contrast, the temperature fluctuations, and thus the temperature contrast of the chromospheric pattern, depend on particular parameters and ingredients. Hence, related implications like the extent of thermal bifurcation and the nature of cool regions, have to be interpreted with some caution. On the one hand, this leads to the conclusion that some details of CO⁵BOLD – in particular the radiative transfer – need to be reviewed for chromospheric conditions, on the other, the remarkable agreements with observational constraints are very reassuring and allow to address the questions posed at the beginning of this thesis:

- *Is there a real temperature increase in the chromosphere or is it just an artefact due to too simple modelling?*

As seen in Sect. 7.4.2, the temporally and horizontally averaged gas temperature of the three-dimensional reference model stays almost constant in the chromosphere, instead of featuring a prominent temperature minimum and an outward directed temperature rise as in “classical” semi-empirical models (see Sect. 3.1). As Carlsson & Stein (1994) inferred on basis of their elaborate one-dimensional simulations (see Sect. 3.5), the temperature profile of the semi-empirical models can be reproduced if the strong non-linearity of the UV *Planck* function is taken into account. This behaviour is simulated by means of an emissivity temperature, which for the three-dimensional reference model indeed reveals a temperature similar to “classical” models. This can be regarded as strong evidence that – as Carlsson & Stein stated – the chromospheric minimum and the increase above are artefacts due to the neglect of temporal and horizontal fluctuations and their non-linear translation into intensities for the construction of the classical models. Hence, the radiative emission, which was thought to be connected to a general temperature rise, can be sustained by hot propagating shock waves alone.

- *How important are spatial and temporal inhomogeneities for a proper description of the outer solar layers?*

The point above already made clear that temporal and spatial inhomogeneities cannot be neglected for the construction of a representative temperature stratification. The same applies to a wide variety of other properties, although the influence of inhomogeneities

differs. However, the dynamics of the outer solar layers, which are manifested by many phenomena like Ca II *H+K* bright points call for time-dependent modelling. Furthermore, observations reveal patterns on a wide range of different spatial scales, ranging from giant convection cells down to the small-scale background pattern of internetwork regions. A realistic comprehensive model thus also cannot neglect spatial inhomogeneities.

Another point should be stated in view of the inhomogeneous nature of the outer layers, namely the formation heights of spectral lines. It is obvious that regions which contribute to the formation of a spectral feature – at least if it originates from the chromosphere – can be distributed in a complicated pattern along the line of sight, rather than in a well-defined height range. Stating a formation height can thus be very misleading and should only be interpreted in an average sense.

- *What is required for a realistic model which is capable of explaining all diagnostics?*

The required ingredients of a model are governed by the underlying intention. For instance, “classical” semi-empirical models were constructed to reproduce average atmospheric properties based on a selected set of observations. By nature, this class of models cannot provide a consistent picture, which includes all diagnostics and observed phenomena. Such one-dimensional static models are perhaps sufficient to describe selected features of the photosphere, where the temperature is closely distributed around an average stratification, but can only represent limited aspects of the chromosphere.

Multi-component models with separate stratifications for a hot and a cool component in different proportions (see Sect. 3.4) provide a much better description of the thermal bifurcation but still cannot account for temporal variations.

Hence, the temporal and spatial inhomogeneities of the outer solar atmosphere ultimately demand a dynamic, three-dimensional approach, which comprises all relevant physical processes. This includes in particular a proper description of chromospheric conditions with, e.g., non-equilibrium ionisation and non-LTE frequency-dependent radiative transfer, taking into account scattering and the explicit role of major cooling agents like, e.g., Ca II *H+K*.

- *Can the observed radiative emission of the quiet solar chromosphere be sustained by heating due to dissipation of acoustic waves?*

In the three-dimensional reference model more mechanical energy is dissipated in the low chromosphere than derived from semi-empirical models. Moreover, the resulting Ca II and Mg II fluxes are high enough to explain the basal flux in solar-type stars. Based on these results, no additional heating by magnetic effects seems to be necessary for the low and middle chromosphere of the hydrodynamical model. However, there is in particular a large difference between models with grey radiation transport and with the applied multi-group scheme. Hence, the divergence of the radiative energy flux remains uncertain to some extent. A quantitative answer to the above question, however, requires further improvements of the modelling with respect to a detailed chromospheric energy balance.

Finally, one can conclude that state-of-the-art three-dimensional radiation hydrodynamic simulations hold large potential for the proper interpretation of observations and thus for a fundamental understanding of the nature of the non-magnetic chromosphere of the Sun.

Bibliography

- Anderson, L. S. 1989, *ApJ*, 339, 558
- Anderson, L. S. & Athay, R. G. 1989a, *ApJ*, 336, 1089
- . 1989b, *ApJ*, 346, 1010
- Ando, H. & Osaki, Y. 1975, *PASJ*, 27, 581
- Avrett, E. H. 1981, in *NATO ASIC Proc. 68: Solar Phenomena in Stars and Stellar Systems*, 173–198
- Avrett, E. H. 1985, in *Chromospheric Diagnostics and Modelling*, 67–127
- Avrett, E. H. 1995, in *Infrared Tools for Solar Astrophysics: What's Next? Proc. 15th NSO Sac Peak Workshop*, eds. J. Kuhn and M. Penn, World Scientific, Singapore, 303–311
- Avrett, E. H., Hoeflich, P., Uitenbroek, H., & Ulmschneider, P. 1996, in *ASP Conf. Ser. 109: Cool Stars, Stellar Systems, and the Sun*, Vol. 9, 105
- Ayres, T. R. 1981, *ApJ*, 244, 1064
- . 1991, *An Infrared Perspective on Chromospheres* (P. Ulmschneider, E. Priest, R. Rosner (Eds.), *Mechanisms of Chromospheric and Coronal Heating*, Springer-Verlag, Heidelberg), 228 – 239
- . 2002, *ApJ*, 575, 1104
- Ayres, T. R. & Brault, J. W. 1990, *ApJ*, 363, 705
- Ayres, T. R. & Linsky, J. L. 1976, *ApJ*, 205, 874
- Ayres, T. R. & Rabin, D. 1996, *ApJ*, 460, 1042
- Ayres, T. R. & Testerman, L. 1981, *ApJ*, 245, 1124
- Ayres, T. R., Testerman, L., & Brault, J. W. 1986, *ApJ*, 304, 542
- Biermann, L. 1946, *Naturwiss.*, 33, 118
- . 1948, *Z. f. Astrophys.*, 25, 161
- Buchholz, B., Ulmschneider, P., & Cuntz, M. 1998, *ApJ*, 494, 700
- Carlsson, M., Judge, P. G., & Wilhelm, K. 1997, *ApJ*, 486, L63

- Carlsson, M. & Stein, R. F. 1991, in *Mechanisms of Chromospheric and Coronal Heating*, eds. P. Ulmschneider, E. R. Priest, and R. Rosner, Springer Verlag, 366
- Carlsson, M. & Stein, R. F. 1992, *ApJ*, 397, L59
- Carlsson, M. & Stein, R. F. 1994, in *Proc. Mini-Workshop on Chromospheric Dynamics*, ed. M. Carlsson (Oslo: Inst. Theor. Astrophys.), 47
- 1995, *ApJ*, 440, L29
- 1997, *ApJ*, 481, 500
- 2002, *ApJ*, 572, 626
- Cram, L. E. 1978, *A&A*, 70, 345
- Cram, L. E. & Dame, L. 1983, *ApJ*, 272, 355
- Dame, L. & Martić, M. 1987, *ApJ*, 314, L15
- Deubner, F. L. 1988, in *Pulsation and Mass Loss in Stars*, eds. R. Stalio, L. A. Willson, Kluwer Academic Publ., 163
- Deubner, F. L., Hoffmann, J., Kossack, E., & Fleck, B. 1994, in *Solar Surface Magnetism*, eds. R. J. Rutten and C. J. Schrijver, NATO ASI Series C433, 155
- Deubner, F.-L., Ulrich, R. K., & Rhodes, E. J. 1979, *A&A*, 72, 177
- Fawzy, D., Rammacher, W., Ulmschneider, P., Musielak, Z. E., & Stępień, K. 2002a, *A&A*, 386, 971
- Fawzy, D., Ulmschneider, P., Stępień, K., Musielak, Z. E., & Rammacher, W. 2002b, *A&A*, 386, 983
- Fleck, B. & Schmitz, F. 1991, *A&A*, 250, 235
- Foing, B. & Bonnet, R. M. 1984a, *A&A*, 136, 133
- 1984b, *ApJ*, 279, 848
- Fontenla, J. M., Avrett, E. H., & Loeser, R. 1990, *ApJ*, 355, 700
- 1991, *ApJ*, 377, 712
- 1993, *ApJ*, 406, 319
- Freytag, B., Ludwig, H.-G., & Steffen, M. 1996, *A&A*, 313, 497
- Freytag, B., Steffen, M., & Dorch, B. 2002, *Astron. Nachr.*, 323, 213
- Gingerich, O. & de Jager, C. 1968, *Sol. Phys.*, 3, 5
- Gingerich, O., Noyes, R. W., Kalkofen, W., & Cuny, Y. 1971, *Sol. Phys.*, 18, 347
- Hauschildt, P. H., Baron, E., & Allard, F. 1997, *ApJ*, 483, 390
- Hoekzema, N. M. 1994, in *Proc. Mini-Workshop on Chromospheric Dynamics*, ed. M. Carlsson (Oslo: Inst. Theor. Astrophys.), 111

- Hoekzema, N. M., Rimmele, T. R., & Rutten, R. J. 2002, *A&A*, 390, 681
- Iglesias, C. A., Rogers, F. J., & Wilson, B. G. 1992, *ApJ*, 397, 717
- Kalkofen, W. 2001, *ApJ*, 557, 376
- Kalkofen, W., Ulmschneider, P., & Avrett, E. H. 1999, *ApJ*, 521, L141
- Keller, C. U., Deubner, F.-L., Egger, U., Fleck, B., & Povel, H. P. 1994, *A&A*, 286, 626
- Kneer, F. 1983, *A&A*, 128, 311
- Kneer, F. & von Uexküll, M. 1993, *A&A*, 274, 584
- Krijger, J. M., Rutten, R. J., Lites, B. W., et al. 2001, *A&A*, 379, 1052
- Kumar, P. 1994, *ApJ*, 428, 827
- Kurucz, R. L. 1970, *SAO Special Report*, 308
- Leighton, R. B. 1960, *IAU Symp.* 12, 321
- Lighthill, M. J. 1952, *Proc. R. Soc. Lond.*, A 211, 564
- Lites, B. W., Rutten, R. J., & Berger, T. E. 1999, *ApJ*, 517, 1013
- Lites, B. W., Rutten, R. J., & Kalkofen, W. 1993, *ApJ*, 414, 345
- Liu, S. 1974, *ApJ*, 189, 359
- Livingston, W. & Harvey, J. 1971, in *IAU Symp.* 43: *Solar Magnetic Fields*, 51–+
- Ludwig, H., Freytag, B., & Steffen, M. 1999, *A&A*, 346, 111
- Ludwig, H.-G. 1992, PhD thesis, University Kiel, Germany
- Maltby, P., Avrett, E. H., Carlsson, M., et al. 1986, *ApJ*, 306, 284
- Mihalas, D. 1978, *Stellar atmospheres /2nd edition/* (San Francisco, W. H. Freeman and Co., 1978. 650 p.)
- Muchmore, D. & Ulmschneider, P. 1985, *A&A*, 142, 393
- Muglach, K. & Schmidt, W. 2001, *A&A*, 379, 592
- Musielak, Z. E., Rosner, R., Stein, R. F., & Ulmschneider, P. 1994, *ApJ*, 423, 474
- Narain, U. & Ulmschneider, P. 1990, *Space Science Reviews*, 54, 377
- . 1996, *Space Science Reviews*, 75, 453
- Nindos, A. & Zirin, H. 1998, *Sol. Phys.*, 179, 253
- Nordlund, A. 1982, *A&A*, 107, 1
- Nordlund, Å. & Stein, R. F. 2001, *ApJ*, 546, 576
- Noyes, R. W. & Hall, D. N. B. 1972a, *BAAS*, 4, 389

- . 1972b, *ApJ*, 176, L89+
- Priest, E. R. 1982, *Solar magneto-hydrodynamics* (Kluwer/Reidel, Dordrecht)
- Proudman, I. 1952, *Proc. R. Soc. Lond., A*, 214, 119
- Quirk, J. 1994, *Int. J. for Numerical Methods in Fluids*, 18, 555
- Roe, P. L. 1986, *Ann.Rev.Fluid Mech.*, 18, 337
- Rutten, R. G. M., Schrijver, C. J., Lemmens, A. F. P., & Zwaan, C. 1991, *A&A*, 252, 203
- Rutten, R. J. 1994, in *Proc. Mini-Workshop on Chromospheric Dynamics*, ed. M. Carlsson (Oslo: Inst. Theor. Astrophys.), 25–46
- Rutten, R. J., Sütterlin, P., de Wijn, A. G., et al. 2002, in *Solar variability: from core to outer frontiers. The 10th European Solar Physics Meeting, 9 - 14 September 2002, Prague, Czech Republic*. Ed. A. Wilson. ESA SP-506, Vol. 2. Noordwijk: ESA Publications Division, ISBN 92-9092-816-6, 2002, p. 903 - 906, 903–+
- Rutten, R. J. & Uitenbroek, H. 1991a, *Sol. Phys.*, 134, 15
- Rutten, R. J. & Uitenbroek, H. 1991b, in *Mechanisms of Chromospheric and Coronal Heating*, eds. P. Ulmschneider, E. R. Priest, and R. Rosner, Springer Verlag, 48
- Schrijver, C. J. 1987, *A&A*, 172, 111
- . 1995, *A&A Rev.*, 6, 181
- Schwarzschild, M. 1948, *ApJ*, 107, 1
- Skartlien, R. 2000, *ApJ*, 536, 465
- Skartlien, R., Stein, R. F., & Nordlund, Å. 2000, *ApJ*, 541, 468
- Smagorinsky, J. S. 1963, *Monthly Weather Rev.*, 91, 99
- Solanki, S. K., Livingston, W., & Ayres, T. 1994, *Science*, 263, 64
- Solanki, S. K. & Steiner, O. 1990, *A&A*, 234, 519
- Steffen, M. 2000, in *Stellar Astrophysics, Proceedings of the Pacific Rim Conference held in Hong Kong, 1999*. Edited by L. S. Cheng, H. F. Chau, K. L. Chan, and K. C. Leung, published by Kluwer Academic Publishers, The Netherlands, 2000., p.25, 25–+
- Steffen, M., Krüss, A., & Holweger, H. 1991, in *Mechanisms of Chromospheric and Coronal Heating*, eds. P. Ulmschneider, E. R. Priest, and R. Rosner, Springer Verlag, 380
- Steffen, M. & Muchmore, D. 1988, *A&A*, 193, 281
- Stein, R. F. 1967, *Sol. Phys.*, 2, 385
- Stein, R. F. & Nordlund, A. 1989, *ApJ*, 342, L95
- . 1998, *ApJ*, 499, 914
- Stein, R. F. & Nordlund, Å. 2001, *ApJ*, 546, 585

- Stix, M. 1989, *The Sun. An Introduction* (Springer-Verlag Berlin Heidelberg New York.)
- Uitenbroek, H. 2000a, *ApJ*, 531, 571
- . 2000b, *ApJ*, 536, 481
- Uitenbroek, H., Noyes, R. W., & Rabin, D. 1994, *ApJ*, 432, L67
- Ulmschneider, P. 1989, *A&A*, 222, 171
- . 1991 (P. Ulmschneider, E. Priest, R. Rosner (Eds.), *Mechanisms of Chromospheric and Coronal Heating*, Springer-Verlag, Heidelberg), 328 – 342
- . 2003, in *Lectures in Solar Physics* (H. M. Antia, A. Bhatnagar, P. Ulmschneider (Eds.), *Lecture Notes in Physics*, Springer Verlag), 234–282 (in press)
- Ulmschneider, P., Muchmore, D., & Kalkofen, W. 1987, *A&A*, 177, 292
- Ulmschneider, P., Schmitz, F., Kalkofen, W., & Bohn, H. U. 1978, *A&A*, 70, 487
- Ulmschneider, P., Theurer, J., & Musielak, Z. E. 1996, *A&A*, 315, 212
- Ulrich, R. K. 1970, *ApJ*, 162, 993
- van Leer, B. 1974, *J. Comput. Phys.*, 14, 361
- Vernazza, J. E., Avrett, E. H., & Loeser, R. 1973, *ApJ*, 184, 605
- . 1976, *ApJS*, 30, 1
- . 1981, *ApJS*, 45, 635
- White, O. R. & Livingston, W. C. 1981, *ApJ*, 249, 798
- Wiedemann, G., Ayres, T. R., Jennings, D. E., & Saar, S. H. 1994, *ApJ*, 423, 806
- Wilhelm, K. 2002, *American Astronomical Society Meeting*, 200, 0
- Wunnenberg, M. 2003, *priv. comm.*
- Wunnenberg, M., Kneer, F., & Hirzberger, J. 2002, *A&A*, 395, L51

Acknowledgements

First of all, I have to thank Hartmut Holweger for giving me the possibility of working together with him on his last “official” project and for his uncomplicated support and useful hints. I appreciated very much the close and pleasing cooperation with Bernd Freytag, Matthias Steffen, and Hans-Günter Ludwig over the last three years – especially considering the large distances our “virtual” working group has to struggle with. At all times they willingly answered my countless questions by phone or e-mail. By the way, sorry for any “flooding” of your inbox folders...;)

I am deeply grateful to Holger Boll for all help with technical problems – in particular for the speedy installation of the 180 GB harddisk which I so badly needed in the last months and getting IDL back to live only a few days before my thesis deadline – although he had some days off. All other colleagues at the institute are thanked for the relaxed atmosphere. Special thanks go to Marc Hempel for all “non-scientific” activities.

Furthermore, I am obliged to the colleagues of the *Astronomy and Astrophysics Group* at the *University of Glasgow* for their hospitality in the summer 2000, offering me a nice start for the PhD project.

I am grateful to Maren Wunnenberg and Peter Sütterlin who allowed me to use their excellent observations, and Mats Carlsson for providing data for comparison.

Moreover, I am also thankful for support by the “*German Academic Exchange Service*” and the *Deutsche Forschungsgemeinschaft*. The numerical simulations were carried out on the CRAY SV1 of the *Rechenzentrum der Universität Kiel*.

Last but not least I have to thank my little daughter Helena for every single smile, which helped me to keep up during the last days, and in particular for every silent night. Of course, Jessica deserves very special thanks for her understanding and help, in particular keeping away from me all the little problems in the last weeks and to “survive” these unbelievably turbulent last months. Not to forget my good friend Alejo Sanchez-Vivar. Thanks for the continuous fun when reading your e-mails, pretending interest for my work and for all your prayers – I am sure you were not able to help doing it ;).

Lebenslauf

Name: Sven Wedemeyer

Geburtsdatum, -ort: 20.06.1975, Neumünster

Staatsangehörigkeit: deutsch

Schulbildung:

Aug. 1981 - Juli 1985 Grund- und Hauptschule im Schulzentrum Einfeld, Neumünster
Aug. 1985 - Juli 1994 Gymnasium: Alexander-von-Humboldt-Schule, Neumünster
02.07.1994 Abitur an der Alexander-von-Humboldt-Schule, Neumünster

Studium:

01.10.1994 - 23.12.1999 Studium des Fachs Physik mit Abschluß Diplom an der Christian-Albrechts-Universität zu Kiel (CAU);
Nebenfächer im Grundstudium: Mathematik und Chemie;
Nebenfach im Hauptstudium: Mathematik (Numerik),
zusätzlich Kurse im Fach Geologie

06.11.1996 Diplom-Vorprüfung im Fach Physik, CAU Kiel
(*Gesamturteil: sehr gut*)

01.12.1998 - 01.12.1999 Diplomarbeit bei Prof. Dr. H. Holweger am Institut für Theoretische Physik und Astrophysik, CAU Kiel,
Thema: „Statistisches Gleichgewicht von Silizium in kühlen Sternen“

04.01.2000 Diplom-Hauptprüfung im Fach Physik, CAU Kiel
(*Gesamturteil: sehr gut*)

02.05.2000 - 31.08.2000 DAAD-Stipendiat am Department of Physics & Astronomy,
University of Glasgow, Großbritannien,

seit 01.10.2000 Promotion bei Prof. Dr. H. Holweger am Institut für Theoretische Physik und Astrophysik, CAU Kiel,
Thema: „Multi-Dimensional Radiation Hydrodynamic Simulations of the Non-Magnetic Solar Atmosphere“

Erklärung

Die Abhandlung mit dem Titel „*Multi-Dimensional Radiation Hydrodynamic Simulations of the Non-Magnetic Solar Atmosphere*“ wurde von mir in Form und Inhalt unter Anleitung von Prof. Dr. H. Holweger und unter Zuhilfenahme der angegebenen Hilfsmittel angefertigt. Sie wurde nicht ganz und auch nicht zum Teil an anderer Stelle im Rahmen eines Prüfungsverfahrens vorgelegt.

Kiel, 28. Mai 2003

Sven Wedemeyer

